

RL-TR-95-212
Final Technical Report
October 1995



LARGE DYNAMIC RANGE RADAR CROSS SECTION PARALLEL TRACKING

Hughes Aircraft Company

Larry Doan, Patrick A. Day, and Oleg Brovko

DTIC QUALITY INSPECTED 4

APPROVED FOR PUBLIC RELEASE; DISTRIBUTION UNLIMITED.

19960212 028

**Rome Laboratory
Air Force Materiel Command
Rome, New York**

This report has been reviewed by the Rome Laboratory Public Affairs Office (PA) and is releasable to the National Technical Information Service (NTIS). At NTIS, it will be releasable to the general public, including foreign nations.

RL-TR-95- 212 has been reviewed and is approved for publication.

APPROVED:



PAUL F. GILGALLON
Project Engineer

FOR THE COMMANDER:



DONALD W. HANSON
Director of Surveillance & Photonics

If your address has changed or if you wish to be removed from the Rome Laboratory mailing list, or if the addressee is no longer employed by your organization, please notify Rome Laboratory/ (OCTM), Rome NY 13441. This will assist us in maintaining a current mailing list.

Do not return copies of this report unless contractual obligations or notices on a specific document require that it be returned.

REPORT DOCUMENTATION PAGE

Form Approved
OMB No. 0704-0188

Public reporting burden for this collection of information is estimated to average 1 hour per response, including the time for reviewing instructions, searching existing data sources, gathering and maintaining the data needed, and completing and reviewing the collection of information. Send comments regarding this burden estimate or any other aspect of this collection of information, including suggestions for reducing this burden, to Washington Headquarters Services, Directorate for Information Operations and Reports, 1215 Jefferson Davis Highway, Suite 1204, Arlington, VA 22202-4302, and to the Office of Management and Budget, Paperwork Reduction Project (0704-0188), Washington, DC 20503.

1. AGENCY USE ONLY (Leave Blank)		2. REPORT DATE October 1995		3. REPORT TYPE AND DATES COVERED Final Jul 89 - Nov 91	
4. TITLE AND SUBTITLE LARGE DYNAMIC RANGE RADAR CROSS SECTION PARALLEL TRACKING				5. FUNDING NUMBERS C - F30602-89-C-0126 PE - 62702F PR - 4506 TA - 17 WU - OF	
6. AUTHOR(S) Larry R. Doan, Patrick A. Day, and Oleg Brovko					
7. PERFORMING ORGANIZATION NAME(S) AND ADDRESS(ES) Hughes Aircraft Company Radar Systems Group 2260 Imperial Highway P.O. Box 92426 Los Angeles CA 90009				8. PERFORMING ORGANIZATION REPORT NUMBER N/A	
9. SPONSORING/MONITORING AGENCY NAME(S) AND ADDRESS(ES) Rome Laboratory/OCTM 26 Electronic Pky Rome NY 13441-4514				10. SPONSORING/MONITORING AGENCY REPORT NUMBER RL-TR-95-212	
11. SUPPLEMENTARY NOTES Rome Laboratory Project Engineer: Paul F. Gilgallon/OCTM/(315) 330-4431					
12a. DISTRIBUTION/AVAILABILITY STATEMENT Approved for public release; distribution unlimited.				12b. DISTRIBUTION CODE	
13. ABSTRACT (Maximum 200 words) Maintaining radar track of small targets in close proximity to much larger targets was the primary thrust of the Large Dynamic Range (LDR) program. Environmental factors and phenomenology associated with the RF tracking problem were explored to determine discriminants that could enhance the tracking performance. An RCS modeling technique was developed and verified against existing known models so the co-target interference phenomena could be simulated in a VAX computer. Six specific methods were studied and algorithms developed to determine the best method for reducing the co-target interference. An additional effect of the co-target interference phenomenology was discovered that may improve the detection process. The algorithms were employed in a tracking simulation to determine their relative performance. A future study to verify the results of the LDR program by physical measurement is recommended.					
14. SUBJECT TERMS Radar parallel tracking, Radar cross section				15. NUMBER OF PAGES 192	
				16. PRICE CODE	
17. SECURITY CLASSIFICATION OF REPORT UNCLASSIFIED	18. SECURITY CLASSIFICATION OF THIS PAGE UNCLASSIFIED	19. SECURITY CLASSIFICATION OF ABSTRACT UNCLASSIFIED	20. LIMITATION OF ABSTRACT UL		

TABLE OF CONTENTS

1.0 INTRODUCTION.....	1
2.0 REFERENCED DOCUMENTS	2
3.0 TECHNICAL DISCUSSIONS.....	3
3.1 Phenomenology.....	3
3.1.1 Introduction	3
3.1.2 Target RCS Model.....	4
3.1.2.1 Aircraft RCS Model.....	5
3.1.2.1.1 Coordinate System.....	6
3.1.2.1.2 Overview of Geometric Optics.....	8
3.1.2.1.3 RCS Computations for Ellipsoids.....	10
3.1.2.1.4 Monostatic RCS of Aircraft.....	11
3.1.2.1.5 Shadowing Effects.....	12
3.1.2.1.6 Bistatic RCS of Aircraft	15
3.1.2.1.7 Bistatic Shadowing.....	16
3.1.2.1.8 Computed RCS of Airplane.....	18
3.1.2.2 Cruise Missile RCS Model.....	24
3.1.2.2.1 Coordinate System.....	25
3.1.2.2.2 Overview of Physical Optics.....	29
3.1.2.2.3 Cylinders.....	30
3.1.2.2.4 Triangular Plates.....	41
3.1.2.2.5 Straight Edges.....	50
3.1.2.2.6 Computed RCS of Missile	55
3.1.3 Target Interaction Model.....	62
3.1.3.1 Path 1.....	69
3.1.3.2 Path 2.....	70
3.1.3.3 Path 3.....	70
3.1.3.4 Path 4.....	71
3.1.3.5 Computed Target Interaction.....	73 A
3.2 Discriminant Study.....	89
3.3 Radar Resolution Trade Study and Workload.....	93
3.4 Statistical Characterization	99
3.5 Algorithms	106
3.5.1 Co-Target Interference Reduction Formulation: Unified Theory	106

3.5.2 Description and Performance Evaluation	112
3.5.2.1 Range Response Cancellation	112
3.5.2.2 Zero-Out Blanking	122
3.5.2.3 Range Sidelobe Suppression	127
3.5.2.4 Doppler Cancellation in the Time Domain	132
3.5.2.5 Other Techniques	136
3.5.3 Error Analysis	139
3.5.4 Processing Requirements	151
3.5.5 Technique Summary	155
3.6 Tracking Implementation	156
3.6.1 Filtering	160
3.6.2 Masking Region and Measurement Biases	165
3.6.3 Results of Tracking	172
4.0 CONCLUSIONS AND FUTURE WORK	182
5.0 FOOTNOTES	183
6.0 APPENDIX	184

1.0 INTRODUCTION

Over the years, airborne threats to the United States and its forces in the field have evolved to include low RCS technology which makes these threats much more difficult to detect by radar systems. The small RCS detection problem, per se, is being pursued by other government and industry programs and was not the primary requirement addressed during this program. However, when such low RCS threats are in close proximity to larger targets, other factors are present which exacerbate the detection problem as well as the related problems of track acquisition and maintaining track over time. It is the characterization and, perhaps, exploitation of this "co-target interference" phenomena which was the purpose for the LDR program.

Cruise missiles may be launched from carriers which are much larger in RCS. Developing feasible processes for detecting the launch by the appearance of two targets where only one originally existed is vital for the surveillance mission. After launch, the smaller RCS threats travel long distances via low level routes in the presence of clutter and noise sources, are often in the same area with high traffic density, and their paths often cross with those of much larger targets, all of which may cause track maintenance difficulties. Additionally, the presence of jamming and other Electronic Countermeasures (ECM) will cause further complications. This demanding environment will be present in all future tactical mission scenarios.

2.0 REFERENCED DOCUMENTS

This Large Dynamic Range Final Report makes references to the Software User's Manual and the Software Test Description.

Also the following references are cited in the Report:

1. Kapogianis, K., and Macfarlane, J. F., Description of a Multiple-Reflector Aircraft Target Model, Hughes Aircraft Co. internal memo., Jan. 26, 1979, Ref. 2312.11/01.
2. Ruck, G. T., Barrick, D. E., Stuart, W. D., and Krichbaum, C. K., *Radar Cross Section Handbook*, Plenum Press, New York (1970).
3. Blackman, S. S., *Multiple-Target Tracking with Radar Applications*, Artech House, Norwood, Mass. (1986).

3.0 TECHNICAL DISCUSSIONS

3.1 PHENOMENOLOGY

3.1.1 Introduction

Two targets flying in close proximity present a challenge for radar signal processing, especially if one of the targets has low RCS. When the two are illuminated by an electromagnetic wavefront, the superposition of the direct return paths, each proportional to their corresponding RCS, may not be appreciable if the targets are in close proximity. Mutual target coupling can now dominate and introduce interesting signal behavior. Figure 3.1.1-1 shows a possible target geometry with large and low RCS targets with wavefront multipath present. Because the large target will have a complex structure with a set of dominant scattering points, many bounce paths may illuminate the low RCS target from various aspect and depression angles. This can in turn enhance the small monostatic target RCS by a path illuminating a favorable bistatic angle.

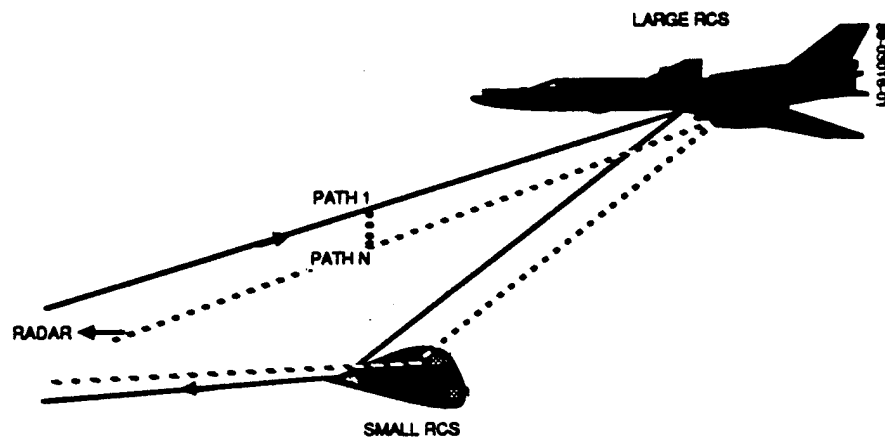


Figure 3.1.1-1. Co-Target Interference May Enhance Small Target RCS

To understand the nature of the mutual target interaction, it is necessary to understand how the wavefront bounces off each target at different bistatic and monostatic angles. Thus it is necessary to have an adequate target RCS model that allows for easy and reliable predictions of target RCS, both monostatic and

bistatic. Once the RCS of different target components are obtained through the RCS model, an interaction model is needed to describe how the wavefront bouncing from one target is received by the other target. The two models are combined to describe and quantify the target interaction signals that are eventually detected at the receiver.

3.1.2 Target RCS Model

As a part of the interaction prediction model, we predict target RCS using a hybrid model that is a combination of geometrical optics and physical optics. These are considered to be high-frequency techniques, applicable when target dimensions are large compared with wavelength. In the LDR simulation, the radar wavelengths used are on the order of a foot or shorter so most airborne targets will be at least 10 wavelengths long. Therefore, the high-frequency modeling is justified. At X-band (0.1 ft), the targets will be hundreds of wavelengths long, and high frequency techniques are even more useful.

It must be pointed out that the electrical size requirement actually applies to individual scattering features and not the overall target length. This was assumed in the LDR interaction simulation and typically assumed in practice because high-frequency techniques can only be applied to relatively simple shapes that are easily described in mathematical terms. Therefore, we must break up the actual target, whether it is an aircraft or a missile, into a collection of approximate simple geometrical shapes. The high-frequency size requirement then applies to these shapes, and not necessarily to the overall target. Even so, most target features are still within the high frequency scattering region. They should be at least five wavelengths in size, although reasonable accurate results may be obtained for some bodies even smaller than this.¹

At the lower end of the high-frequency region and in the resonant scattering region, where the target features are less than 5 wavelengths, high-frequency techniques lose their accuracies. Other prediction techniques such as the Method of Moments (MOM) should be used, and this would certainly enhance the capability of LDR software to predict target RCS. On the other hand, it must be kept in mind that the scope of the LDR project is to investigate 2-target bistatic interaction, it is not a comprehensive target RCS modeling

project. Refined high-frequency prediction techniques such as geometric theory of diffraction (GTD), method of equivalent currents (MEC), and physical theory of diffraction (PTD) have to be left out of the LDR model. These techniques demand a great deal of mathematical and software complexity that can not be provided within the scope of this study.

In the high-frequency region, collective interactions are very small, so that a body can be treated as a collection of independent scattering centers. Each part of the body scatters energy essentially independently of all other parts. The fields induced on a portion of the target are only due to the incident wave and not the energy scattered by other parts.² The simplest high frequency method is geometric optics (GO). The RCS is given by a simple formula that involves only the local radii of curvature at the specular point. When the radii of curvature becomes infinite, as in the case of a cylinder or flat plate, then GO fails and we would then have to use physical optics (PO) instead. Physical optics give good results if the surface is not too small and if the scattering direction does not swing too far from the specular direction. At wide angles from specular, however, physical optics fails. This is because the contributions from the edges are ignored, which can be accounted for by the GTD method.³

The LDR interaction model uses geometric optics to predict the RCS of the generic aircraft and physical optics for the cruise missile. This is because the aircraft can be modeled as a collection of ellipsoids that are several wavelengths in size. With an ellipsoid, the easiest way to compute the RCS is to use geometric optics formulas that are easily available. The cruise missile, being smaller than the aircraft and being more "flat", is modeled as a collection of other geometric shapes. The main component, the fuselage, is modeled as a hemispherically-capped cylinder. The rest of the missile is modeled using flat plates and wires. For these shapes, the RCS formulas are derived using physical optics theory.

3.1.2.1 Aircraft RCS Model

When the aircraft is illuminated by electromagnetic energy, it has been observed experimentally⁴ that most of the energy is reflected from a discrete number of locations. Each location can be modeled as a single scattering point, and thus a finite number of scatterers can be used to model the entire aircraft.

In practice, the major sections of the aircraft are modeled as basic geometrical shapes such as ellipsoids. Each ellipsoid has one reflection point, referred to as the "specular point", which is determined by geometric optics. A good approximation of the aircraft's radar cross section can then be estimated as a function of aspect angle.

The LDR interaction simulation employs this model as developed in Reference 1. A Cessna A-37B aircraft was used although any aircraft can be modeled when its actual physical dimensionings are specified.

3.1.2.1.1 Coordinate System

An illustration of the ellipsoids is shown in Figure 3.1.2.1.1-1. The coordinate system X_T , Y_T , and Z_T is the reference coordinate system for the aircraft RCS computation. The origin is the center of the fuselage ellipsoid with the X_T axis always pointing in the nose direction of the aircraft. Each component ellipsoid has its own local coordinate system generated by rotating the reference coordinate system by the angles α , β , and γ , and then translated by X , Y , and Z . A local coordinate system is shown in Figure 3.1.2.1.1-2. The ellipsoids and their related parameters for the Cessna are listed in Table 3.1.2.1.1-1.

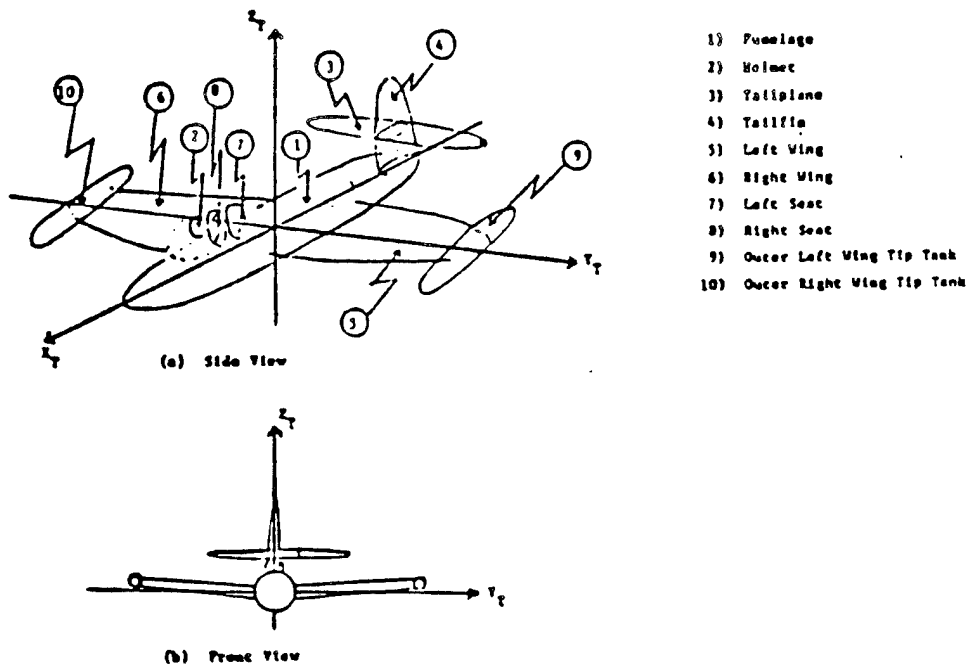


Figure 3.1.2.1.1-1. Ellipsoid Components of Aircraft

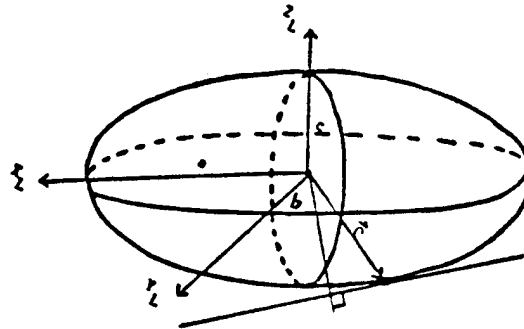


Figure 3.1.2.1.1-2. Local coordinate system of an ellipsoid

To transform from the reference coordinate system to a local coordinate system we use the transformation matrix T :

$$\begin{bmatrix} X_L \\ Y_L \\ Z_L \end{bmatrix} = \begin{bmatrix} \cos\alpha \cos\beta & \sin\alpha \cos\beta & -\sin\beta \\ \cos\alpha \sin\beta \sin\gamma - \sin\alpha \cos\gamma & \sin\alpha \sin\beta \sin\gamma + \cos\alpha \cos\gamma & \sin\gamma \cos\beta \\ \cos\alpha \sin\beta \cos\gamma + \sin\alpha \sin\gamma & \sin\alpha \sin\beta \cos\gamma - \cos\alpha \sin\gamma & \cos\gamma \cos\beta \end{bmatrix} \cdot \begin{bmatrix} X_T - X \\ Y_T - Y \\ Z_T - Z \end{bmatrix}$$

or more compactly,

$$\vec{x}_L = T(\vec{x}_T - \vec{x}_D)$$

where \vec{x}_D is the displacement vector composed of X , Y , and Z .

The radar location is specified in terms of the azimuth and elevation angles as measured in the reference coordinate system. An illustration is shown in Figure 3.1.2.1.1-3. Thus, nose-on aspect is 0° azimuth and 0° elevation while tail aspect is 180° azimuth and 0° elevation. The line of sight to the radar is a vector with reference coordinates given by:

$$\begin{bmatrix} R_X \\ R_Y \\ R_Z \end{bmatrix} = \begin{bmatrix} \cos az \cos el \\ \sin az \cos el \\ \sin el \end{bmatrix}$$

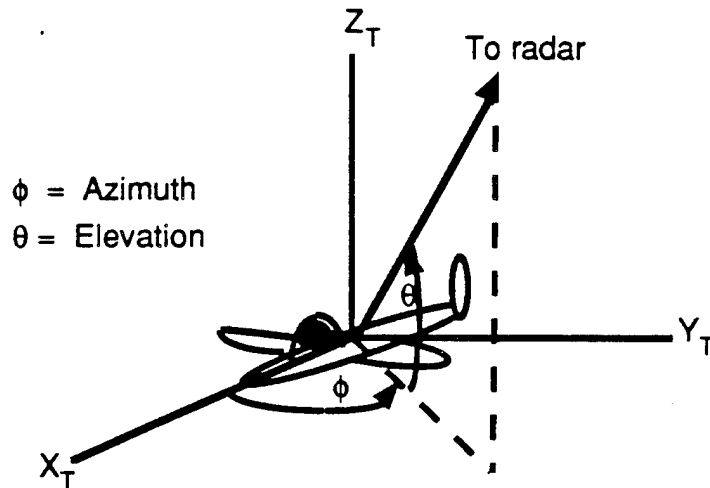


Figure 3.1.2.1.1-3. Reference coordinate system

3.1.2.1.2 Overview of Geometric Optics

Some basic principles of geometric optics are presented here for reference. This technique is a ray-tracing procedure whereby the energy incident upon the surface of the object travels in ray bundles. The reflection coefficient for a perfectly conducting surface is -1, implying no reduction of the intensity of the reflected wave. This is only true at the point of reflection (the specular point), and as is noted above, the ellipsoids are modeled in terms of their specular points. Because of this, the decay in intensity of the reflected wave does not come into play when computing the ellipsoid RCS.

The polarization of the incident wave is also neglected. The RCS of the ellipsoid is the same regardless of the type of incident polarization.

Geometric optics is not valid in the neighborhood of sharp points or boundaries, such as the tip of a cone, the edge of a wedge, etc. For these cases, other techniques must be used, such as GTD or PTD. As mentioned previously, the Large Dynamic Range project does not use these more sophisticated theories.

The results of geometric optics give the RCS in terms of the radii of curvature of the body at the specular point. The formula is given by:

$$\sigma = a_1 a_2,$$

TABLE 3.1.2.1.1-1. PARAMETERS FOR THE AIRCRAFT ELLIPSOIDS

No.	Ellipsoid Component	a (ft)	b (ft)	c (ft)	alpha (deg.)	beta (deg.)	gamma (deg.)	x (ft)	y (ft)	z (ft)
1	Fuselage	14.14	2.74	1.39	0.00	0.00	0.00	0.00	0.00	0.00
2	Helmet	0.50	0.49	0.49	0.00	-90.00	0.00	4.90	1.00	2.58
3	Tailplane	6.99	2.27	0.23	90.00	0.00	0.00	-11.86	0.00	3.67
4	Tailfin	4.59	2.28	0.10	90.00	-90.00	0.00	-11.86	0.00	2.29
5	Left Wing	14.94	2.96	0.47	90.00	-3.64	0.00	1.82	2.99	0.92
6	Right Wing	14.94	2.96	0.47	-90.00	-3.64	0.00	1.82	-2.99	0.92
7	Left Seat	0.80	0.60	0.26	0.00	-90.00	0.00	4.20	1.00	2.10
8	Right Seat	0.80	0.60	0.26	0.00	-90.00	0.00	4.20	-1.00	2.10
9	Outer Left Wing Tip Tank	5.02	0.75	0.69	0.00	0.00	0.00	1.82	16.96	0.92
10	Outer Right Wing Tip Tank	5.02	0.75	0.69	0.00	0.00	0.00	1.82	-16.96	0.92

where a_1 and a_2 are the principal radii of curvature of the body at the specular point. From this expression, it can be seen that the RCS is not dependent upon the frequency of the incident wave. Also, this formula is valid for perfectly conducting bodies. The difficulty with this formula is that for flat or singly curved surfaces (not quadric), one or both radii of curvature are infinite, giving infinite RCS. Physical optics is needed to overcome this dilemma.

The geometric optics approach is valid for wavelengths that are small compared to the dimensions of the objects. In the LDR simulation, we use wavelengths that are 1 foot or less. Thus the model is more accurate at the higher ends of the spectrum, such as above 5 GHz (0.2 ft) or so. Some of the smaller ellipsoids used in the model of the aircraft have dimensions of this order (0.2 ft) so their RCS values are not as accurate as the larger ellipsoids. Ideally, the objects should be at least 5 wavelengths in size although as mentioned above, reasonably accurate results can still be obtained for smaller objects. It is also necessary to have objects that are sufficiently smooth. The ellipsoids in the LDR simulation certainly satisfy these conditions.

For longer wavelengths more sophisticated RCS computational methods must be used such as method of moments, integral equations, etc. However, the LDR simulation is not expected to simulate targets at below L-band (1 GHz or 1 ft).

3.1.2.1.3 RCS Computations for Ellipsoids

The RCS of an ellipsoid as given by geometric optics is:⁵

$$\sigma = \pi \frac{a^2 b^2 c^2}{p^2}$$

where

$$p = a^2 D_x^2 + b^2 D_y^2 + c^2 D_z^2$$

a , b , c are the ellipsoid semi-axes, and

D_x , D_y , and D_z are the components of the local radar line of sight.

Geometric optics assumes that each ellipsoid is represented by only one point, the specular point, where most of the electromagnetic energy is reflected back. The local coordinates of this point is given by the vector \vec{Q} with components:

$$Q_x = \frac{D_x a^2}{\sqrt{p}}, \quad Q_y = \frac{D_y b^2}{\sqrt{p}}, \quad Q_z = \frac{D_z c^2}{\sqrt{p}}.$$

An illustration of the specular point geometry and the radar scenario can be seen in Figure 3.1.2.1.1-1.

3.1.2.1.4 Monostatic RCS of Aircraft

When computing the scattered power from a complex object in the high-frequency region, the fields scattered by the many different components must be calculated and then added together before squaring to obtain the scattered power. Interference effects may thus be represented because the phase relationship between the various scatterers are preserved. Since the scattered power is proportional to the RCS, this implies that the square root of the RCS of the various aircraft components are algebraically summed with appropriate phases to obtain the total RCS.

The total monostatic RCS of the aircraft can be computed by summing the square root of the RCS of all ellipsoids. It is given by:

$$\sigma_T = \left| \sum_{j=1}^N (\sigma_j)^{1/2} \exp(i\phi_j) \right|^2$$

where σ_j is the RCS of the j -th ellipsoid and ϕ_j is the relative phase angle of the j -th ellipsoid. The magnitude of ϕ_j is determined by selecting a reference plane normal to the direction of incidence and measuring the distance from this plane to the specular point of the ellipsoid. The reference plane is chosen to pass through the reference coordinate origin. This plane and the direction of incidence as the X-axis form what is called the reference line-of-sight (LOS) coordinate system. To go from the reference coordinate system to this system we rotate by a transformation matrix S :

$$\vec{x}_{los} = S \vec{x}_T$$

Therefore, the specular point \vec{Q} in the reference LOS coordinate system is given by:

$$\vec{Q}_{los} = S \left(T^T \vec{Q} + \vec{x}_D \right),$$

with T^T being the transpose of T . The first component of \vec{Q}_{los} is the distance from the reference plane to the specular point of an ellipsoid. Call this d_j for the j -th ellipsoid. Then the phase is given by

$$\phi_j = 2\pi \frac{2d_j}{\lambda}.$$

The factor 2 is to account for the incident and reflecting path.

3.1.2.1.5 Shadowing Effects

Because the geometric optics model assumes that for each ellipsoid most of the electromagnetic energy is reflected from a single specular point, it follows that there will be instances where the specular point is obstructed by another ellipsoid. This is called "shadowing". An ellipsoid is assumed to not contribute to the total aircraft RCS when it is shadowed. Large sections of the ellipsoid may be visible, but its RCS will be set to zero if its specular point is shadowed. In reality, a small amount of energy is scattered from these sections because they are accessible to the incident plane wave. However, for the purpose of the LDR simulation, this energy can be neglected since it contributes little to the total scattered energy from the ellipsoid. Most of the scattered energy would have come from the unobstructed specular point, which in this case is blocked.

Another type of shadowing, "layered shadowing" occurs when part of the ellipsoid model is nonexistent. Sometimes it is necessary to model certain target components as partial ellipsoids to represent the true target as closely as

possible. For example, the wings of the aircraft are modeled as ellipsoids but they are actually half-ellipsoids. Thus if the specular point of a wing, when seen from a particular aspect angle, happens to fall in the non-existent portion of the ellipsoid then the wing is shadowed, and its RCS is set to zero. Another example is the tailplane where the central portion of the ellipsoid does not exist, but is actually considered a part of the tailfin. Other regions where layered shadowing occurs are listed in Table 3.1.2.1.5-1.

The components that are partial ellipsoids have reduced RCS. If the specular point of such an ellipsoid falls in an actual portion of the ellipsoid (i.e. layered shadowing does not occur), and the first type of shadowing does not occur, then the RCS of the ellipsoid is computed from the ellipsoid RCS formula above using dimensions of the full ellipsoid. This value, however, is then reduced in the simulation by the corresponding fraction of the ellipsoid that is real. For example, the RCS of the wings of the airplane are half of what would be computed using the formula.

The actual implementation of the shadowing algorithm begins by sorting the specular points in order of their distances from the LOS reference plane. In other words, the ellipsoids with larger d_j are considered to be in front of other ellipsoids with respect to the oncoming wavefront. Suppose that the i -th ellipsoid is in front of the k -th ellipsoid, then the k -th ellipsoid is shadowed if its specular point satisfies the equation:

$$\frac{(q_x + \zeta L_x)^2}{a^2} + \frac{(q_y + \zeta L_y)^2}{b^2} + \frac{(q_z + \zeta L_z)^2}{c^2} = 1$$

for some $\zeta > 0$, where

q_x, q_y , and q_z = the components of the k -th specular point in the i -th local coordinate system,

L_x, L_y , and L_z = the components of the radar LOS in the i -th local coordinate system, and

a, b , and c are the semi-axes of the i -th ellipsoid.

An illustration of this equation is shown in Figure 3.1.2.1.5-1.

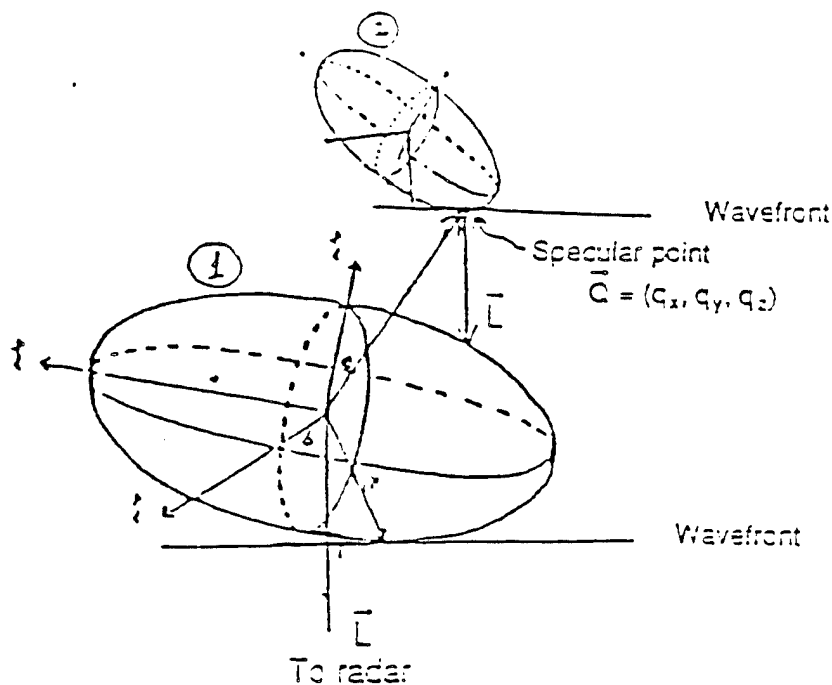


Figure 3.1.2.1.5-1. Shadowing Geometry

Any ellipsoidal component which is shadowed will have its RCS (σ_i) set to zero in the equation for σ_T above.

TABLE 3.1.2.1.5-1. LAYERED SHADOWING REGIONS

Component	Layered Shadowing
Fuselage	None
Pilot's Helmet	None
Tailplane	$[90^\circ < \phi \leq 270^\circ \text{ and } \theta < 145^\circ]$ and $-0.267 < C(1) < 0.267 \text{ ft}$
Tailfin	1. $X_T(3) < 0.0$ 2. $3.30 < X_T(3) < 3.94 \text{ ft}$
Left Wing	$X_T(2) < 2.99 \text{ ft}$
Right Wing	$X_T(2) > -2.99 \text{ ft}$
Left Seat	None
Right Seat	None
Outer Left Wing Tip Tank	None
Outer Right Wing Tip Tank	None

$C(1)$, $C(2)$, and $C(3)$ are the local component coordinates of specular point.
 $X_T(1)$, $X_T(2)$, $X_T(3)$ are in the aircraft reference coordinates.

3.1.2.1.6 Bistatic RCS of Aircraft

In the high-frequency region it can be shown that most of the scattered field comes from the immediate neighborhood of the specular point even in bistatic scattering⁶. Figure 3.1.2.1.6-1 illustrates the geometry of bistatic scattering. For incident direction \hat{k}_i and scattering direction \hat{k}_s , $\hat{k}_i \neq \hat{k}_s$, the specular point is that point whose normal vector \hat{n} bisects the angle between \hat{k}_i and \hat{k}_s and lies in the plane formed by these vectors. The specular point can be found by assuming that an equivalent monostatic radar line-of-sight is along the vector \hat{n} and applying the formulas above. This is also the basis for computing bistatic RCS from monostatic RCS using what is known as the *monostatic/bistatic equivalence theorem*. This theorem states that as the wavelength tends to zero, the bistatic RCS for transmitter (incident) direction \hat{k}_i and receiver (scattering) direction \hat{k}_s , $\hat{k}_i \neq \hat{k}_s$, is equal to the monostatic RCS for the transmitter-receiver direction $\hat{k}_i + \hat{k}_s$ for bodies that are sufficiently smooth. Therefore, we can determine the bistatic RCS of the aircraft by applying the monostatic results in the direction $\hat{k}_i + \hat{k}_s$.

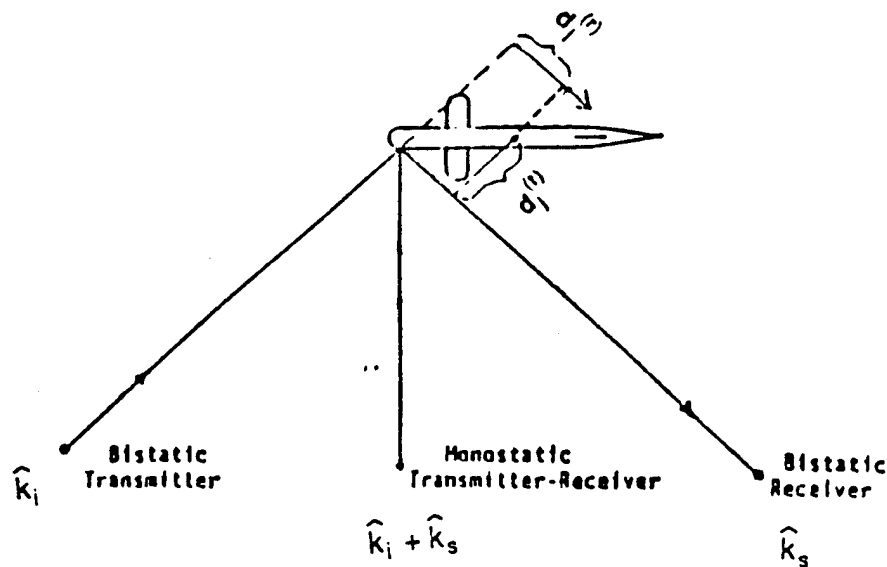


Figure 3.1.2.1.6-1. Bistatic scattering geometry

In computing the total bistatic RCS of the aircraft, the relative phase of each ellipsoid is computed in a slightly different way than that of the monostatic

case. We compute the distance of each specular point as measured from two reference planes. One plane is normal to the transmitter direction \hat{k}_t while the other is normal to the receiver direction \hat{k}_s . Call these distances $d_j^{(t)}$ and $d_j^{(r)}$ for the j -th ellipsoid. Then the phase is given by

$$\phi_j = 2\pi \frac{(d_j^{(t)} + d_j^{(r)})}{\lambda}$$

The monostatic/bistatic equivalence theorem has certain limitations that limit its usefulness. First of all, it is not accurate for bistatic angles greater than about 135° . The bistatic angle is the angle between \hat{k}_t and \hat{k}_s . Furthermore, its accuracy decreases as the radar frequency is lowered. Despite these weaknesses, the theorem is used for bistatic scattering from the airplane because it is the most accessible method for computing bistatic RCS with ellipsoids and geometric optics. However, the theorem is not used to compute bistatic scattering from the missile.

3.1.2.1.7 Bistatic Shadowing

Shadowing in the bistatic case is similar to the monostatic case but is more complex. Even though the direction $\hat{k}_t + \hat{k}_s$ is used to compute the equivalent bistatic RCS, the actual transmitting and receiving directions of the electromagnetic energy must be used to check for shadowing. If the specular point of an ellipsoid is obstructed when seen from either the transmitting or the receiving direction, then a shadowed condition for that ellipsoid must exist. Thus it is necessary to check for shadowing with respect to two directions in the bistatic case.

Bistatic shadowing also differs from monostatic shadowing in some interesting ways. First, a specular point can be in the clear with respect to one LOS, but is shadowed with respect to the other LOS. In this case, the net effect is that the ellipsoid is shadowed. Second, in the bistatic case, when the specular point of an ellipsoid is in front of the specular point of another ellipsoid, as seen from a given direction, it can still be shadowed by the ellipsoid that is behind. This means that we must be careful to check if "front" components are

shadowed by "rear" components. In the monostatic case, components in front are never shadowed by components behind them. Figures 3.1.2.1.7-1 (a) & (b) contain some examples of bistatic shadowing.

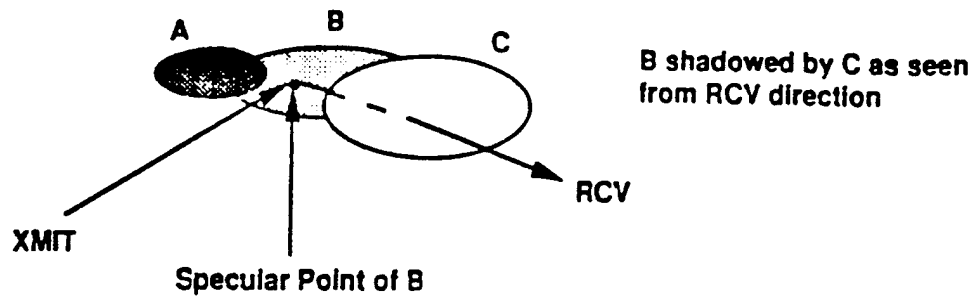


Figure 3.1.2.1.7-1 (a). Either line-of-sight can shadow ellipsoid

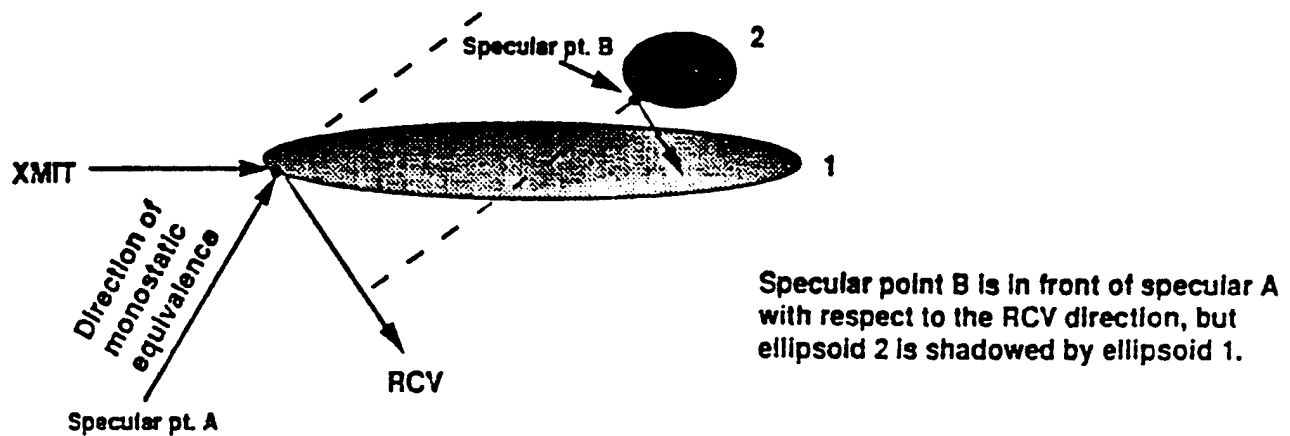


Figure 3.1.2.1.7-1 (b). Another type of bistatic shadowing

3.1.2.1.8 Computed RCS of Airplane

In this section we present the results for the computed RCS of the airplane. Figures 3.1.2.1.8-1 (a) & (b) show the monostatic RCS of the aircraft as a function of the azimuth angle for L-band and X-band. Both figures are for the case of a radar in the 0° elevation plane. The most striking features of the plots are the peaks at broadside (90°). This is not surprising since at broadside the fuselage of the aircraft presents itself most completely to the incident wave. The peaks are about 35 dBsm in magnitude while the average RCS in both cases is about 0 to 5 dBsm. The X-band curve fluctuates much more than the L-band curve, and this is due to the much smaller wavelength, thus increasing the phase difference from aspect to aspect.

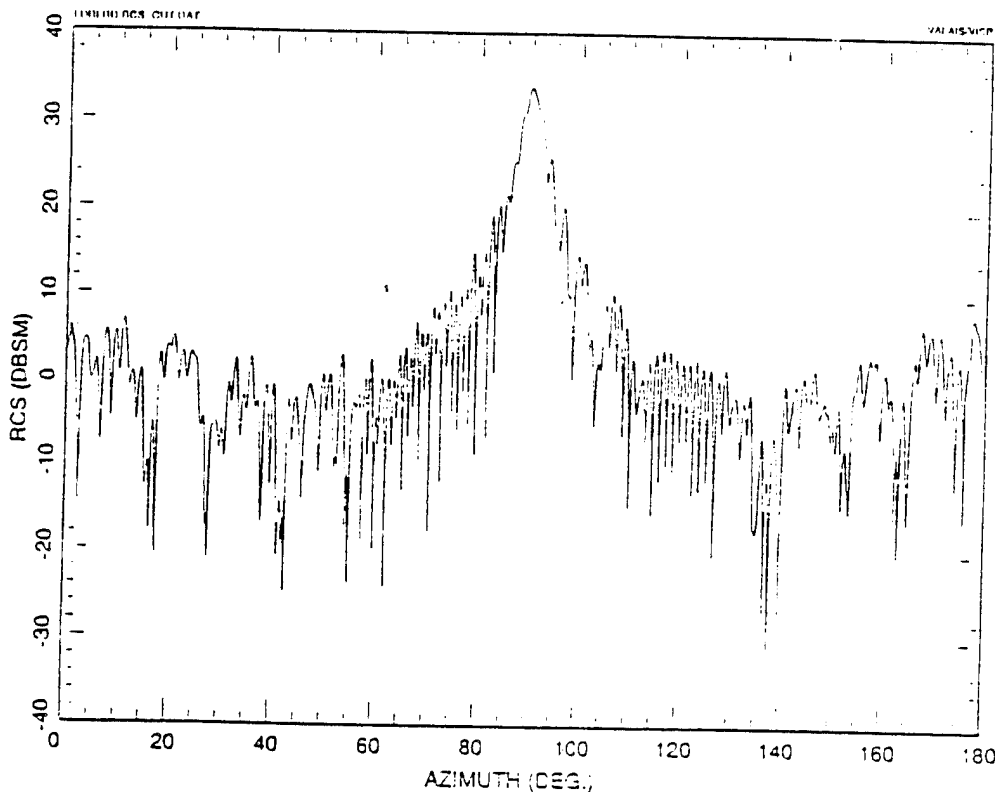


Figure 3.1.2.1.8-1 (a). Monostatic RCS of aircraft @ 0° elevation
L-band

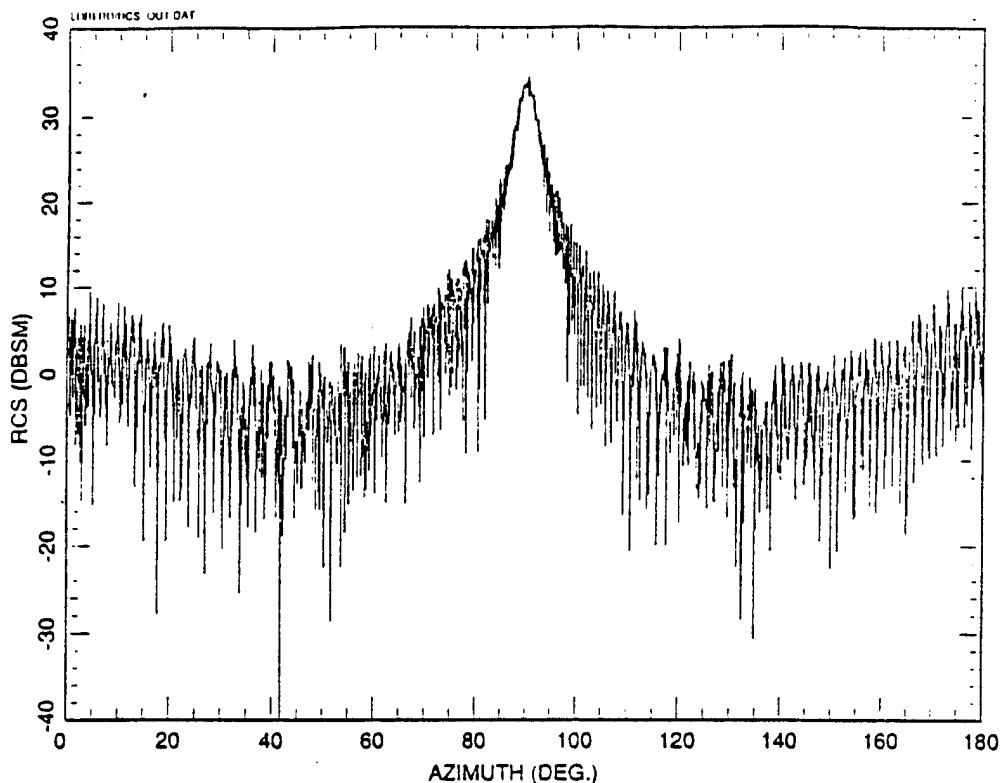


Figure 3.1.2.1.8-1 (b). Monostatic RCS of aircraft @ 0° elevation
X-band

It is interesting to look at the individual component RCS for this geometry. Figures 3.1.2.1.8-2 (a) & (b) present the RCS of the ten ellipsoids making up the aircraft as functions of azimuth. At 90°, the main contributors to the aircraft RCS are the tailfin, the fuselage, and the left tank. Surprisingly, the tailfin is the main component responsible for the peak at 90°. The discontinuities in the curves, where a component RCS suddenly drops off to zero, are the aspects where that component is shadowed. For example, the helmet is visible all the way out to 140° azimuth, then it is shadowed.

Next, Figures 3.1.2.1.8-3 (a) & (b) show the aircraft RCS for the case where the radar is pointing down at the aircraft with an elevation angle of -45°. We immediately see that the strong sharp peaks at broadside have been replaced by weaker broader peaks. A look at the component RCS plots for this elevation plane in Figures 3.1.2.1.8-4 (a) & (b) shows why. The tailfin is no longer a big contributor to the aircraft RCS; its RCS has now fallen way down to -30 dBsm at 90°. The fuselage is now the biggest contributor but at 90° it is shadowed, as shown by the sudden "gap" in RCS. The other main contributors

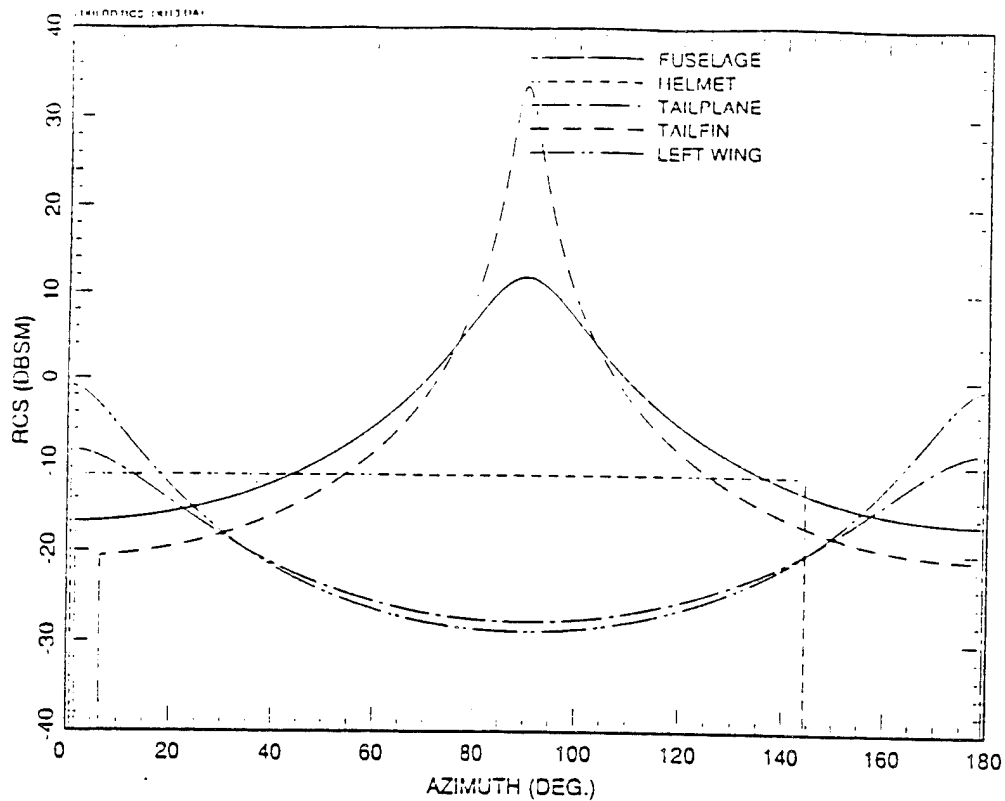


Figure 3.1.2.1.8-2 (a). RCS of aircraft components @ 0° elevation

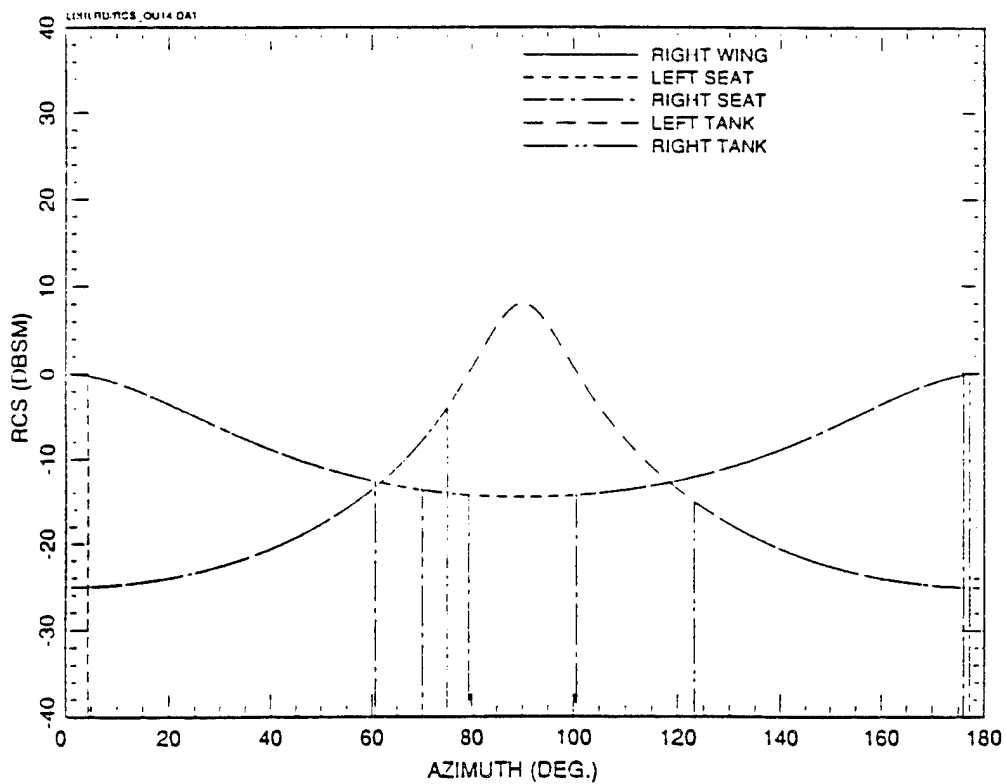


Figure 3.1.2.1.8-2 (b). RCS of aircraft components @ 0° elevation

to the RCS at 90° are now the left tank and the right tank, as shown in Figure 3.1.2.1.8-4 (b).

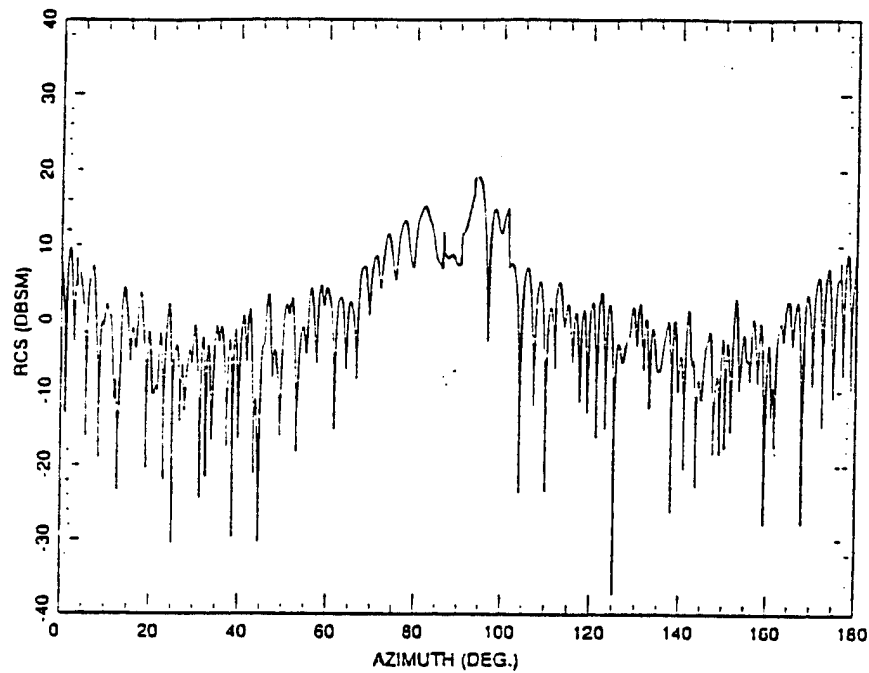


Figure 3.1.2.1.8-3 (a). Monostatic RCS of aircraft @ 45° elevation
L-band

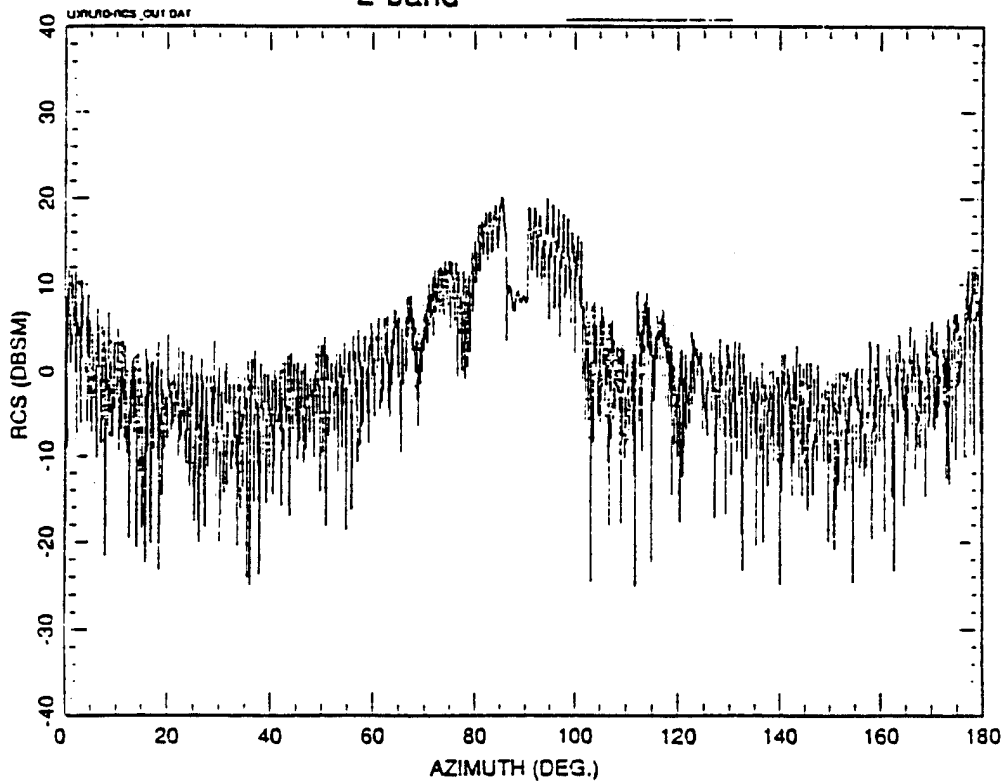


Figure 3.1.2.1.8-3 (b). Monostatic RCS of aircraft @ 45° elevation - X band.

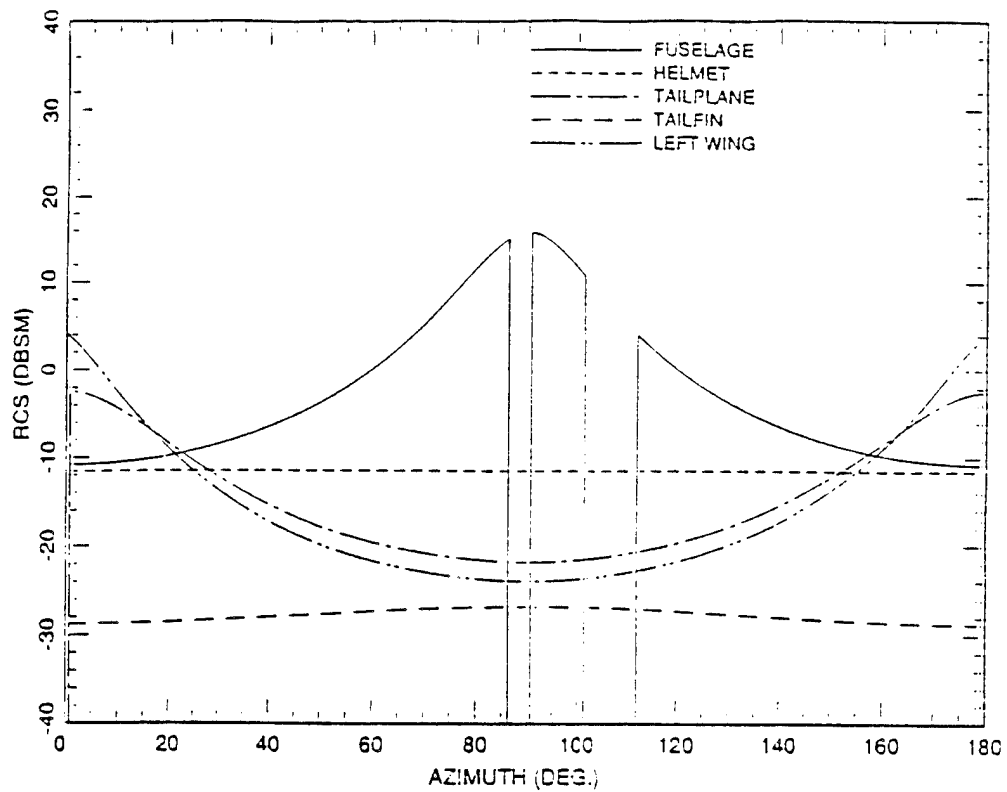


Figure 3.1.2.1.8-4 (a). RCS of aircraft components @ 45° elevation

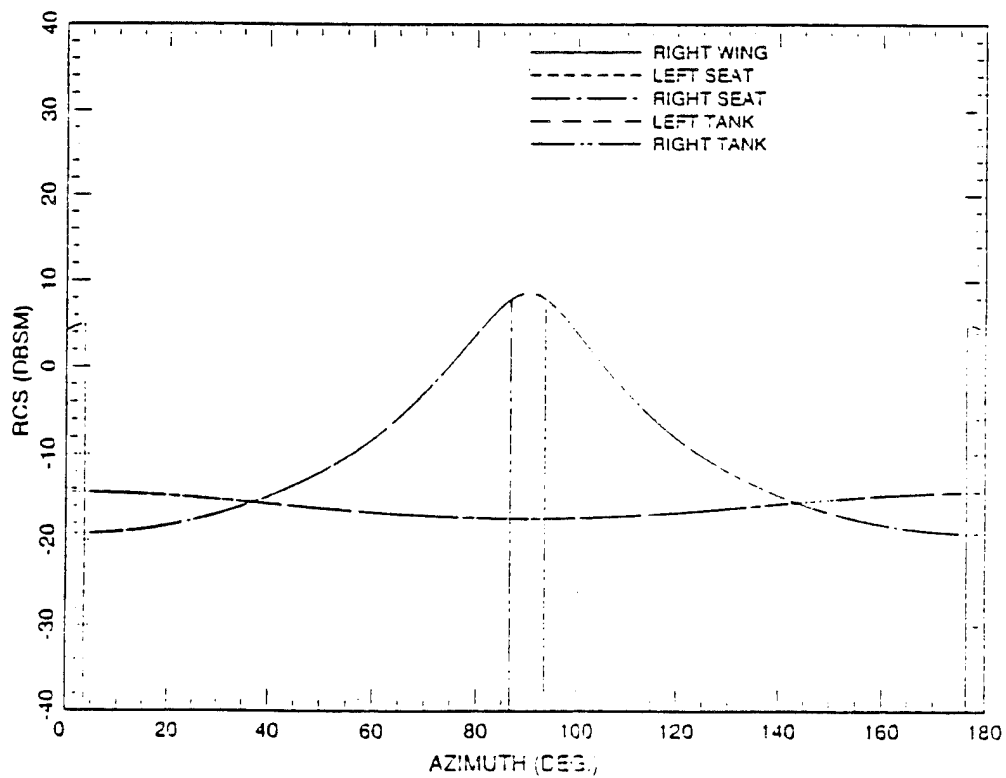


Figure 3.1.2.1.8-4 (b). RCS of aircraft components @ 45° elevation

Next, we show the monostatic RCS of the aircraft as a function of varying elevation angle in Figure 3.1.2.1.8-5. The azimuth angle of the radar is 0° , or nose aspect. Negative elevation angles mean that the radar is underneath and looking up at the aircraft. Positive elevation is radar looking down. The figure shows that between -10° and -80° , the aircraft RCS is weak, in comparison with 10° to 80° . Between 0° and -10° the aircraft RCS is essentially constant at around 5 dBsm. This is useful to know in the case of a ground radar looking up at the airplane from a distance.

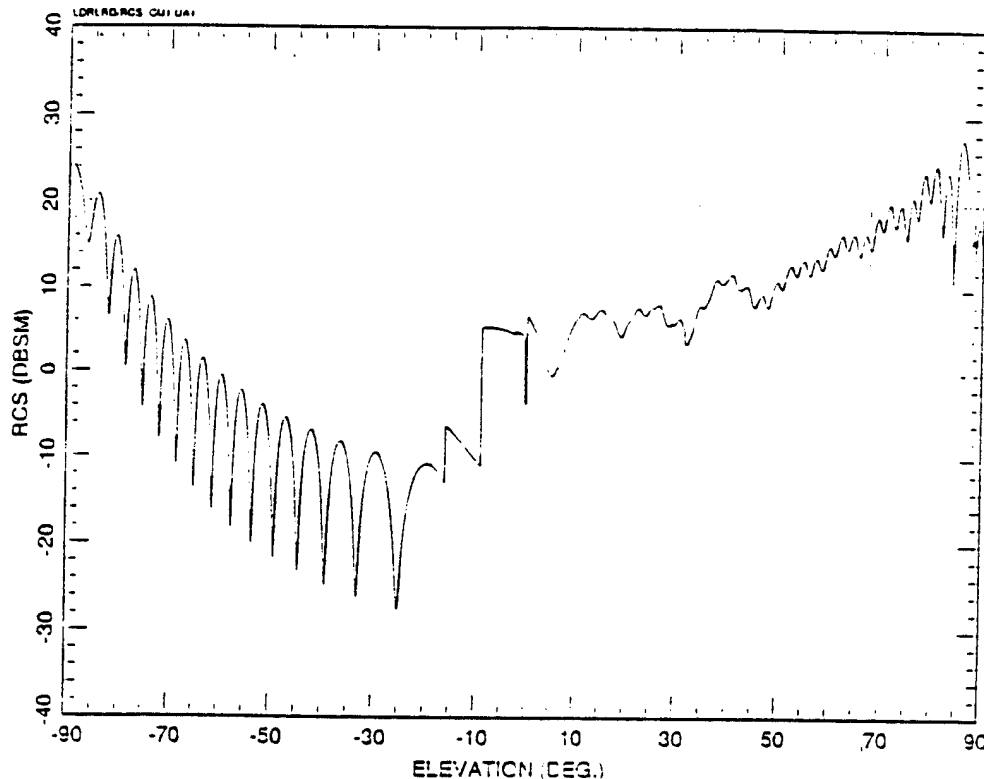


Figure 3.1.2.1.8-5. Monostatic RCS of aircraft @ 0° azimuth
L-band

Finally, the bistatic RCS of the aircraft is shown in Figure 3.1.2.1.8-6. The transmitter and the receiver are always set at 150° apart in azimuth, and the angle plotted is the varying azimuth angle of the transmitter. In comparing this plot with the plot in Figure 3.1.2.1.8-3 (a) above, it is interesting to note that the RCS obtained bistatically in this way is generally higher than the monostatic

RCS. In certain situations this would be very helpful. It may be possible to exploit bistatic scattering when we discuss the target interactions later.

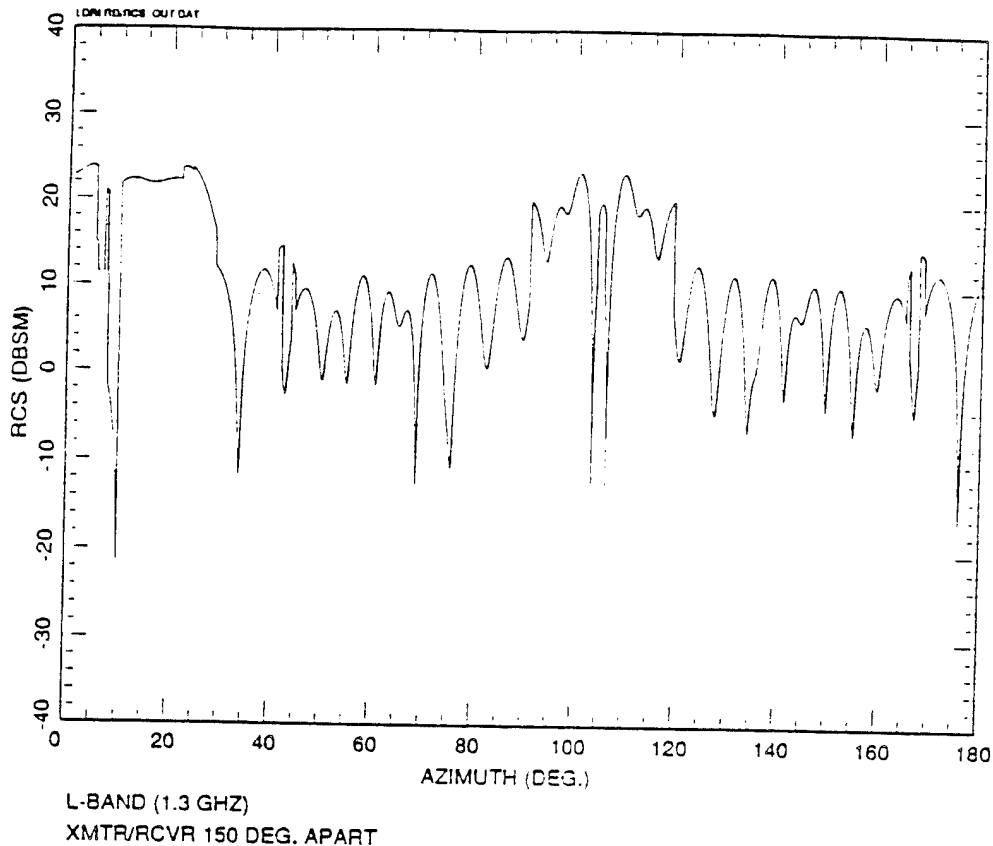


Figure 3.1.2.1.8-6. Bistatic RCS of aircraft @ 45° elevation
L-band

3.1.2.2 Cruise Missile RCS Model

Like the aircraft, the cruise missile is modeled as a collection of discrete components. Unlike the aircraft, however, the missile includes non-spherical shapes such as a cylinder, flat plates, and wires. As noted before, the smaller and "flat" shape of the cruise missile does not lend itself well to ellipsoid modeling, and other geometric objects must be used.

The missile fuselage is the main contributor to missile RCS. It is modeled as a hemispherically-capped cylinder. This means that the central portion of the fuselage is a right circular cylinder with flat ends while the rounded ends are modeled as two hemispheres (half-spheres). The wings, tailfin, and tailplane are modeled as a collection of triangular flat plates while the straight edges of

these parts are modeled as thin wires. Other parts of the missile such as air ducts, dams, propellers, etc. are not modeled. Different views of the generic cruise missile are shown in Figure 3.1.2.2-1.

The RCS of the non-spherical shapes are computed using the physical optics technique. Since geometric optics fails for shapes such as cylinder, and flat plates, we must turn to physical optics instead as the other high-frequency technique that is easily implemented.

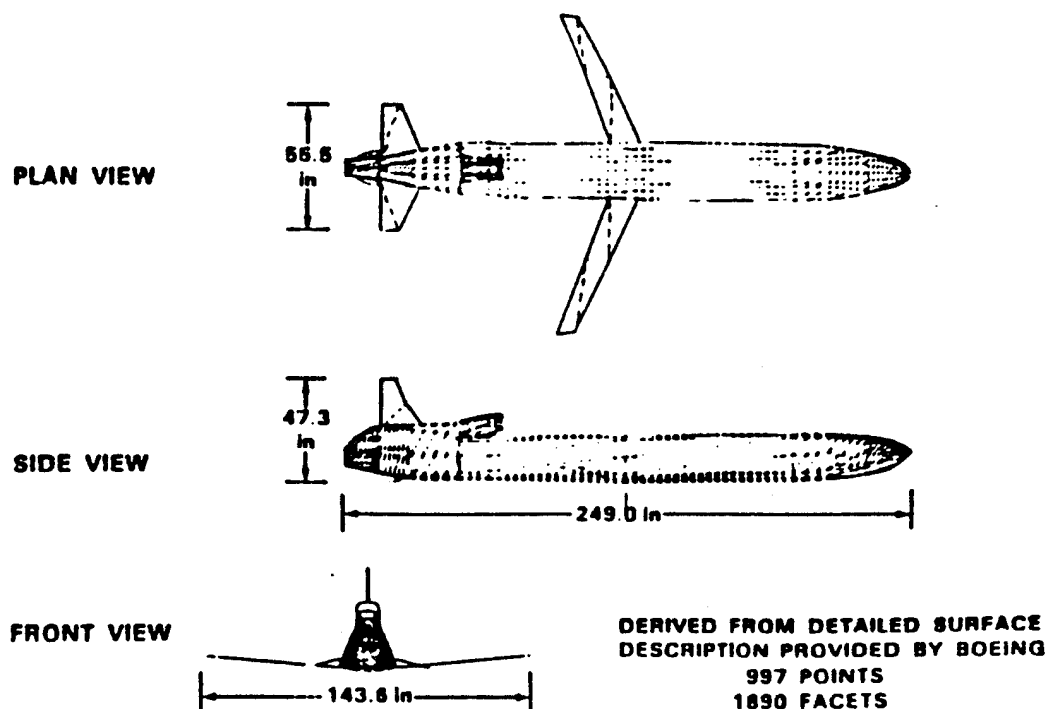


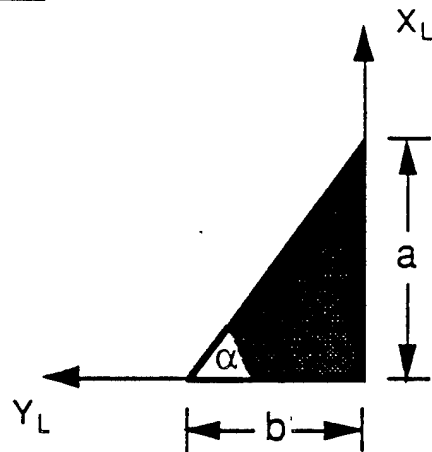
Figure 3.1.2.2-1. Views of generic cruise missile

3.1.2.2.1 Coordinate System

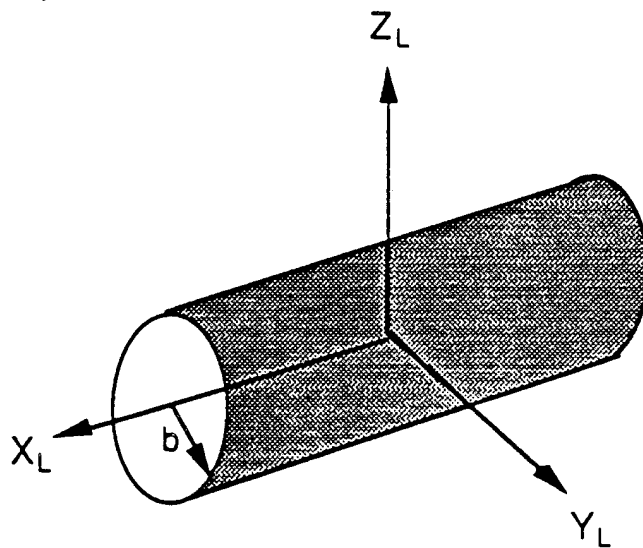
The reference coordinate system for the missile is oriented in the same way as that of the aircraft (shown in Figure 3.1.2.1.1-3). The origin is the center of the missile fuselage cylinder with the X_T axis pointing in the direction of the nose of the missile. Each missile component has its own local coordinate system generated by rotating the reference coordinate system by the angles α ,

β , and γ , and then translated by X , Y , and Z . For each type of geometric shape the local coordinate system is shown:

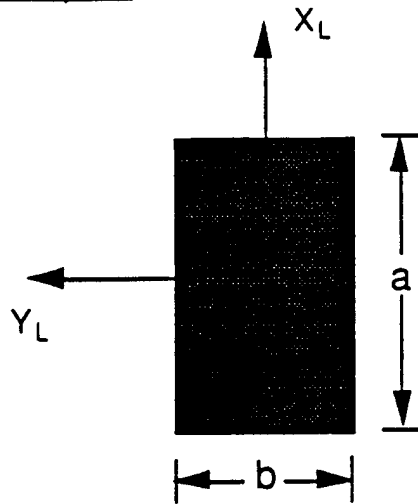
Triangular plate



Circular cylinder



Rectangular plate



The wire does not have a local coordinate system. We simply look at its dimension along the missile reference coordinate system.

The various missile components and their related parameters are listed in Table 3.1.2.2.1-1,

As with the aircraft, to transform from the reference coordinate system to a local coordinate system we use the transformation matrix T :

$$\vec{x}_L = T (\vec{x}_T - \vec{x}_D),$$

where \vec{x}_D is the displacement vector of the missile component from the origin and is composed of X , Y , and Z . For most of the missile components, the matrix T is exactly the same matrix as that given in the aircraft section above. However, the triangle plates making up the tailfin of the missile are treated differently. The orientation of these plates cannot be adequately represented by the three rotation angles α , β , and γ . More angles are needed which change the transformation matrix for these components. This alternative matrix is given in the Appendix.

TABLE 3.1.2.2.1-1. COMPONENTS OF THE CRUISE MISSILE

No.	Component	Type	a (ft)	b (ft)	c (ft)	alpha (deg.)	beta (deg.)	gamma (deg.)	x (ft)	y (ft)	z (ft)
1	Fuselage	Cylinder	19.08	0.83	0.83	0.0	0.0	0.0	0.00	0.00	0.00
2	Fuselage End	Ellipsoid	0.83	0.83	0.83	0.0	0.0	0.0	9.54	0.00	0.00
3	Fuselage End	Ellipsoid	0.83	0.83	0.83	180.0	0.0	0.0	-9.54	0.00	0.00
4	Left Wing Part	Triangle Plate	1.08	2.31	25.06	0.0	0.0	8.0	-0.18	0.00	0.00
5	Left Wing Part	Triangle Plate	0.87	2.31	19.41	180.0	0.0	-8.0	-0.93	2.37	-0.62
6	Left Wing Part	Triangle Plate	0.87	2.75	17.50	0.0	0.0	8.0	-1.12	4.06	-0.38
7	Left Wing Part	Triangle Plate	0.73	2.75	14.77	180.0	0.0	-8.0	-1.65	4.98	-0.25
8	Left Wing Front Edge	Wire Edge	-2.62	4.92	0.78	0.0	0.0	0.0	-0.77	3.29	-0.44
9	Left Wing Side Edge	Wire Edge	-1.79	5.19	0.78	0.0	0.0	0.0	-1.44	3.43	-0.44
10	Left Wing Rear Edge	Wire Edge	-0.73	0.23	0.00	0.0	0.0	0.0	-1.77	6.01	-0.35
11	Right Wing Part	Triangle Plate	2.31	1.08	64.94	-90.0	-8.0	0.0	-0.18	-1.60	-0.73
12	Right Wing Part	Triangle Plate	2.31	0.87	70.59	90.0	8.0	0.0	-0.83	-2.37	-0.52
13	Right Wing Part	Triangle Plate	2.75	0.87	72.50	-90.0	-8.0	0.0	-1.12	-4.06	-0.38
14	Right Wing Part	Triangle Plate	2.75	0.73	75.23	90.0	8.0	0.0	-1.65	-4.98	-0.25
15	Right Wing Front Edge	Wire Edge	-2.62	-4.92	0.78	0.0	0.0	0.0	-0.77	-3.29	-0.44
16	Right Wing Side Edge	Wire Edge	-1.79	-5.19	0.78	0.0	0.0	0.0	-1.44	-3.43	-0.44
17	Right Wing Front Edge	Wire Edge	-0.73	-0.23	0.00	0.0	0.0	0.0	-1.77	-6.01	-0.35
18	Left Tailplane Part	Triangle Plate	1.59	0.73	65.51	-90.0	-8.0	0.0	-8.79	1.78	-0.54
19	Left Tailplane Part	Triangle Plate	1.88	1.52	51.90	107.7	8.0	0.0	-8.17	1.35	-0.37
20	Left Tailplane Front Edge	Wire Edge	-0.85	1.67	-0.63	0.0	0.0	0.0	-8.09	1.56	-0.52
21	Left Tailplane Side Edge	Wire Edge	0.00	1.81	-0.63	0.0	0.0	0.0	-9.03	1.41	-0.52
22	Left Tailplane Rear Edge	Wire Edge	-0.73	0.00	0.00	0.0	0.0	0.0	-8.67	2.31	-0.33
23	Right Tailplane Part	Triangle Plate	0.73	1.59	24.49	0.0	0.0	8.0	-8.79	-1.78	-0.54
24	Right Tailplane Part	Triangle Plate	1.52	1.88	38.97	162.3	0.0	-8.0	-8.17	-1.35	-0.37
25	Right Tailplane Front Edge	Wire Edge	-0.85	-1.67	-0.63	0.0	0.0	0.0	-8.09	-1.56	-0.52
26	Right Tailplane Side Edge	Wire Edge	0.00	-1.81	-0.63	0.0	0.0	0.0	-9.03	-1.41	-0.52
27	Right Tailplane Rear Edge	Wire Edge	-0.73	0.00	0.00	0.0	0.0	0.0	-8.67	-2.31	-0.33
28	Tailfin Part	Triangle Plate	1.16	1.01	48.95	-90.0	90.0	-49.0	-8.17	0.00	1.55
29	Tailfin Part	Triangle Plate	1.27	1.16	47.59	-90.0	90.0	-137.5	-8.56	0.00	1.88
30	Tailfin Part	Triangle Plate	0.75	0.43	60.00	-90.0	90.0	60.0	-8.60	0.00	2.25
31	Tailfin Part	Triangle Plate	0.43	0.43	45.00	-90.0	90.0	135.0	-8.82	0.00	2.41
32	Tailfin Front Edge	Wire Edge	-0.66	0.00	0.76	0.0	0.0	0.0	-7.84	0.00	1.50
33	Tailfin Front Edge	Wire Edge	-0.38	0.00	0.65	0.0	0.0	0.0	-8.36	0.00	2.21
34	Tailfin Top Edge	Wire Edge	-0.61	0.00	0.00	0.0	0.0	0.0	-8.82	0.00	2.56
35	Tailfin Rear Edge	Wire Edge	0.00	0.00	-1.72	0.0	0.0	0.0	-9.13	0.00	1.70

3.1.2.2.2 Overview of Physical Optics

Physical optics overcomes the difficulty of infinite radii of curvature of flat or singly curved surfaces in computing RCS. It does this by approximating the induced surface fields and integrating them to obtain the scattered field. In the general case of scattering from an arbitrary body, the scattered fields are given by the Stratton-Chu integral equations.⁷ They are extremely difficult to solve, however, in the general case, and many simplifying assumptions can be made. In solving the Stratton-Chu integrals, physical optics makes these assumptions:

1. The incident field is assumed to be time harmonic and a plane wave over the entire finite scattering object.
2. The total fields at the surface on the "shadowed side" of the object are zero. This assumption is valid only when the wavelength is small in comparison with the dimensions of the object.
3. The observation point (or receiving antenna) is far from the object in terms of wavelength and object dimensions: $r > 2D^2/\lambda$, where r is the distance from object to the observation point, D is the largest object dimension, and λ is the wavelength.
4. Tangent-Plane Approximation. In this approximation, the surface at and near any point is assumed to be an infinite plane tangent to the surface at that point. This leads to the following expressions for the total surface fields for a perfectly conducting surface:

$$\begin{aligned}\hat{n} \times \mathbf{E}^T &= 0 \\ \hat{n} \times \mathbf{H}^T &= 2 \hat{n} \times \mathbf{H}^I\end{aligned}$$

where \mathbf{E}^T and \mathbf{H}^T are the total surface \mathbf{E} and \mathbf{H} fields, respectively, \mathbf{H}^I is the incident \mathbf{H} field, and \hat{n} is the normal vector to the surface.

These assumptions simplify the Stratton-Chu integrals tremendously and lead to the physical optics integral for the scattered \mathbf{H}^S field:

$$\mathbf{H}^S(P) = \frac{-ik \exp(ikR_0)}{2\pi R_0} \int_{s_1} (\hat{n} \times \mathbf{H}^I) \times \hat{k}^S \exp(-ik_0 \hat{k}^S \cdot \mathbf{r}') ds'$$

where

P is the far-field observation point,
 R_0 is the distance from the origin to P ,
 $k = 2\pi / \lambda$,
 S_1 is the surface,
 $\hat{\mathbf{k}}^s$ is the unit vector in the scattered field direction of propagation, and
 \mathbf{r} is the vector from the origin to a surface patch ds' .

When the surface such as a flat plate lies on the xy -plane, the integral can be written in terms of x and y and simplified to:

$$H^s(P) = \frac{-ik \exp(ikR_0)}{2\pi R_0} \hat{\mathbf{k}}^s \times [H_0 \times \hat{\mathbf{z}}] \iint_{S_1} \exp[ik(\hat{\mathbf{k}}^i - \hat{\mathbf{k}}^s) \cdot \mathbf{r}] dx dy$$

(Eqn. 3.1.2.2.2-1)

where

$\hat{\mathbf{k}}^i$ is the unit vector in the incident field direction of propagation,
 H_0 is found in $H^i = H_0 \exp[i\mathbf{k}^i \cdot \mathbf{r}]$, and H_0 is a constant vector perpendicular to the direction of incidence,
 $\hat{\mathbf{z}}$ is the unit vector in z .

This is the equation we later use to derive the bistatic scattering formula for the triangular plates.

3.1.2.2.3 Cylinders

While only ellipsoids were used to model components of the aircraft, the central portion of the cruise missile is modeled as a hemispherically-capped cylinder. Thus, it was necessary to develop an RCS model for the cylinder.

The scattering geometry and symbols for the cylinder are shown in Figure 3.1.2.2.3-1. The plane of incidence is defined as the plane with the incident wave propagation direction and the cylinder axis (the x -axis here), and is the x - z plane in the figure (although not in general). The incident direction makes an angle Ψ_i as shown with the y - z plane. The plane of scattering is defined as the plane with the scattering propagation direction and the cylinder

axis, and is shown rotated by azimuth angle ϕ' from the z axis. The scattering direction makes an angle Ψ_s as shown with the y-z plane. As shown, the two angles Ψ_i and Ψ_s have the same sign. There are two polarization modes of interest. The TM mode is when the E-field is in the plane of incidence and scattering (H-field perpendicular). The TE mode is when the E-field is perpendicular to the plane of incidence and scattering.

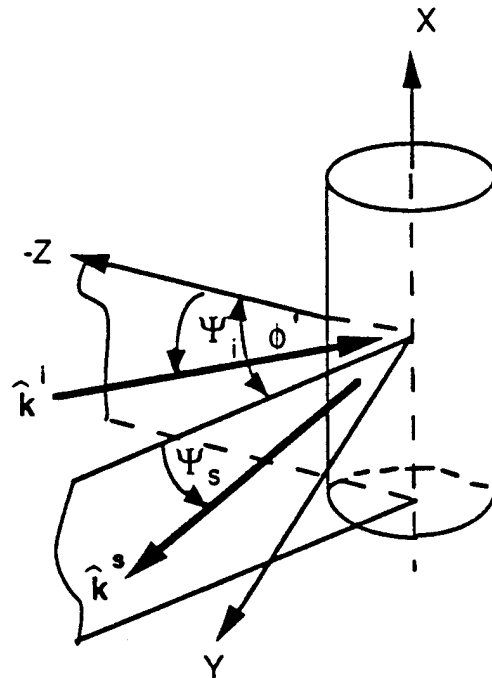


Figure 3.1.2.2.3-1. Scattering geometry for circular cylinder

In general, a scattered field from a cylinder of finite length propagates in all directions, so that one can consider the scattered field at arbitrary angle Ψ_s . However, for cylinders whose length is very much greater than the radius, the scattered field at and near $\Psi_s = -\Psi_i$ is much larger than the scattered field in other directions. This is specular reflection. For the cruise missile, the length is much larger than the radius so this statement is true. The angle ϕ' is arbitrary so the propagation vectors of the scattered field from the cylinder form a cone in the forward direction which has a half-angle of $\pi/2 - \Psi_s$ with respect to the x axis as shown.

Given the range of radar frequency we will be dealing with (L to X band) and the radius of the missile cylinder (0.83 ft), there are two cases of interest when computing the RCS of the cylinder.

Case 1. Cylinder radius of same order as wavelength ($0.5 < k_0 a < 10$)

In this case the scattered field becomes more concentrated in the specular direction $\psi_s = -\psi_i$ because the cylinder length (20 ft) is large compared to the radius. Using the techniques in Reference 2, pp.302-304, the bistatic scattering cross section is given by

$$\sigma(\psi_i, \psi_s, \phi') = \frac{4 k h^2}{\pi} \cos^2 \psi_s \sigma^c(\psi_i, \phi') \left[\frac{\sin[k(\sin\psi_i + \sin\psi_s)h]}{k(\sin\psi_i + \sin\psi_s)h} \right]^2,$$

where $\sigma^c(\psi_i, \phi')$ is defined as the bistatic scattering width for an infinitely long cylinder at oblique incidence, which we can use for a finite cylinder. It is defined for the TM and TE polarizations and is given by:

$$\sigma_p^{c TM}(\phi') = \frac{4}{k \cos^2 \psi} \left| \sum_{n=-\infty}^{\infty} (-1)^n C_n^{TM} e^{in\phi'} \right|^2$$

$$\sigma_p^{c TE}(\phi') = \frac{4}{k \cos^2 \psi} \left| \sum_{n=-\infty}^{\infty} (-1)^n C_n^{TE} e^{in\phi'} \right|^2,$$

with

$$C_n^{TM} = -\frac{J_n(k a_0 \cos \psi)}{H_n^{(1)}(k a_0 \cos \psi)} = C_{-n}^{TM}$$

and

$$C_n^{TE} = -\frac{J'_0(k a_0 \cos \psi)}{H_n^{(1)'}(k a_0 \cos \psi)} = C_{-n}^{TE},$$

where J_n is the Bessel function of the first kind and $H_n^{(1)}$ is the Hankel function of the first kind. The prime on the J and H denotes first derivative. In the LDR software, the infinite series is truncated to only go from $n=-10$ to 10.

Case 2. Cylinder radius and length much greater than wavelength
($ka > 10, 2h > \lambda$)

With this case, physical optics gives an expression for the bistatic RCS that is valid for directions at and near the specular direction (to within about 45° on either side of the specular direction). In this specular region, the strong return from the cylinder sides makes the contributions from the ends and edges negligible. For the perfectly conducting cylinder, the bistatic RCS for either TE or TM polarization is given by:

$$\sigma(\psi_i, \psi_s, \phi') = \frac{4ka^2 \cos^2 \psi_s}{\pi \cos \psi_i} \cos \phi'/2 \left[\frac{\sin[k(\sin \psi_i + \sin \psi_s)h]}{k(\sin \psi_i + \sin \psi_s)h} \right]^2,$$

where $2h$ is the cylinder length and a is the radius.

In the specular direction, $\psi_s = -\psi_i$, and the cross section and scattered power are maximum, or

$$\sigma(\psi_i, -\psi_i, \phi') = 4ka^2 \cos \psi_i \cos \phi'/2.$$

In the backscattering direction, $\psi_s = \psi_i$ and $\phi' = 0$. The RCS for incidence angles near broadside becomes

$$\sigma(\psi_i, \psi_i, 0) = 4ka^2 \cos \psi_i \left[\frac{\sin(2kh \sin \psi_i)}{2kh \sin \psi_i} \right]^2,$$

and at broadside ($\psi_i = 0$), the backscattering RCS is

$$\sigma(0,0,0) = 4ka^2.$$

We now present results of the bistatic RCS of the cylinder using the equations in this Section. The cylinder used to model the fuselage of the cruise missile is 19 ft long, and has a radius of 10 in. We will be using the geometry shown below:

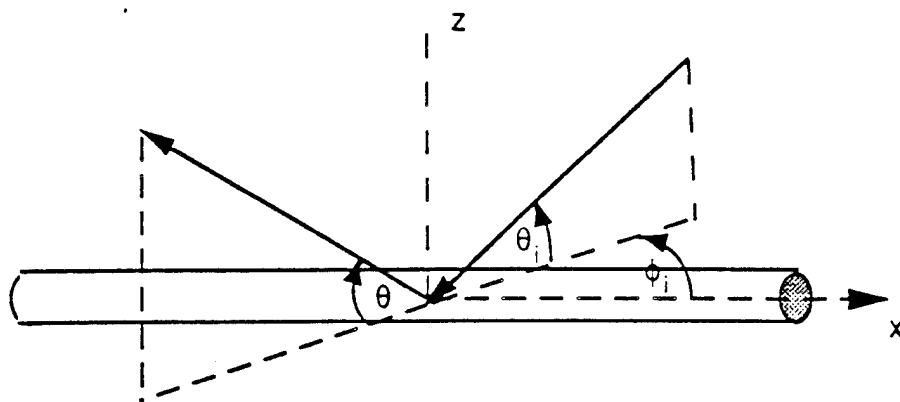


Figure 3.1.2.2.3-2. Bistatic scattering geometry for cylinder

The azimuth angle is ϕ and the elevation angle is θ . Figures 3.1.2.2.3-3 (a), (b), and (c) show the bistatic RCS of the cylinder as a function of the scattering elevation angle θ . Figure 3.1.2.2.3-3 (a) is the case where $\phi_i = 45^\circ$ and $\theta_i = 12^\circ$. As stated above, we would expect scattering in the specular

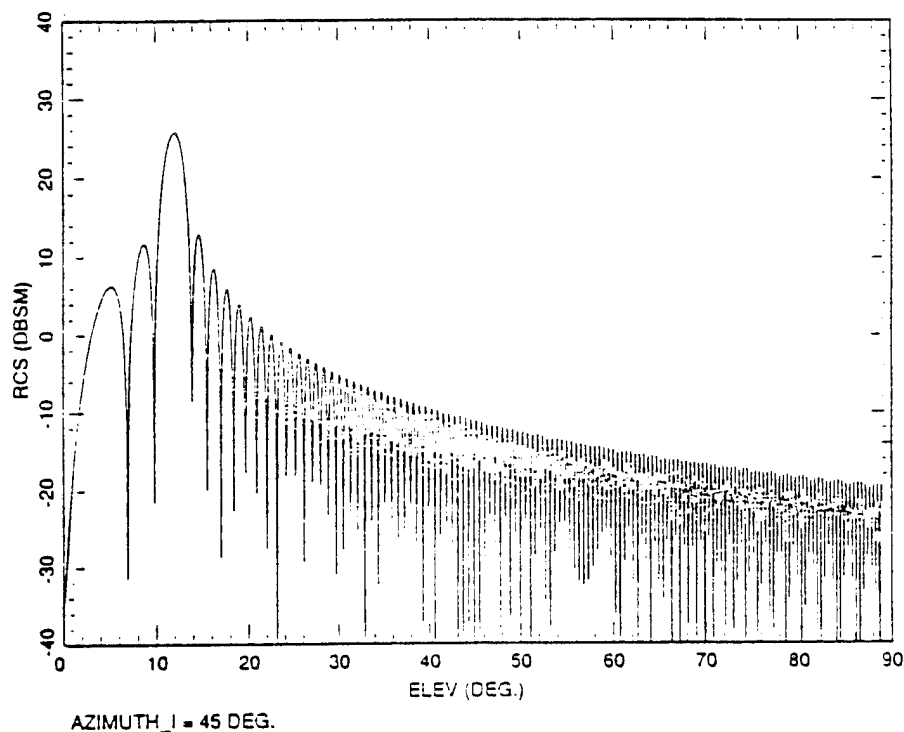


Figure 3.1.2.2.3-3 (a). Bistatic RCS of cylinder @ 12° incident elevation
X-band

direction to be dominant since the cylinder used in the missile has length much greater than radius. In this geometry, the specular direction is where $\theta = \theta_i$. As shown in the plot, the peak RCS occurs for θ around 12° just as expected in the specular direction. The highest sidelobe is about 13 dB down from the peak. The magnitude of the peak is about 26 dBsm, which shows that in the specular direction the cylinder scattering is considerable.

Next, Figures 3.1.2.2.3-3 (b) & (c) both show further that specular reflection is the dominant scattering contribution from the cylinder. Figure 3.1.2.2.3-3 (b) is the case where $\phi_i = 45^\circ$ and $\theta_i = 45^\circ$ while in Figure 3.1.2.2.3-3 (c) is the case where $\phi_i = 0^\circ$ and $\theta_i = 75^\circ$. We see that in both cases the peak goes as high as 32 dBsm while it narrows at the same time.

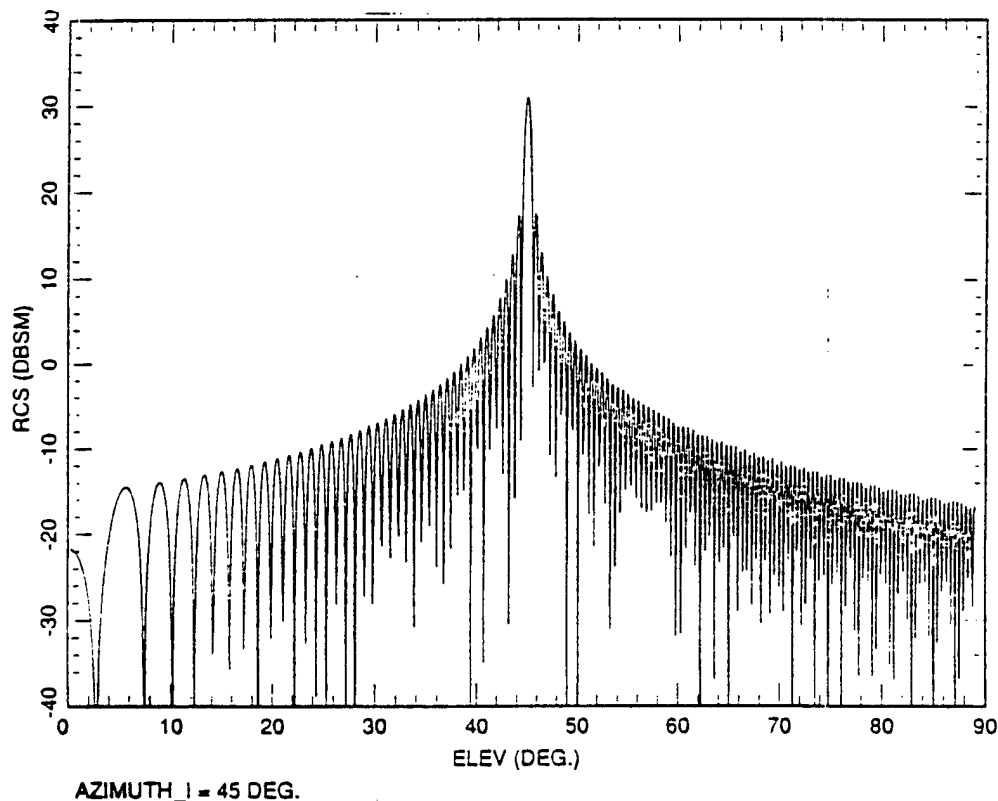


Figure 3.1.2.2.3-3 (b). Bistatic RCS of cylinder @ 45° incident elevation
X-band

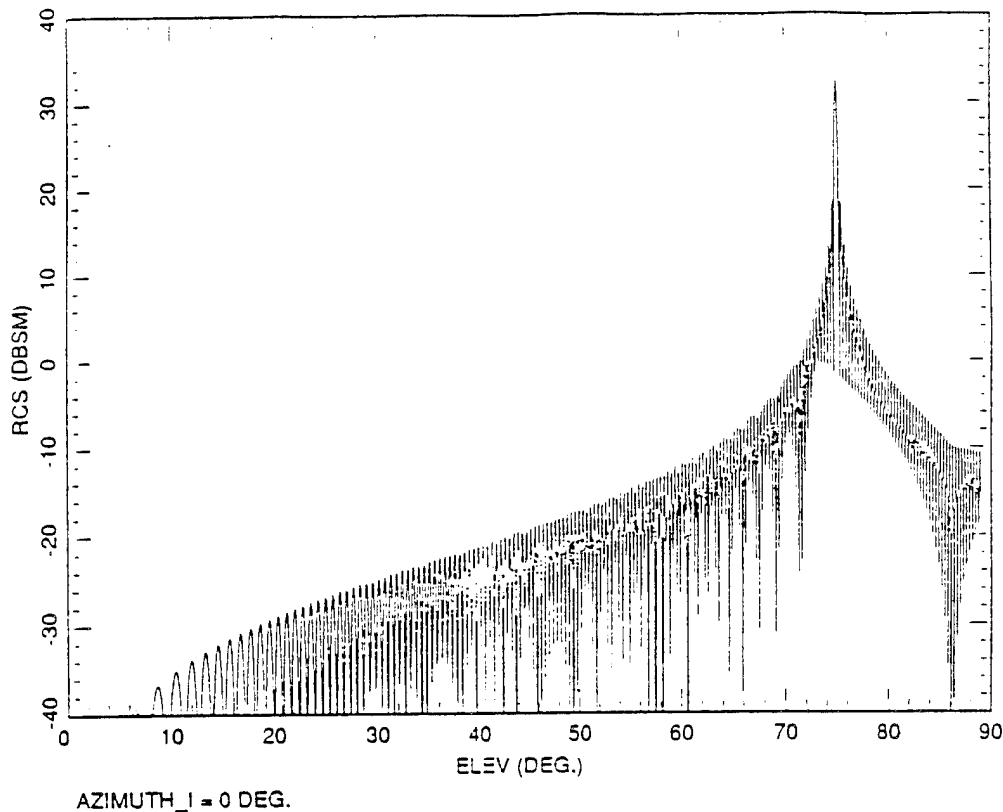


Figure 3.1.2.2.3-3 (c). Bistatic RCS of cylinder @ 75° incident elevation
X-band

At L-band (1.3 GHz) specular reflection is also strong, as shown in Figures 3.1.2.2.3-4 (a) & (b). Figure 3.1.2.2.3-4 (a) is the case where $\phi_i = 0^\circ$, $\theta_i = 15^\circ$ and TM mode, and Figure 3.1.2.2.3-4 (b) is the case where $\phi_i = 45^\circ$, $\theta_i = 60^\circ$, and TE mode. The peaks in these two Figures are 14 dBsm and 18 dBsm, which are smaller than in the X-band case. Also, because the frequency is lower, the mainlobes are much bigger in width, especially in Figure 3.1.2.2.3-4 (a).

Now we look at the situation when the scattering vector is on the same side of the z-axis as the incident vector in Figure 3.1.2.2.3-2 above. This would include the monostatic backscattering case. We have two cases to illustrate this situation. Figure 3.1.2.2.3-5 (a) is for the same incident vector as in Figure 3.1.2.2.3-3 (b) above at X-band. As can be seen, the scattering is very weak in

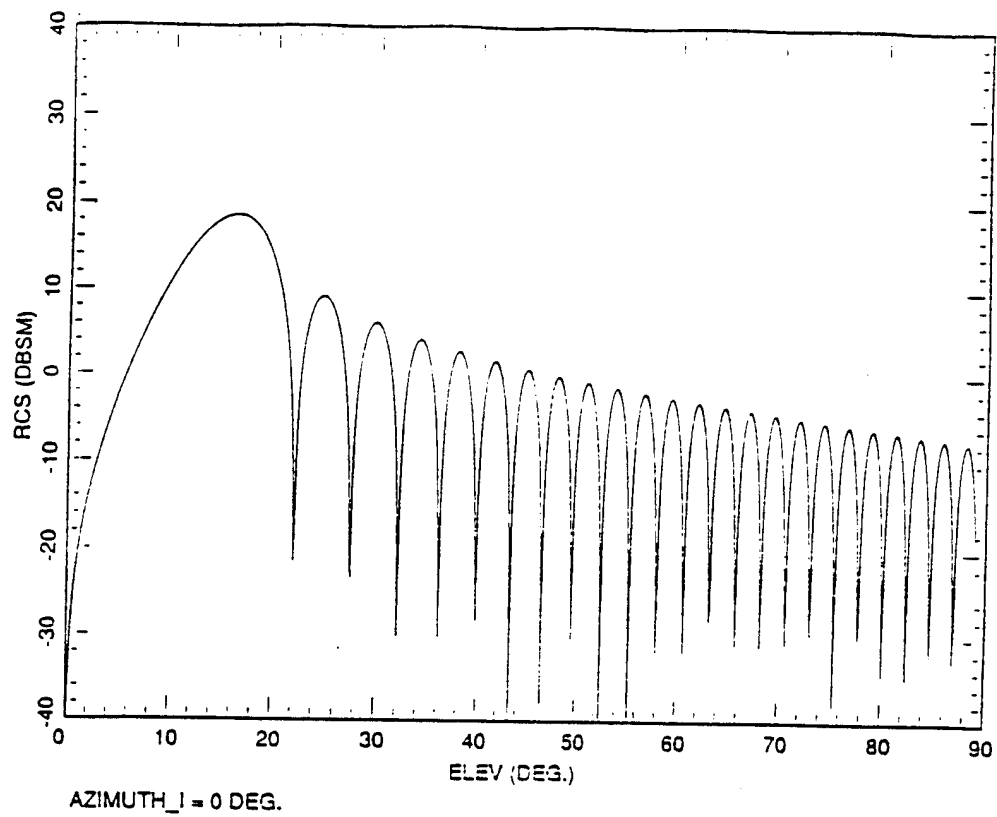


Figure 3.1.2.2.3-4 (a). Bistatic RCS of cylinder @ 15° incident elevation
L-band/TM mode

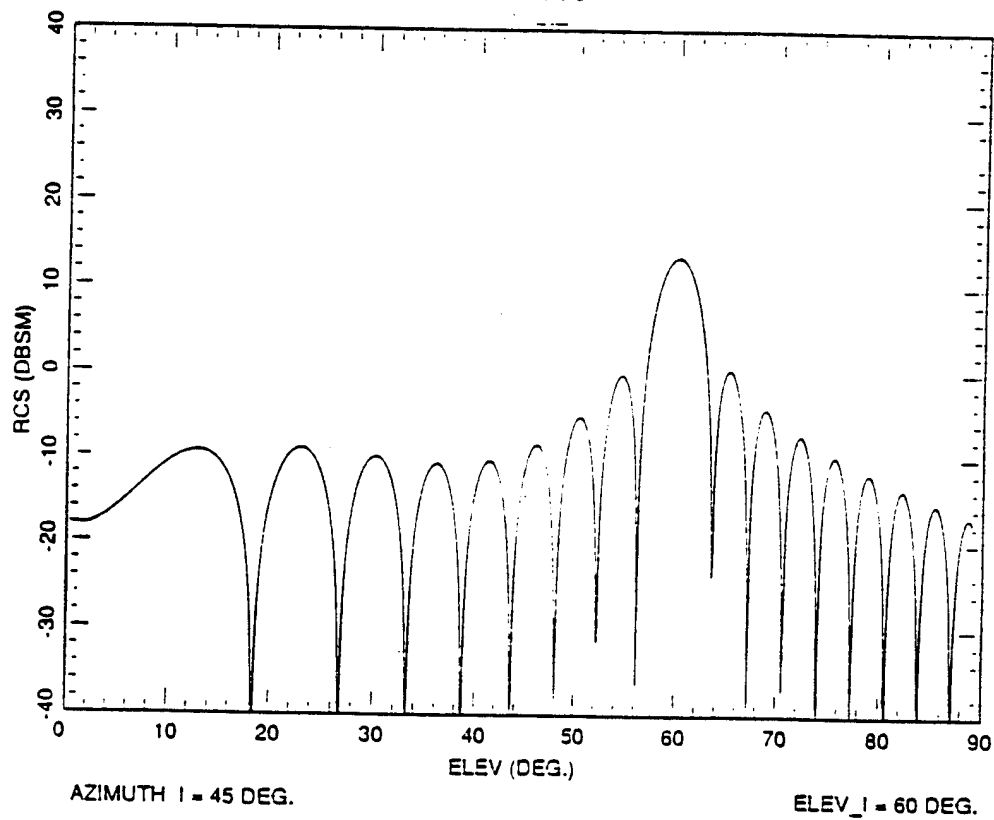


Figure 3.1.2.2.3-4 (b). Bistatic RCS of cylinder @ 60° incident elevation
L-band/TE mode

this region by comparison. Even in the backscattering direction ($\theta = 45^\circ$) the RCS is only -25 dBsm. Figure 3.1.2.2.3-5 (b) is for the same geometry at L-band as in Figure 3.1.2.2.3-4 (a) above. Once again, the scattering is weak in this region by comparison, about 10 to 20 dB weaker.

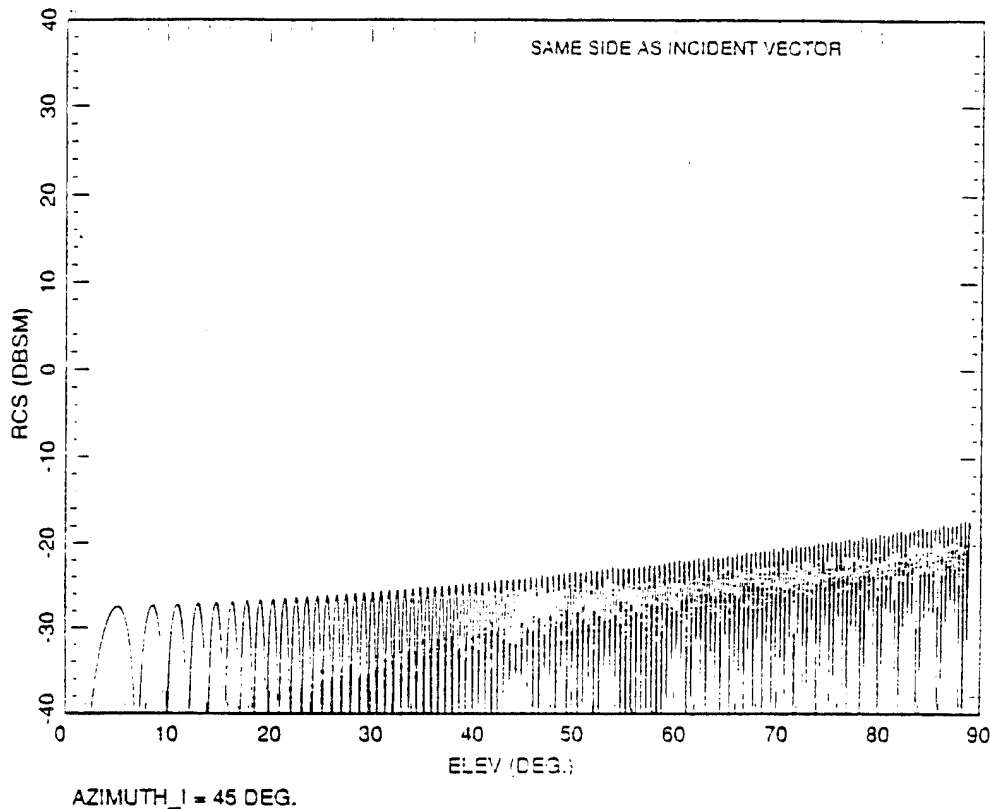


Figure 3.1.2.2.3-5 (a). Bistatic RCS of cylinder in backscatter region
@ 45° incident elevation - X-band

The RCS formulas for the cylinder were not derived using geometric optics, and therefore a specular point is not defined. The cylinder forms the central portion of the missile body, and we assume that this portion is never shadowed by any other component of the missile.

The two ends of the missile are modeled as hemispheres, which are half-ellipsoids that are easily modeled as before. We can define specular points for these two components, and they can be shadowed by the cylinder at certain aspect angles. For example, at head-on incidence, the rear hemisphere is shadowed.

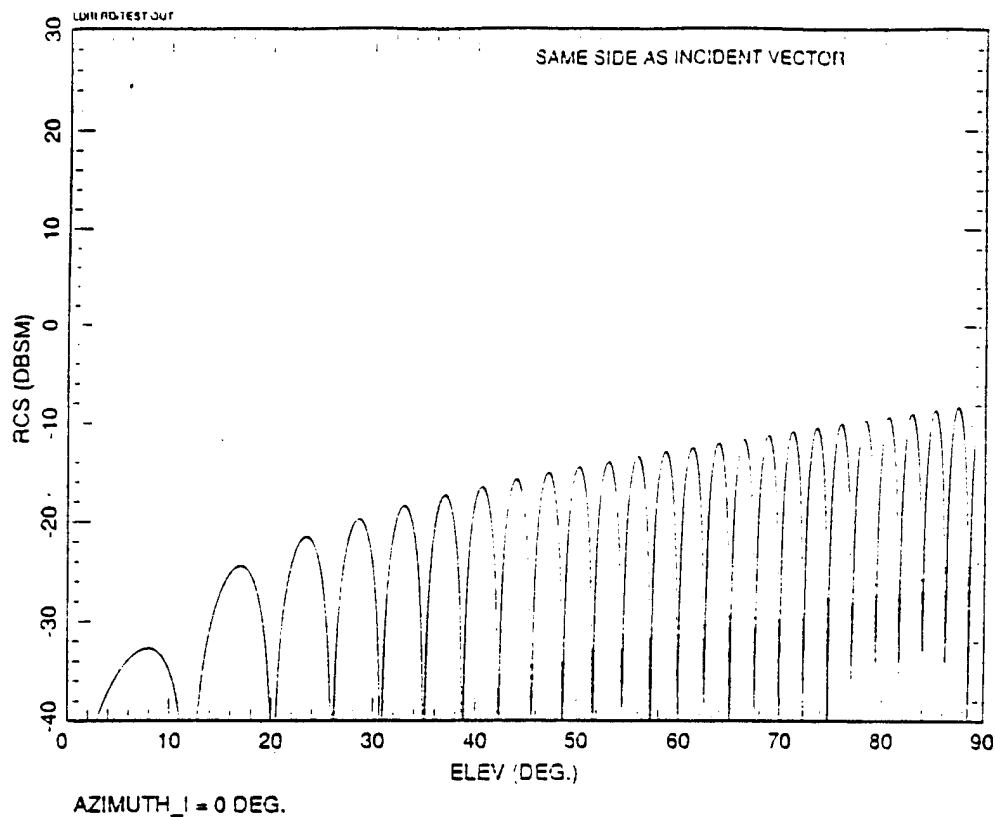
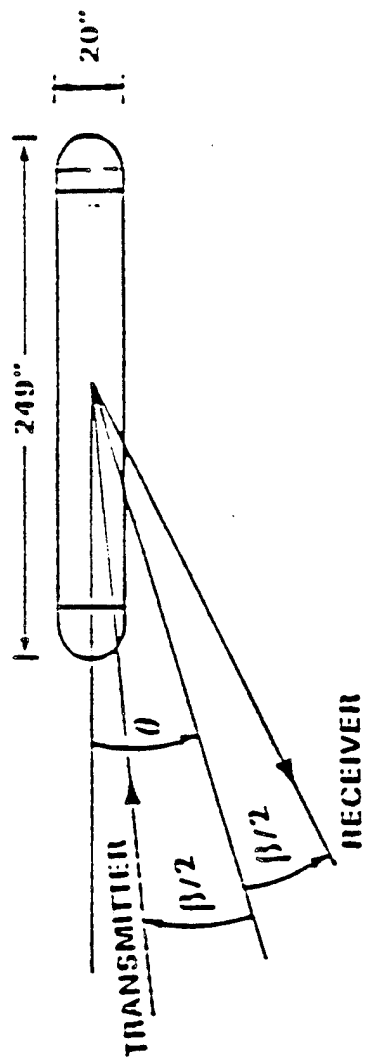


Figure 3.1.2.2.3-5 (b). Bistatic RCS of cylinder in backscatter region
@ 15° incident elevation - L-band/TM mode

A comparison of the results of the LDR model and the Lincoln Lab model of the capped cylinder is shown in Figure 3.1.2.2.3-6. As can be seen, the two models agree quite well with each other. In both plots the peak RCS at broadside is about 24 dBsm. The RCS at small aspect angles average about -10 dBsm in both plots. The very deep nulls in the LDR model is due to the TM mode, the TE mode does not have them. It is possible that the Lincoln Lab plot is due to a combination of both modes, and therefore, it has the shallow nulls at high aspect angles plus the peak at broadside. In any event, the similarity of results is **very** encouraging to the further development of the LDR missile model.



1300 MHz
20° TILT
16° BISTATIC ANGLE

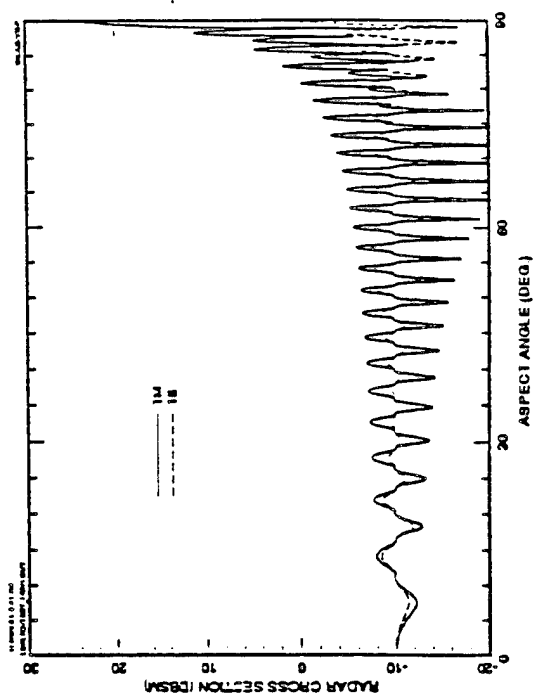
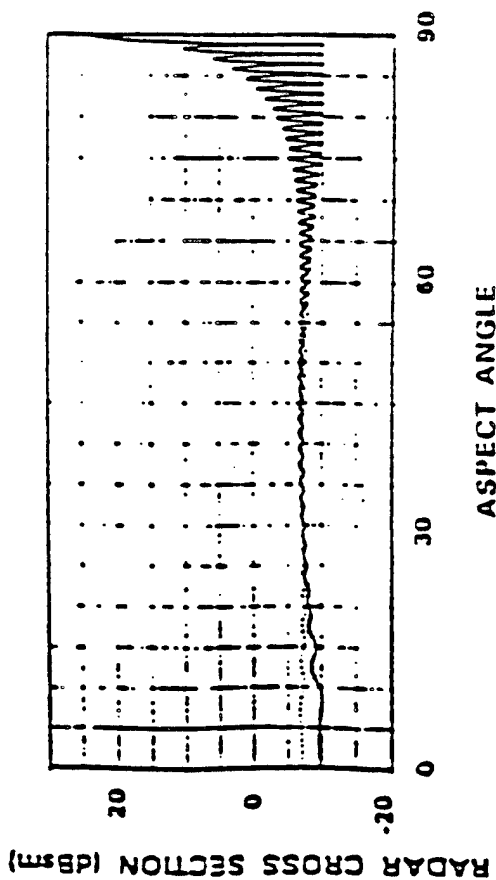


Figure 3.1.2.2.3-6. Lincoln Lab capped cylinder model vs. LDR model

3.1.2.2.4 Triangular plates

Using physical optics and Equation 3.1.2.2-1 above, we can derive the RCS of the triangular plate for any aspect angle. The coordinate system used in the derivations are shown in Figure 3.1.2.2.4-1. As in the cylinder, the plane of incidence is defined as the plane with the incident wave propagation direction and the x axis. The plane of scattering is defined as the plane with the scattering propagation direction and the x axis. It is useful to note that the incident and scattering unit vectors are given respectively by:

$$\begin{aligned}\hat{\mathbf{k}}^i &= (\cos\theta\cos\phi, \cos\theta\sin\phi, \sin\theta) \\ \hat{\mathbf{k}}^s &= (\cos\theta'\cos\phi', \cos\theta'\sin\phi', \sin\theta')\end{aligned}$$

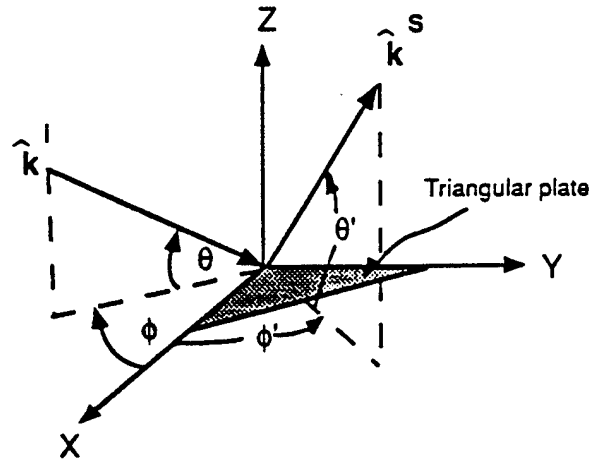


Figure 3.1.2.2.4-1. Bistatic geometry for triangular plate

We need to derive the expressions for the incident field H_0 above. There are 2 polarizations to consider: TM and TE.

Case 1. TM mode

The H field is perpendicular to the incidence plane while the E field is in the incidence plane. This H field is perpendicular to both the incidence vector and the x axis, or:

$$\begin{aligned}H_0^{\text{TM}} &= H_0(\hat{\mathbf{k}}^i \times \hat{\mathbf{x}}) \\ &= H_0(0, \sin\theta, -\cos\theta\sin\phi)\end{aligned}$$

$$= H_0(0, k_3, -k_2)$$

where

\hat{x} is the unit vector along x,

and H_0 is a constant proportional to the H-field magnitude.

Case 2. TE mode

The H field is in the incidence plane while the E field is perpendicular to the incidence plane. This H field is perpendicular to both the incidence vector and H_0^{TM} , or:

$$\begin{aligned} H_0^{TE} &= H_0(\hat{k}^i \times H_0^{TM}) \\ &= H_0(-\cos^2\theta \sin^2\varphi - \sin^2\theta, \cos^2\theta \sin\varphi \cos\varphi, \sin\theta \cos\theta \cos\varphi) \\ &= H_0(-k_2^2 - k_3^2, k_1 k_2, k_1 k_3) \end{aligned}$$

Finally, using the equation for the scattered field, Equation 3.1.2.2.2-1, we can write from the definition of cross-section:

$$\begin{aligned} \sigma &= 4\pi \lim_{R_0 \rightarrow \infty} R_0^2 \frac{|H^S(P)|^2}{|H_0^{TE/TM}|^2} \\ &= \frac{k^2}{\pi} \frac{|\hat{k}^S \times [H_0^{TE/TM} \times \hat{z}]|^2}{|H_0^{TE/TM}|^2} \left| \iint_{s'} \exp[ik(\hat{k}^i - \hat{k}^S) \cdot \mathbf{r}] dx dy \right|^2 \end{aligned}$$

The double integral is integrated over the triangular surface in the x'y' plane. We will define the variable J by:

$$\begin{aligned} J &= \frac{|\hat{k}^S \times [H_0^{TE/TM} \times \hat{z}]|^2}{|H_0^{TE/TM}|^2} \\ &= \frac{\left[(\hat{k}^S \cdot \hat{z})^2 |H_0^{TE/TM}|^2 + (\hat{k}^S \cdot H_0^{TE/TM})^2 - 2(\hat{k}^S \cdot \hat{z})(\hat{k}^S \cdot H_0^{TE/TM})(H_0^{TE/TM} \cdot \hat{z}) \right]}{|H_0^{TE/TM}|^2} \end{aligned}$$

For the monostatic case, the cross section is the same for either polarization and is given by:

$$\sigma = \frac{k^2 J}{\pi Z^2} \left| e^{-iaZ} e^{(ibZ \tan \alpha)/2} \frac{\sin bX}{X} - \frac{2}{W} \sin (bW/2) \right|^2,$$

where

$$X = k (\cos \phi \cos \theta \tan \alpha - \sin \phi \cos \theta),$$

$$Z = 2 k \cos \phi \cos \theta,$$

$$W = 2 k \sin \phi \cos \theta,$$

and a , b , and α are the dimensions and angle of the triangular plate as in the Figure in Section 3.1.2.2.1.

If $Z = 0$ then the cross section is given by:

$$\sigma = \frac{k^2 J}{\pi} \left| \frac{[a + (b \tan \alpha - a) e^{-iWb}] e^{-i\pi/2}}{W} - \frac{\tan \alpha [e^{-iWb} - 1]}{W^2} \right|^2$$

(Eqn. 3.1.2.2.4-1)

In the bistatic case, the cross-section is different for each polarization. It is given by:

$$\sigma = \frac{4k^2 J}{\pi Z^2} \left| e^{-iaZ} e^{(ibZ \tan \alpha)/2} \frac{\sin (bQ/2)}{Q} - \frac{\sin (bW/2)}{W} \right|^2,$$

where

$$W = k (\sin \phi \cos \theta + \sin \phi' \cos \theta') \quad (\text{Eqn. 3.1.2.2.4-2})$$

$$Z = k (\cos \phi \cos \theta + \cos \phi' \cos \theta'), \text{ and}$$

$$Q = Z \tan \alpha - W.$$

The only term that changes with polarization is the term J . When $Z = 0$, the cross section is given by Equation 3.1.2.2.4-1 above, except that the bistatic definition for W in Equation 3.1.2.2.4-2 is used.

As stated before in the section on bistatic scattering, it can be shown with physical optics that in the high frequency case, most of the scattered field comes from the immediate neighborhood of the specular point, as long as k is sufficiently large⁸. Thus, we would expect that for the flat plate the strongest scattering is in the specular direction, just as in a mirror.

Figure 3.1.2.2.4-2 (a) & (b) shows the bistatic RCS of a plate for the case where the incident vector makes a 45° elevation angle ($\theta_i = 45^\circ$) with the surface of the plate as shown in the small figure. The elevation angle is defined as the angle θ in the small figure. The frequency used is X-band (10 GHz). We would expect the strongest scattering when $\theta = 45^\circ$, and this plot certainly verify this fact. Even though the mainlobe is quite large, the sidelobes are about 30 dB down.

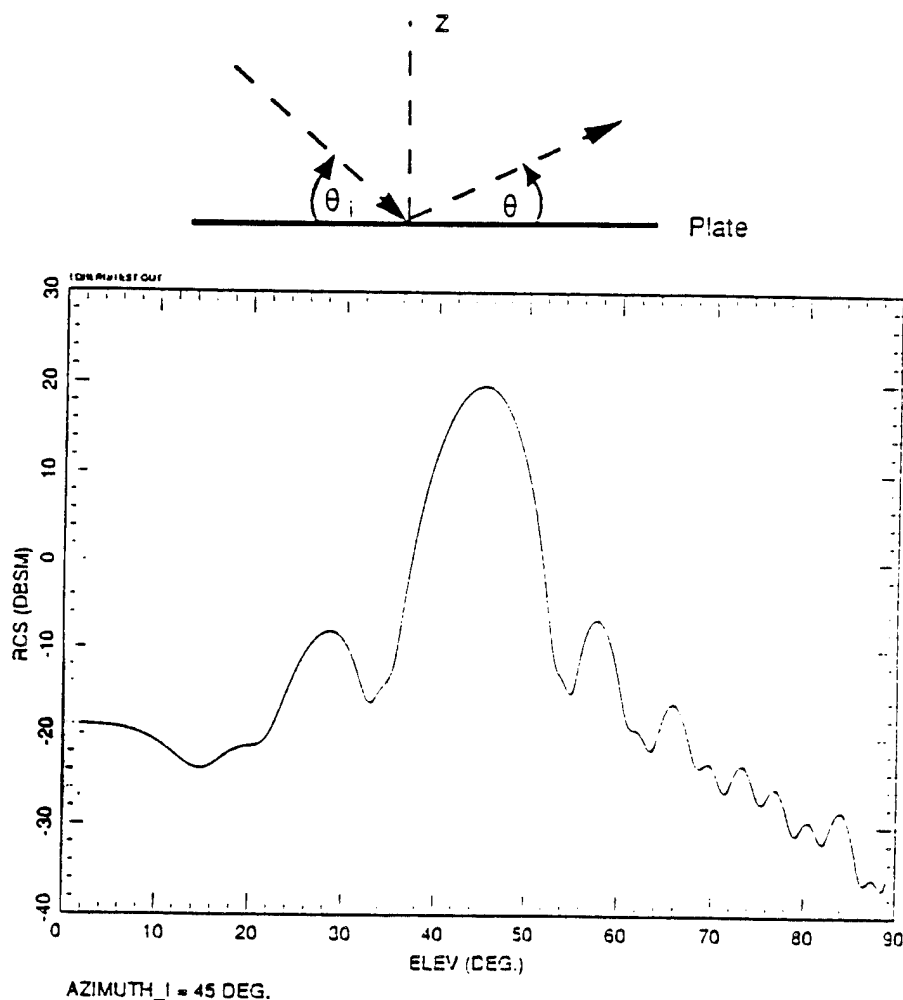


Figure 3.1.2.2.4-2 (a) & (b). Bistatic RCS of triangular plate
@ 45° incident elevation - X-band

Next we have a case where $\theta_i = 30^\circ$. Figure 3.1.2.2.4-2 (c) shows that the strongest scattering is in the neighborhood of $\theta = 30^\circ$. The mainlobe is much bigger here, probably because the incident vector grazes the surface of the plate more closely. Still, if we go further out, the scattering power is at least 20 dBsm down from the peak.

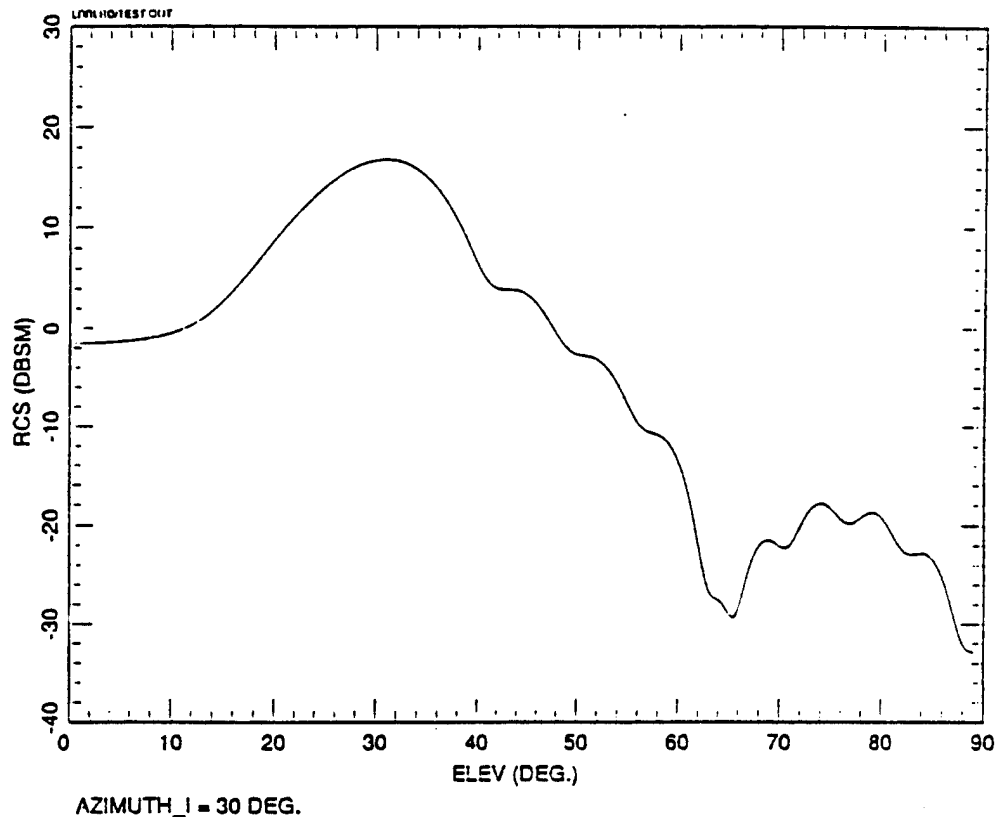


Figure 3.1.2.2.4-2 (c). Bistatic RCS of triangular plate @ 30° incident elevation
X-band

Next we have the case where the incident vector is almost head-on to the plate, making an elevation angle of 75° with the plate. Figure 3.1.2.2.4-2 (d) shows that the strongest scattering does indeed occur for the specular reflection ($\theta = 75^\circ$). The mainlobe is even narrower than the 45° case of Figure 3.1.2.2.4-2 (b).

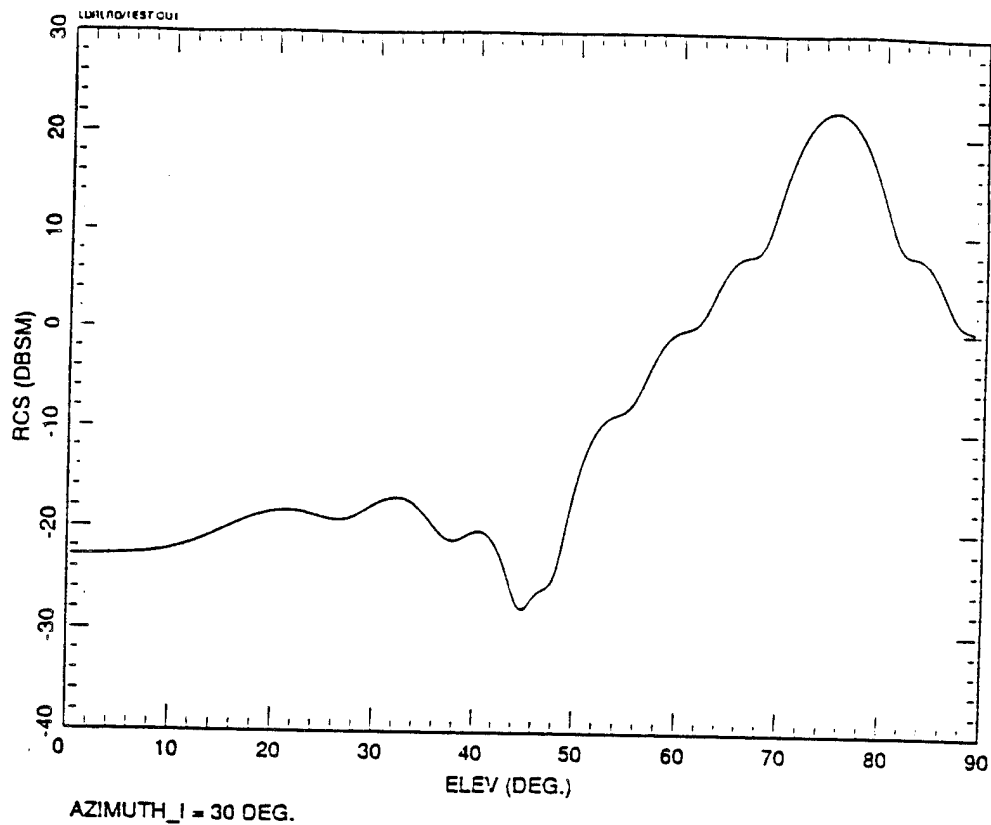


Figure 3.1.2.2.4-2 (d). Bistatic RCS of triangular plate @ 75° incident elevation
X-band

At L-band (1.3 GHz), however, the physical optics formulas derived above do not give good specular reflection results for the bistatic RCS of the plate. This is shown in Figures 3.1.2.2.4-3 (a) & (b). In Figure 3.1.2.2.4-3 (a) the incident vector makes an elevation angle of 15° with the surface of the plate, yet the peak RCS is somewhere around 40° elevation angle. Even though the RCS at $\theta = 15^\circ$ is only 2 dB or so down from the peak, specular reflection is not as definite in this case as with X-band. Next, Figure 3.1.2.2.4-3 (b) suggests that when θ_i is larger, then the peak scattering will tend to occur more at the angle $\theta = \theta_i$. However, the mainlobe is still much too large compared to the X-band case.

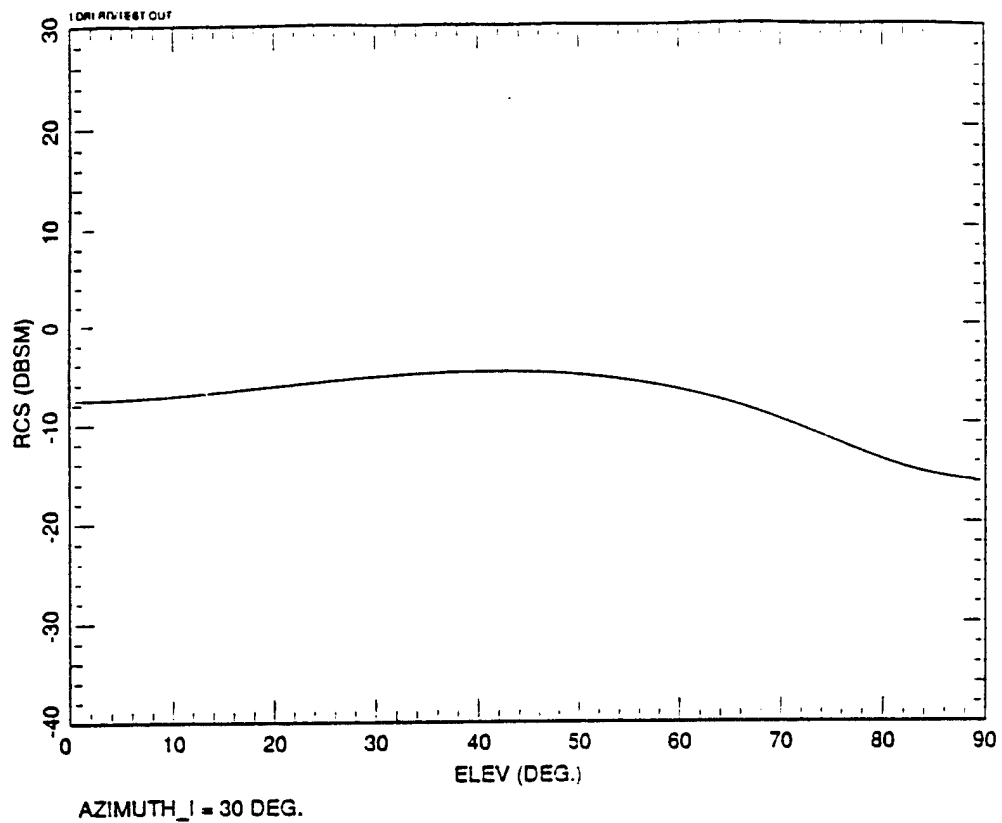


Figure 3.1.2.2.4-3 (a). Bistatic RCS of triangular plate @ 15° incident elevation
L-band/TM mode

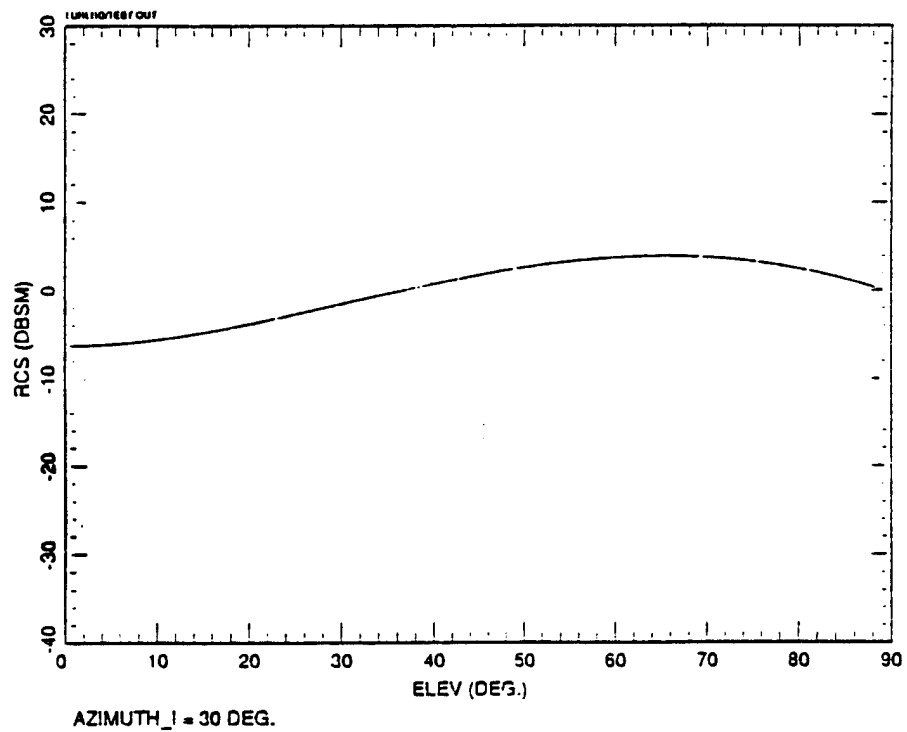
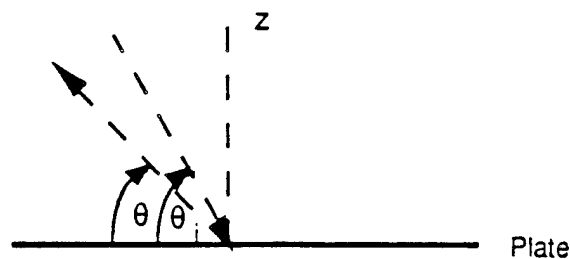


Figure 3.1.2.2.4-3 (b). Bistatic RCS of triangular plate @ 60° incident elevation
L-band/TM mode

The backscattering region for the same triangular plate is shown below:



We would expect the scattering to be weak on this side of the plate because this is not in the specular region. This is definitely the case, as shown in Figures 3.1.2.2.4-4 (a) & (b). Figure 3.1.2.2.4-4 (a) shows the X-band case where $\theta_i = 30^\circ$. Scattering is nonexistent for small θ ; compare with Figure 3.1.2.2.4-2 (c) above. In fact, at the backscattering angle ($\theta = 30^\circ$), the scattering is beneath the minimum plotted. The scattering climbs up, however, as θ gets closer to the normal angle. This is reasonable because in this region we move toward the specular region on the other side of the normal vector z .

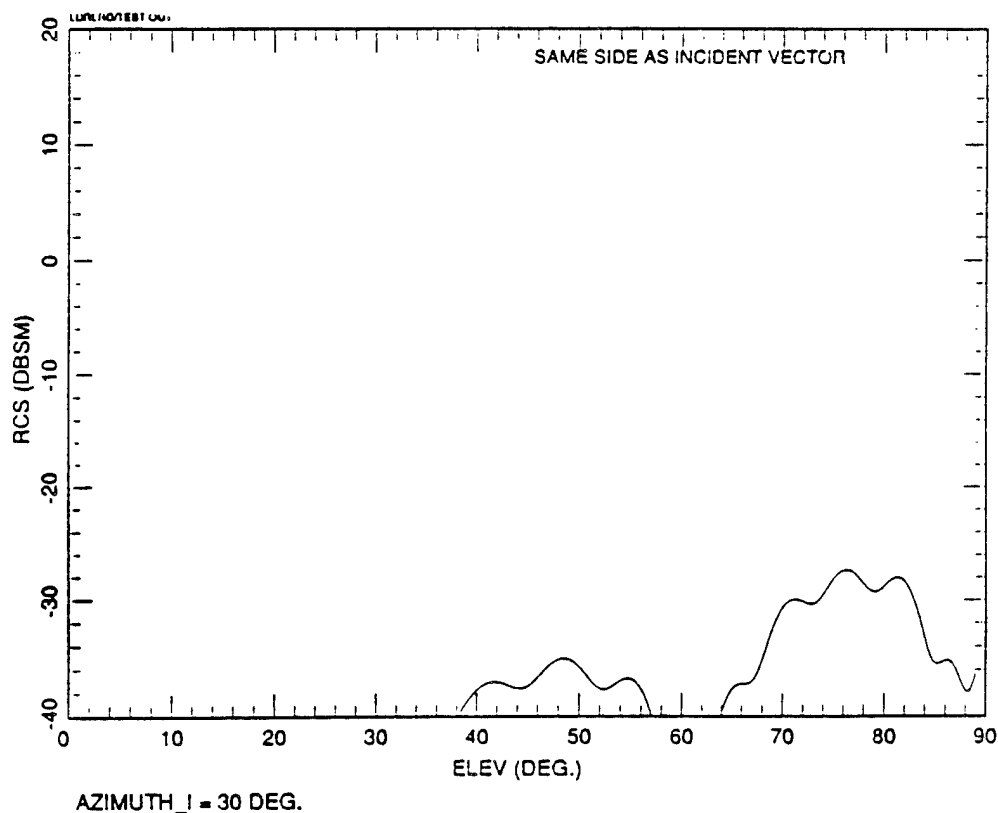


Figure 3.1.2.2.4-4 (a). Bistatic RCS of triangular plate in backscatter region
@ 30° incident elevation - X-band

For the L-band case, there is more scattering in this backscattering region than for X-band. Figure 3.1.2.2.4-4 (b) shows results for the same geometry but at L-band (1.3 GHz). The RCS of the plate in this region is between -30 dBsm and about -10 dBsm. Comparing this Figure with Figure 3.1.2.2.4-3 (a), we see that the RCS is 10 to 20 dB lower in this region.

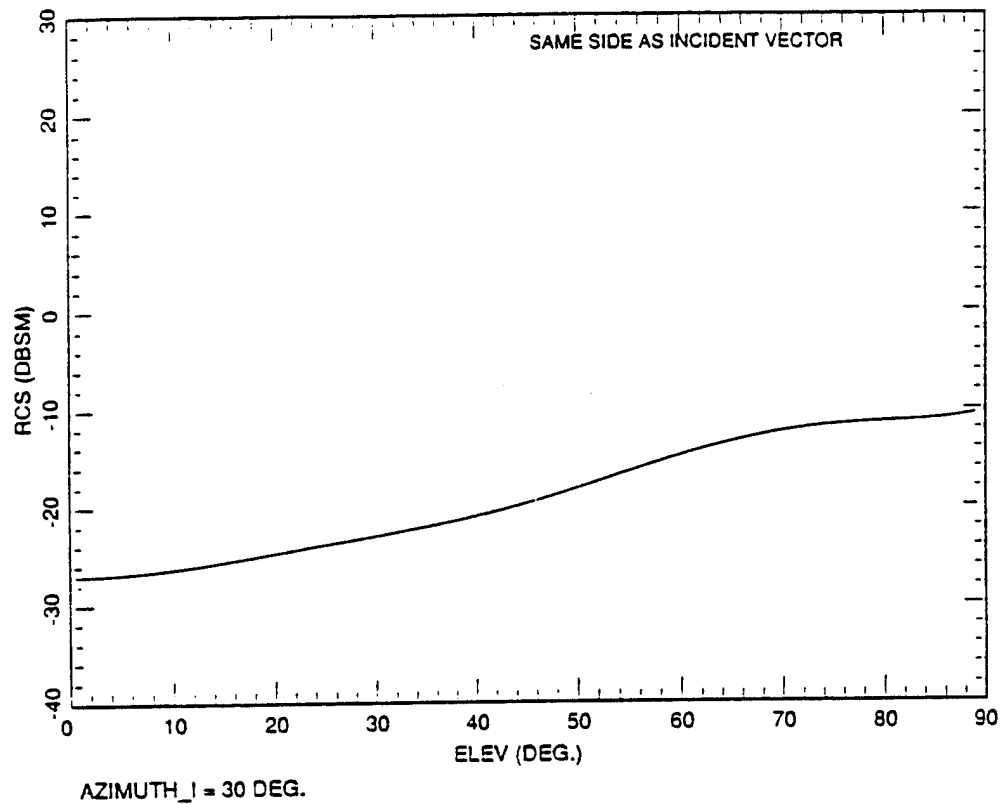


Figure 3.1.2.2.4-4 (b). Bistatic RCS of triangular plate in backscatter region
@ 30° incident elevation - L-band/TE mode

3.1.2.2.5 Straight Edges

The edges of the wings, tailfin, and tailplane can contribute significant scattering. We model these elements of the missile by assuming that their scattering behavior is similar to that of thin wires. Thin wires can be thought of as cylinders with radius much smaller than the wavelength. When this is the case it makes essentially no difference how the cylinder ends are terminated as far as the scattered fields are concerned. The cylinder ends may be flat, rounded, or pointed, and the results are the same.⁹

There are two cases of interest. The first case is when the length of the wire is of the same order as the wavelength. This is same situation as in antenna theory, the dipole. There are two simple expressions for the bistatic cross section of the thin wire when its length is the half-wave dipole and the full-wave dipole.

For the half-wave dipole the bistatic cross section is:

$$\sigma_{\gamma_i, \gamma_s}(\psi_i, \psi_s) = 0.86 \lambda^2 \cos^2 \gamma_i \cos^2 \gamma_s \left[\frac{\cos(\pi/2 \sin \psi_i)}{\cos \psi_i} \right]^2 \left[\frac{\cos(\pi/2 \sin \psi_s)}{\cos \psi_s} \right]^2,$$

where

ψ_i = the angle between the direction of incidence and the vector that is perpendicular to the wire,

ψ_s = the angle between the direction of scattering and the vector that is perpendicular to the wire,

γ_i = the polarization angle of the E-field measured from the plane of incidence. $\gamma_i = 0^\circ$ is the TM mode while $\gamma_i = 90^\circ$ is the TE mode,

γ_s = the same as γ_i except with respect to the plane of scattering.

As can be seen from the expression above, the cross section is zero for the TE mode because $\gamma_i = 90^\circ$ and $\gamma_s = 90^\circ$ in that mode.

For the full-wave dipole, the bistatic cross section is given by:

$$\sigma_{\gamma_i, \gamma_s}(\psi_i, \psi_s) = 0.93 \lambda^2 \cos^2 \gamma_i \cos^2 \gamma_s \left[\frac{\sin(\pi \sin \psi_i)}{\cos^2 \psi_i} \right]^2 \left[\frac{\sin(\pi \sin \psi_s)}{\cos^2 \psi_s} \right]^2$$

When the radar wavelength in the LDR simulation is about between 0.5 ft and 1 ft, some of the wire edges will have length on the order of a wavelength. In these cases, we will make the approximation that the wire is either a half-wave or a full-wave dipole.

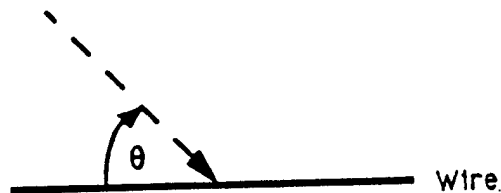
The other case of interest is when the length of the wire is more than about λ . Then the general bistatic scattering cross section is given by:

$$\sigma(\psi_i, \psi_s) = 4 \pi h^2 \frac{\cos^2 \psi_s}{\cos^2 \psi_i} \cos^2 \gamma_i \cos^2 \gamma_s \left[\frac{1}{\ln^2(0.8905 k a \cos \psi_i) + \pi^2/4} \right] \times \left[\frac{\sin[k(\sin \psi_i + \sin \psi_s)h]}{k(\sin \psi_i + \sin \psi_s)h} \right]^2,$$

where

a = radius of wire, which we will take to be $\lambda/85$.¹⁰

Results for the cross sections of the wires are shown below. Figures 3.1.2.2.5-1 (a) & (b) show the monostatic RCS of different wires for the case of 0° and 45° azimuth. The wires are all assumed to lie along the x-axis. The elevation angle is defined as the angle θ in the small figure.



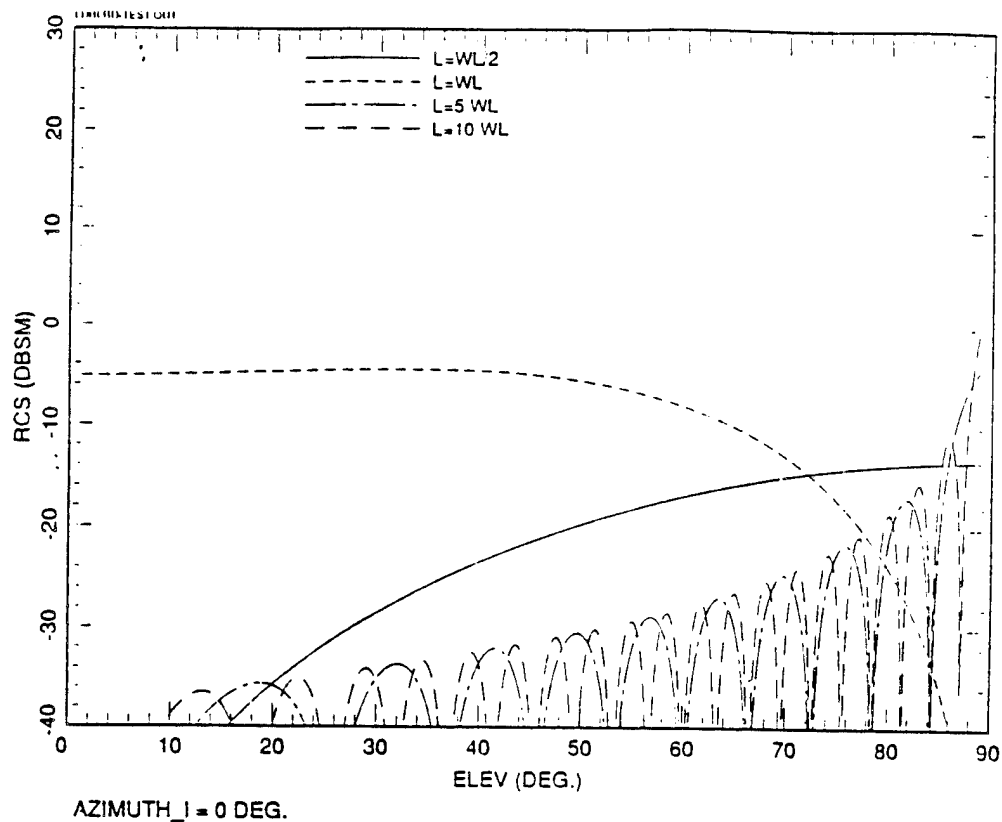
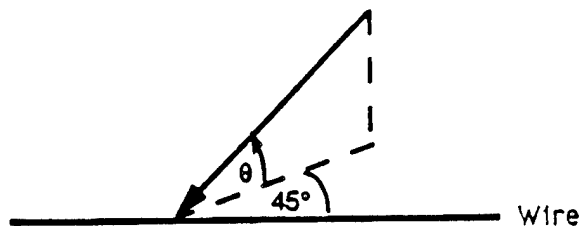


Figure 3.1.2.2.5-1 (a). Monostatic RCS of wires @ 0° azimuth - L band/TM

Except for the full-wave dipole ($L = \lambda$), all the wires have the peak RCS at broadside ($\theta = 90^\circ$). When the elevation angle is below 10° , the RCS is very small or zero, except for the full-wave dipole. Curiously enough, at broadside, the RCS of the full-wave dipole is zero. Another thing to note is that the longer wires have peak RCS between -5 to 0 dBsm.

The case of 45° azimuth is shown in Figure 3.1.2.2.5-1 (b). It is similar to the 0° azimuth case, except that the wires which are not the full-wave dipole have higher RCS at low elevation angles than before. This is especially true of the half-wave dipole.



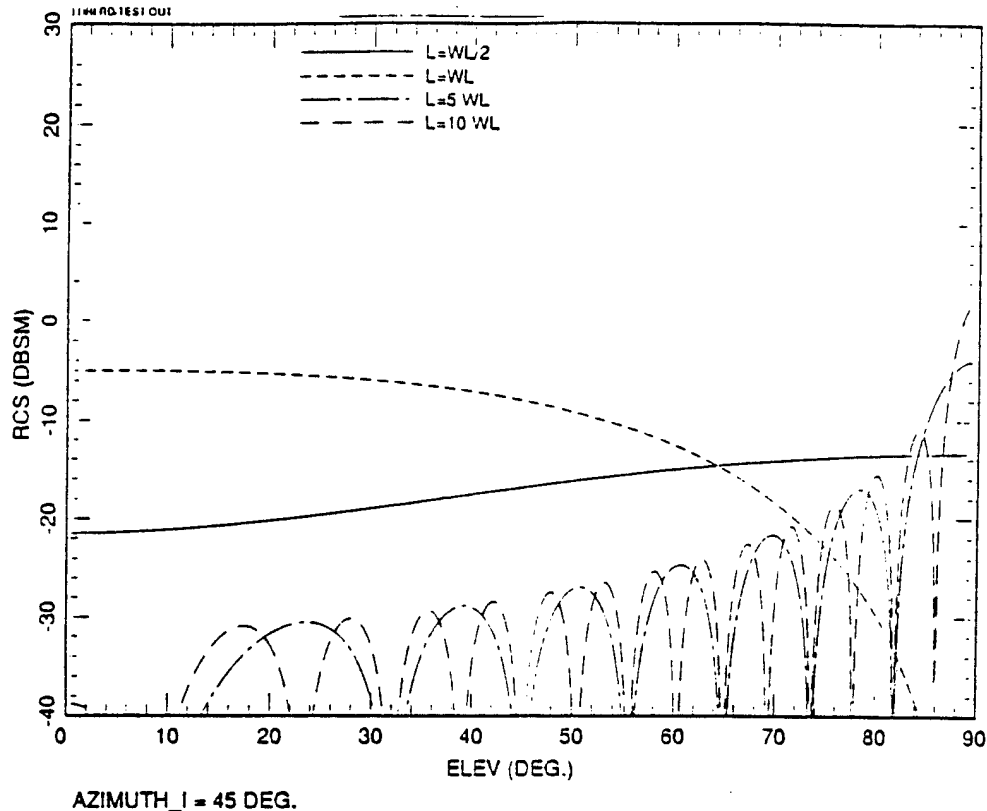


Figure 3.1.2.2.5-1 (b). Monostatic RCS of wires @ 45° azimuth - L band/TM

We also have bistatic RCS results for the wire. The geometry shown in Figure 3.1.2.2.5-2 (a). The incident vector is at 0° azimuth but has a 45° elevation angle with respect to the wire. The scattering vector is varied as a function of the elevation angle θ .

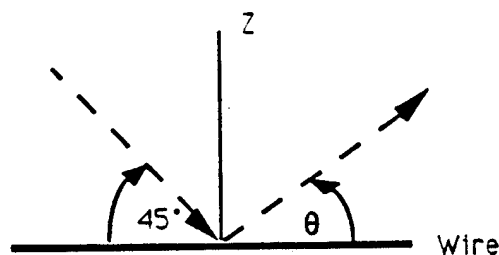


Figure 3.1.2.2.5-2 (a)

The bistatic RCS of the same 4 wires are shown in Figure 3.1.2.2.5-2 (b). It can be seen that with this geometry the full-wave dipole gives the highest RCS value through most of the aspects. The other wires have similar shapes as the

0° azimuth monostatic case although they don't have the high peaks at $\theta = 90^\circ$. This is to be expected since we expect the high peaks to occur at broadside in the backscattering case.

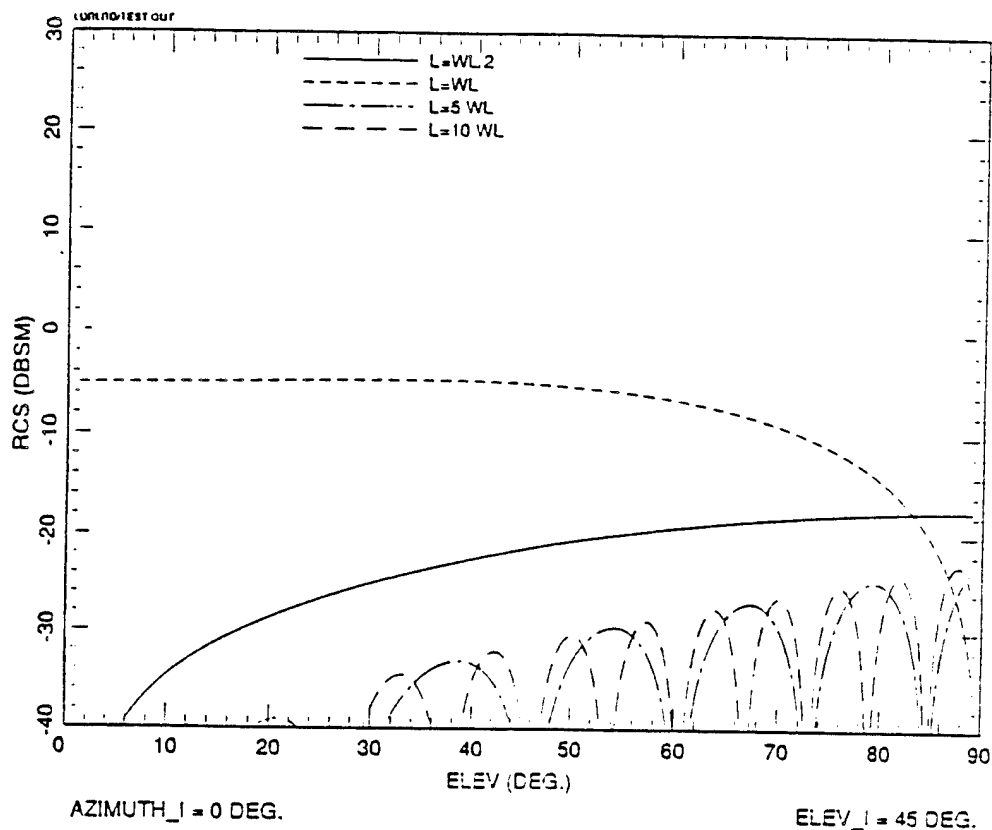


Figure 3.1.2.2.5-2 (b). Bistatic RCS of wires @ 0° azimuth - L band/TM

3.1.2.2.6 Computed RCS of Missile

In this section we present the results for the computed RCS of the cruise missile. The RCS is a combination of all the individual equations we presented above for the different types of shapes.

Figure 3.1.2.2.6-1 (a) is a monostatic RCS plot of the missile varying with azimuth angle. The radar is at 0° elevation, i.e. in the same xy-plane as the missile. 0° azimuth is when the radar is nose-on with the missile while 180° is the radar looking at the tail of the missile. The frequency is L-band (1.3 GHz).

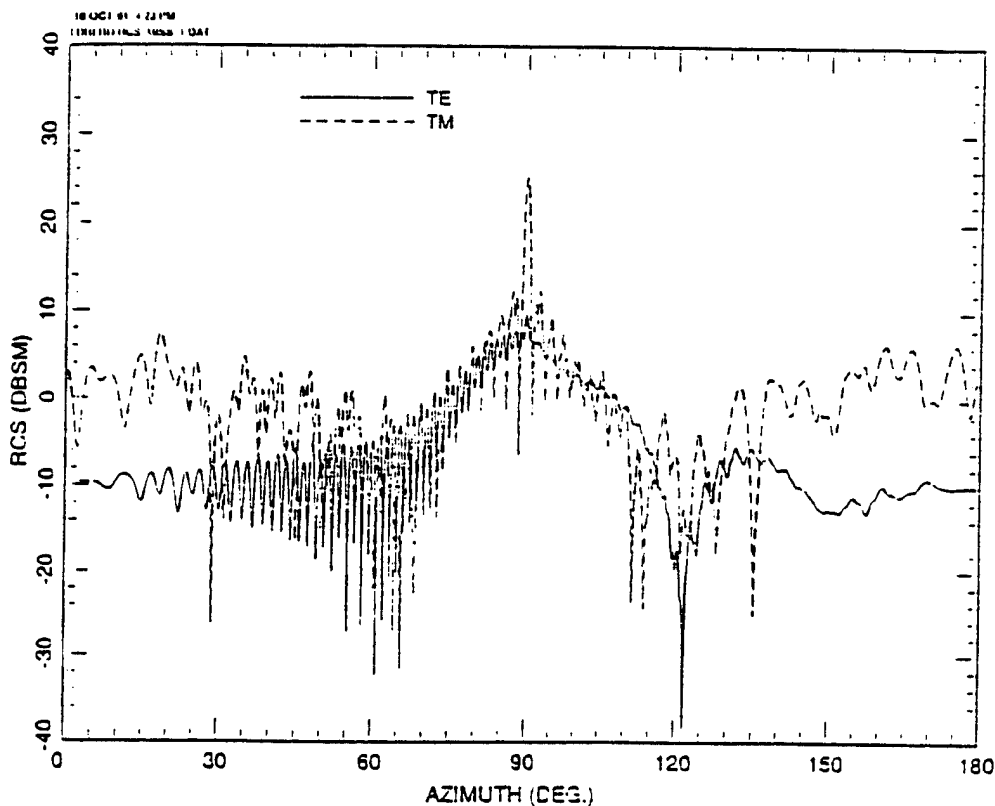


Figure 3.1.2.2.6-1 (a). Monostatic RCS of missile @ 0° elevation - L band

As the plot shows, the average RCS of the missile for the TE mode over most aspects is about -10 dBsm, except for the region near broadside (90°). In that region, as is expected, the missile has a peak RCS of about 10 dBsm. The average RCS is about 5 to 10 dBsm less than the average RCS of the aircraft for the same radar geometry. Recall that the TE mode is the mode where the electric vector is perpendicular to the plane of the missile cylinder axis and the direction of incidence. Thus, the electric vector is not aligned with the cylinder

axis. In contrast, the TM mode has the electric vector aligned in the same plane with the cylinder axis. This is a more favorable alignment and as expected the average and peak RCS are larger than in the TE mode. The average RCS is about 0 dBsm while the peak at broadside jumps up to 25 dBsm. Thus the polarization makes a big difference in the missile RCS at L-band.

In Figure 3.1.2.2.6-1 (b) we show the RCS results for the case of a radar pointing down at the missile with an elevation angle of -45° . Once again the TM mode gives far larger RCS values than the TE mode. At broadside the TE mode does not even have a peak while the peak for TM there is about 24 dBsm.

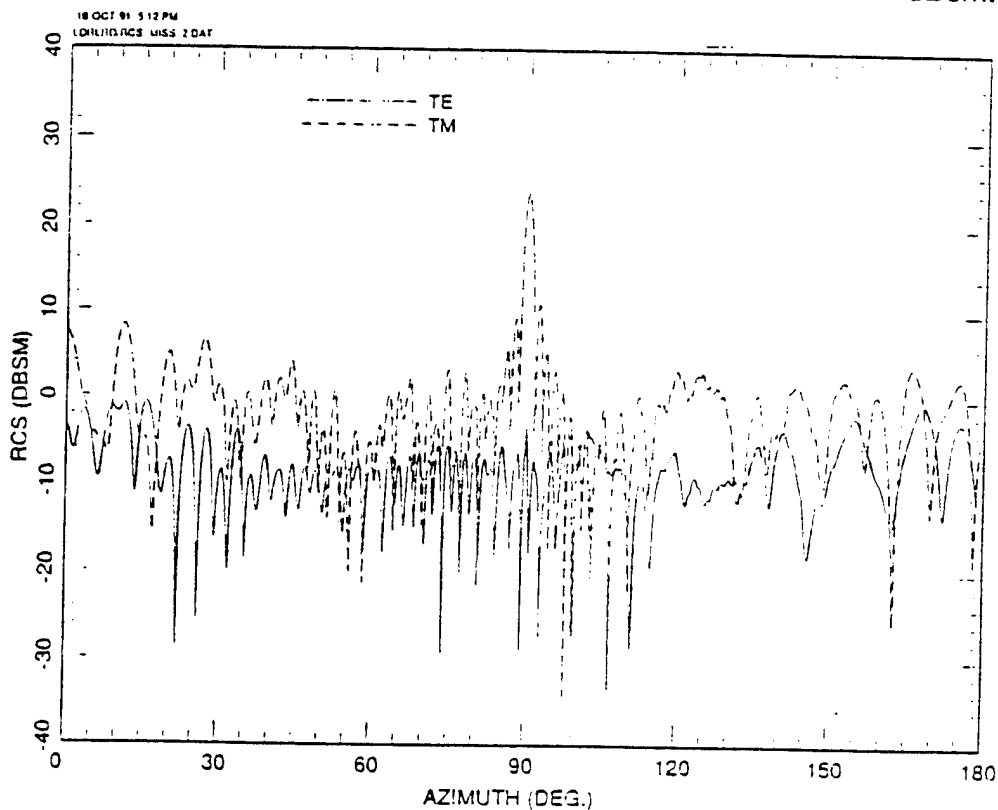


Figure 3.1.2.2.6-1 (b) Monostatic RCS of missile @ -45° elevation - L band

At X-band (10 GHz), however, the difference between the two polarization modes are not as pronounced. This is shown in Figures 3.1.2.2.6-2 (a) & (b). The mainlobe region around broadside has about the same width and amplitude for both polarizations. This can be explained by the fact that the cylinder contribution dominates in this region, and the RCS equation for the cyl-

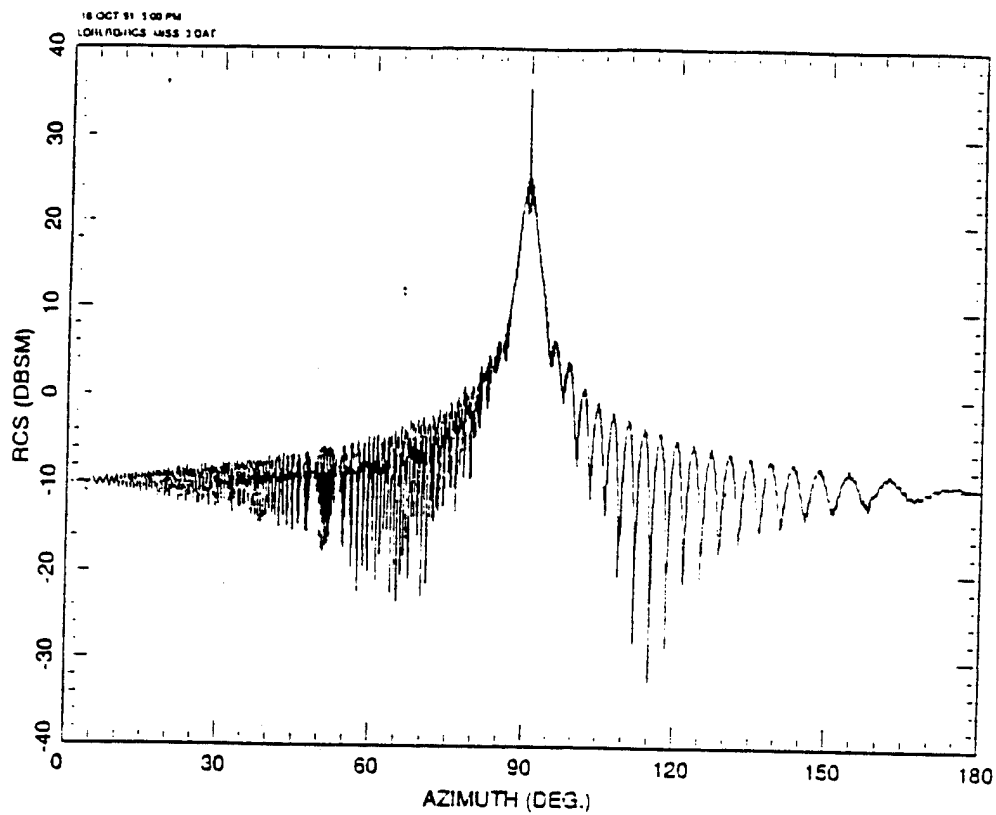


Figure 3.1.2.2.6-2 (a). Monostatic RCS of missile @ 0° elevation - X band - TE

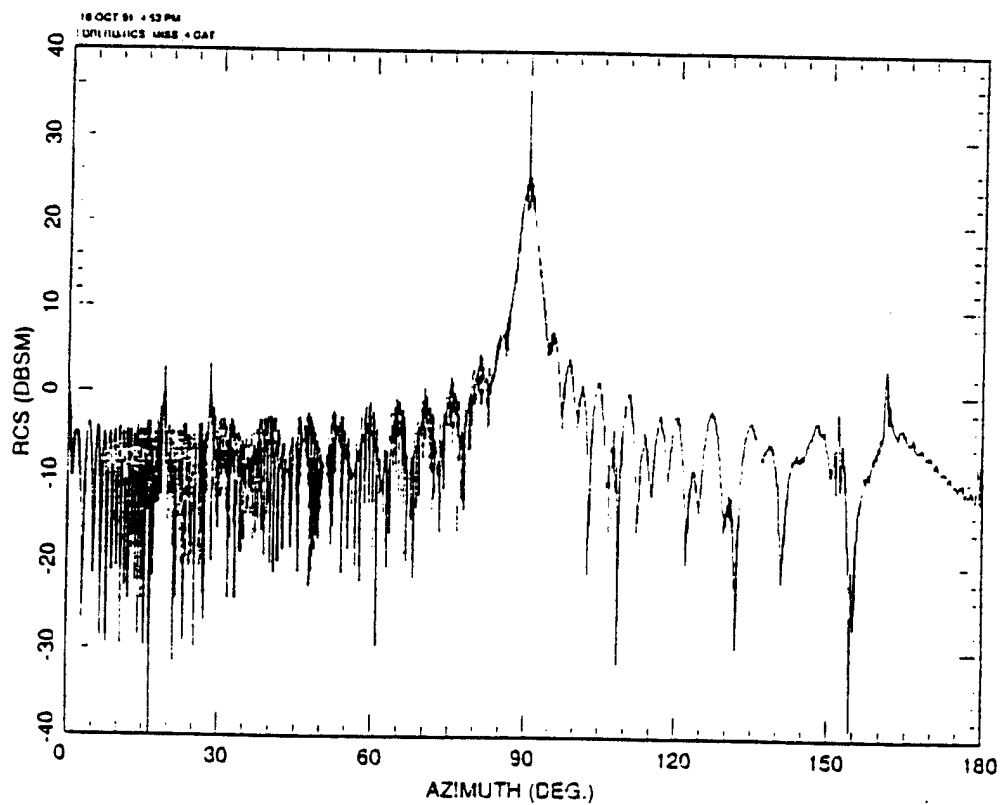


Figure 3.1.2.2.6-2 (b). Monostatic RCS of missile @ 0° elevation - X band - TM

inder when the frequency is high ($ka > 10$) is the same for either polarization. In the other aspect regions, the TM mode still tends to give higher RCS values than the TE mode.

In Figures 3.1.2.2.6-3 (a) & (b) we present the X-band case where the radar looks down with an elevation angle of -45° . Once again, the two modes give essentially the same RCS results with little differences.

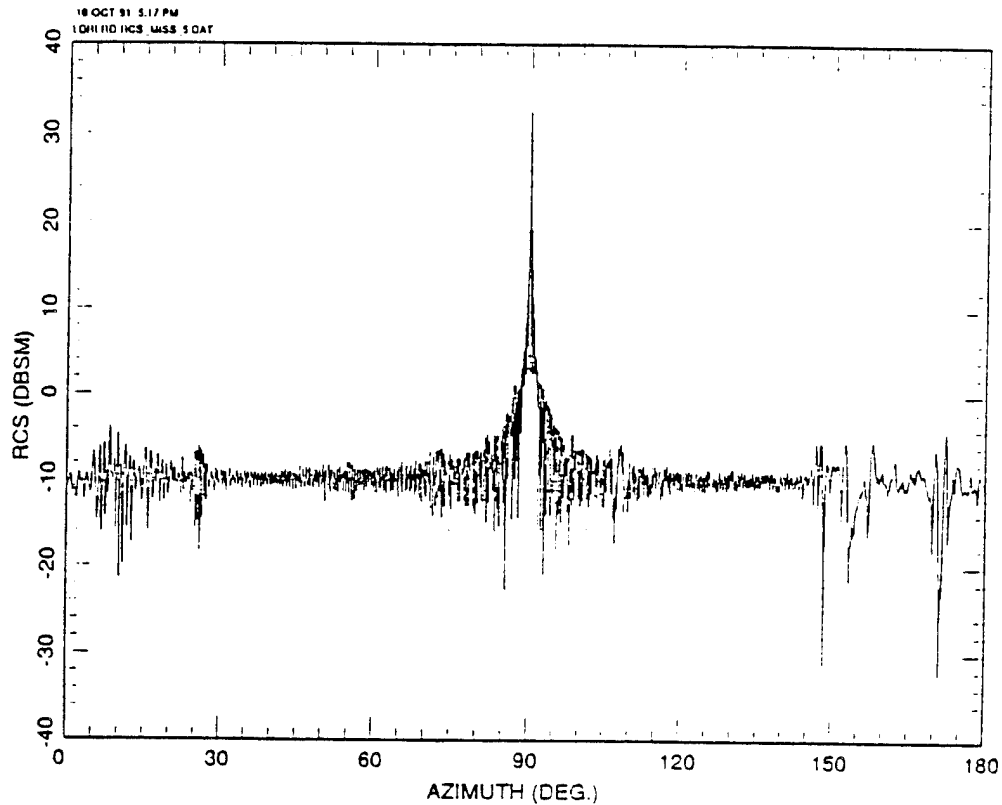


Figure 3.1.2.2.6-3 (a). Monostatic RCS of missile @ -45° elevation
X-band - TE

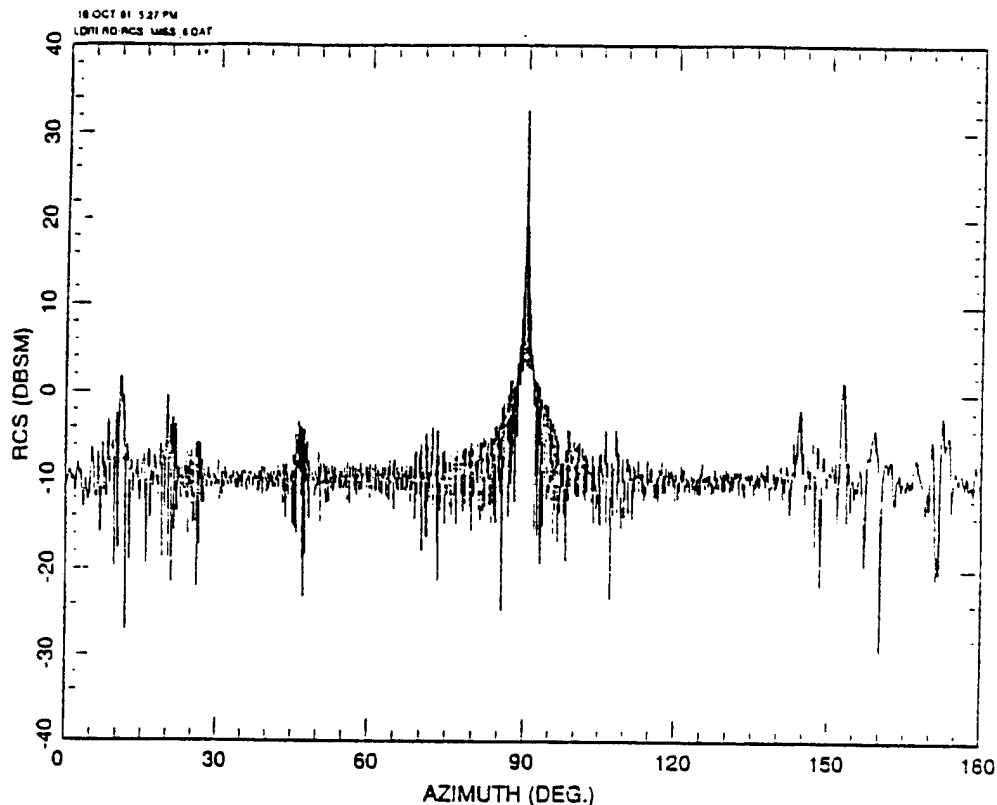


Figure 3.1.2.2.6-3 (b). Monostatic RCS of missile @ -45° elevation
X-band - TM

And finally in Figure 3.1.2.2.6-4 we have the RCS of the missile as a function of the elevation angle of the radar with respect to missile. -90° elevation in the plot is when the radar is on the ground looking straight up while 90° is when the radar is looking straight down at the missile. The radar has 0° azimuth angle, i.e. the nose aspect. The RCS for both modes is fairly symmetric with respect to 0° elevation. As expected at L-band, the TM mode gives higher RCS values, especially around 0° elevation.

These results indicate that polarization plays an important role at the lower range of radar frequencies. The TM mode, where the electric vector is in the same plane as the missile main axis, results in greater scattering than the TE mode. Missile RCS averages around -10 dBsm at most aspects except near broadside where the RCS can climb up to as high as 30 dBsm. At higher radar frequencies, the missile RCS tends to be the same regardless of polarization.

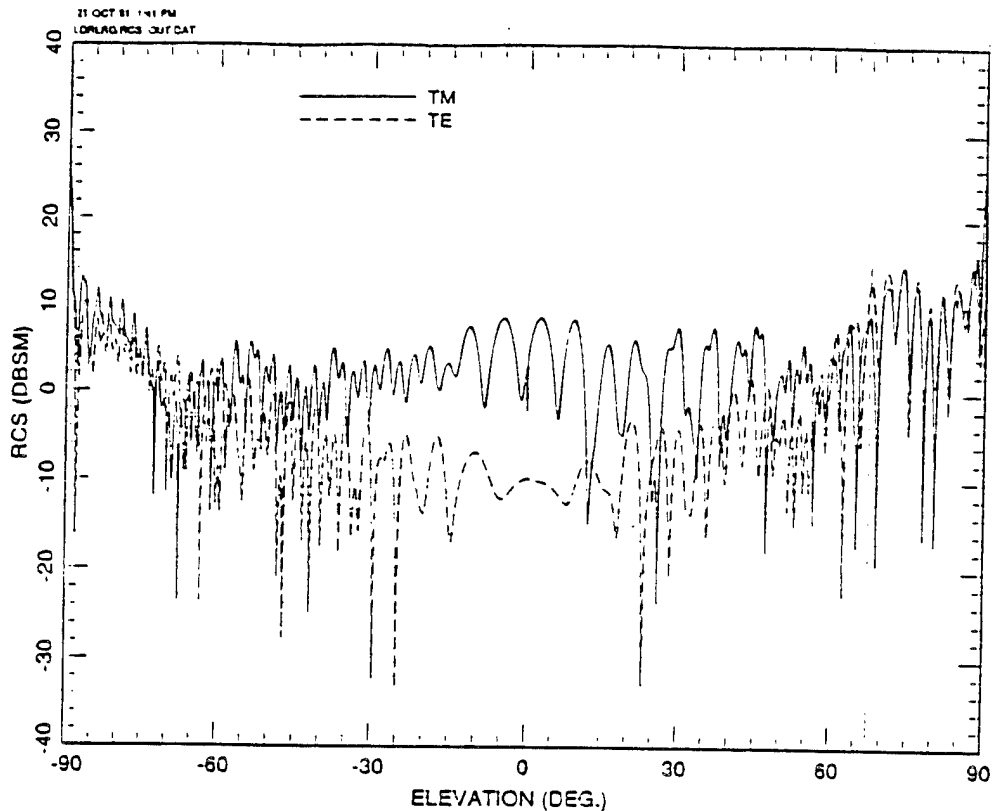


Figure 3.1.2.2.6-4. Monostatic RCS of missile for radar @ 0° azimuth
L band

In Figure 3.1.2.2.6-5 we compare the missile RCS obtained by our model with that of the Lincoln Lab model. The first plot is the same RCS curve for the TM mode that is shown in Figure 3.1.2.2.6-1 (a) above. The second plot is the Lincoln Lab results for the missile RCS. It is not clear if the Lincoln Lab results are measured RCS or computed RCS. In any case, the plots are quite similar for most aspects, except that the LDR results show a stronger peak at 90° than the Lincoln Lab results, about 7dBsm more. This could be because of the different types of polarization used. Nevertheless, the similarity of results reaffirms the validity of the LDR cruise missile model to a large extent.

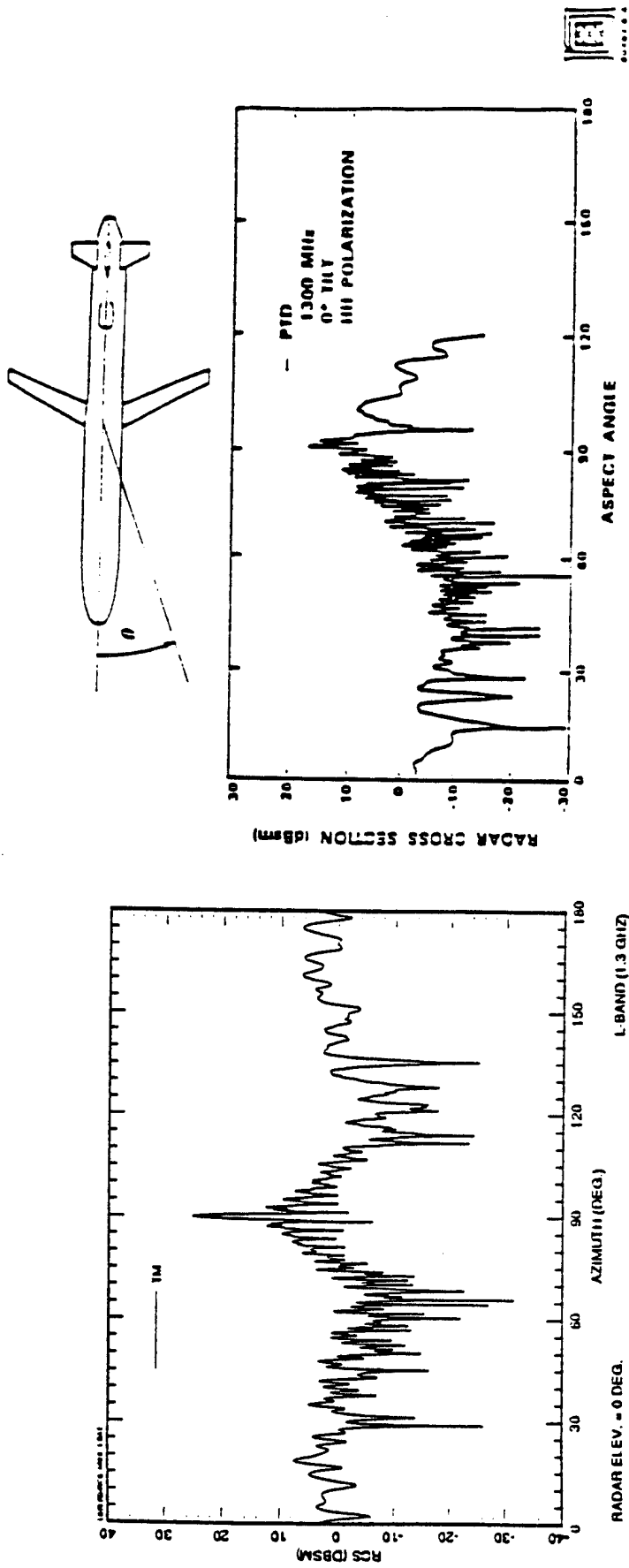


Figure 3.1.2.2.6-5. LDR missile RCS model vs. Lincoln Lab model

3.1.3 Target Interaction Model

After obtaining the RCS models for the aircraft and missile, monostatic and bistatic, we now develop the interaction model between the two targets. This section is at the heart of the phenomenology that is explored by the LDR program.

We begin with the general bistatic radar geometry shown in Figure 3.1.3-1. The aircraft and missile are at respective distances R_{TA} and R_{TM} from the transmitter, and distances R_{RA} and R_{RM} from the receiver. R_{AM} is the distance between them. The radar energy follows a bistatic path as it bounces off the aircraft at a bistatic angle β_1 , travels to the missile and bounces back to the receiver at a bistatic angle β_2 . Restricting ourselves for now to just the area around the aircraft, we know that the power density of the incident wave as seen by the aircraft is given by:

$$\text{Power density} = \frac{P_t G_t}{4\pi R_{TA}^2},$$

where

P_t = transmitter power, and

G_t = transmitter antenna gain.

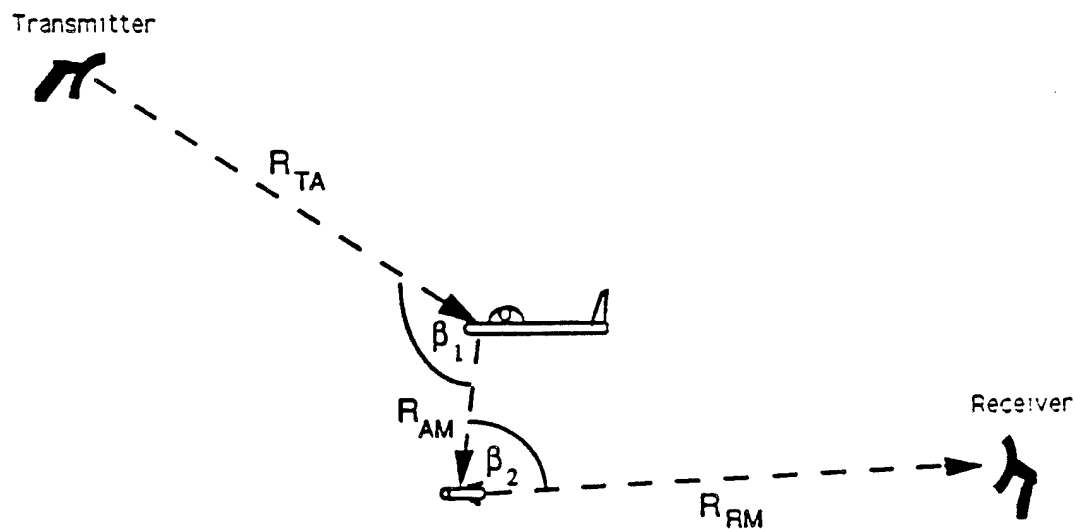


Figure 3.1.3-1. Basic interaction path (path 1)

Now suppose that the aircraft is modeled as just one component and has a bistatic RCS at angle β_1 given by σ_A^{bi} . Then the radar power scattered by the aircraft toward the missile is given by:

$$P_A = \frac{P_t G_t}{4\pi R_{TA}^2} \sigma_A^{bi}$$

In a sense the aircraft is acting as an antenna radiating energy to the missile, and similarly, the missile is an antenna capturing energy from the aircraft. This being the case, we can introduce two quantities: A_A and A_M . A_A is the effective aperture area of the aircraft acting as an antenna while A_M is the same for the missile. Not all the energy scattered by the aircraft toward the missile will be captured by the latter. If the missile aperture is too small compared to the aircraft aperture, then the missile can only capture a fraction of the energy. This fraction of energy is given by

$$\begin{cases} \frac{A_M}{A_A}, & \text{if } A_M < A_A \\ 1, & \text{if } A_M \geq A_A \end{cases}$$

This is one of the key elements in the LDR target interaction model. We also implicitly assume that $R_{AM} \ll R_{RM}$.

The power captured by the missile is then given by:

$$P_M = \frac{P_t G_t}{4\pi R_{TA}^2} \sigma_A^{bi} \min\left[\frac{A_M}{A_A}, 1\right]$$

Next, this power is reflected back to the radar receiver. The distance it has to travel in going back is given by $R_{AM} + R_{RM}$. Also, assume that the effective aperture area of the receiving antenna is given by A_r . Then the total power received by the receiver is given by:

$$P_r = \frac{P_t G_t}{4\pi R_{TA}^2} \sigma_A^{bi} \min\left[\frac{A_M}{A_A}, 1\right] \frac{A_r}{4\pi (R_{AM} + R_{RM})^2}$$

Now, A_r can be expressed in terms of the antenna gain G_r through the relationship:

$$A_r = \frac{G_r \lambda^2}{4\pi}$$

Also, the effective antenna aperture areas of the aircraft and the missile can be related to the bistatic RCS of each through the expressions:

$$\sigma_A^{bi} = \frac{4\pi A_A^2}{\lambda^2}, \text{ and } \sigma_M^{bi} = \frac{4\pi A_M^2}{\lambda^2}$$

where σ_M^{bi} is the bistatic cross section of the missile at bistatic angle β_2 .

Therefore, we can finally express the interaction power received by the receiver as:

$$P_{TAMR} = P_r = \frac{P_t G^2 \lambda^2 \sqrt{\sigma_A^{bi} \sigma_M^{bi}}}{4\pi^3 R_{TA}^2 (R_{AM} + R_{RM})^2} \quad \text{if } \sigma_A^{bi} > \sigma_M^{bi}$$

$$\frac{P_t G^2 \lambda^2 \sigma_A^{bi}}{4\pi^3 R_{TA}^2 (R_{AM} + R_{RM})^2} \quad \text{if } \sigma_A^{bi} \leq \sigma_M^{bi}$$

where we have also assumed that $G_t = G_r = G$.

This equation for P_{TAMR} is the basic interaction equation between an aircraft and a missile. It assumes that the interaction path is from transmitter to aircraft to missile and back to receiver. There is another signal path possible. It is from the transmitter to missile to aircraft and back to receiver. This path scenario is shown in Figure 3.1.3-2. The expressions for this path is almost identical:

$$P_{\text{TAMR}} = \frac{P_i G^2 \lambda^2 \sqrt{\sigma_A^{\text{bi}} \sigma_M^{\text{bi}}}}{4\pi^3 R_{\text{TM}}^2 (R_{\text{AM}} + R_{\text{RA}})^2} \quad \text{if } \sigma_M^{\text{bi}} > \sigma_A^{\text{bi}}$$

$$\frac{P_i G^2 \lambda^2 \sigma_M^{\text{bi}}}{4\pi^3 R_{\text{TM}}^2 (R_{\text{AM}} + R_{\text{RA}})^2} \quad \text{if } \sigma_M^{\text{bi}} \leq \sigma_A^{\text{bi}}$$

where now

σ_M^{bi} = bistatic RCS of missile at angle β_3 ,

σ_A^{bi} = bistatic RCS of aircraft at angle β_4 .

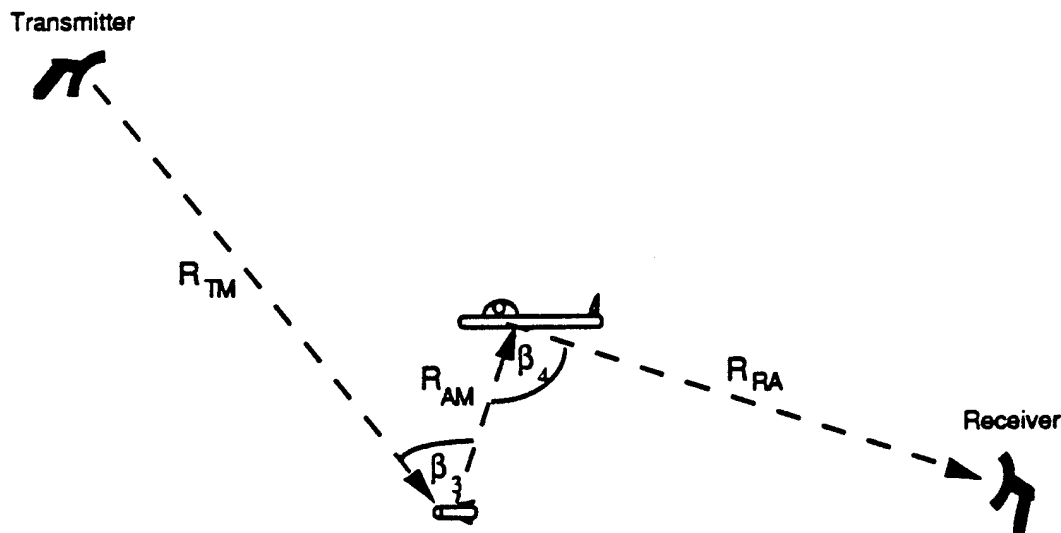


Figure 3.1.3-2. Alternative interaction path (path 2)

The expressions for P_{TAMR} and P_{TMAR} form the starting point that enables us to derive the full interaction equations in the general case when the targets consist of many components. These two paths are called the primary interaction paths. There are two more paths possible. They are illustrated in Figures 3.1.3-3 and 3.1.3-4. In path 3, the energy is scattered from aircraft to missile but back to aircraft then to receiver. Thus, unlike paths 1 and 2, there is a monostatic RCS of the missile to be computed here. In path 4, the energy is scattered from missile to aircraft and back to missile then to receiver. So there

is a monostatic RCS of the aircraft to be computed here. These two alternate paths are called the secondary interaction paths.

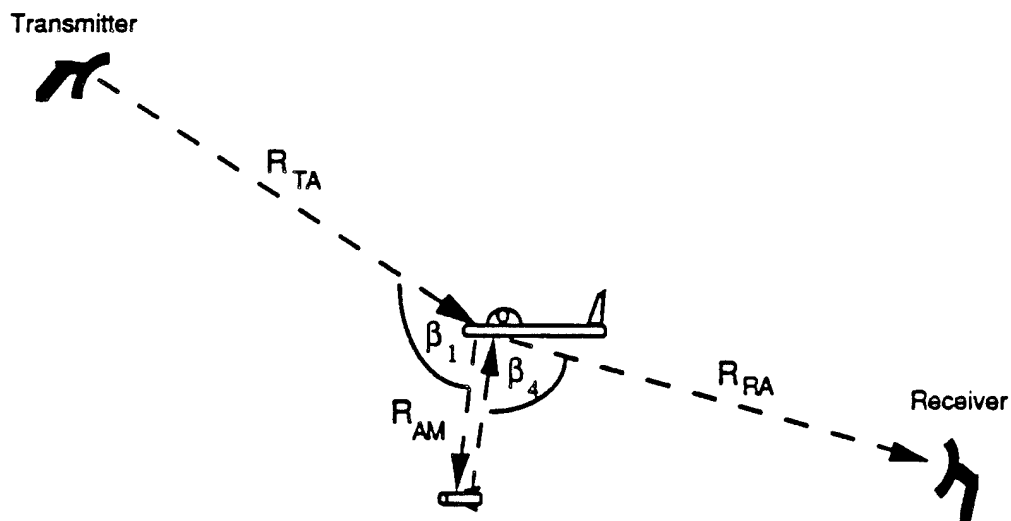


Figure 3.1.3-3. Interaction path 3

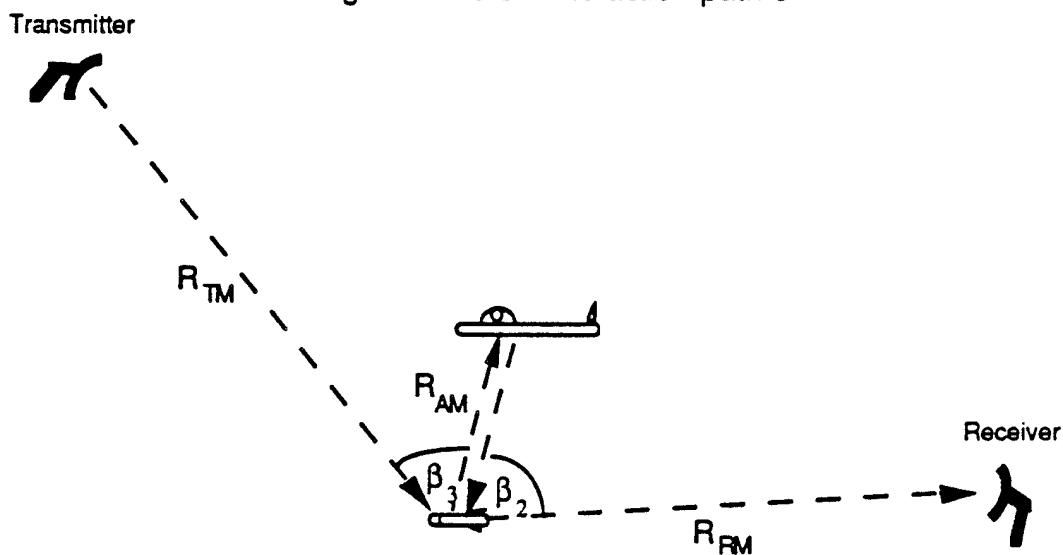


Figure 3.1.3-4. Interaction path 4

The interaction equations for paths 3 and 4 are derived in the same way as before. We make use of the same concept of effective antenna aperture area of each target. For path 3, the interaction power received by the radar is given by:

$$P_r = \frac{P_t G}{4\pi R_{TA}^2} \frac{\sigma_A^{bi_1}}{(2R_{AM} + R_{RA})^2} \min \left[\frac{A_M^{mono}}{A_A^{bi_1}}, 1 \right] \min \left[\frac{A_A^{bi_2}}{A_M^{mono}}, 1 \right] \frac{G \lambda^2}{4\pi},$$

where

$\sigma_A^{bi_1}$ = bistatic RCS of aircraft at angle β_1 ,

A_M^{mono} = effective aperture area of missile acting as antenna,

$A_A^{bi_1}$ = effective aperture area of aircraft acting as antenna at angle β_1 ,

$A_A^{bi_2}$ = effective aperture area of aircraft acting as antenna at angle β_4 .

Using the relationship between effective aperture area and RCS that was presented before, we can simplify the expression for path 3 interaction to become:

$$P_{TAMAR} = \frac{P_t G^2 \lambda^2 \sqrt{\sigma_A^{bi_1} \sigma_A^{bi_2}}}{4\pi^3 R_{TA}^2 (2R_{AM} + R_{RA})^2} \text{ if } \sigma_A^{bi_1} > \sigma_M^{mono}, \sigma_M^{mono} > \sigma_A^{bi_2}$$

$$\frac{P_t G^2 \lambda^2 \sqrt{\sigma_A^{bi_1} \sigma_M^{mono}}}{4\pi^3 R_{TA}^2 (2R_{AM} + R_{RA})^2} \text{ if } \sigma_A^{bi_1} > \sigma_M^{mono}, \sigma_M^{mono} \leq \sigma_A^{bi_2}$$

$$\frac{P_t G^2 \lambda^2 \sigma_A^{bi_1} \sqrt{\sigma_A^{bi_2}}}{4\pi^3 R_{TA}^2 (2R_{AM} + R_{RA})^2 \sqrt{\sigma_M^{mono}}} \text{ if } \sigma_A^{bi_1} \leq \sigma_M^{mono}, \sigma_M^{mono} > \sigma_A^{bi_2}$$

$$\frac{P_t G^2 \lambda^2 \sigma_A^{bi_1}}{4\pi^3 R_{TA}^2 (2R_{AM} + R_{RA})^2} \text{ if } \sigma_A^{bi_1} \leq \sigma_M^{mono}, \sigma_M^{mono} \leq \sigma_A^{bi_2}$$

where

$\sigma_A^{bi_2}$ = bistatic RCS of aircraft at angle β_4 ,

σ_M^{mono} = monostatic RCS of missile.

And for path 4 the interaction equations are:

$$P_{\text{TMAMR}} = \frac{P_t G^2 \lambda^2 \sqrt{\sigma_M^{\text{bi}_1} \sigma_M^{\text{bi}_2}}}{4\pi^3 R_{\text{TM}}^2 (2 R_{\text{AM}} + R_{\text{FM}})^2} \quad \text{if } \sigma_M^{\text{bi}_1} > \sigma_A^{\text{mono}}, \sigma_A^{\text{mono}} > \sigma_M^{\text{bi}_2}$$

$$\frac{P_t G^2 \lambda^2 \sqrt{\sigma_M^{\text{bi}_1} \sigma_A^{\text{mono}}}}{4\pi^3 R_{\text{TM}}^2 (2 R_{\text{AM}} + R_{\text{FM}})^2} \quad \text{if } \sigma_M^{\text{bi}_1} > \sigma_A^{\text{mono}}, \sigma_A^{\text{mono}} \leq \sigma_M^{\text{bi}_2}$$

$$\frac{P_t G^2 \lambda^2 \sigma_M^{\text{bi}_1} \sqrt{\sigma_M^{\text{bi}_2}}}{4\pi^3 R_{\text{TM}}^2 (2 R_{\text{AM}} + R_{\text{FM}})^2 \sqrt{\sigma_A^{\text{mono}}}} \quad \text{if } \sigma_M^{\text{bi}_1} \leq \sigma_A^{\text{mono}}, \sigma_A^{\text{mono}} > \sigma_M^{\text{bi}_2}$$

$$\frac{P_t G^2 \lambda^2 \sigma_M^{\text{bi}_1}}{4\pi^3 R_{\text{TM}}^2 (2 R_{\text{AM}} + R_{\text{FM}})^2} \quad \text{if } \sigma_M^{\text{bi}_1} \leq \sigma_A^{\text{mono}}, \sigma_A^{\text{mono}} \leq \sigma_M^{\text{bi}_2}$$

where

$\sigma_M^{\text{bi}_1}$ = bistatic RCS of missile at angle β_3 ,

$\sigma_M^{\text{bi}_2}$ = bistatic RCS of missile at angle β_2 ,

σ_A^{mono} = monostatic RCS of aircraft.

The interaction equations for the 4 paths presented so far are for the ideal case of targets with just 1 component. Also, the equations can be used for rough estimations of the interaction when both targets are given by a single RCS value, i.e. after the component cross sections have been summed up appropriately. To compute the interaction signals more correctly, however, it is necessary to compute the interaction signal with respect to each target component. This is because each aircraft component interacts individually with

each missile component. Each of these individual interaction signals has a phase that is proportional to its interaction path length. In the end, the signals can be summed algebraically, just as in computing the RCS of the entire target. Each interaction path will have a signal of its own. We now derive the full interaction equations for each path.

3.1.3.1 Path 1 (TAMR)

The interaction signal power between the i -th aircraft component and the j -th missile component as seen by the radar is given by:

$$P_{ij}^{(1)} = \begin{cases} k_1 \sigma_{i(A)}^{1/2} \sigma_{j(M)}^{1/2} & \text{if } \sigma_{i(A)} > \sigma_{j(M)}, \\ k_1 \sigma_{i(A)} & \text{if } \sigma_{i(A)} \leq \sigma_{j(M)} \end{cases}$$

where $\sigma_{i(A)}$ = bistatic RCS of i -th aircraft component at angle β_1 ,

$\sigma_{j(M)}$ = bistatic RCS of j -th missile component at angle β_2 , and

$$k_1 = \frac{P_t G^2 \lambda^2}{4\pi^3 R_{TA}^2 (R_{AM} + R_{FM})^2}.$$

When the interaction signals from different components are summed with appropriate phases, it is necessary to work with voltage rather than power. The interaction signal voltage is given by:

$$V_{ij}^{(1)} = \begin{cases} k_1^{1/2} \sigma_{i(A)}^{1/4} \sigma_{j(M)}^{1/4} & \text{if } \sigma_{i(A)} > \sigma_{j(M)}, \\ k_1^{1/2} \sigma_{i(A)}^{1/2} & \text{if } \sigma_{i(A)} \leq \sigma_{j(M)}. \end{cases}$$

Now we sum over all aircraft and all missile components to find the interaction signal for path 1:

$$V_1 = k_1^{1/2} \sum_{\text{All } j} \left(\sigma_{j(M)}^{1/4} \sum_{i \in S_1} \sigma_{i(A)}^{1/4} e^{i\phi_{ij}} + \sum_{i \in S_2} \sigma_{i(A)}^{1/2} e^{i\phi_{ij}} \right)$$

where $S_1 = \{i \text{ s.t. } \sigma_{i(A)} > \sigma_{j(M)}\}$,

$$S_2 = \{i \text{ s.t. } \sigma_{i(A)} \leq \sigma_{j(M)}\},$$

ϕ_{ij} is the relative phase angle of the ij -path. This path is from the transmitter to the i -th aircraft component to the j -th missile component and back to the receiver.

3.1.3.2 Path 2 (TMAR)

The interaction signal for this path is similarly derived. The interaction signal voltage between the i -th aircraft component and the j -th missile component as seen by the radar is given by:

$$V_{ij}^{(2)} = \begin{cases} k_2^{1/2} \sigma_{i(A)}^{1/4} \sigma_{j(M)}^{1/4} & \text{if } \sigma_{j(M)} > \sigma_{i(A)}, \\ k_2^{1/2} \sigma_{j(M)}^{1/2} & \text{if } \sigma_{j(M)} \leq \sigma_{i(A)}, \end{cases}$$

where $\sigma_{i(A)}$ = bistatic RCS of i -th aircraft component at angle β_4 ,

$\sigma_{j(M)}$ = bistatic RCS of j -th missile component at angle β_3 , and

$$k_2 = \frac{P_t G^2 \lambda^2}{4\pi^3 R_{TM}^2 (R_{AM} + R_{RA})^2}.$$

Summing over all aircraft and all missile components we find the interaction signal for path 2:

$$V_2 = k_2^{1/2} \sum_{\text{All } j} \left(\sigma_{j(M)}^{1/4} \sum_{i \in S_1} \sigma_{i(A)}^{1/4} e^{i\phi_{ij}} + \sigma_{j(M)}^{1/2} \sum_{i \in S_2} e^{i\phi_{ij}} \right),$$

where $S_1 = \{i \text{ s.t. } \sigma_{j(M)} > \sigma_{i(A)}\},$

$S_2 = \{i \text{ s.t. } \sigma_{j(M)} \leq \sigma_{i(A)}\}.$

3.1.3.3 Path 3 (TAMAR)

The interaction signal voltage between the i -th aircraft component and the j -th missile component as seen by the radar is given by:

$$\begin{aligned}
V_{ij}^{(3)} = & k_3^{1/2} \sigma_{i(A)_1}^{1/4} \sigma_{i(A)_2}^{1/4} & \text{if } \sigma_{i(A)_1} > \sigma_{j(M)}, \sigma_{j(M)} > \sigma_{i(A)_2}, \\
& k_3^{1/2} \sigma_{i(A)_1}^{1/4} \sigma_{j(M)}^{1/4} & \text{if } \sigma_{i(A)_1} > \sigma_{j(M)}, \sigma_{j(M)} \leq \sigma_{i(A)_2}, \\
& k_3^{1/2} \sigma_{i(A)_1}^{1/2} \sigma_{i(A)_2}^{1/4} \sigma_{j(M)}^{-1/4} & \text{if } \sigma_{i(A)_1} \leq \sigma_{j(M)}, \sigma_{j(M)} > \sigma_{i(A)_2}, \\
& k_3^{1/2} \sigma_{i(A)_1}^{1/2} & \text{if } \sigma_{i(A)_1} \leq \sigma_{j(M)}, \sigma_{j(M)} \leq \sigma_{i(A)_2}
\end{aligned}$$

where $\sigma_{i(A)_1}$ = bistatic RCS of i-th aircraft component at angle β_1 ,

$\sigma_{i(A)_2}$ = bistatic RCS of i-th aircraft component at angle β_4 ,

$\sigma_{j(M)}$ = monostatic RCS of j-th missile component, and

$$k_3 = \frac{P_t G^2 \lambda^2}{4\pi^3 R_{TA}^2 (2R_{AM} + R_{RA})^2}.$$

As in paths 1 and 2, the interaction signal for path 3 can be written as:

$$V_3 = \sum_{\text{All } j} \sum_{\text{All } i} V_{ij}^{(3)} e^{i\phi_{ij}}.$$

3.1.3.4 Path 4 (TMAMR)

The interaction signal voltage between the i-th aircraft component and the j-th missile component as seen by the radar is given by:

$$\begin{aligned}
V_{ij}^{(4)} = & k_4^{1/2} \sigma_{j(M)_1}^{1/4} \sigma_{j(M)_2}^{1/4} & \text{if } \sigma_{j(M)_1} > \sigma_{i(A)}, \sigma_{i(A)} > \sigma_{j(M)_2}, \\
& k_4^{1/2} \sigma_{j(M)_1}^{1/4} \sigma_{i(A)}^{1/4} & \text{if } \sigma_{j(M)_1} > \sigma_{i(A)}, \sigma_{i(A)} \leq \sigma_{j(M)_2}, \\
& k_4^{1/2} \sigma_{j(M)_1}^{1/2} \sigma_{j(M)_2}^{1/4} \sigma_{i(A)}^{-1/4} & \text{if } \sigma_{j(M)_1} \leq \sigma_{i(A)}, \sigma_{i(A)} > \sigma_{j(M)_2}, \\
& k_4^{1/2} \sigma_{j(M)_1}^{1/2} & \text{if } \sigma_{j(M)_1} \leq \sigma_{i(A)}, \sigma_{i(A)} \leq \sigma_{j(M)_2}
\end{aligned}$$

where $\sigma_{j(M)_1}$ = bistatic RCS of j-th missile component at angle β_3 ,

$\sigma_{j(M)_2}$ = bistatic RCS of j-th missile component at angle β_2 ,

$\sigma_{i(A)}$ = monostatic RCS of i-th aircraft component, and

$$k_4 = \frac{P_t G^2 \lambda^2}{4\pi^3 R_{TM}^2 (2R_{AM} + R_{RM})^2}$$

As in path 3, the interaction signal for path 4 can be written as:

$$V_4 = \sum_{\text{All } j} \sum_{\text{All } i} V_{ij}^{(4)} e^{i\phi_{ij}}$$

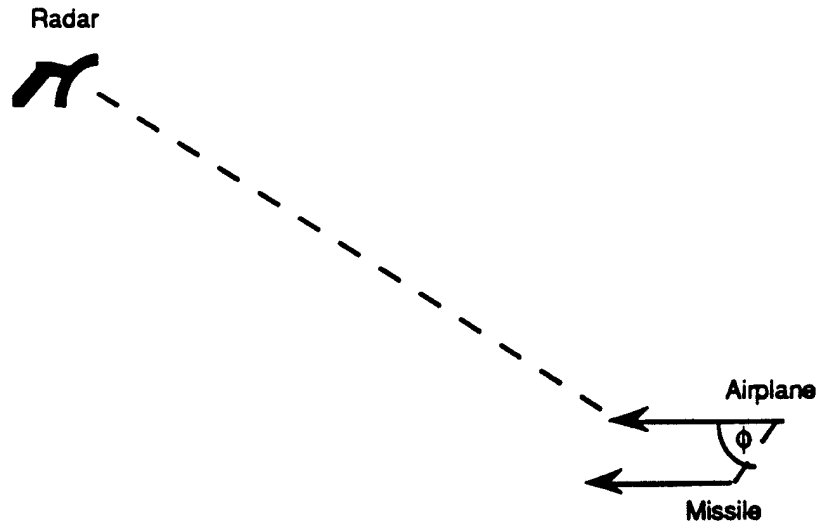


Figure 3.1.3.5-1. Air-to-air monostatic radar scenario

The interaction signals between the aircraft and the missile are computed as a function of time for a monostatic radar looking down at the targets with an initial elevation angle of -45° . The aircraft and the missile fly along a straight trajectory in parallel at a constant Mach 1 speed. The initial range from the radar to the targets is 50 nm while the interaction angle between the targets stays constant at 30° . The radar polarization used is the TE mode.

The skin return signals for this scenario is shown in Figure 3.1.3.5-2 (a) while the interaction results are shown with paths 1 and 2 in Figure 3.1.3.5-2 (b) and paths 3 and 4 in Figure 3.1.3.5-2 (c). The skin return signals are the RCS signals received directly from each target by the radar without any cotarget interference.

3.1.3.5 Computed Target Interaction

This section presents the results of the interaction model developed thus far. Before continuing, a word needs to be said about the appropriate units for the interaction signals. Looking back at the interaction equations, it will be seen that the interaction signal power received by the radar is always proportional to the cross section σ :

$$P_r = k \sigma_a \text{ or } k \sigma_a^{1/2} \sigma_b^{1/2} \text{ or } k \sigma_a^{1/2} \sigma_b^{1/2} \sigma_c^{-1/2}$$

where k is always in the form:

$$k = \frac{P_t G^2 \lambda^2}{(4\pi)^3 R_x^2 R_y^2}$$

Now, from the basic radar equation we know that a skin return signal received by the radar from a target is given by:

$$P_r = \frac{P_t G^2 \lambda^2 \sigma}{(4\pi)^3 R^4}$$

Obviously, the received power for the target skin return is also in the form $k\sigma$, and therefore it is proportional to the cross-section. When specifying the power of this signal, we do so in terms of the size of the cross-section (m^2). Thus, it seems natural to specify the interaction signal strength in terms of an equivalent cross-section. The equivalent cross section has units of m^2 and it is given by the different forms shown above, depending on the particular interaction path:

$$\sigma_e = \sigma_a \text{ or } \sigma_a^{1/2} \sigma_b^{1/2} \text{ or } \sigma_a^{1/2} \sigma_b^{1/2} \sigma_c^{-1/2}$$

The interaction signals will be plotted in units of dBsm.

The first case is for an air-to-air monostatic radar at L-band. The scenario is shown in Figure 3.1.3.5-1.

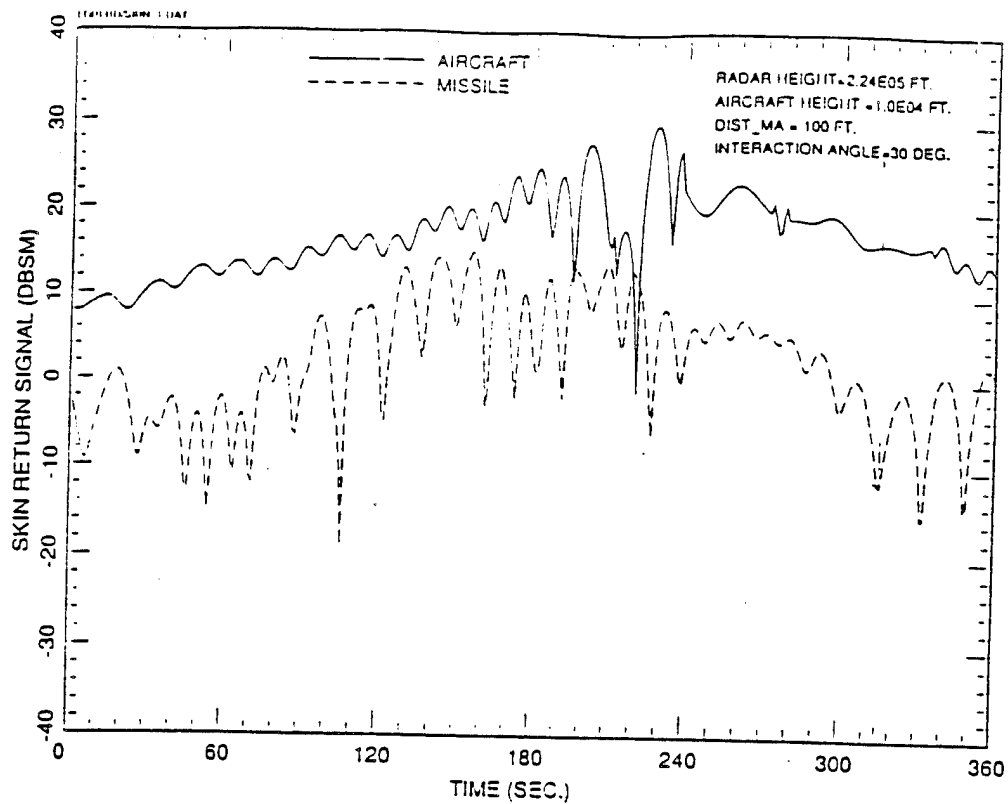


Figure 3.1.3.5-2 (a). Skin returns for mono. radar pointing @ -45° elevation
L-band/TE mode

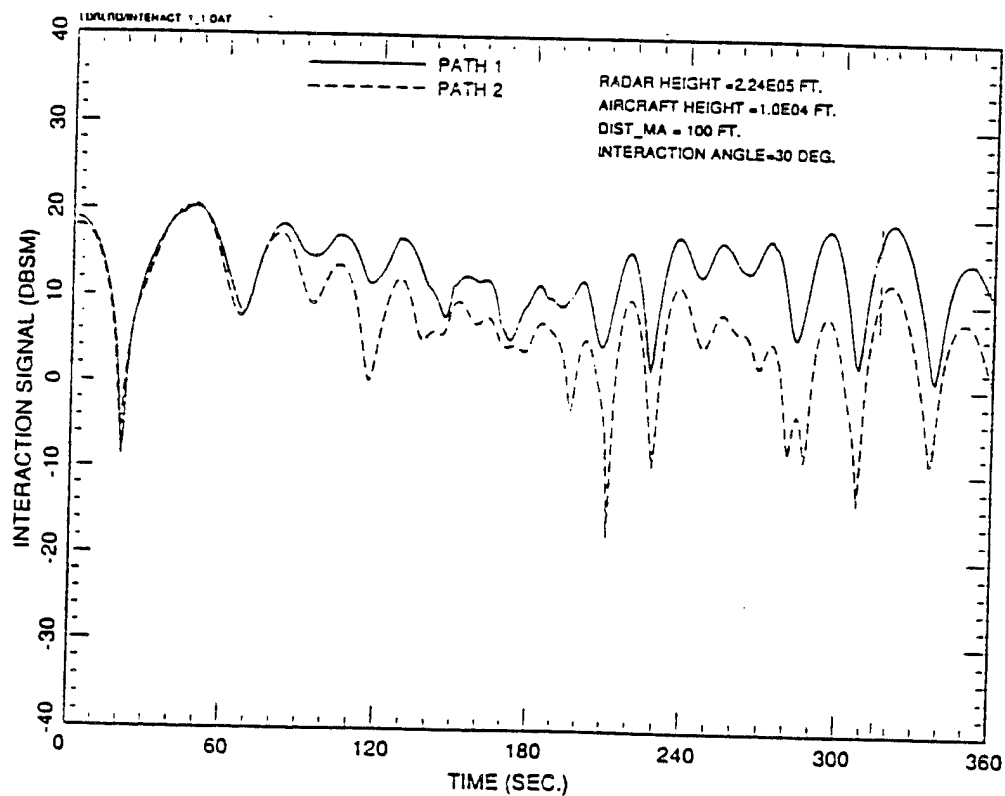


Figure 3.1.3.5-2 (b). Interaction paths 1 and 2 for mono. radar pointing
@ -45° elevation. L-band/TE mode

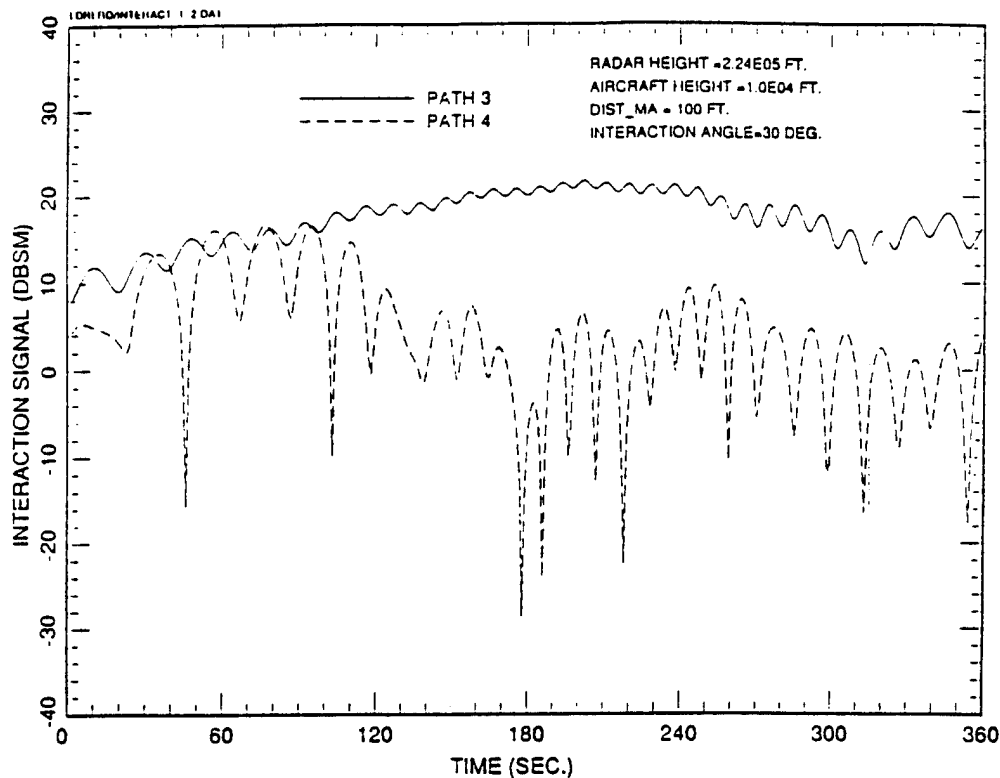


Figure 3.1.3.5-2 (c). Interaction paths 3 and 4 for mono. radar pointing @ -45° elevation. L-band/TE mode

At about $T=218$ sec., the targets pass directly beneath the radar for a broadside aspect. Hence, as shown in Figure 3.1.3.5-2 (a), the RCS of the aircraft peaks up to about 30 dBsm and the RCS of the missile is about 12 dBsm. Figures 3.1.3.5-2 (b) & (c) show that the interaction signals of path 1 and path 3 are the strongest with peaks of about 20 dBsm. Path 2 is slightly weaker than path 1. Figure 3.1.3.5-2 (c) shows that path 3 dominates after about $T=120$ sec. where it is consistently 20 dBsm. Path 4 is about 10 to 20 dB weaker in strength.

Most of the time in this run, the RCS of the missile is between -10 and 10 dBsm as seen in Figure 3.1.3.5-2 (a). The other figures here show that 2 out of the 4 interaction paths have signals consistently stronger than 10 dBsm. Hence, the results suggest that the interaction signals provide us with much more information about the low RCS target (the missile) than the skin returns by themselves can. The presence of these strong interaction paths alert us to the presence of another target that may be masked by the larger target. It is interesting to note that in some instances, an interaction signal can even be

stronger than the skin return from the aircraft. For example, this happens with paths 1 and 2 at $T=50$ sec.

Next we have the case of a bistatic radar looking at essentially the same geometry. The transmitter and the receiver will be offset 150° in azimuth although the initial elevation angle for both will still be -45° (look-down). The aircraft and the missile will be flying along a straight trajectory in parallel as before. The initial range to both the transmitter and the receiver is 50 nm. The geometry is shown below. The receiver position shown is not entirely accurate, and should be slightly out of the page.

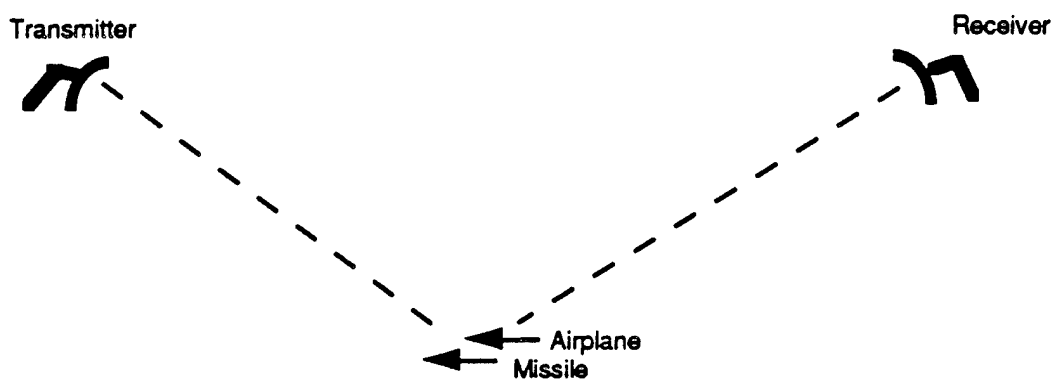


Figure 3.1.3.5-3. Air-to-air bistatic radar scenario

The skin return signals are shown in Figure 3.1.3.5-4 (a). For both targets, the signals decrease slowly with time as this run progresses. The aircraft has peaks of about 23 dBsm while the missile has peaks at about 17 dBsm.

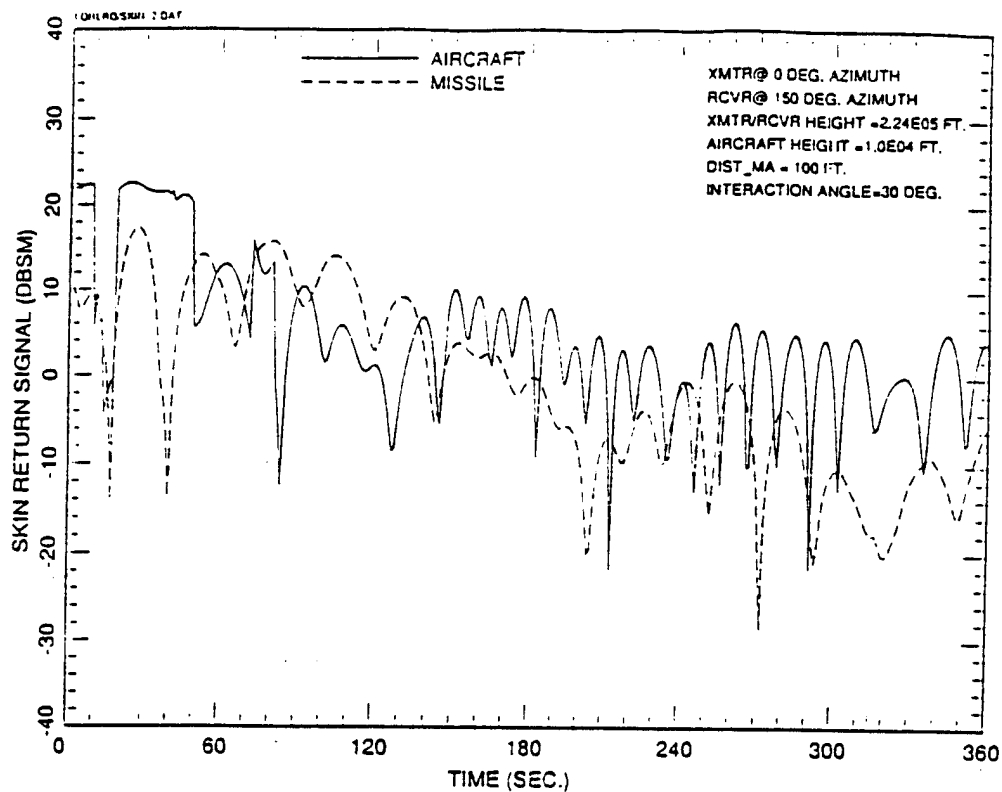


Figure 3.1.3.5-4 (a). Skin returns for bistatic radar pointing @ -45° elevation
L-band/TE mode

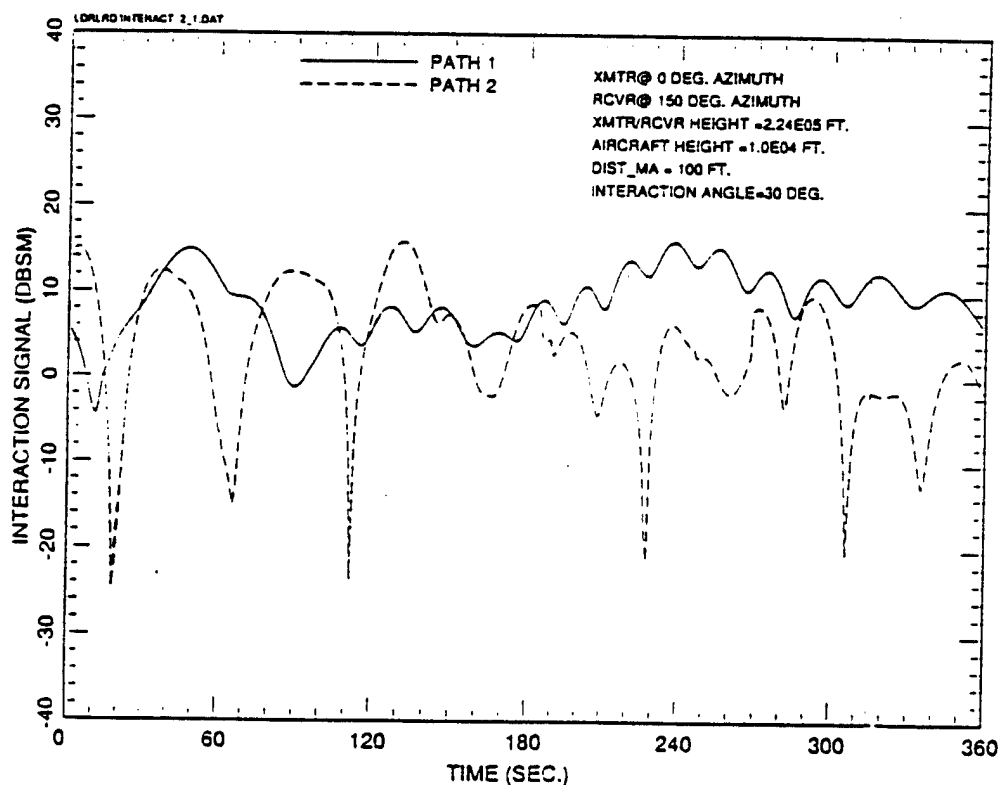


Figure 3.1.3.5-4 (b) . Interaction paths 1 and 2 for bistatic radar pointing
@ -45° elevation. L-band/TE mode

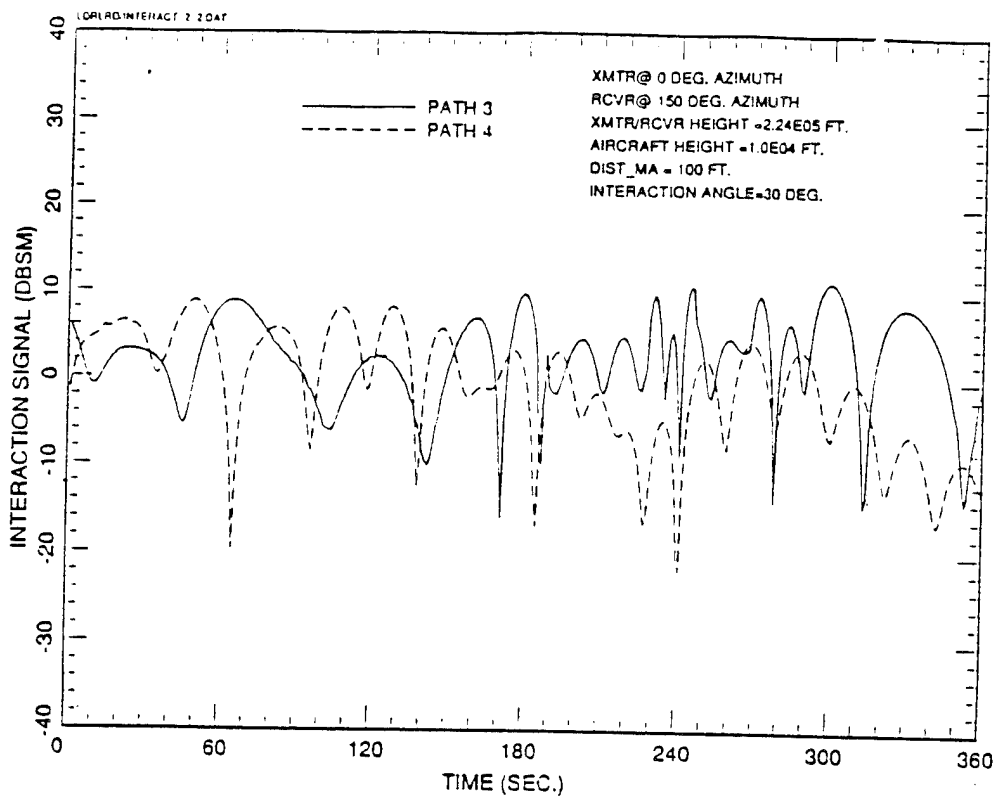


Figure 3.1.3.5-4 (c) . Interaction paths 3 and 4 for bistatic radar pointing @ -45° elevation. L-band/TE mode

A very interesting case is the case of a monostatic ground radar looking up at the targets. This scenario is illustrated in Figure 3.1.3.5-5 below:

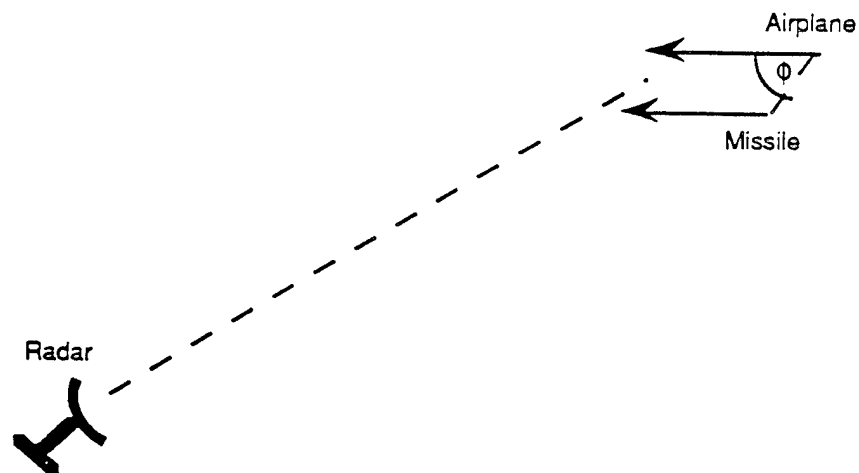


Figure 3.1.3.5-5. Ground-to-ground monostatic radar scenario

The skin return signals are shown in Figure 3.1.3.5-6 (a). The signals are essentially constant until about $T=245$ sec. This can be explained as followed. The initial range to the targets is 50 nm while the height of the targets is 10 kft. Hence, the initial elevation angle the radar points up is 1.89° (radar at -1.89° elevation with respect to targets), so the radar is looking up at the underside of the targets. Even at $T=245$ sec., the elevation angle is still only 9° . As Figure 3.1.2.1.8-5 shows, the RCS of the aircraft for small negative elevation angles (between 0° and about -10°) is mostly constant at 5 dBsm. Similarly, Figure 3.1.2.2.6-4 shows that with the TE mode the RCS of the missile for small negative elevation angles is also fairly constant.

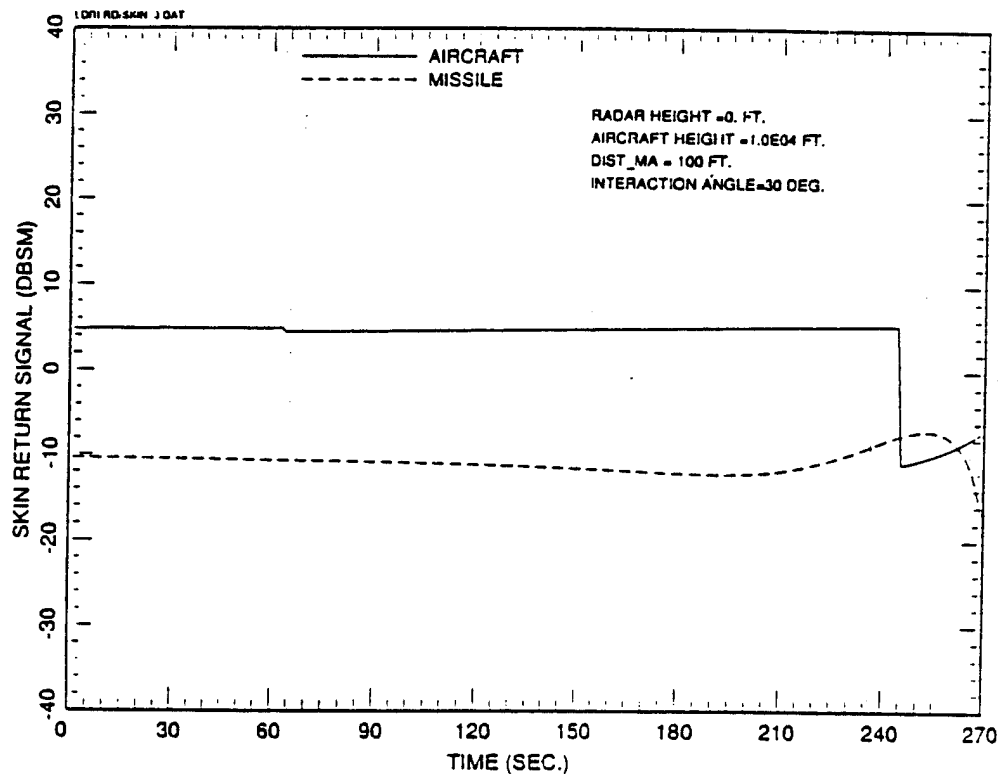


Figure 3.1.3.5-6 (a). Skin returns for mono. radar pointing @ 1.89° elevation
L-band/TE mode

Then in Figures 3.1.3.5-6 (b) & (c) we have the interaction signals for this case. Only path 4 is larger than the skin returns, but not until after $T=240$ sec. The interaction signals are mostly about -10 dBsm, which is the same as the missile skin return. This is a case where during most of the run, the interaction signals do not give us more information about co-target interference. One

reason why the interaction signals are weak for this case is that since the radar is on the ground, some of the paths involve forward scattering toward the shadowed sides of certain missile components, such as the triangular plates. Recall that one of the assumptions of physical optics is that there is no surface current on the shadowed side of an object. If the incident wave is on one side of the plate, the RCS model assumes that there is no scattering toward the other side of the plate. Hence, many of the missile components have zero RCS on the interaction paths. This will reduce the interaction signals.

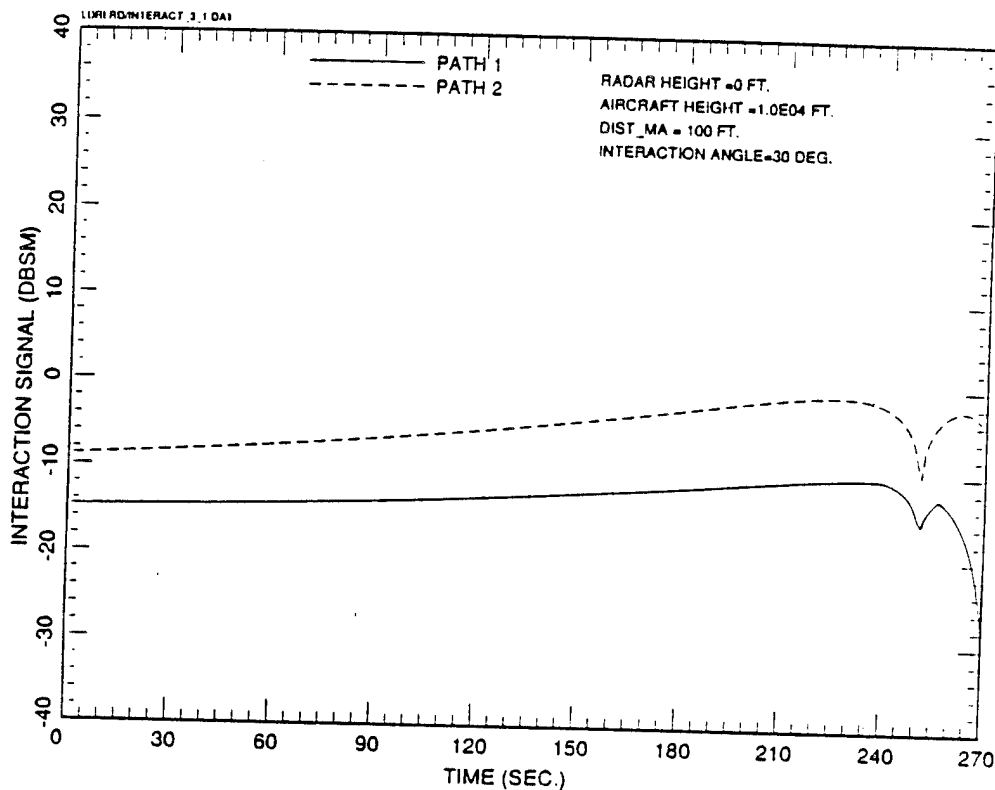


Figure 3.1.3.5-6 (b). Interaction paths 1 and 2 for mono. radar pointing @1.89° elevation. L-band/TE mode

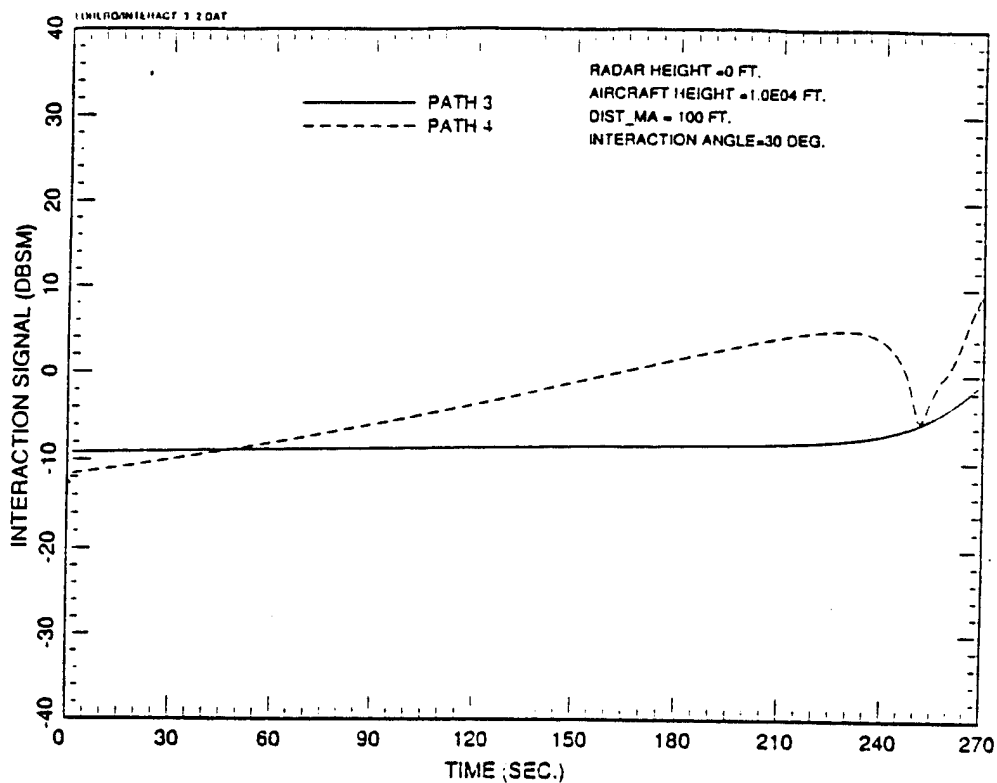


Figure 3.1.3.5-6 (c). Interaction paths 3 and 4 for mono. radar pointing @1.89° elevation. L-band/TE mode

Finally, we present the case of a bistatic ground radar where the receiver is offset in azimuth from the transmitter by 150°. The initial elevation angle for both units is 1.89°. The geometry is shown below:

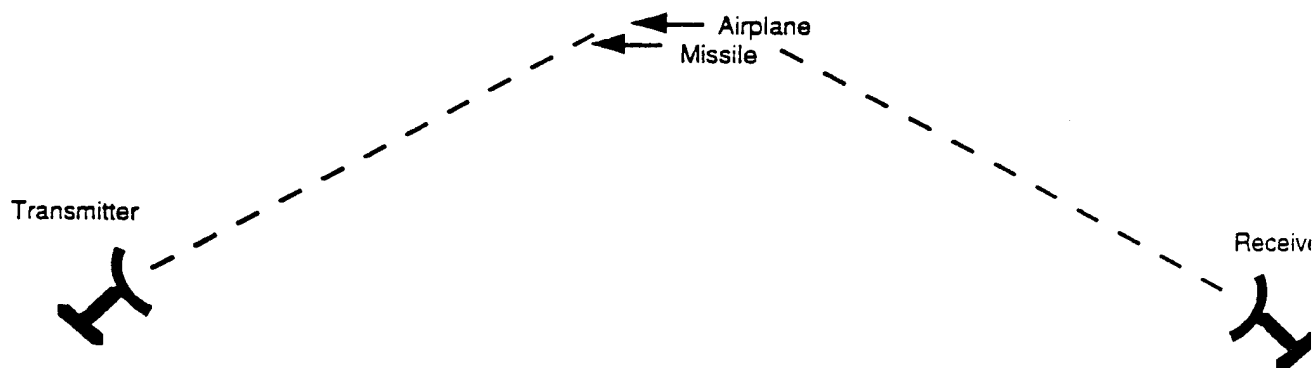


Figure 3.1.3.5-7. Ground-to-ground bistatic radar scenario

This is another case where as shown in Figures 3.1.3.5-8 (a), (b), and (c), the interaction path signals are mostly weaker than the skin returns. Path 2 is the only path that is comparable to the aircraft skin return. The rest of the paths are -10 dBsm or less, which is even less than the missile skin return. Once again, with a ground radar, many of the missile components have zero RCS on the interaction paths, and this leads to weaker interaction signals.

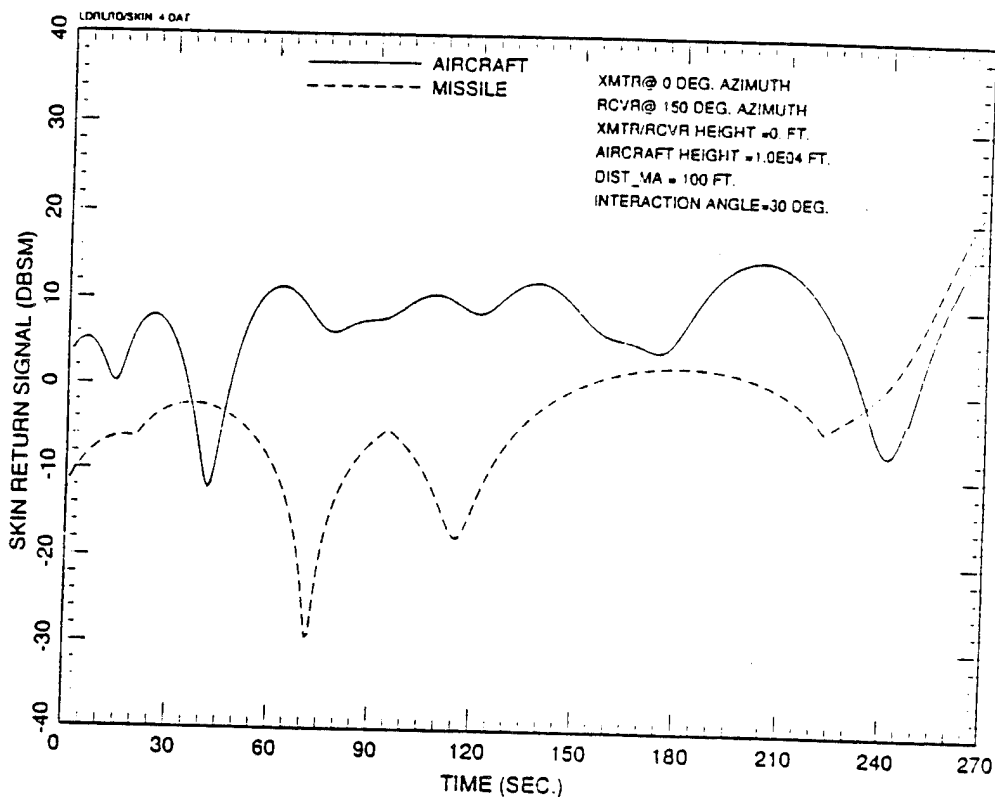


Figure 3.1.3.5-8 (a). Skin returns for bistatic radar pointing @ 1.89° elevation
L-band/TE mode

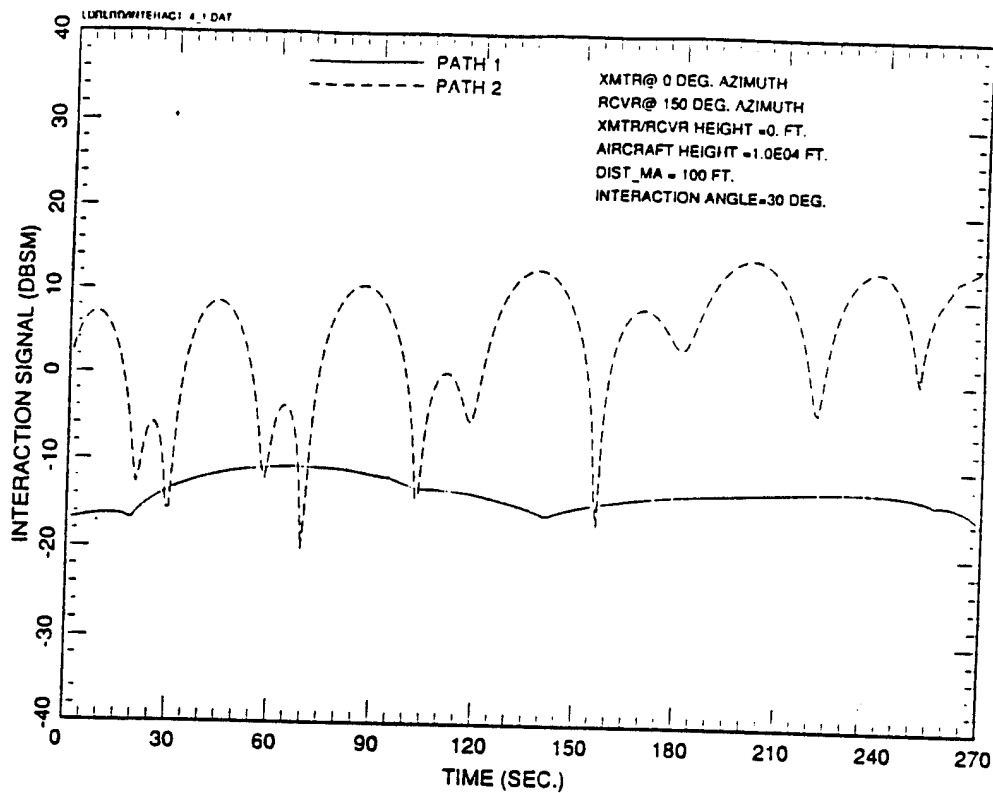


Figure 3.1.3.5-8 (b). Interaction paths 1 and 2 for bistatic radar pointing @1.89° elevation. L-band/TE mode

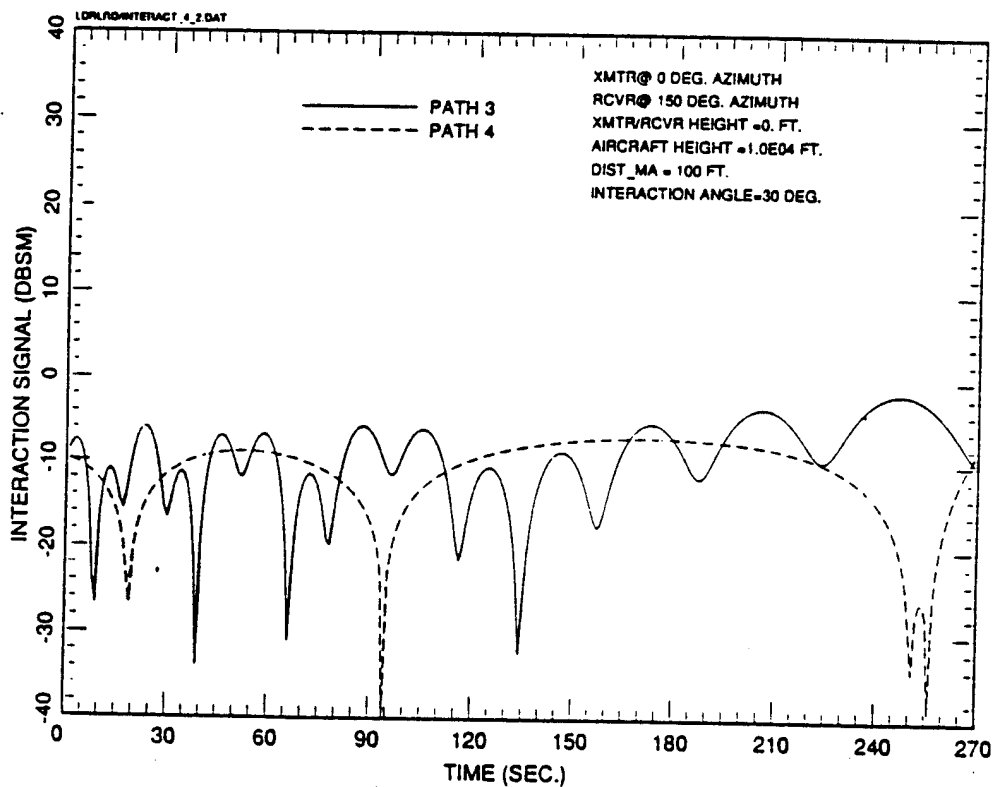


Figure 3.1.3.5-8 (c). Interaction paths 3 and 4 for bistatic radar pointing @1.89° elevation. L-band/TE mode

TIME RETURN 8 DAT

— AIRCRAFT
- - - MISSILE

RADAR HEIGHT = 2.24E05 FT.
AIRCRAFT HEIGHT = 1.0E04 FT.
DIST_MA = 100 FT.
INTERACTION ANGLE = 30 DEG.

SKIN RETURN SIGNAL (DBSM)

TIME (SEC.)

84

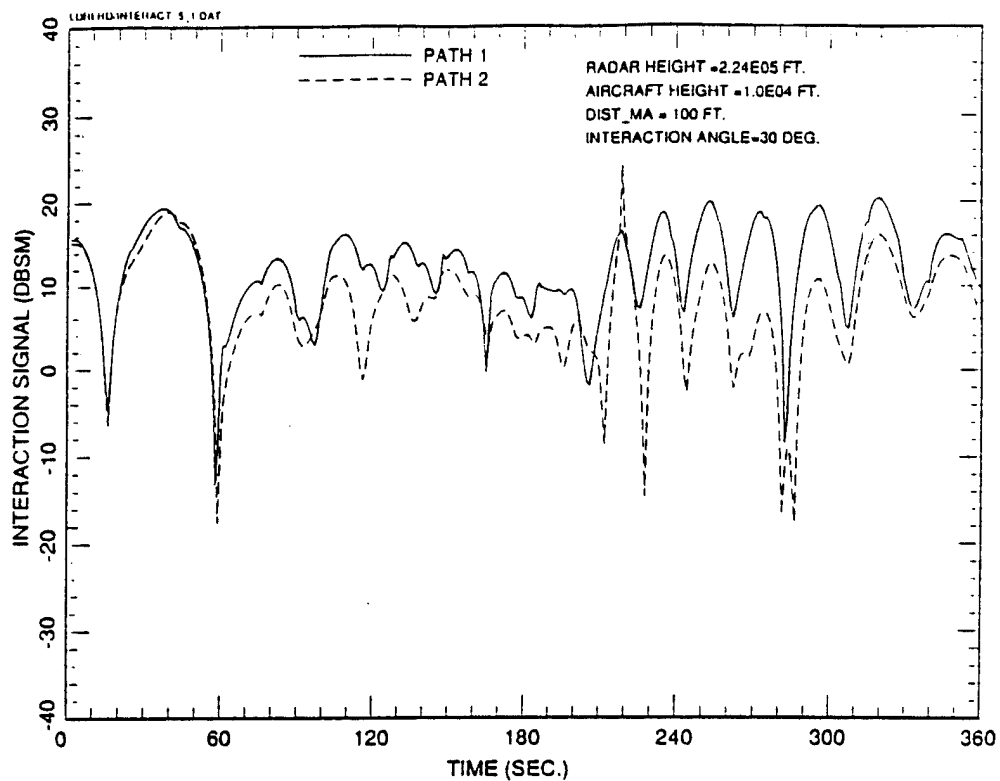


Figure 3.1.3.5-9 (b). Interaction paths 1 and 2 for mono. radar pointing @-45° elevation. L-band/TM mode

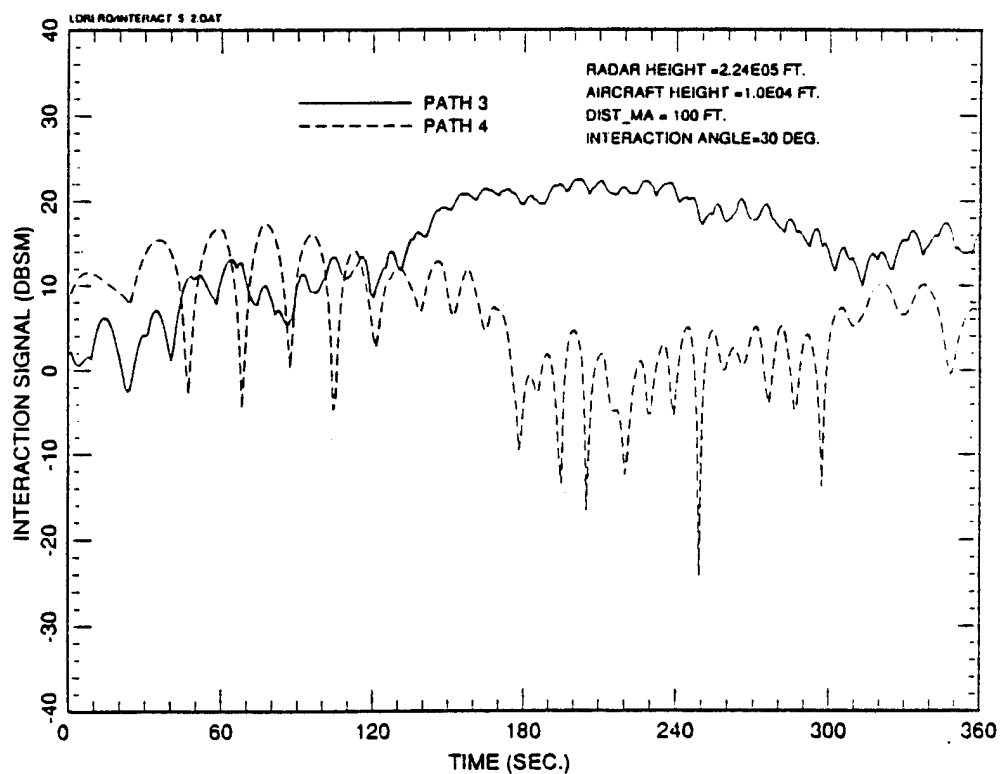


Figure 3.1.3.5-9 (c). Interaction paths 3 and 4 for mono. radar pointing @-45° elevation. L-band/TM mode

We also now present the results for a case at X-band (10 GHz). This case is for an air-to-air bistatic radar with TM mode. The geometry is exactly the same as in Figure 3.1.3.5-3 above. We see from Figure 3.1.3.5-10 (a) that the skin returns at X-band are similar in magnitude with that of Figure 3.1.3.5-4 (a) (L-band case), except that there are much more fluctuations here. Also, the missile skin return here has a peak of 32 dBsm. Paths 1, 2, and 3 in Figures 3.1.3.5-10 (a) & (b) are similar in shape to the L-band case. But path 4 is much weaker than the L-band case.

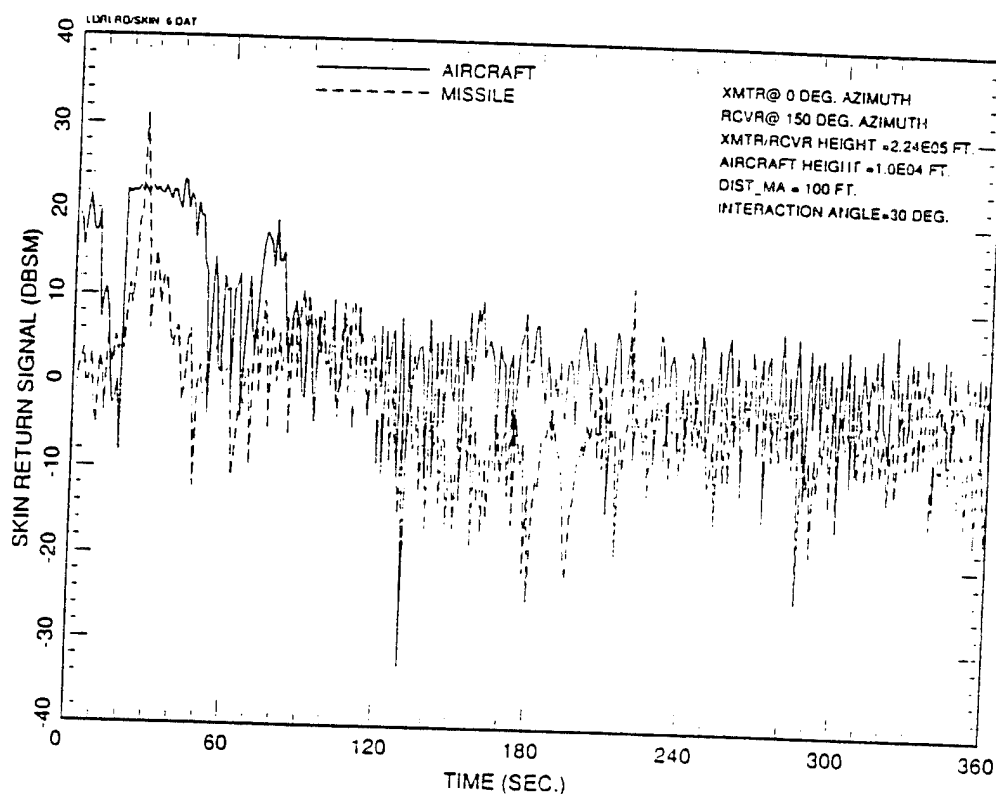


Figure 3.1.3.5-10 (a). Skin returns for bistatic radar pointing @ -45° elevation
X-band/TM mode

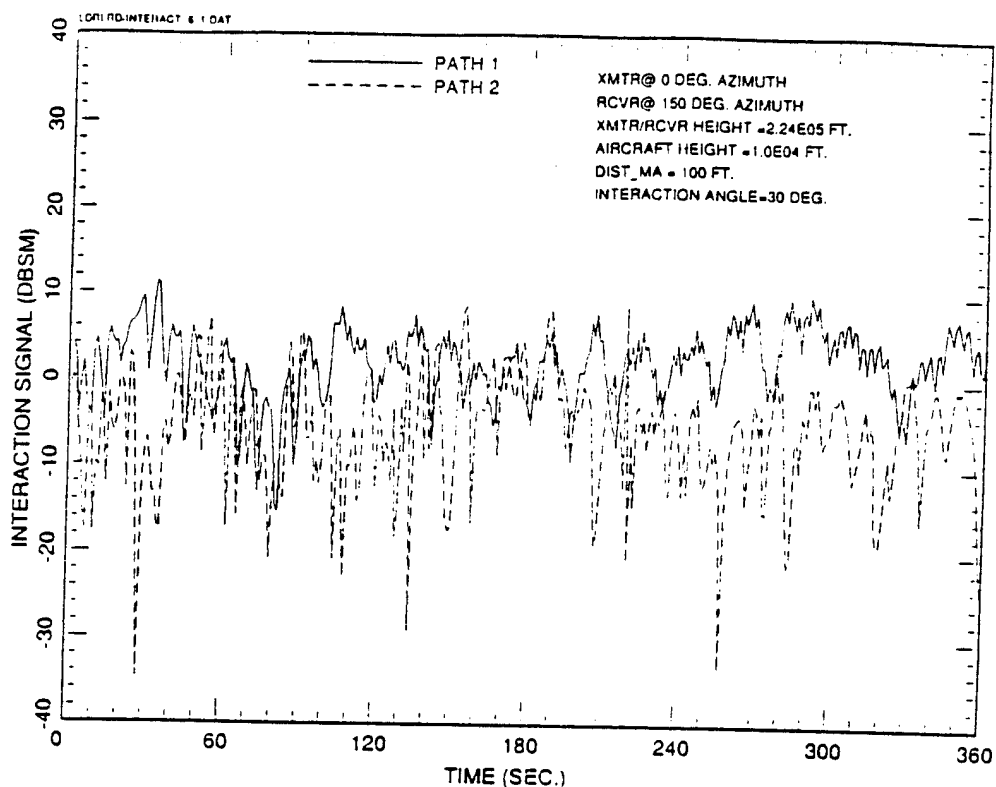


Figure 3.1.3.5-10 (b). Interaction paths 1 and 2 for bistatic radar pointing @-45° elevation. X-band/TM mode

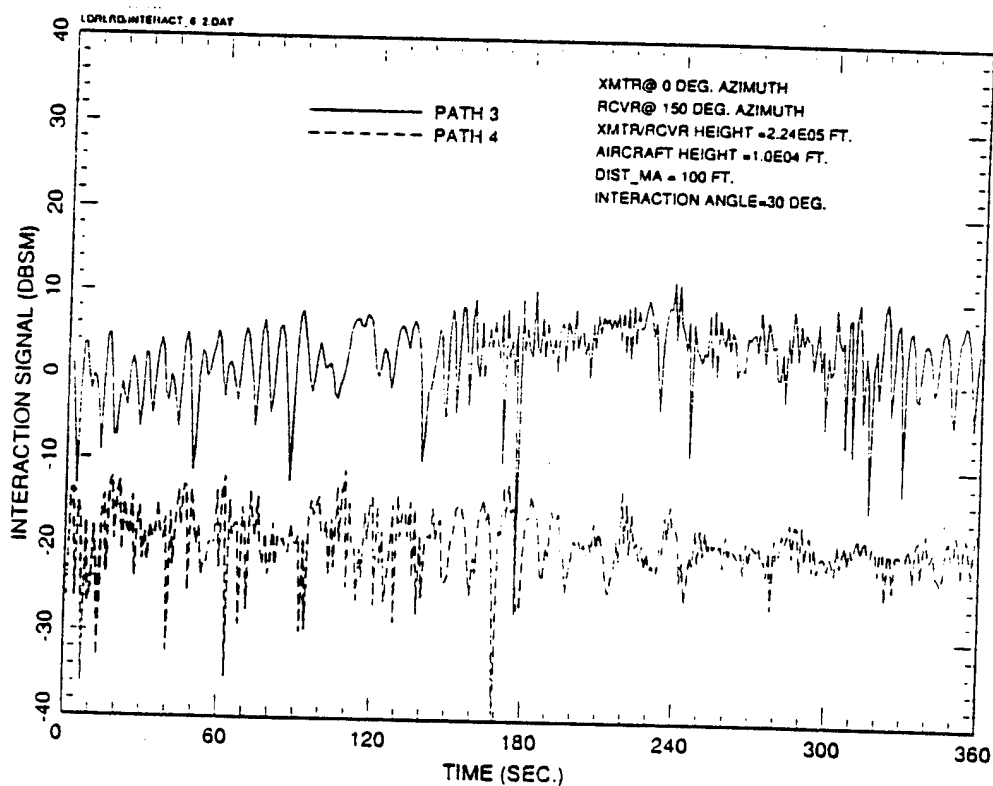


Figure 3.1.3.5-10 (c). Interaction paths 3 and 4 for bistatic radar pointing @-45° elevation. X-band/TM mode

3.2 Discriminant Study

Given that the large /small target interaction exists, a logical question that follows is whether any target parameters can be extracted from these signals. That is, can one form any measurement discriminants. Figure 3.2-1 shows an interaction geometry and the appropriate terms associated with each path. Table 3.2-1 lists all of the signals, the corresponding path length and observed angles which form the basis in forming any discriminants. The variables R_1 , R_2 , L , θ_1 , θ_2 are the unknown. With a monopulse radar, if the three interaction signals are observed, then all of the target parameters can be determined.

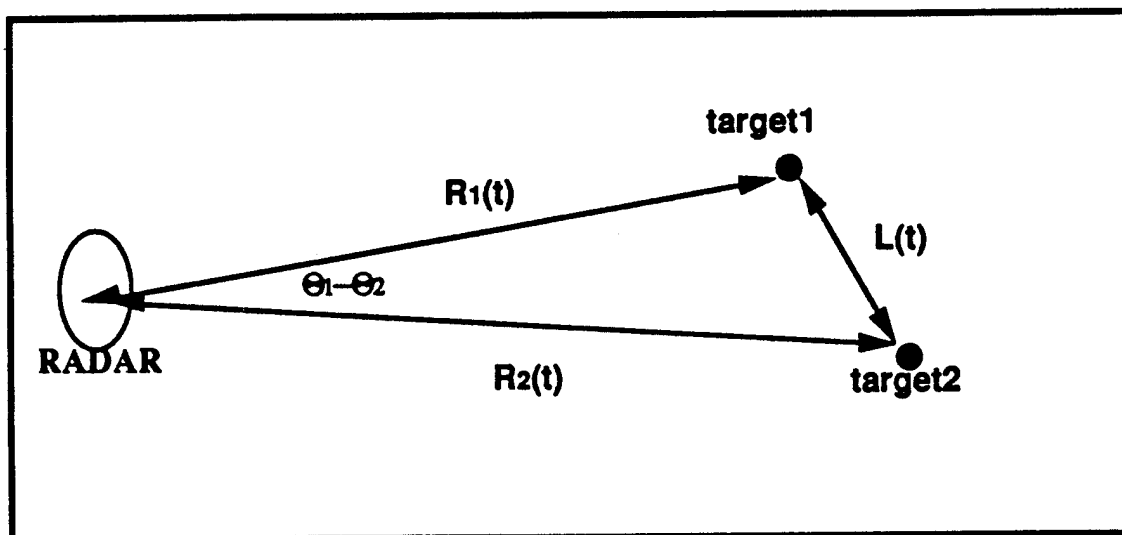


Figure 3.2-1 Information content embeded in the interaction signal allows prediction of small target skin return.

TABLE 3.2-1 Tabulation of the signal paths and observations

Path	Signal	Length	Observed Angle
R to T1 to R	$Y_1(t)$	$2 R_1(t)$	$\theta_1(t)$
R to T2 to R	$Y_2(t)$	$2 R_2(t)$	$\theta_2(t)$
R to T1 to T2 to R Plus vice-versa	$Y_3(t)$	$R_1(t) + L(t) + R_2(t)$	$\frac{\theta_1(t) + \theta_2(t)}{2}$
R to T1 to T2 to T1 to R	$Y_4(t)$	$2 (R_1(t) + L_1(t))$	$\theta_1(t)$
R to T2 to T1 to T2 to R	$Y_5(t)$	$2 (R_2(t) + L(t))$	$\theta_2(t)$

Notation: R=Radar , T1=Target 1, T2=Target2

With the geometry illustrated in the figure and applying the law of cosines, one obtains

$$L(t) = R_1^2(t) + R_2^2(t) - 2 R_1(t) R_2(t) \cos(\theta_1 - \theta_2)$$

This equation can be used to check for consistency if one directly estimates the target parameters from the analytically tractable discriminants..Consider a linear least squares estimation that directly solves for the target parameters. From the table, one can write the set of vector equations in the following two tables.

TABLE 3.2-2. Direct parameter estimation vector values for the example computation.

- Assume $Y_2(t)$ not detectable

Range and Doppler Vectors	Angle Vectors
$y_1 = (2 \ 0 \ 0) \underline{R} + n_1$	$y_1 = (1 \ 0) \underline{\theta} + n_1$
$y_3 = (1 \ 1 \ 1) \underline{R} + n_3$	$y_3 = (1/2 \ 1/2) \underline{\theta} + n_3$
$y_4 = (2 \ 2 \ 0) \underline{R} + n_4$	$y_4 = (1 \ 0) \underline{\theta} + n_4$
$y_5 = (0 \ 2 \ 2) \underline{R} + n_5$	$y_5 = (0 \ 1) \underline{\theta} + n_5$
with	
$R = (R_1 \ L \ R_2)^T$ or $(\dot{R}_1 \ \dot{L} \ \dot{R}_2)^T$	$\theta = (\theta_1 \ \theta_2)^T$

and T denotes the transpose of the row vector

Least squares solution and corresponding error

Given observations

$$Y_n = \underline{W}_n + \theta + n \quad ; \quad n = 1, 2, \dots, N$$

$\underline{\theta}$ is the parameter vector

Find $\hat{\theta}$ that minimizes the least-square error

$$\epsilon^2 = \sum_n \gamma_n [Y_n - \underline{W}_n + \hat{\theta}]^2$$

$$\hat{\theta} = R^{-1} \sum_n \gamma_n \underline{W}_n Y_n \quad ; \quad E[\hat{\theta}] = \theta$$

$$E[\hat{\theta} - \theta]^2 = \sigma^2 \sum_n \gamma_n^2 |R^{-1} \underline{W}_n|^2$$

$$\text{or } \Lambda_{\epsilon} = E(\theta - \hat{\theta})(\theta - \hat{\theta})^* = \sigma^2 R^{-1} \left(\sum_n \gamma_n^2 \underline{W}_n \underline{W}_n^* \right) R^{-1}$$

where

$$R = \sum_n \gamma_n \underline{W}_n \underline{W}_n^*$$

Figure 3.2-2. Least-Squares Estimate: Direct approach Mathematics

Small target angle error computation, $\gamma_n = 1$

$$R = 2 \begin{bmatrix} 1 \\ 0 \end{bmatrix} \begin{bmatrix} 1 & 0 \end{bmatrix} + \begin{bmatrix} 1/2 \\ 1/2 \end{bmatrix} \begin{bmatrix} 1/2 & 1/2 \end{bmatrix} + \begin{bmatrix} 0 \\ 1 \end{bmatrix} \begin{bmatrix} 0 & 1 \end{bmatrix}$$

$$R^{-1} = \frac{1}{11} \begin{bmatrix} 5 & -1 \\ -1 & 9 \end{bmatrix}$$

$$E (\theta - \theta_2)^2 = \frac{9}{11} \sigma^2 \quad ; \quad \sigma^2 \text{ interaction discriminant variance}$$

Figure 3.2-3. An example of angle estimation error.

An example of the predicted accuracy follows. The required mathematics are given in Figure 3.2-2 which includes the estimation error prediction. A sample computation is given in Figure 3.2-3. The computation in the figure assumes that small target skin return is not detected and uses the weights from the Table 3.2-1. The results indicate that target parameter estimation error is proportional to the discriminant errors. Because enhanced interaction paths provide small target parameter estimates even with an undetectable skin return, one can question the need for co-target interference rejection techniques. This intriguing result has the following implications:

1. Standard resolution is sufficient for small target detection and estimation.
2. Dynamic range requirement is reduced by the interaction signals.
3. **Power-Aperture** products for small target detection is reduced to **values** as required by the interaction signals.
4. The masking tactic of small target hiding near the large target risks detection via these secondary signals.

3.3 Radar Resolution Trade Study and Workload

In order to properly conduct a radar resolution trade study with respect to radar type, frequency, waveform, pulse-repetition frequency, pulse compression codes, dwell time, antenna agility, etc., one must quantitatively define a resolution "cell" as it applies to surveillance radars. The most tractable definition is basically a four dimensional hypercube ρ , defined as

$$\rho = \pi R_o^2 (\beta_{AZ} \times \beta_{EL}) \times \Delta r \times \Delta v$$

where

$(\beta_{AZ} \text{ \& } \beta_{EL})$ is the two-dimensional antenna beamwidth proportional to the covered angular volume by a beam

Δr is the radar range resolution (instantaneous bandwidth)

Δv is the radar velocity resolution (proportional to dwell time

R_o a specified range.

It should be noted that two conditions must be satisfied in order for two targets to be resolved with conventional radar processing. First, the mainlobe response of the 4D cell must be narrower than the two target separation. Second, the sidelobe response does not mask the neighboring targets. That is, the sidelobe response supports the target dynamic range. The small target masking levels establish the cancellation or suppression requirements or equivalently the sidelobe relative to the mainlobe level required. To derive this requirement, one must establish the small and large target RCS model. Our frequency resolution trade approach attempts to depend minimally on specific system parameters and address the two conditions parametrically with respect to wavelength (frequency).

The first class of systems examined are surveillance radars with mechanically scanned antennas. The surveillance systems operating at VHF, L, S, C and X are configured to satisfy the surveillance and track workloads. This implies the same surveillance volume, frame time, number of target types, track update times, RCS versus frequency, etc., which establish detection

performance requirements for a given surveillance system when targets are non-interfering. A reasonable model for large complex targets is that the backscatter is independent of frequency. Small targets, modelled as cone spheroids, have RCS that vary proportionally to a fractional power of wavelength until a base level limit (eg. -30dBsm @ 3GHz) which then remains constant at that level for all higher frequencies. For such a system satisfying the surveillance equation, the velocity resolution ΔV satisfies

$$\Delta v = (\lambda/2) \phi V_0 / \beta T_f$$

where ϕ is the beam overlap factor, V_0 is the search volume, β is the two dimensional beamwidth and T_f is the frame time. Therefore, the four dimensional cell is

$$\rho = \pi R_0^2 \Delta r (\phi V_0 / 2 T_f) \lambda$$

Now Δr will be evaluated for two design constraints. For a system without the processing constraints and equal RF complexity, range resolution is limited by the system percent bandwidth and therefore, the 4D cell is proportional to wavelength squared. For a system that is processor limited, driven by range bin processing, range resolution is independent of wavelength and therefore, the 4D cell is only proportional to wavelength. Thus, depending on which constraint is active, the 4D resolution cell ρ will be proportional to λ or λ^2 .

TABLE 3.3-1. System Configurations with HPRF waveform. Velocity resolution is reduced by the range cell resolution factor.

Freq.	VALUE (GHz)	SURFACE RADAR				AIR BORNE RADAR		
		PRF (KHz)	Rumb (n.m)	No. RB	Minimum No. PRFs	PRF	Minimum No PRFs	Cell Factor
UHF	0.3	1.8	45.0	2734	2	3.6	2	2.0
L	1.25	7.5	11.0	668	2	15.0	3	2.5
S	2.5	15.0	5.4	328	3	30.0	3	3.0
C	5.0	30.0	2.7	164	3	60.0	4	3.5
X	10.0	60.0	1.35	82	4	120.0	5	4.5

TABLE 3.3-2. System Configurations with LPRF waveform. Range resolution is reduced by the velocity cell resolution factor.

FREQUENCY	REQ. VEL COVERAGE (kHz)	NO. OF FILTERS	MIN NUMBER PRFS	CELLFACTOR
UHF	2.0	2000	2	2
L	7.5	200	2	2
S	15.0	4	3	3
C	30.0			
X	60.0			

Waveform ambiguities reduce the resolution dependence on frequency. High PRF requires range resolving and depends on radar instantaneous bandwidth. Table 3.3-1 list a HPRF waveform configuration for each operating frequency where the range resolution is 100ft. and velocity coverage includes target velocities up to 3000 ft/sec. The number of PRFs required to resolve to 200 n.m. while satisfying the surveillance constraint, velocity resolution is reduced by a value defined as the range cell factor in the table. Therefore, HPRF velocity resolution improves as $-\log(\lambda)$.

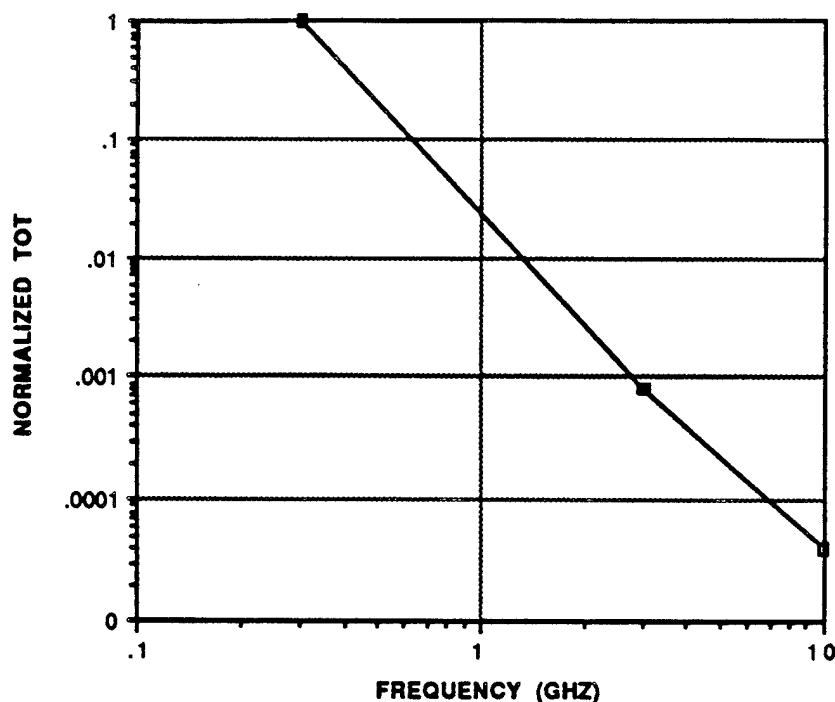


Figure 3.3-1. Normalized Time on Target versus Operating Frequency

Low PRF requires velocity ambiguity resolution which depends on doppler filter resolution or equivalently the time on target. This implies that a radar workload must be defined to determine dwell time. Figure 3.3-1 shows a plot of normalized time on target versus operating frequency for a fixed power aperture product. The small target RCS frequency dependence is the same as used in the surveillance constraint. Fixing range resolution, and using 300Hz PRF, the cell factor is almost constant with wavelength as shown in Table 3.3-2.

Based on the above discussion, the following can be summarized for a surveillance system with mechanically scanned antenna. The cell size is proportional to a value between

λ and λ^2

LPRF Waveform, and

$\lambda \log(1/\lambda)$ and $\lambda^2 \log(1/\lambda)$

HPRF Waveform.

From a system design point of view, an electronically scanned antenna system decouples the surveillance, track acquisition and track maintenance modes. With this level of beam agility, resolution criteria may be more relevant to track acquisition and track dwells rather than surveillance. Consider an Alert/Confirm Policy utilized with an electronically scanned antenna radar in which the target resolution is only attempted during the confirm stage. This allows time-energy management and adaptive dwells as they are required. For example, it is feasible to increase track dwell times for attaining resolution and minimize smearing. The predictive nature of tracking filters, as large and small RCS targets cross each other's path, allows one to allocate the appropriate dwell time for resolution as well as for detection. Then the 4D cell is strictly a function of the two dimensional beamwidth and range resolution established from the point search requirement. This implies that ρ is proportional to

$$\lambda^3 \text{ and } \lambda^4$$

HPRF and LPRF waveform

TABLE 3.3-3. Dynamic Range Requirements versus Frequency. Requirements are less stringent for the low operating frequency.

FREQUENCY	DYNAMIC RANGE REQUIREMENT
0.25	22 to 28 dB
1.0	34 to 40 dB
2.0	40 to 46 dB
3.0	40 to 46 dB
5.0	40 to 46 dB

TABLE 3.3-4. Dynamic Range Error Limit. Optimal designs favor the highest frequency choice.

RESOLUTION DOMAIN	DYNAMIC RANGE ERROR LIMIT
Angle	70 to 90 dB
Range	40 to 50 dB
Doppler	90dB

The dynamic range versus frequency is given in Table 3.3-3. It is assumed that the large target RCS is 10 dBsm and is independent of frequency. The dynamic range follows from the dependence of the small target RCS with frequency (described in the above paragraphs). The only limiting factor is the capability of designing the hardware so that sufficient dynamic range exists to maintain an unmasked small target. Table 3.3-4 shows typical dynamic range limits due to hardware tolerances. It is clear that range resolution dynamic range tends to be the most difficult as it is limited 40 to 50 dB.

3.4 Statistical Characterization

The RCS model developed in Section 3.1, the Phenomenology Section, gives the capability to predict target RCS as function of target aspect angle. The interaction model then quantifies the interaction between the targets. To apply these models in further statistical and detection studies, however, it is necessary to account for the cross-section and interaction signal fluctuations by characterizing their probability distribution functions.

A common model of target fluctuation is the Swerling model. In the Swerling 1 and 2 cases, the probability-density function for the cross section is given by

$$p(\sigma) = \frac{1}{\sigma_{av}} \exp\left(-\frac{\sigma}{\sigma_{av}}\right) \quad \sigma \geq 0 \quad (\text{Eqn. 3.4-1})$$

where σ_{av} is the average cross section over all target fluctuations. In the Swerling 3 and 4 cases, the probability-density function is given by:

$$p(\sigma) = \frac{4\sigma}{\sigma_{av}^2} \exp\left(-\frac{2\sigma}{\sigma_{av}}\right)$$

The Swerling cases 1 and 2 have the exponential, or Rayleigh-power distribution. Analysis of measurements on actual aircraft have shown that the cross-section fluctuations are well fitted by this distribution, except at broadside¹¹. We now examine the cross section profile of the aircraft as computed by the LDR model in Section 3.1.2.1, and determine if the exponential distribution fits the predicted profile.

First of all, a histogram of the aircraft cross section was made. Using Figure 3.1.2.1.8-1 (a), the case at L-band and 0° radar elevation angle, we exclude the broadside peak from the computations. The region with azimuth between 75° and 105° was removed because the peak may bias the statistical characterization. Then we made a histogram of the frequency of the cross section, and this is shown in Figure 3.4-1. The histogram represents the empirical probability distribution function of the aircraft cross section. The figure

also shows the result of curve-fitting Swerling cases 1 and 3 to the histogram using the least-mean square criterion. In other words, we minimize the error given by

$$e = \sum_{n=1}^N [y_n - p(x_n)]^2$$

where y_n is the histogram at each RCS point x_n , p is the probability density function being tested at each RCS point x_n , and $N = 2000$.

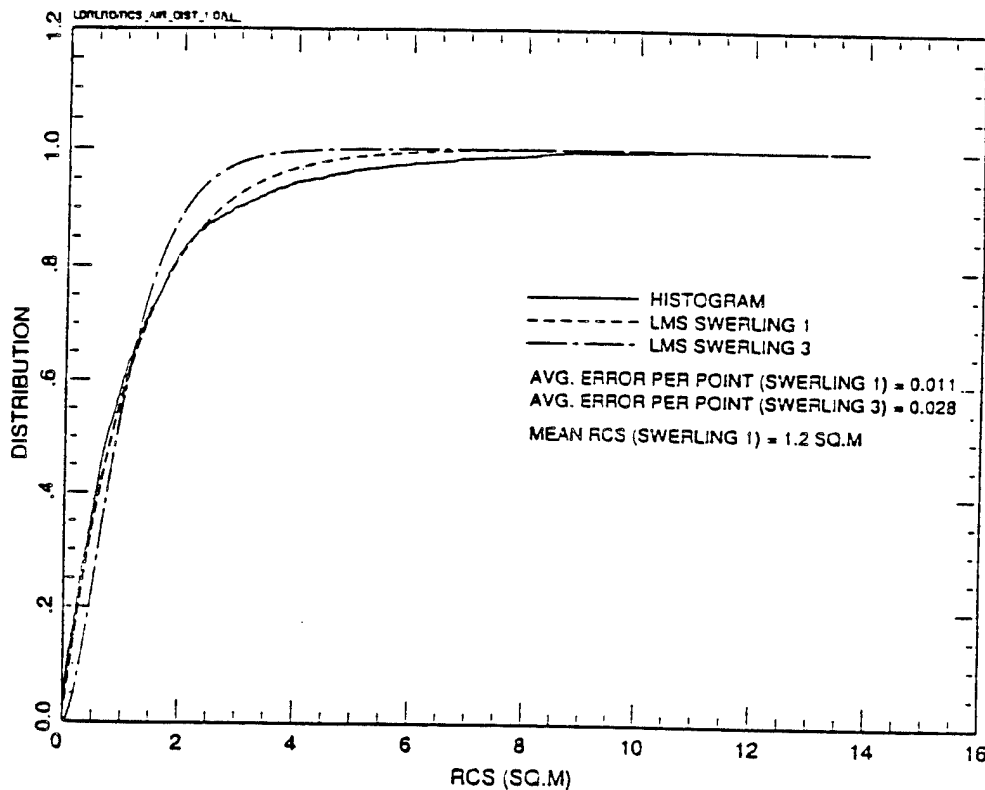


Figure 3.4-1. Histogram and Swerling models for aircraft RCS
@0° elevation. L-band

It can be seen that the Swerling 1 case, the exponential distribution, fits quite well, and that it is a much better fit than the Swerling 3 case. The average RCS, represented by the variable σ_{av} in Equation 3.4-1 is 1.2 m². The average error between the histogram and the Swerling 1 density is also quite good at 0.011.

In Figure 3.4-2 we have the X-band case also at 0° elevation. Once again the region out to 15° on either side of the peak was removed. Only the

Swerling case 1 is shown here. The exponential distribution fits about as well with this case as with Figure 3.4-1.

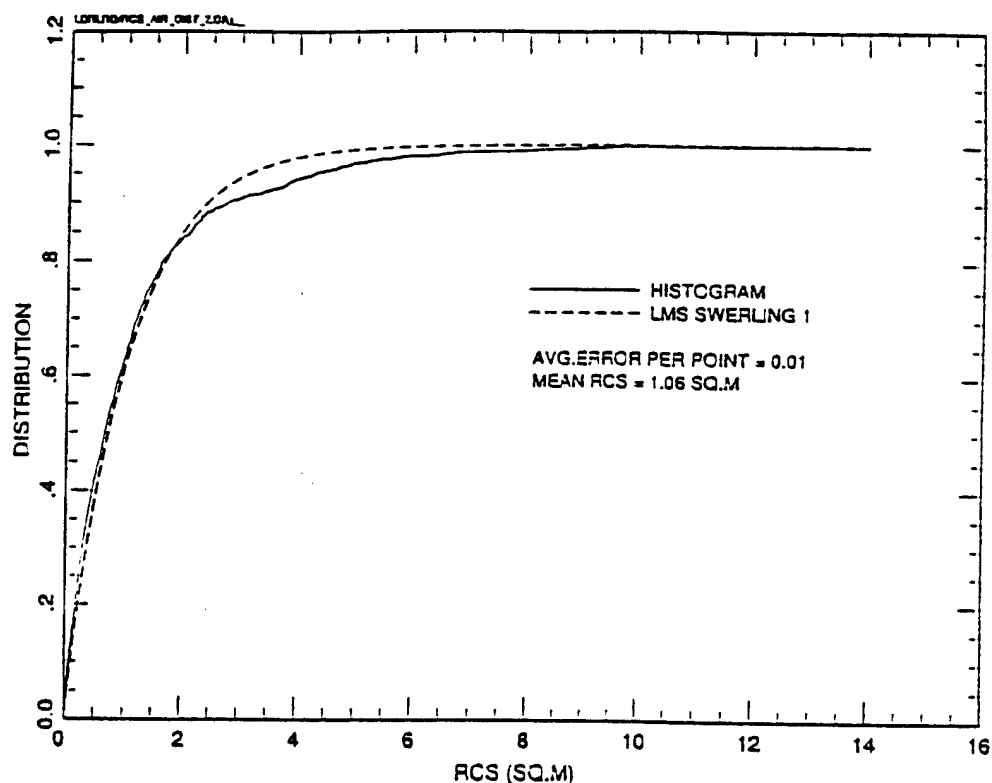


Figure 3.4-2. Histogram and exponential distribution for aircraft RCS @0° elevation. X-band

Next, we look at the missile cross section. We use the monostatic RCS of the missile for L-band, TE mode, and 0° elevation in Figure 3.1.2.2.6-1 (a). Figure 3.4-3 shows the histogram and exponential distribution fit for this case. It is apparent that the fit is not as good as with the aircraft case. The average error per point is now 0.04. Only the Swerling 1 case is shown; the Swerling 3 case is even worse.

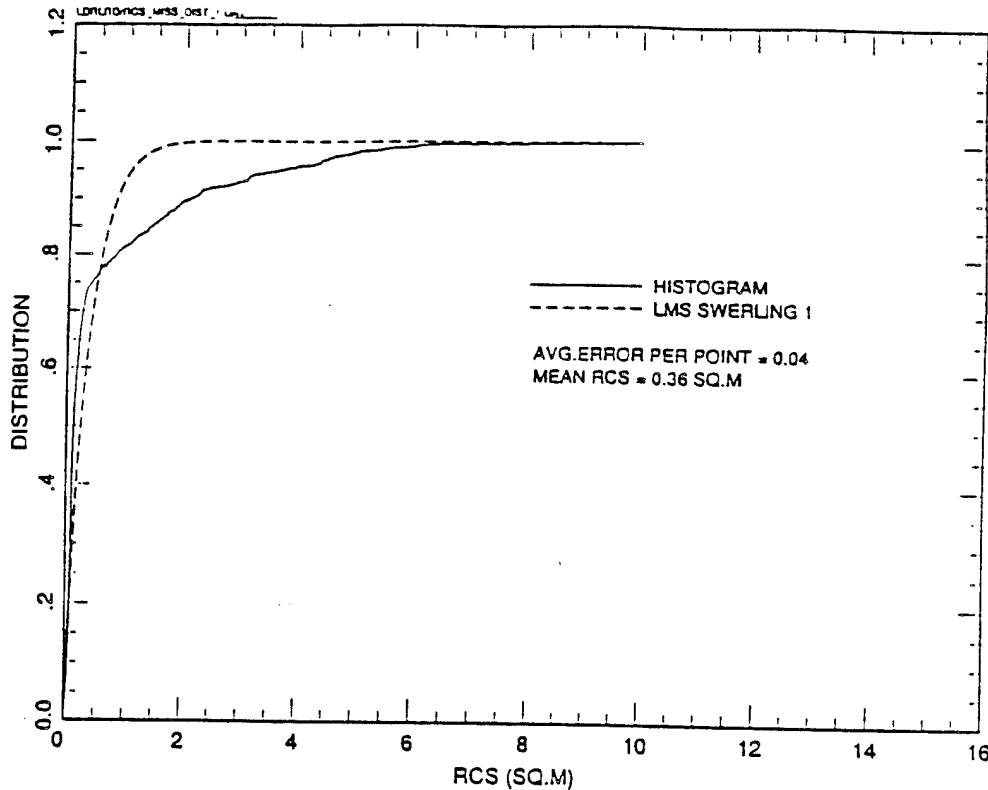


Figure 3.4-3. Histogram and exponential distribution for missile RCS
@0° elevation. L-band - TE mode

In searching for another probability distribution for the missile RCS, the log-normal distribution has been suggested. There is no theoretical model of target scattering that leads to the log-normal distribution, although it has been suggested that echoes from some satellite bodies, cylinders, plates, and arrays can be approximated by a log-normal probability distribution¹². This distribution (density) can be expressed as

$$p(\sigma) = \frac{1}{\sqrt{2\pi} s_d \sigma} \exp \left\{ -\frac{1}{2 s_d^2} \left[\ln \left(\frac{\sigma}{\sigma_m} \right) \right]^2 \right\}, \quad \sigma > 0$$

where s_d = standard deviation of $\ln (\sigma/\sigma_m)$, and σ_m = median of σ . This form of the log-normal distribution can easily be written in the standard form of the normal distribution as

$$p(\zeta) = \frac{1}{\sqrt{2\pi} s_d} \exp \left[-\frac{1}{2 s_d^2} (\zeta - \zeta_\mu)^2 \right]$$

where $\zeta = \ln \sigma$, and $\zeta_{\mu} = \ln \sigma_m - s_d^2 = \ln \sigma_{\mu}$

Figure 3.4-4 shows the result of applying the log-normal distribution to the missile RCS. The average error per point is now only 0.018, much better than the exponential distribution. Even though it seems there are large areas of error between the histogram and the distribution, we must keep in mind that the x-axis is plotted here in terms of dBsm, or $10 \log_{10} \sigma$. For comparison, most of the error in Figure 3.4-3 is in the region of $0.5 < \sigma < 6 \text{ m}^2$, which in dBsm corresponds to $-3 < \sigma < 7.8 \text{ dBsm}$. Figure 3.4-4 shows that in this region the log-normal distribution is much closer to the histogram than the exponential distribution. The large error region in the left tail of the distribution is not significant enough to give a large average error. We note also that the mean RCS for the missile in this case is -8.1 dBsm, which is what we expect for the missile.

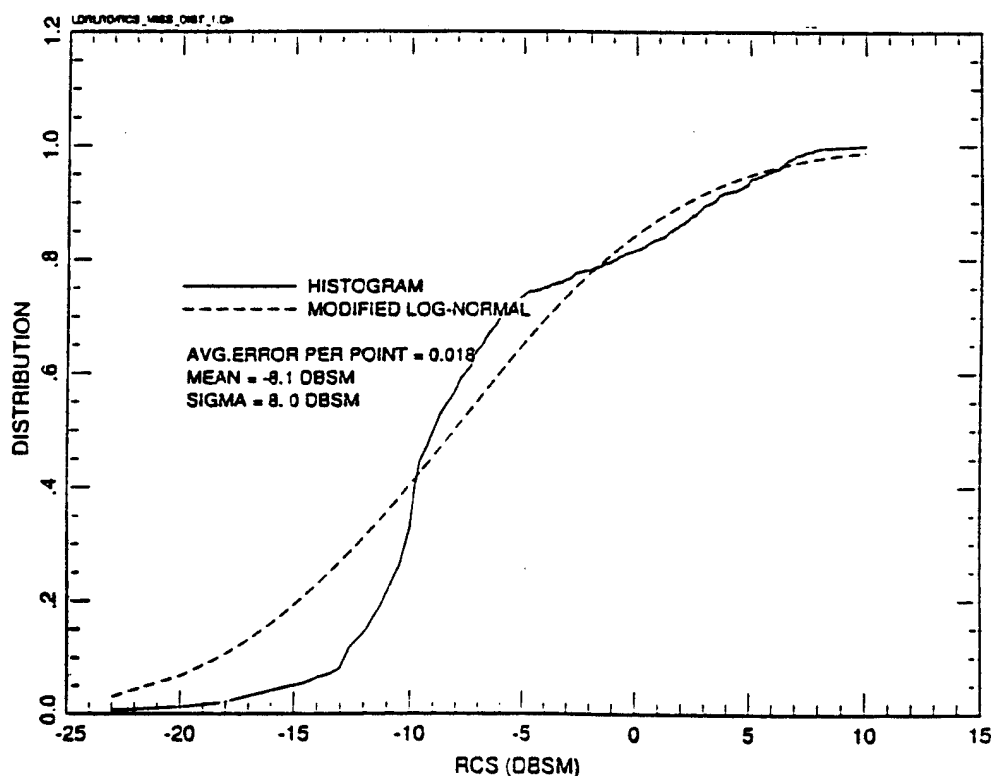


Figure 3.4-4. Histogram and log-normal distribution for missile RCS
@0° elevation. L-band - TE mode

In Figure 3.4-5 we fit the log-normal distribution to the missile RCS at X-band, TM mode, and 0° elevation of Figure 3.1.2.2.6-2 (b). The log-normal fits the histogram very well, and the average error per point is only 0.005. The mean RCS is now -6.8 dBsm. The good fit of the log-normal distribution makes it a good probability distribution to use for the missile.

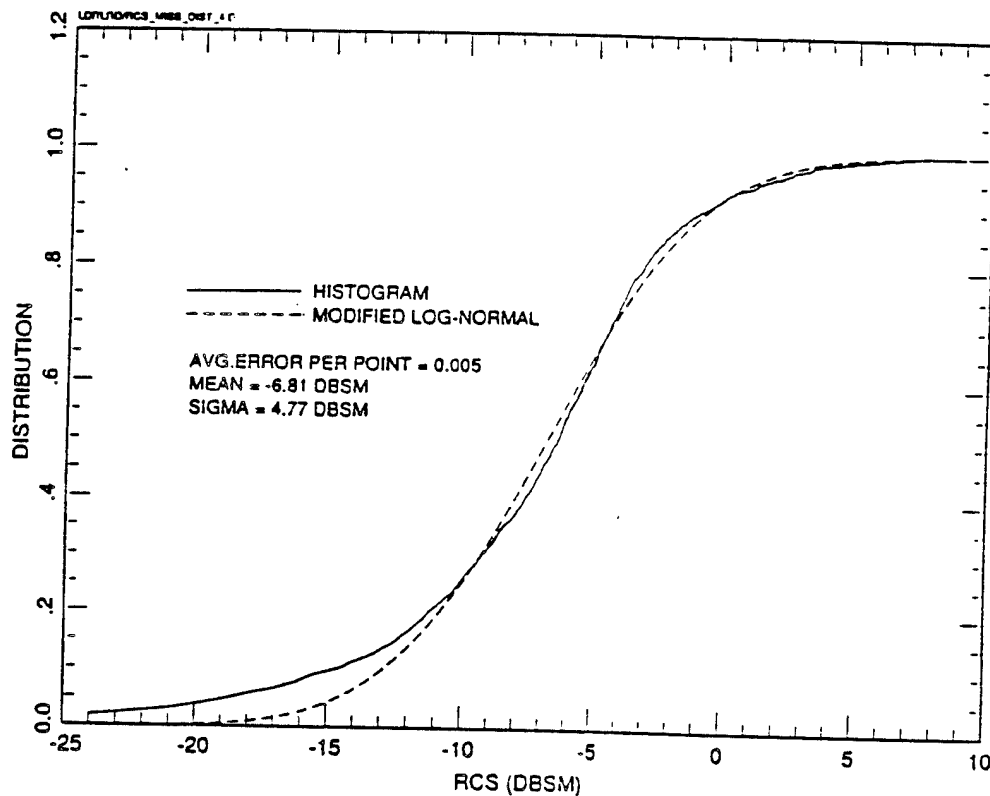


Figure 3.4-5. Histogram and log-normal distribution for missile RCS @0° elevation. X-band - TM mode

Naturally, the log-normal distribution is also applied to the interaction signals. We present two cases in Figures 3.4-6 (a) & (b). The first case is the path 1 interaction signal of the air-to-air monostatic scenario of Figure 3.1.3.5-2 (b), and the second case is the path 3 interaction signal of the air-to-air bistatic scenario of Figure 3.1.3.5-10 (b). In both cases the log-normal distribution does a good job of fitting the histogram with the average error per point about 0.025.

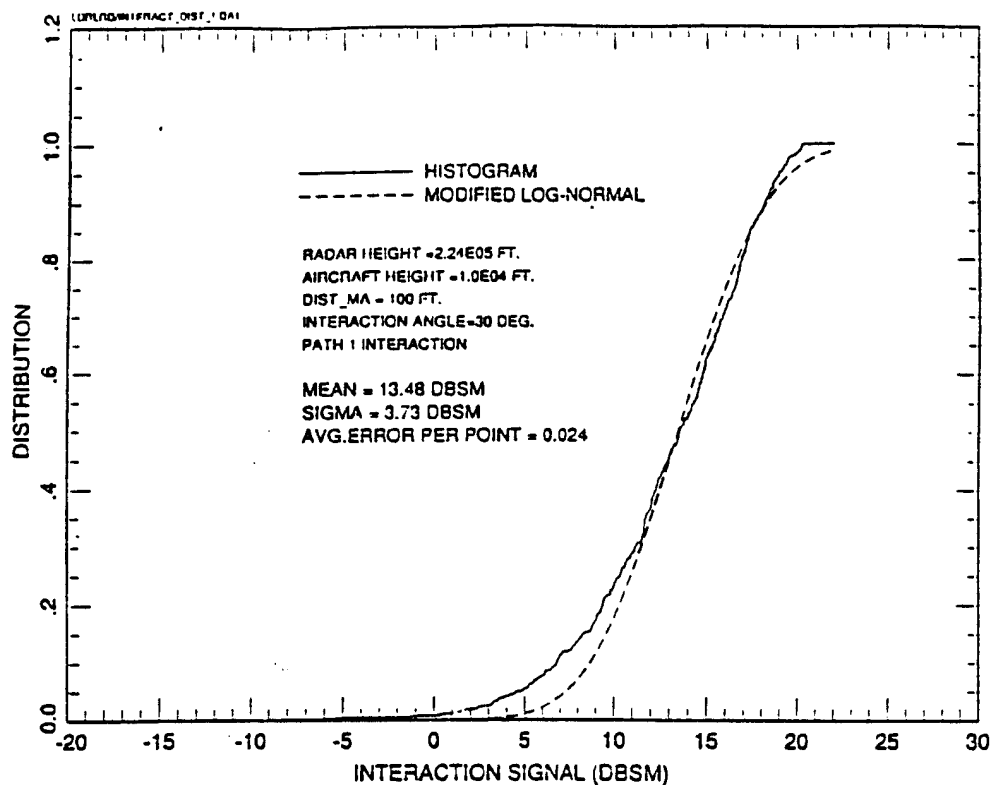


Figure 3.4-6 (a). Histogram and log-normal distribution for interaction path 1
Mono. radar pointing @-45° elevation. L-band/TE mode

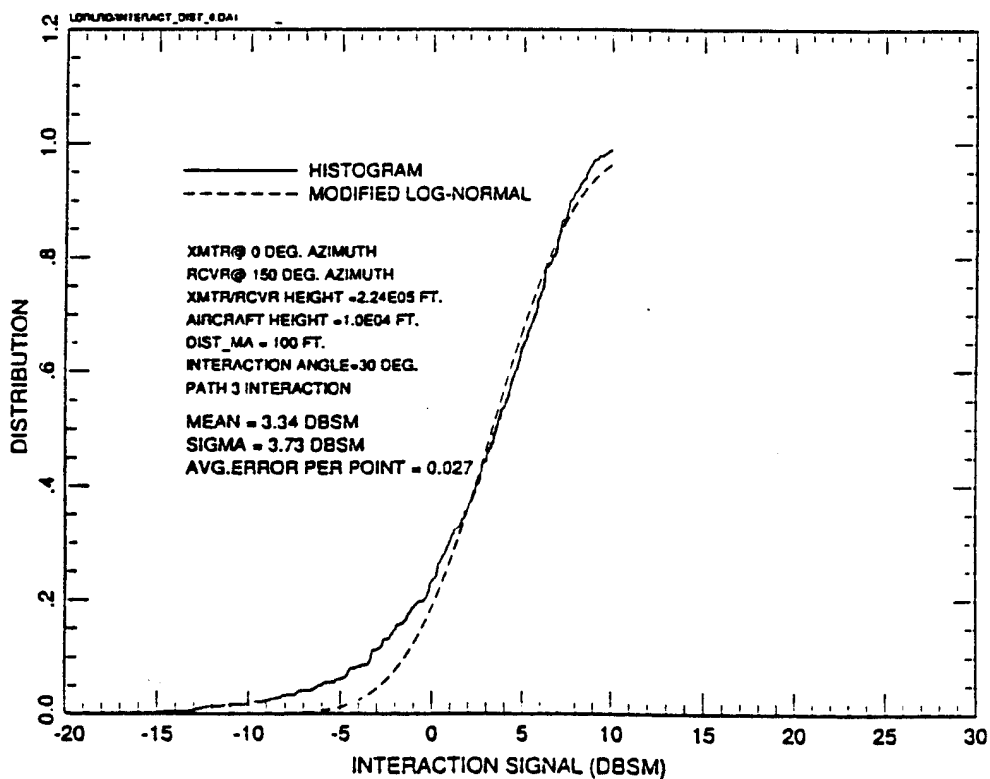


Figure 3.4-6 (b). Histogram and log-normal distribution for interaction path 3
Bistatic radar pointing @-45° elevation. X-band/TM mode

3.5 ALGORITHMS

3.5.1 Co-Target Interference Reduction Formulation: Unified Theory

Mathematical formulation provide algorithmic understanding and extentions that otherwise would be difficult to deduce. This section derives the optimal techniques for cotarget interference rejection. The following paragraphs show that the optimal detection statistics lead towards suppression or cancellation schemes. Thresholds for Constant False Alarm Control are also be defined as byproducts. It should be noted that there are two distinct characteristics that make co-target interference rejection different from adaptive noise interference suppression. These are:

1. Insufficient number of samples limit any hope of direct adaptivity and, hence, a signal model must eventually be assumed.
2. Sample cross-covariance of sensor degree of freedom yield high correlation between large and small target. Thus, adaptive cancellation, as in Sample Matrix Inversion Techniques, do not apply because both large and small target will be suppressed.

Because of these two reasons, Adaptive Processing Theory is not directly applied to reject large targets. However, adaptive techniques are still required for ECM, clutter, and thermal noise suppression which is shown to be part of the Whitening Process of the co-target interference rejection algorithm.

Our approach is to use statistical decision theory and derive the optimal solutions based on likelihood functions. The model (1) assumes combined simultaneous space, time (doppler), and range observations, (2) includes ECM and noise processes, (3) the presence of clutter, and (4) multiple interacting targets. A maximum likelihood test statistic is derived for all Swerling target models. This general approach establishes the optimal performance and the algorithm structures which can be modified to account for design constraints compromises. Figure 3.5.1-1 shows mathematical formulation for small target detection. This formulation assumes that in a small range doppler region, two targets can be present and possibly interfering with each other. Range, doppler and angle are unknown parameters. Without loss of generality, the formulation can be extended to more than two targets. Our problem focuses on co-target

interference in a radar with adequate energy-aperture products to detect the low RCS target. The challenge is to decide between hypothesis H_1 and H_2 and determining performance of such a decision rule.

PROBLEM FORMULATION	
Hypothesis Set	
$H_0:$	$y(t) = l(t)$, interference only
$H_1:$	$y(t) = z_1 S_1(t) + l(t)$, signal and interference
$H_2:$	$y(t) = z_1 S_1(t) + z_2 S_2(t) + l(t)$, two signals and interference
where	
$l(t) = n(t) + c(t) + \sum_{k=1}^{N_J} g_k J_k(t)$	
$n(t)$	is thermal noise vector with independent components
$c(t)$	is the clutter process as observed from each spatial channel
$J_k(t)$	is the k^{th} jammer process
g_k	gain and phase vector associated with k^{th} jammer process observations from each channel
z_1, z_2	signal 1 and 2 gains from each of the spatial channels
$S_1(t)$	$a_1 S(t - t_1(t))$
$S_2(t)$	$a_2 S(t - t_2(t))$
$S(t)$	is a replica of the transmitted signal
$t_k(t) = \frac{2}{c} (R_k + \dot{R}_k t + \dots)$	
a_k	deterministic or random variable depending on target Swerling model
R_k	is the k^{th} target range
\dot{R}_k	is the k^{th} target doppler

Figure 3.5.1-1. Hypothesis Testing Formulation for Small Target Detection with the Presence of Large Interfering Target, Clutter, Noise and Jammers.

To simplify our notation, one can equivalently consider a super vector with component indices being samples of space range, and doppler domain. Thus, one defines the vector \underline{S}_1 as the large signal vector and \underline{S}_2 as the small target vector. The first derivation that follows assumes that no apriori information is used. One can basically eliminate the noise hypothesis since large target presence competing with noise can be declared with high probability. For Swerling I through IV target model, the log likelihood function can be written in terms of a quadratic functional given below

$$-\ln L(y) = \left[\underline{y}^+ (\Lambda_1^{-1} - \Lambda_2^{-1}) \underline{y} + \ln \frac{|\Lambda_1|}{|\Lambda_2|} \right] \begin{matrix} > \\ < \end{matrix} T$$

where Λ_0 is the noise, clutter, and ECM interference covariance matrix and

$$\Lambda_1 = \Lambda_0 + \underline{S}_1 \underline{S}_1^+ \quad \Lambda_2 = \Lambda_1 + \underline{S}_2 \underline{S}_2^+$$

The ratio of the two determinants can be shown as

$$\frac{|\Lambda_1|}{|\Lambda_2|} = \left| 1 + \underline{S}_2^+ \Lambda_1^{-1} \underline{S}_2 \right|^{-1}$$

The use of the Matrix Inversion Lemma yields the following relationship among the two covariance inverses

$$\Lambda_1^{-1} = \Lambda_0^{-1} \left(1 + \frac{\underline{S}_1 \underline{S}_1^+ \Lambda_0^{-1}}{1 + \underline{S}_1^+ \Lambda_0^{-1} \underline{S}_1} \right)$$

Define $\langle \underline{a}, \underline{b} \rangle = \underline{a}^+ \Lambda_0^{-1} \underline{b}$

as an inner product between vector \underline{a} and \underline{b} , then the likelihood terms can be rewritten as

$$\underline{S}_2^+ \Lambda_1^{-1} \underline{S}_2 = \|\underline{S}_2\|^2 - \frac{|\langle \underline{S}_2, \underline{S}_1 \rangle|^2}{1 + \|\underline{S}_1\|^2}$$

$$|1 + \underline{S}_2^+ \Lambda_1^{-1} \underline{S}_2|^{-1} = \left| \left(1 + \|\underline{S}_2\|^2 \right) - \frac{|\langle \underline{S}_2, \underline{S}_1 \rangle|^2}{1 + \|\underline{S}_1\|^2} \right|^{-1} \quad \text{Eq. (a)}$$

$$\underline{y}^+ (\Lambda_1^{-1} - \Lambda_2^{-1}) \underline{y} = \frac{\frac{|\langle \underline{y}, \underline{S}_2 \rangle - \langle \underline{y}, \underline{S}_1 \rangle \langle \underline{S}_1, \underline{S}_2 \rangle|^2}{1 + \|\underline{S}_1\|^2}}{1 + \|\underline{S}_1\|^2 - \frac{|\langle \underline{S}_1, \underline{S}_2 \rangle|^2}{1 + \|\underline{S}_1\|^2}} \quad \text{Eq. (b)}$$

The complete likelihood ratio test then becomes,

$$-\ln L(y) = \frac{\frac{|\langle \underline{y}, \underline{S}_2 \rangle - \langle \underline{y}, \underline{S}_1 \rangle \langle \underline{S}_1, \underline{S}_2 \rangle|^2}{1 + \|\underline{S}_1\|^2}}{1 + \|\underline{S}_2\|^2 - \frac{|\langle \underline{S}_1, \underline{S}_2 \rangle|^2}{1 + \|\underline{S}_1\|^2}} + \ln \left| \left(1 + \|\underline{S}_2\|^2 \right) - \frac{|\langle \underline{S}_2, \underline{S}_1 \rangle|^2}{1 + \|\underline{S}_1\|^2} \right| \underset{<}{>} T \quad \text{Eq. (c)}$$

For $\|\underline{S}_1\|^2 \gg 1$, then $\|\underline{S}_1\|^2 - \frac{|\langle \underline{S}_1, \underline{S}_2 \rangle|^2}{\|\underline{S}_1\|^2} = \|\underline{\eta}\|^2$ where $\underline{\eta}$ is the component of the small target \underline{S}_2 which is orthogonal to the large target \underline{S}_1 .

That is, for large target sufficiently above noise, the likelihood statistic results in

$$-\ln L(y) = \frac{|\langle \underline{y}, \underline{\eta} \rangle|^2}{1 + \|\underline{\eta}\|^2} + \ln \left(1 + \|\underline{\eta}\|^2 \right)^{-1} \underset{<}{>} T \quad \text{Eq. (d)}$$

Just as in the standard detection theory, the equation shows that whitening followed by a matched filter is the proper detection rule. The unique difference of this optimal co-target interference rejection rule is instead of the filter being matched to the original small target signal, the filter is being matched to the small signal component which is orthogonal to the large signal. It also follows that detection and false alarm probabilities can be computed from the available standard curves for all the Swerling target models. This is computed by modifying the signal energy contained only in the orthogonal component in the signal to noise power ratio. The first formulation concludes that large target suppression is optimal.

A second formulation capitalizes on the capability of reprocessing the data given the large target is present. Given a detected large target, via standard methods, one would like to search for small targets in the large target vicinity. Again, only two hypothesis are considered. The log likelihood statistic is

$$-\ln L(\underline{y}) = (\underline{y} - \underline{S}_1)^+ (\Lambda_1^{-1} - \Lambda_2^{-1})(\underline{y} - \underline{S}_1) + \ln \frac{|\Lambda_1|}{|\Lambda_2|}$$

where

$$\Lambda_1 = \Lambda_0, \text{ and } \Lambda_2 = \Lambda_0 + \underline{S}_2 \underline{S}_2^+$$

Again the determinant ratio is

given as

$$\frac{|\Lambda_1|}{|\Lambda_2|} = \left| 1 + \underline{S}_2^+ \Lambda_0^{-1} \underline{S}_2 \right|^{-1} = \left| 1 + \|\underline{S}_2\|^2 \right|^{-1}$$

Analogous to the previous derivation, the Matrix Inversion Lemma yields,

$$\Lambda_1^{-1} - \Lambda_2^{-1} = \frac{\Lambda_0^{-1} \underline{S}_2 \underline{S}_2^+ \Lambda_0^{-1}}{1 + \underline{S}_2^+ \Lambda_0^{-1} \underline{S}_2} = \frac{\Lambda_0^{-1} \underline{S}_2 \underline{S}_2^+ \Lambda_0^{-1}}{1 + \|\underline{S}_2\|^2}$$

resulting in the following log likelihood function

$$-\ell n L(y) = \frac{\|(y - \underline{s}_1, \underline{s}_2)\|^2}{1 + \|\underline{s}_2\|^2} + \ell n |1 + \|\underline{s}_2\|^2|^{-1}$$

The above equation indicates that cancellation algorithm is optimal if the presence of the large target is assumed apriori.

The results from the two formulations indicate that either suppression or cancellation is optimal and that each requires a signal model. Once the orthogonal or residual component is used, one applies the standard detection techniques and the Newman-Pearson Lemma lays the foundation for the CFAR algorithms.

3.5.2 Description and Performance Evaluation

This section describes and evaluates the performance of several cancellation algorithms that have the potential to reduce co-target interference. Four effective algorithms have been identified. They are:

1. Range Response Cancellation
2. Zero-Out Blanking
3. Range Sidelobe Suppression
4. Doppler Cancellation in Time Domain

The first three techniques are in the range domain while the last is in the doppler domain. Two other techniques, doppler cancellation in the doppler domain and lattice filter cancellation were also evaluated, but their performance was inadequate.

Range Domain Issues. Cancellation in the range domain is probably the most challenging since it is very difficult to control errors that affect the pulse compression sidelobe response. The main error factors are target complex scattering structure, transmit code fidelity video filter distortion and doppler mismatch errors (see system errors section 3.5.3), which makes difficult the prediction of pulse compression sidelobes. Knowledge of the sidelobe structure is required if the techniques are to be fully effective.

The first approach estimates the large target complex amplitude, range and doppler, predicts the sidelobe contributions to other bins from the data with the response model, and subtracts these directly from the compressed data. Alternatively, to minimize processor finite word length distortions, one can subtract the large target from the uncompressed data and then recompressing the neighboring range samples.

3.5.2.1 Range Response Cancellation

A simple suboptimal technique that illustrates range domain cancellation using sidelobe response is presented below. Consider a 13:1 Barker pulse compression code along with its range response at the output of a matched pulse compressor shown in Figures 3.5.2.1-1 (a) and (b). Given the large target

range estimate, one determines the range samples with the common voltage values at the output. For example, range samples with common voltage V_2 occur at times t_{12} , t_8 , t_4 , t_4 , t_8 , and t_{12} . If one divides the peak voltage V_0 by 13 and subtract the values at these sample times, the large target is cancelled. The large target range estimate is used to choose the set of range bin samples and the indexing. Table 3.5.2.1-1 lists the sidelobe samples with common voltages from a large target response and Barker sidelobe and mainlobe relationships. These relationships are used for cancellation. Figure 3.5.2.1-1 (a) also shows a radar return pulse compression code after video filtering. The transitions between $\pm 180^\circ$ phases are most notably affected as shown by the dashed curve. This can limit performance since one must account for the smoothing of the code. Furthermore, video filters are typically not well matched from channel to channel and system to system, and their responses can vary with time. Therefore, periodic calibration may be necessary for such a cancellation scheme to yield the required performance.

TABLE 3.5.2.1-1. RANGE SAMPLE PROPERTIES OF 13:1 BARKER PULSE COMPRESSION CODE RESPONSE FOR A TARGET STRADDLED IN RANGE

VOLTAGE CONSTRAINTS	RANGE SAMPLE TIMES WITH COMMON VOLTAGE AFTER P.C.	CODE
V_1	$t_{13}, t_9, t_5, t_3, t_7, \text{ and } t_{11}$	$\frac{1}{13} V_0 = V_2$
V_2	$t_{12}, t_8, t_4, t_4, t_8, \text{ and } t_{12}$	$\frac{1}{13} V_{-1} = V_1$
$-V_1$	$t_{11}, t_7, t_3, t_1, t_5, \text{ and } t_9$	and
$-V_2$	$t_{10}, t_6, t_2, t_2, t_6, \text{ and } t_{10}$	
$V_1 + V_0 = V_{\max}$		

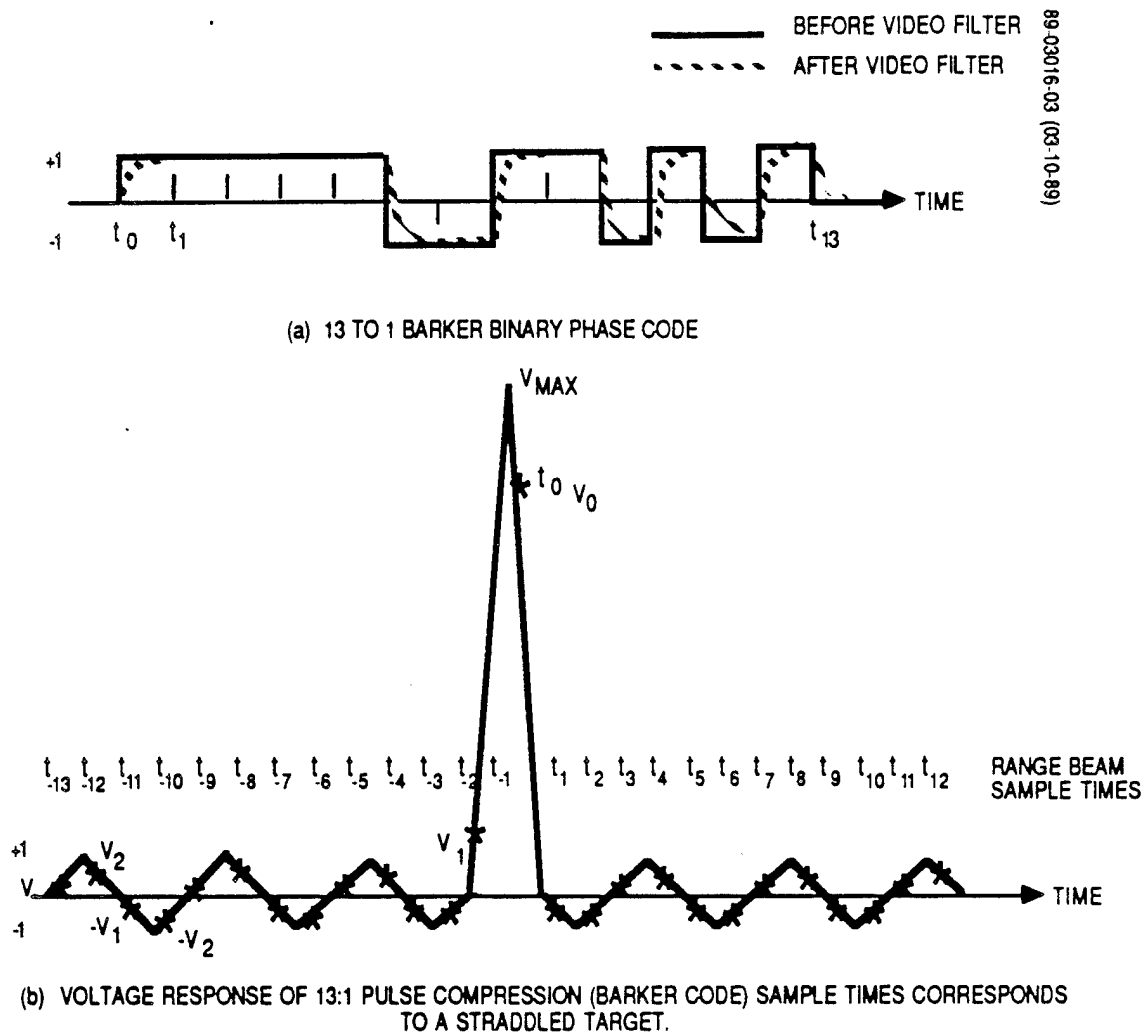


Figure 3.5.2.1-1 (a) & (b). Barker Pulse Compression Code Properties.

Figure 3.5.2.1-2 (a) & (b) show the functional block diagrams for the normal pulse doppler radar system and the range response cancellation algorithm. Pulse compression is done right after doppler filtering. In Figure 3.5.2.1-2 (b), the THRESHOLD block on top represents the detection of the large target peak response location (mainlobe) and response. Then 1/13 of the peak is subtracted from the adjacent range bins which predominantly contain the sidelobes of the large target. This is done in the CANCEL block. Although not shown, the responses of the large range bin and the next closest range bin (before or after, depending upon the straddling) are set to zero. Finally, the residual response is passed through a second THRESHOLD for detection of small targets.

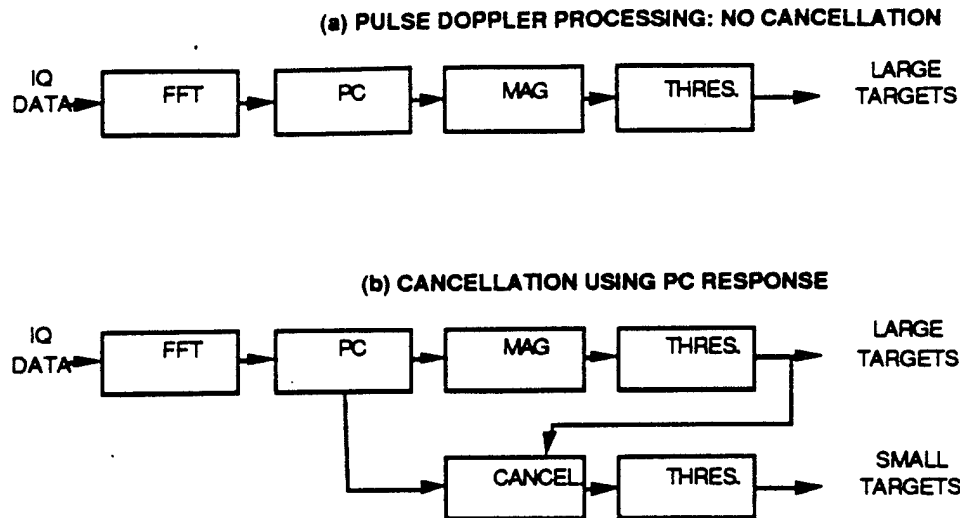


Figure 3.5.2.1-2. Functional Block Diagram for (a) Standard Pulse Doppler Processing (b) Range Domain Cancellation Using the Response

The performance of this cancellation technique is examined next. Figure 3.5.2.1-3 (a) shows the case where only the large target is present at range bin 15. Only the doppler filter where the large target is present is shown. Also, system errors such as hardware errors, timing control errors, etc. are not taken into account in all the following performance plots. This will simplify the task of ascertaining the effectiveness of the different cancellation algorithms. The expected sidelobe response of the Barker code can be clearly seen, even though a small amount of noise is present. We note that in the no-noise case the sidelobes should be -22.3 dB down from the peak, which the sidelobes in the figure generally are about that value. Figure 3.5.2.1-3 (b) shows the same doppler filter after cancellation has been performed. The large target peak at range bin 15 has been effectively cancelled, while the sidelobes have also been reduced about 15 to 20 dB.

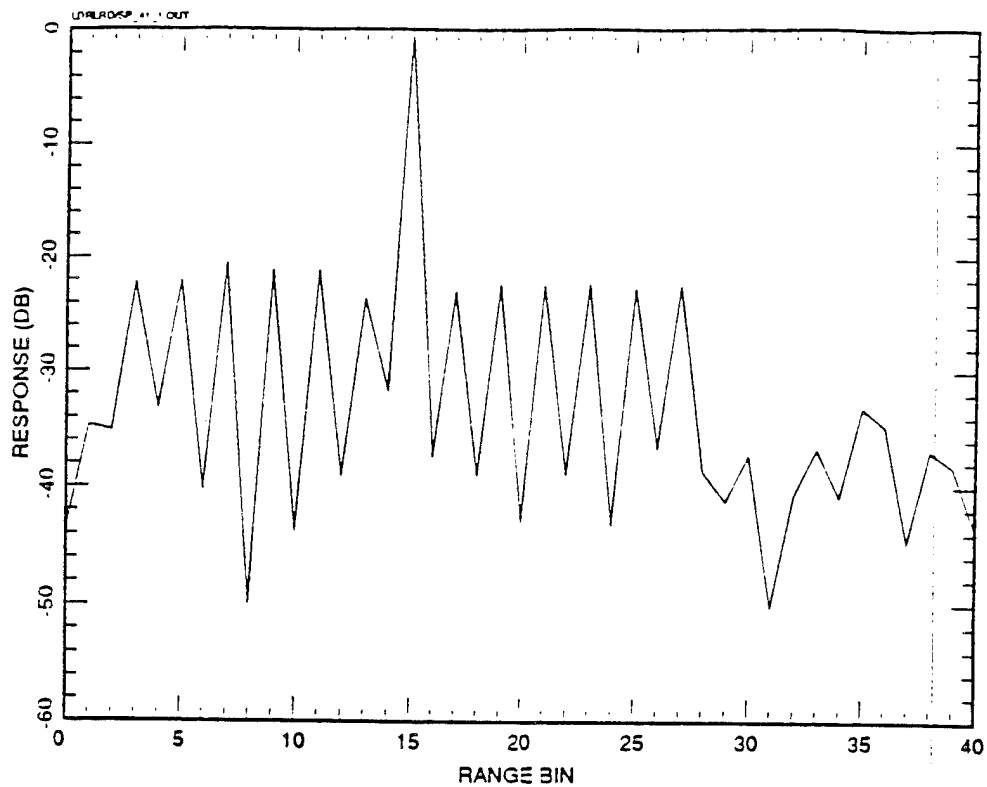


Figure 3.5.2.1-3 (a). Pulse compression response before cancellation.
One target case.

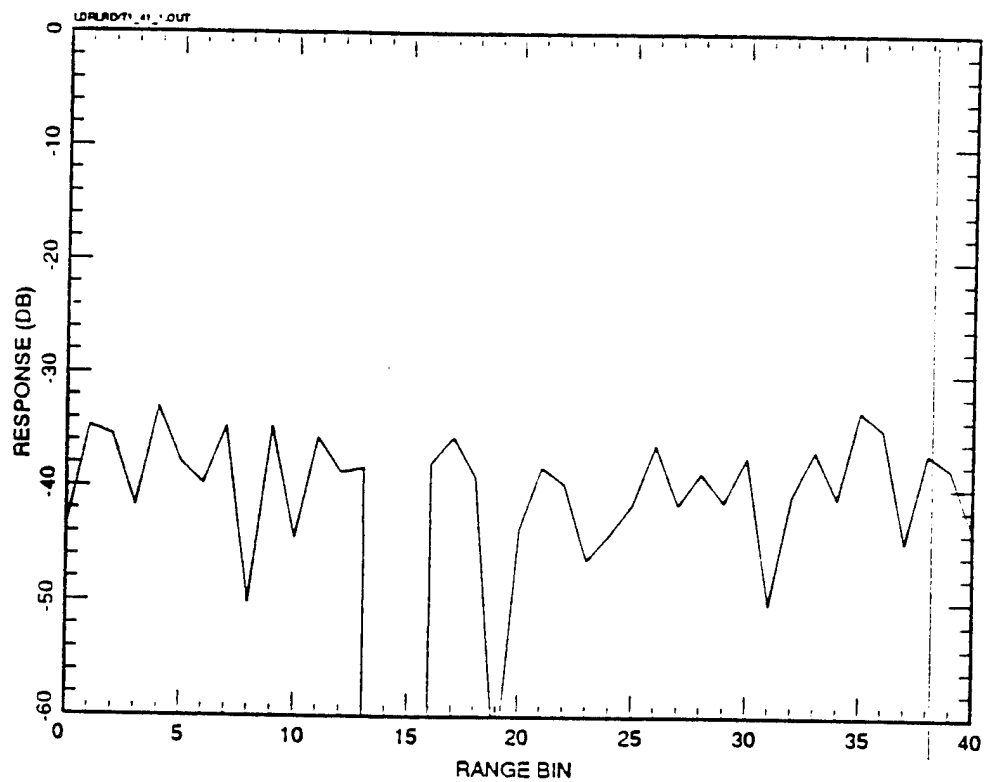


Figure 3.5.2.1-3 (b). Response after cancellation. One target case.

Figures 3.5.2.1-4 (a) & (b) show the most important case of a large target interfering with a nearby small target. The small target at range bin 17 is only 2 range bins away from the large target. Also, its power is 20 dB below that of the large target peak. The two targets are assumed to have the same velocity so they will be in the same doppler filter for simplicity. As Figure 3.5.2.1-4 (a) shows, the small target peak (-20 dB) and the large target sidelobe at range bin 17 (-22.3 dB) combine to produce the response in that range bin of about -16 dB. After cancellation, the small target clearly stands out in range bin 17, and as shown in Figure 3.5.2.1-4 (b) its response is indeed 20 dB down from the large target peak, as expected. As this peak stands out so clearly, it can be easily detected and a small target is declared. Hence, the range response cancellation scheme is seen to be very effective for target separation as close as 2 range bins.

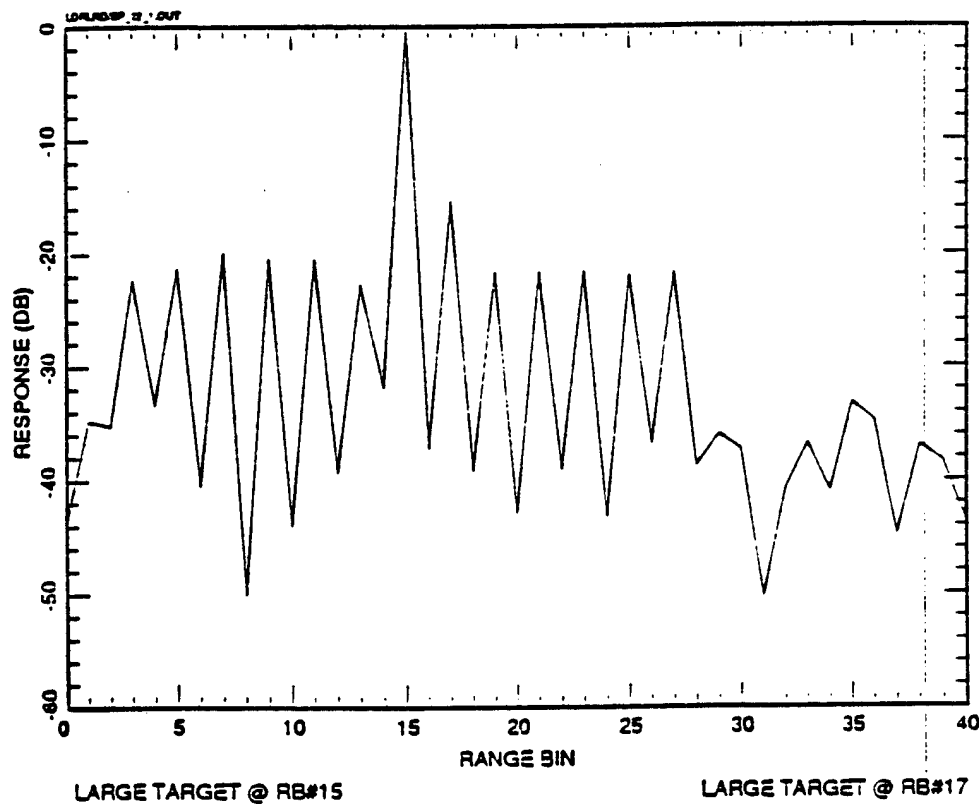


Figure 3.5.2.1-4 (a). Response before cancellation. Two targets case.

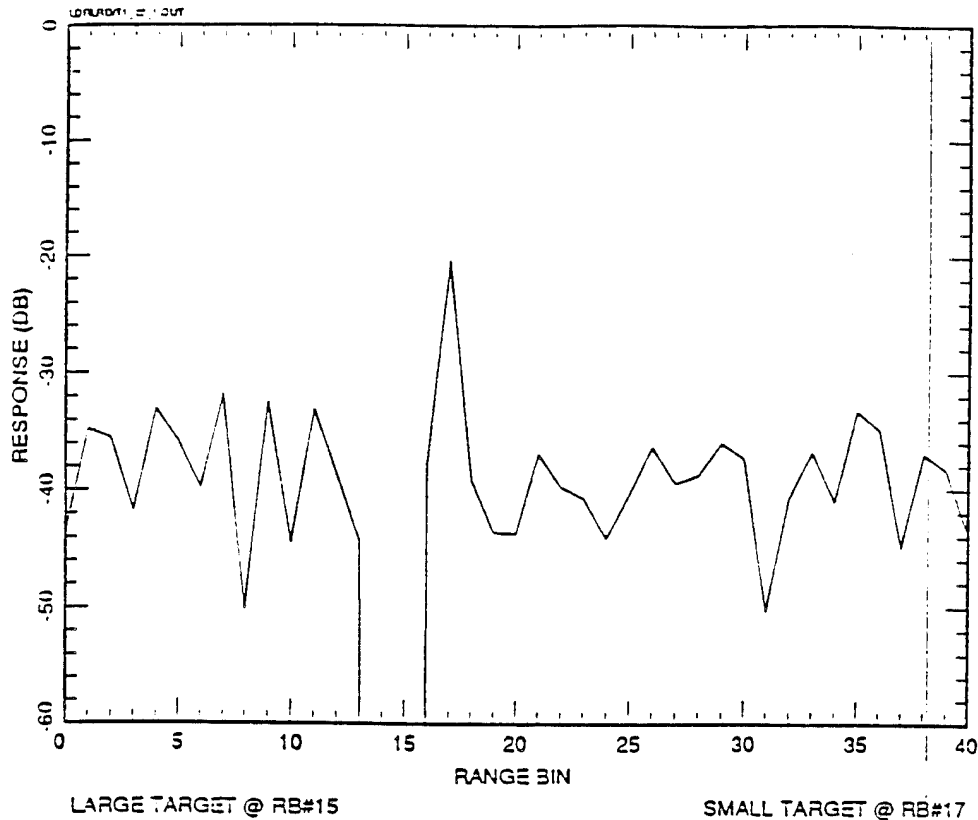


Figure 3.5.2.1-4 (b). Response after cancellation. Two targets case.

To show that the inter-target separation should be at least 2 range bins, we look at Figures 3.5.2.1-5 (a) & (b), which depict smaller separations. In (a), the separation is 1.5 range bin for a small target 20 dB below the large. After cancellation, the small target remains at range bin 17 (it's been shifted), but it is not much above the sidelobe residuals of the large target. The problem here is that the small target energy in range bin 17 is about 26 dB below the peak, which is 6 dB worse than the case of Figure 3.5.2.1-4 (b). Hence, it would be difficult to detect this small target. Next, in Figure 3.5.2.1-5 (b), the small target is only 1 range bin away. As can be seen, after cancellation, it was cancelled out along with the large target, and therefore 1 range bin separation is too small.

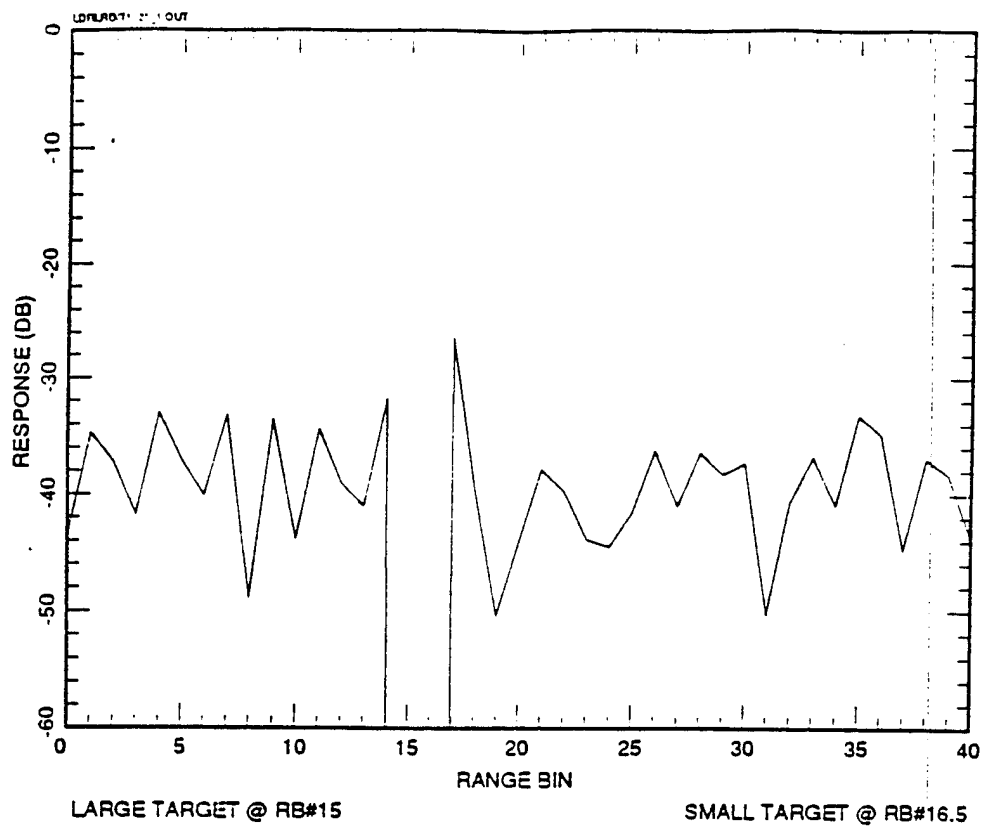


Figure 3.5.2.1-5 (a). Response after cancellation. Two targets case. 1.5 range bin separation.

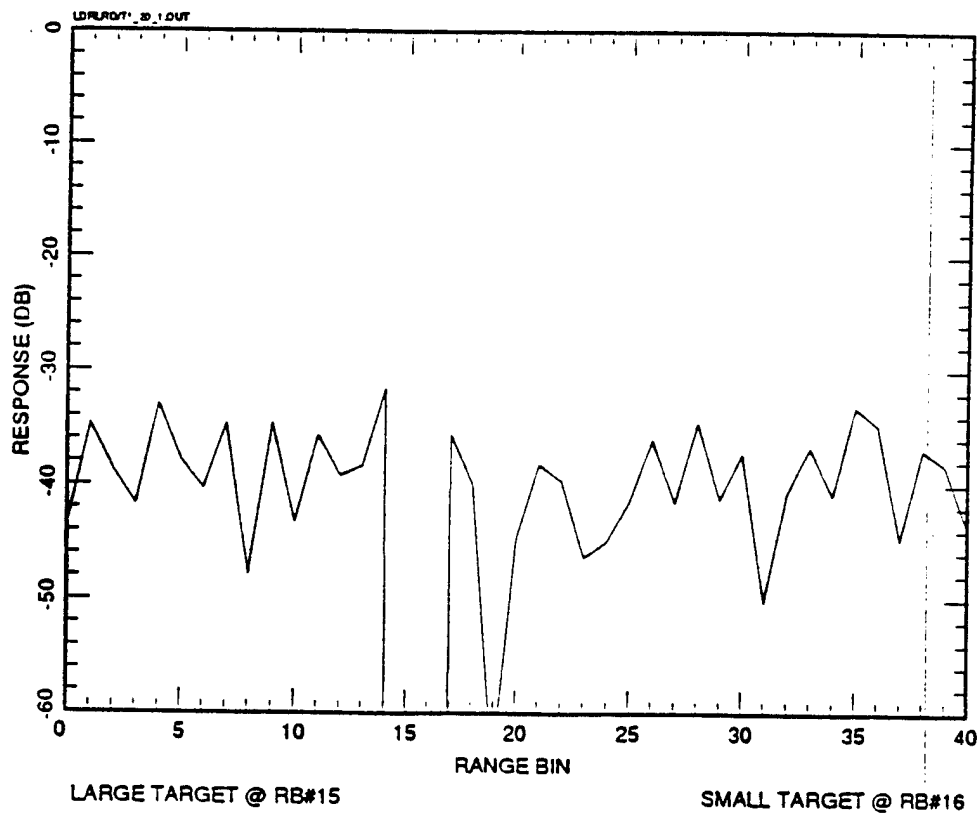


Figure 3.5.2.1-5 (b). Response after cancellation. Two targets case. 1 range bin separation.

Next, we present the case where the small target power is 40 dB below that of the large target. Figure 3.5.2.1-6 shows this case. The small target is 2 range bins away. After cancellation the small target actually gains some energy, as its response in range bin 17 is 37 dB below the large target peak, while we expect the response to be 40 dB below. The explanation is that not all the large target sidelobe energy in range bin 17 was cancelled.

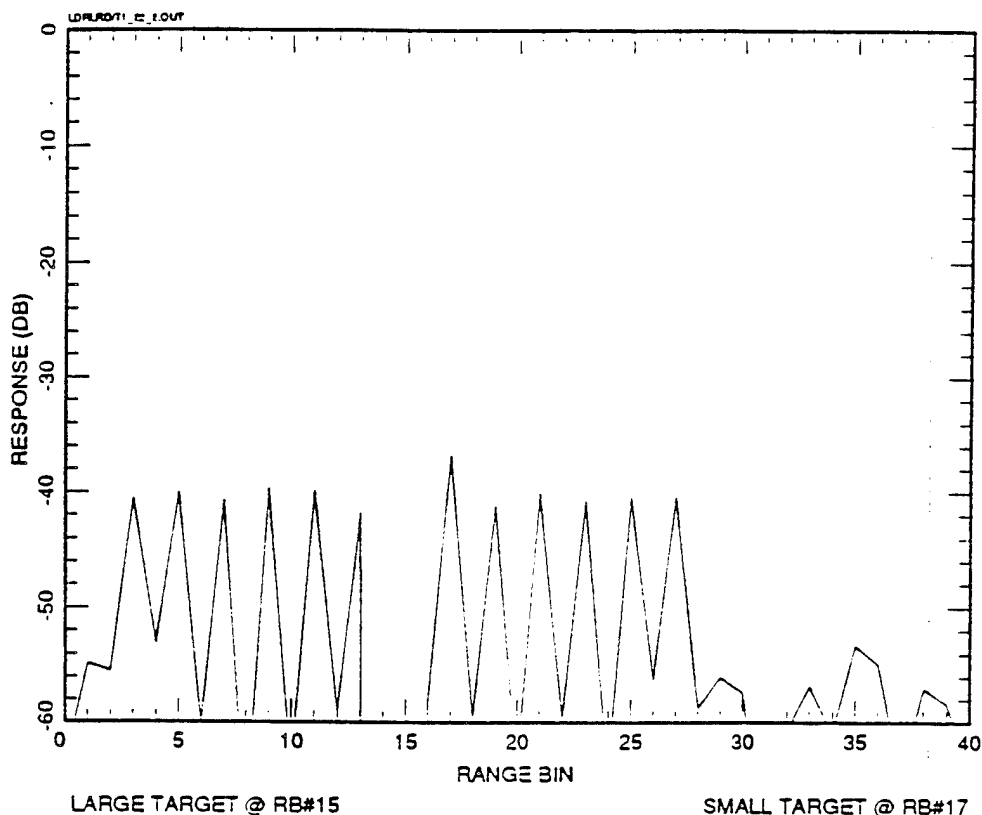
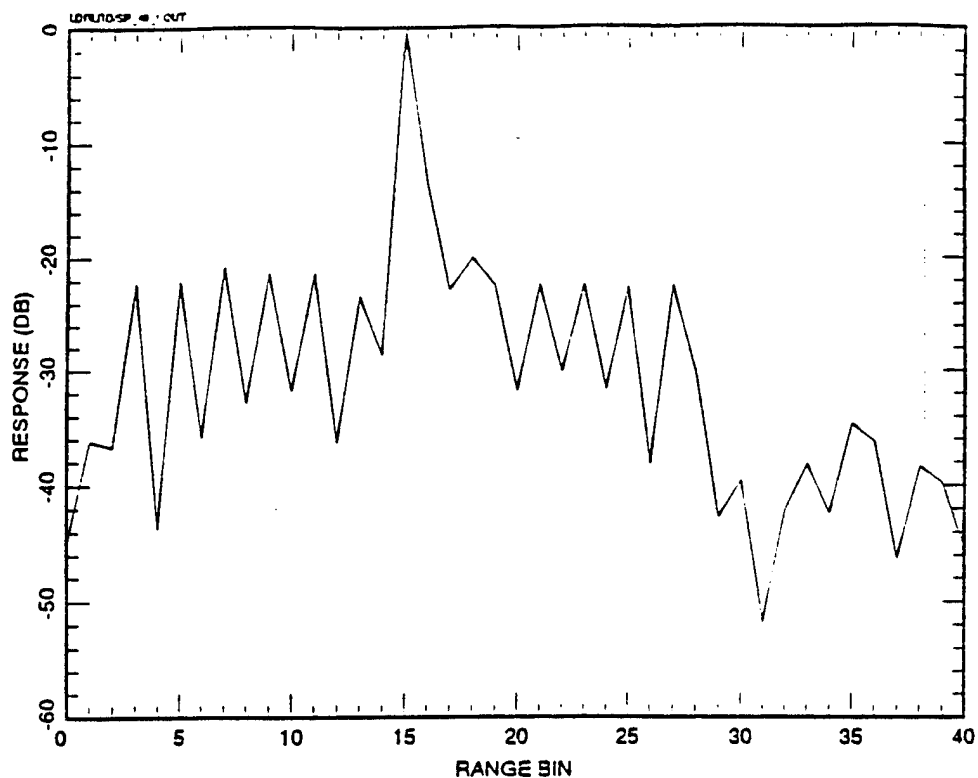


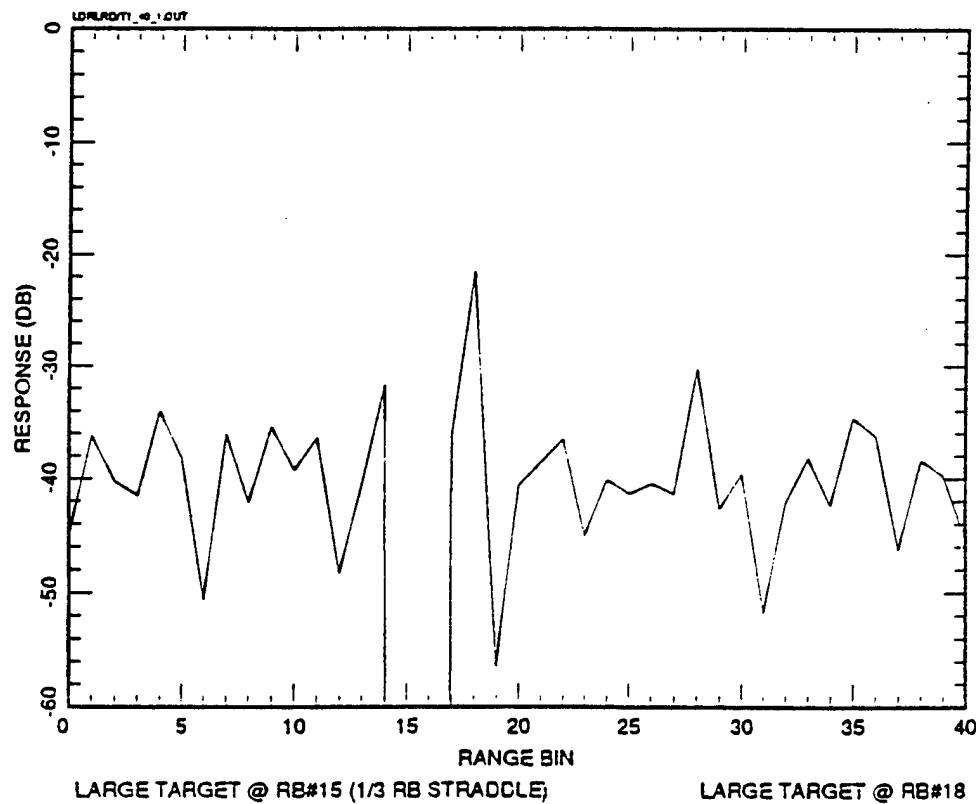
Figure 3.5.2.1-6. Response after cancellation. Two targets case.
40 dB dynamic range.

Next, we look at the case where the large target has 2 components: one component centered at range bin 15 and the other component straddling at 1/3 range bin away with each component having half the power. The small target is 3 range bins away and is 20 dB down. Figure 3.5.2.1-7 (a) shows the response before cancellation and in (b) we have the response after cancellation. As the Figure shows, the cancellation is quite effective, and the small target is easily detected.



LARGE TARGET @ RB#15 (1/3 RB STRADDLE) LARGE TARGET @ RB#18

Figure 3.5.2.1-7 (a). Response before cancellation. Two targets case.
2-components large target.



LARGE TARGET @ RB#15 (1/3 RB STRADDLE) LARGE TARGET @ RB#18

Figure 3.5.2.1-7 (b). Response after cancellation. Two targets case.
2-components large target.

3.5.2.2 Zero-Out Blanking

Blanking techniques to remove large interfering signals have been used extensively in radars. Algorithms utilizing spatial, range and doppler observations offer a simple effective method of maintaining detection sensitivity without significantly increasing processing. Blanking effectiveness decreases, however, as target separation decreases. This occurs because with small separations, masking increases and blanking removes the large target cells together with a significant portion of the small target. The classical blanking techniques maintains detection sensitivity by not allowing large targets to influence the threshold estimates in a constant False Alarm Rate (CFAR) system. Given a large target detection with standard processing in the range-doppler cell domain, the technique basically sets to zero the sidelobe and mainlobe cells containing large target energy. Then, a new local threshold is estimated to which the neighboring cells are compared. With very low doppler filter sidelobes, it may not be necessary to blank sidelobe doppler cells except for the two cells nearest the mainlobe (depends on filter broadening due to heavy amplitude weighting). It is clear that that blanking is undesirable in the doppler domain since it completely desensitizes the full PRF for the large target range bin.

A variation of range domain blanking has been developed that progressively, rather than abruptly, degrades detection sensitivity as the small target is closer to the large target. After large target detection, the set of uncompressed large target range samples in the target doppler filter are set to zero and then the set of $(2N_{PC} + 1)$ of range samples are recompressed. Figure 3.5.2.2-1 shows the functional block diagram for the zero-out blanking algorithm. As the diagram shows, after the large target is detected, its location

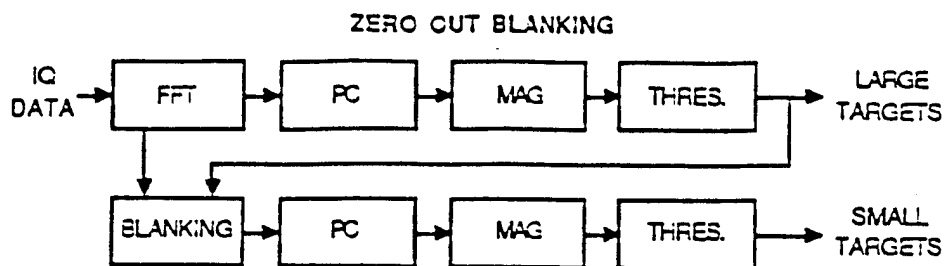


Figure 3.5.2.2-1. Zero-Out Blanking in the Range Domain Functional Block Diagram.

is fed into the BLANKING block. Here, the uncompressed N_{PC} large target range samples are blanked (set to zero). Pulse compression is done once again and the result is passed through thresholding for small target detection.

The effectiveness of the zero-out blanking is next determined. Figure 3.5.2.2-2 (a) & (b) show the case where the small target is 5 range bins from the large target. As range bin 20 is in one of the nulls of the large target response, when it is combined with the small target peak there (20 dB down), the resultant response is 19.6 dB down from the large target peak. This is shown in Figure

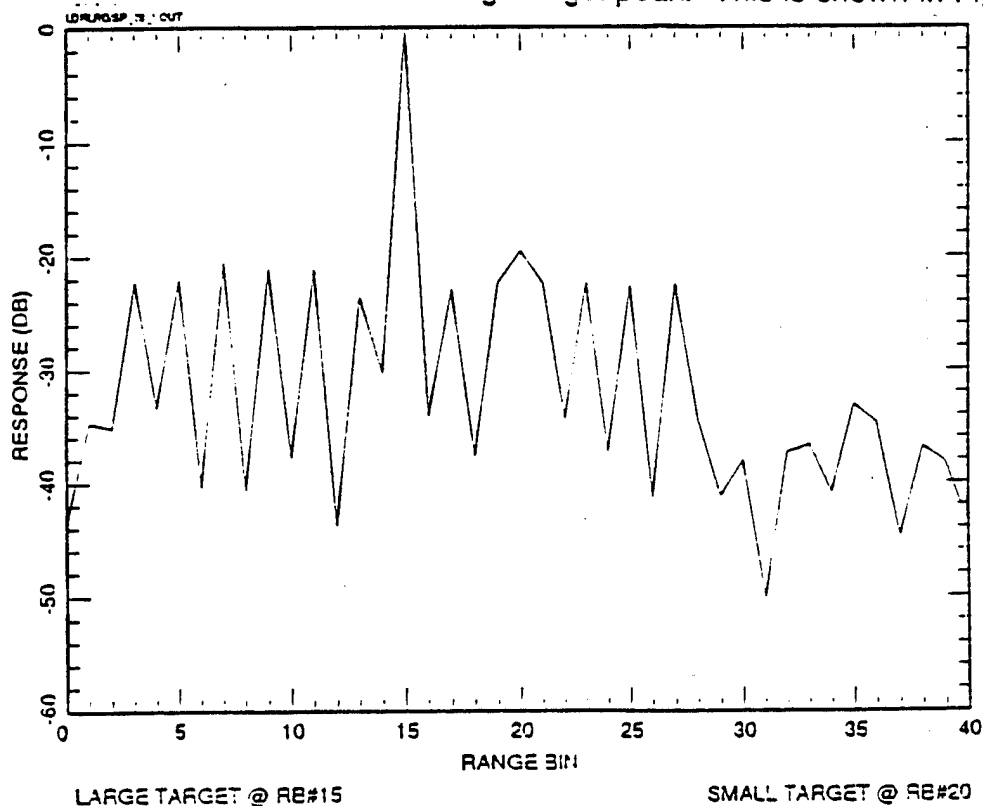


Figure 3.5.2.2-2 (a). Pulse compression response before blanking.
Two target case. 5 range bin separation.

3.5.2.2-2 (a). After the blanking algorithm is applied, in (b), the response in range bin 20 is only -29.2 dB, or a loss of about 9.2 dB of its own power. However, the small target energy remaining in range bin 20 is sufficiently above the residual in the surrounding range bins to allow a detection of the small target.

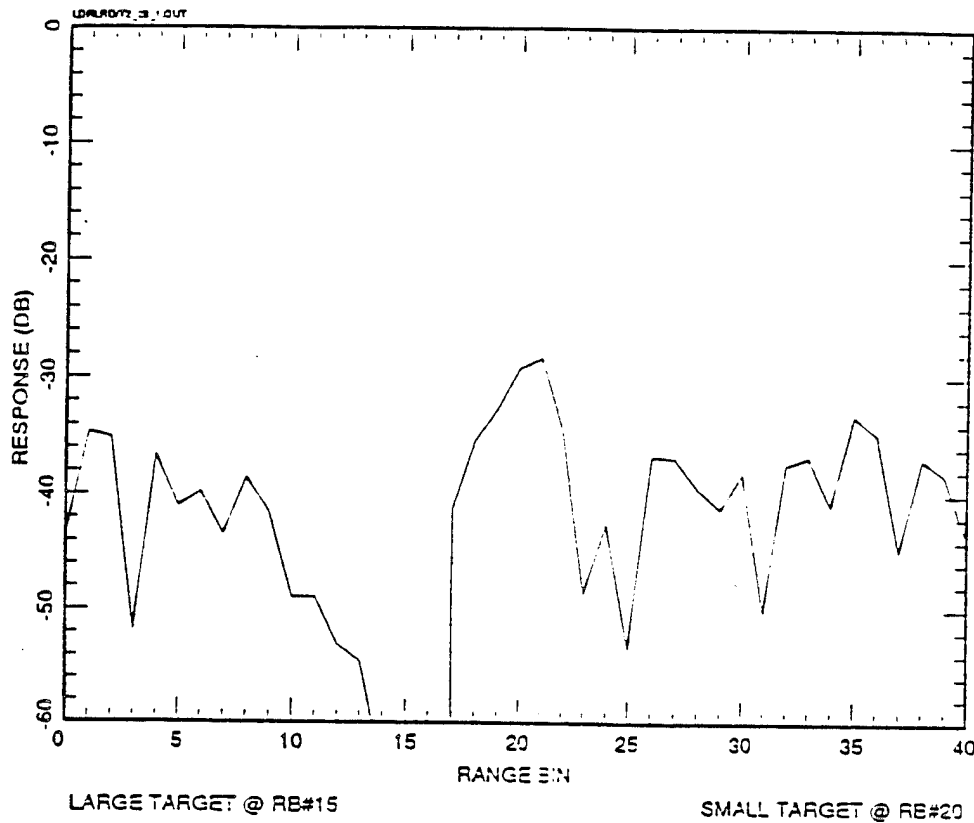
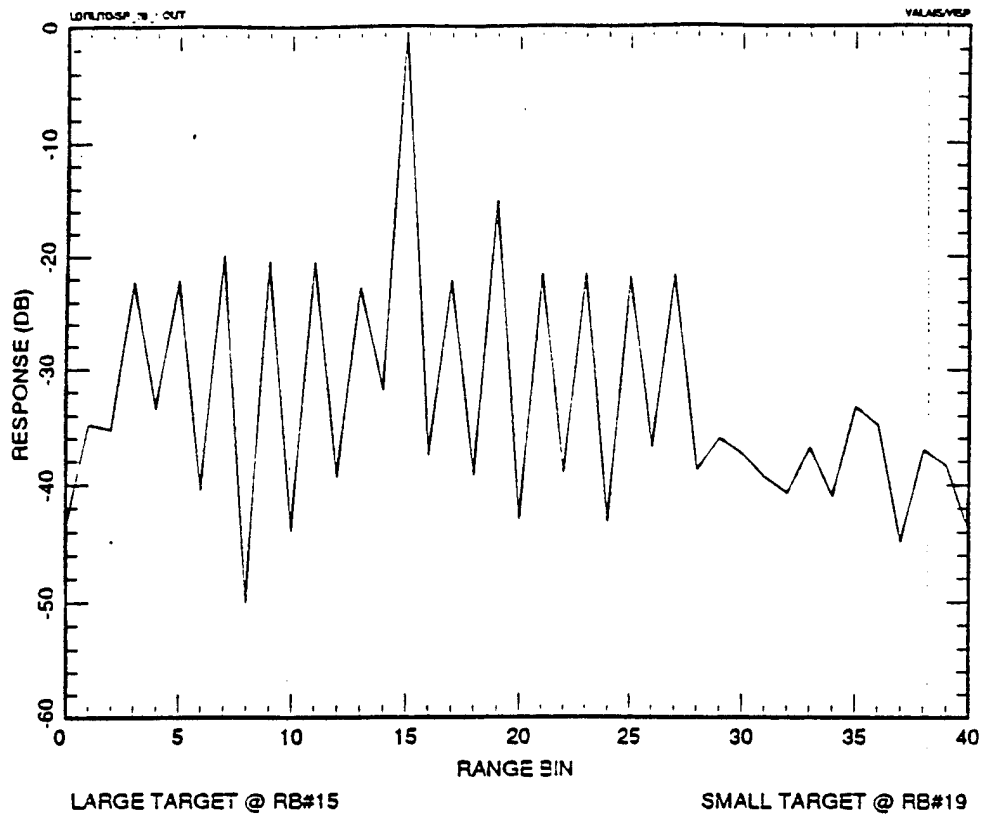


Figure 3.5.2.2 (b). Response after blanking. Two target case.
5 range bin separation.

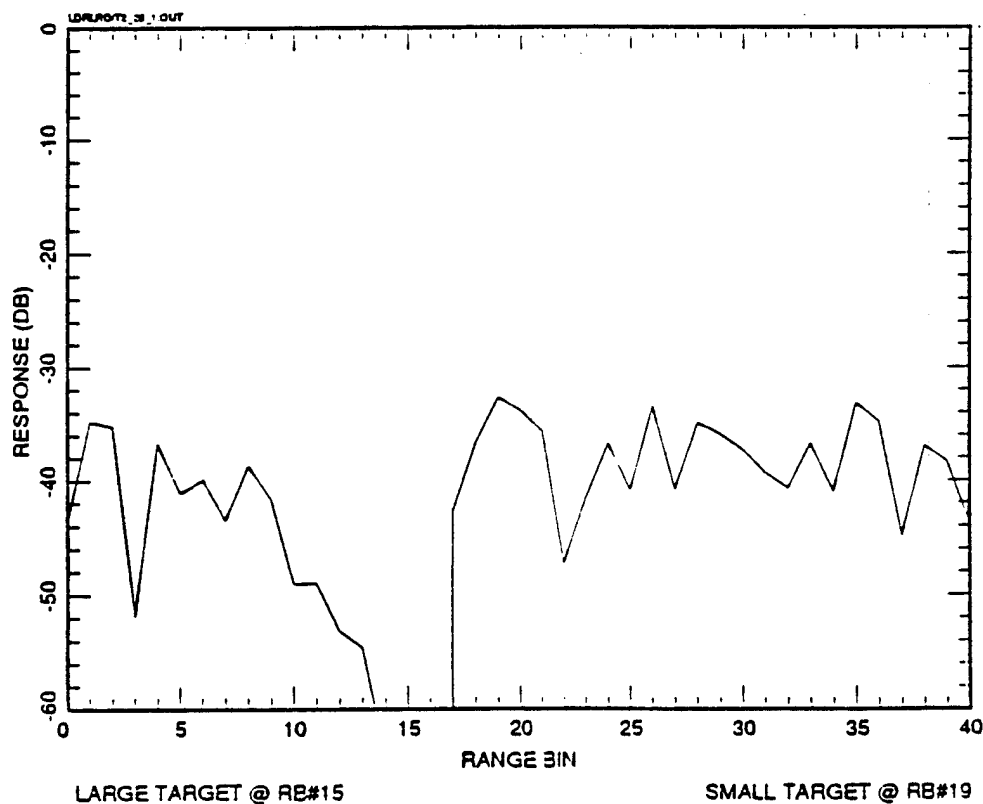
In Figures 3.5.2.2-3 (a) & (b) we move the small target to range bin 19 so that it is slightly closer to the large target, 4 range bins away. In (a) we see that since range bin 19 is in one of the sidelobe peaks of the large target, when it is combined with the small target (20 dB down) the resultant response is 15.1 dB. After the blanking algorithm is applied, in (b), the response in range bin 19 is about 32.7 dB down from the large target peak. Hence the small target has lost about 12.7 dB of its power. The small target power remaining is about the same as the residual in some surrounding range bins. It would be difficult to declare a detection given this amount of power. Thus given a 4 range bin separation, this is too close for the zero-out blanking algorithm to be effective.



LARGE TARGET @ RB#15

SMALL TARGET @ RB#19

Figure 3.5.2.2-3 (a). Pulse compression response before blanking.
Two target case. 4 range bin separation.



LARGE TARGET @ RB#15

SMALL TARGET @ RB#19

Figure 3.5.2.2-3 (b). Response after blanking. Two target case.
4 range bin separation.

At 5 range bin separation and 40 dB dynamic range, the zero-out blanking is still effective. This is shown in Figure 3.5.2.2-4. The response in range bin 20 is the small target residual, about 48 dB down from the large target peak. Compared to the surrounding range bins, however, it's still enough to declare the detection of a small target.

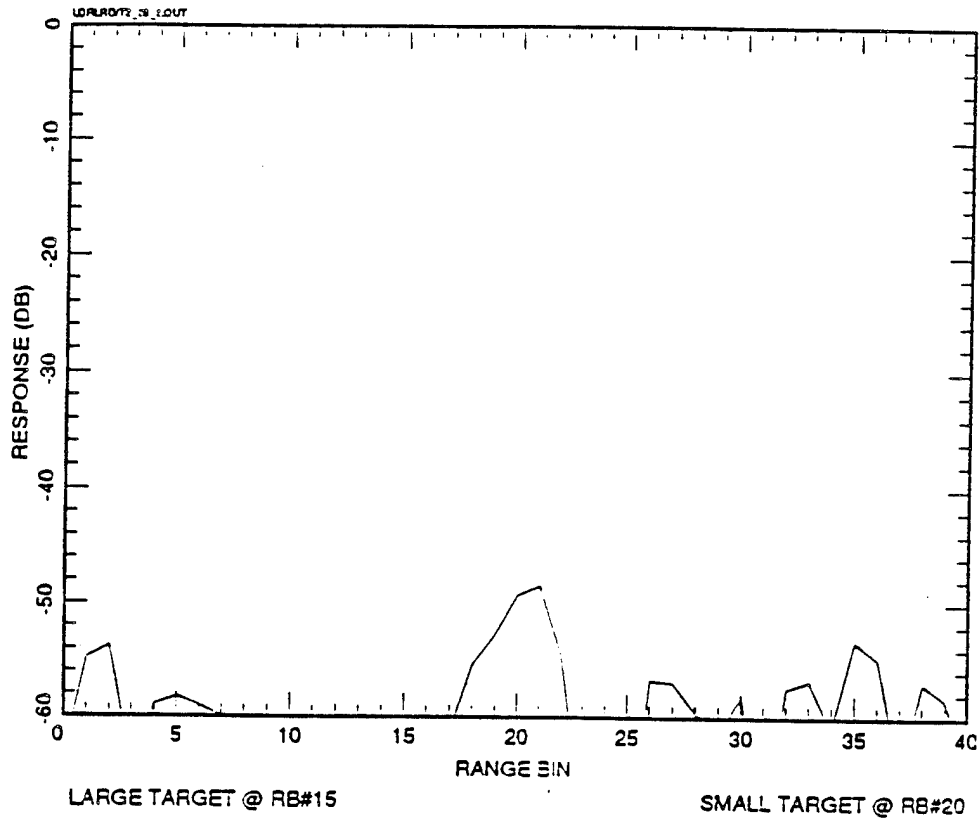


Figure 3.5.2.2-4. Response after blanking. Two target case.
5 range bin separation. 40 dB dynamic range.

3.5.2.3 Range Sidelobe Suppression

In radar applications, pulse compression waveforms are frequently used to increase the amount of energy radiated, and a pulse compressor is required to process the received signal. For these applications, the compressor is often an implementation of a matched filter (maximizes detection range) whose range sidelobes can be relatively high. If one assumes that only a single target is present, then one can reject those detections due to the high sidelobes, and false targets are eliminated. However, if the environment contains both large and small targets, all the sidelobes from the large target will interfere with the detection of potential small targets in the range region where the sidelobes are present. Hence, for the scenario where large and small targets are present, the control of the sidelobes is extremely important.

Sidelobe control for pulse compression waveforms takes on many forms. For digital codes, this is achieved by forming a mismatched filter, as opposed to a matched filter whose filter weights specify the response. There are algorithms to minimize integrated sidelobe ratio (ISLR) or peak sidelobe ratio (PSLR), but both approaches extend the length of the mismatch filter beyond the length of the matched filter. For air-to-air environment where sensitivity is important, extending the weight length extensively will induce higher SNR losses from the weights. An acceptable approach is one which uses a matched filter to initially detect targets, then re-processes the data to examine regions where the sidelobes from the initial detections hindered sensitivity using sidelobe control techniques. The following discusses such an approach to the sidelobe control problem and gives some examples.

One approach to control sidelobes is to re-process the data for a set of range samples with a weighting sequence that provides large target suppression. Figure 3.5.2.3-1 depicts the desired properties of the resultant response using the weights. The response has very low sidelobes in the region of the large target and for all ranges in the set of range samples. The data must be re-processed for each range region as shown in the figure. It is assumed that the large target is not eclipsed in range, since one can always find a PRF that insures that the large target will not be eclipsed once the range is known.

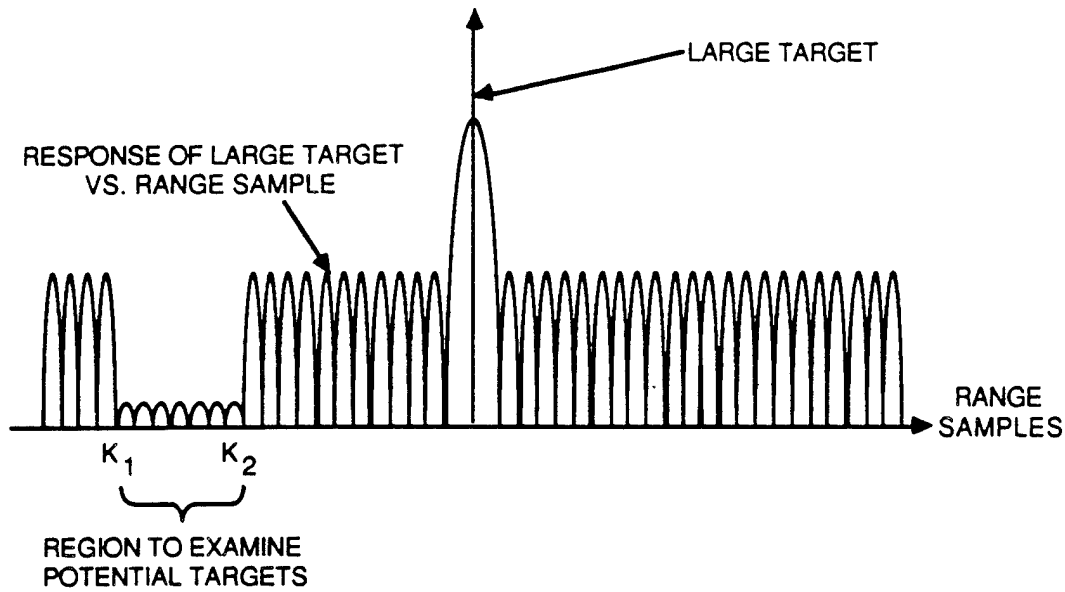


Figure 3.5.2.3-1. Placement of Low Sidelobes

The weighting sequence that gives a specific low sidelobe response can be easily constructed by using the Gram-Schmidt procedure to orthogonalize a set of vectors. Let $c(n)$, $n=1, N_c$ be the sequence which specifies the digital code whose length is N_c . For a matched filter, the weights are $c(n)$. For the mismatched filter, begin by forming the vectors \underline{x}_k given by

$$[\underline{x}_k] = \begin{cases} c(n-k), & n = k+1, \dots, k+N_c \\ 0, & \text{otherwise} \end{cases}$$

which are the various shifts of the signal where \underline{x}_0 is the assumed shift of the signal where a potential target is. For a set of weights given by a weight vector \underline{w} , the response $r(k)$ at shift k is given by

$$r(k) = \underline{w}^t \underline{x}_k$$

where $r(0)$ is the mainlobe response. The weight vector is then selected such that $r(k)$ is zero for k in the range K_1 and K_2 (one of the range regions), the sum of the weights is unity ($\underline{w}^t \underline{w}_k = 1$), and $r(0)$ is maximized. This criterion will select the weight vector such that the sidelobes are zero in the desired range region and the signal-to-noise loss due to the mismatched weights is

minimized. With these definitions the Gram-Schmidt procedure can be used to form a set of unit vectors \underline{e}_i , $i=1, \dots, E$ which span the set of vectors \underline{x}_k , $k=K_1, K_2$. Then the weight \underline{w} is found by extending the Gram-Schmidt procedure one stage further and finding the unit vector \underline{w} which is orthogonal to all \underline{e}_i , $i=1, \dots, E$ and minimizes the quantity $\underline{w}^t \underline{x}_0$. Hence the desired weight vector is given by

$$\underline{w} = \frac{\underline{x}_0 - \sum_{i=1}^E \underline{e}_i^t \underline{x}_0 \underline{e}_i}{\left| \underline{x}_0 - \sum_{i=1}^E \underline{e}_i^t \underline{x}_0 \underline{e}_i \right|}$$

Figure 3.5.2.3-2 shows the functional block diagram for the range sidelobe suppression algorithm. As the diagram shows, after the large target is detected, its location is utilized in the weight computation procedure. Then the FFT data is recompressed and multiplied by the weight sequence to null out the sidelobes. Although not shown in the figure, the range bin containing the large target peak is zeroed out. Also, in the implementation of the suppression algo-

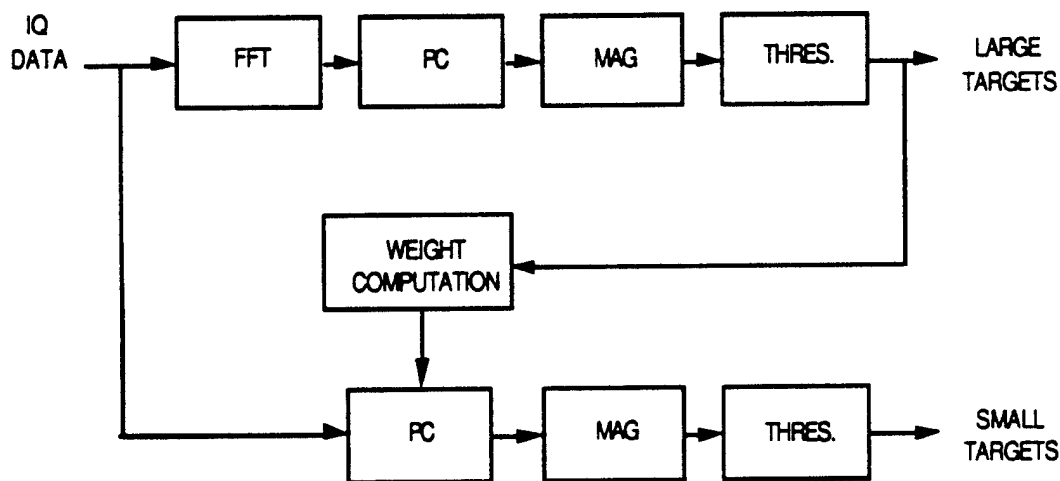


Figure 3.5.2.3-2. Range Sidelobe Suppression Functional Block Diagram

rithm, the region to search for potential small targets (between the K_1 and K_2 sidelobes) covers the entire sidelobe region of the large target on both sides of the large target peak. Hence all 12 sidelobes of the large target response will be suppressed.

The performance of the range sidelobe suppression algorithm is similar to the performance of the range response cancellation looked at before. Figure 3.5.2.3-3 below is the response after the suppression algorithm has been applied for the case where only 1 target is present at range bin 15. The response before suppression has been shown before in Figure 3.5.2.1-3 (a). As Figure 3.5.2.3-3 shows, the target peak at range bin 15 is completely suppressed, while all the sidelobes are minimized as much as possible. Hence, if there is only one large target present, range suppression will not create any false alarm.

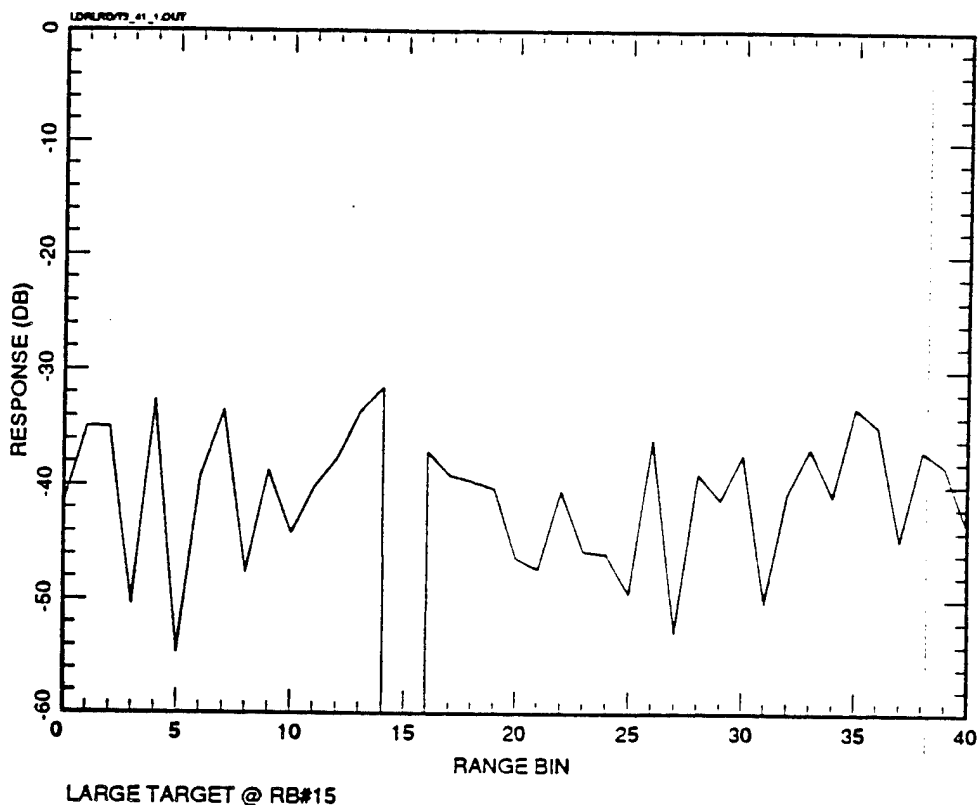


Figure 3.5.2.3-3. Response after range suppression. One target case.

The two-target case is shown next in Figure 3.5.2.3-4. The small target is 20 dB below the large target peak and is 2 range bins away from the large. Range suppression clearly reveals the small target at range bin 17 with the

residual response there slightly less than 20 dB down. It would be easy to detect this small target since it towers over the residuals in surrounding range bins. The small target has lost about 0.88 dB of its own power. This is slightly more than the signal loss after range response cancellation for the same scenario (Figures 3.5.2.1-4 (a) & (b)), when the small target loss was 0.34 dB. Thus, the performance of range suppression and range cancellation are quite similar with range cancellation slightly more effective.

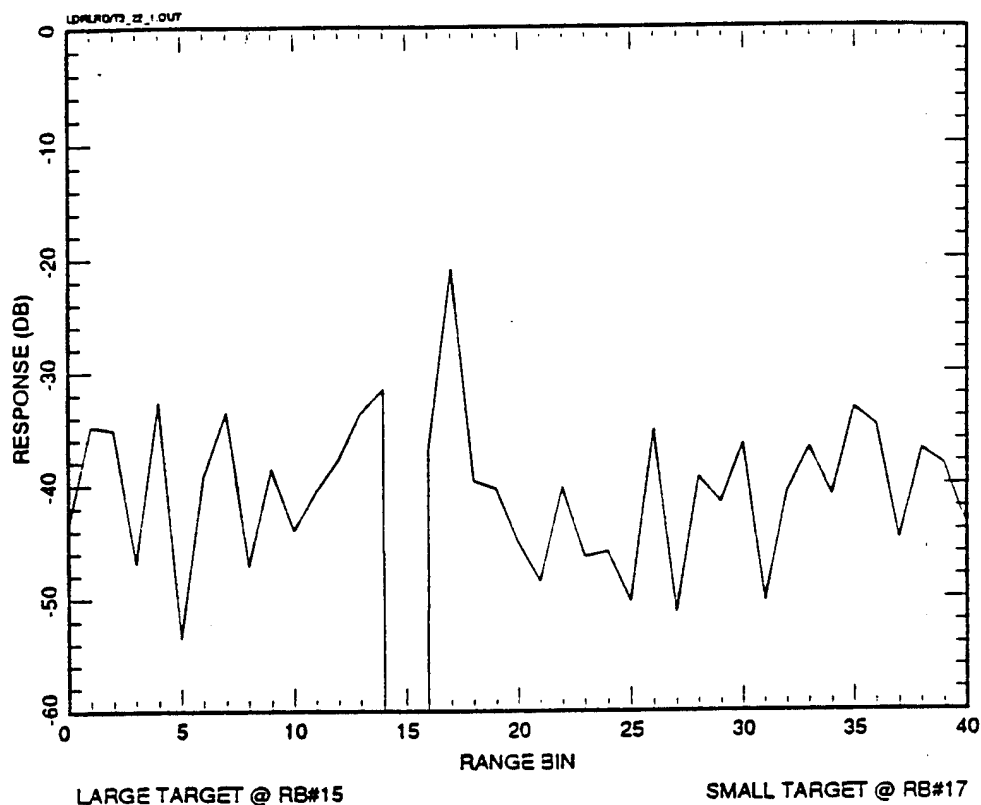


Figure 3.5.2.3-4. Response after range suppression. Two- target case.
2 range bins separation.

With 40 dB dynamic range, the range suppression algorithm is somewhat effective. Figure 3.5.2.3-5 shows the result for a small target also at 2 range bins away from the large target but with power 40 dB down. The region between range bin 2 and 28 contains the sidelobe response of the large target before suppression. After suppression, the residual response in range bin 17 is of the small target, which is about 41 dB down, and this is what we expect. However, as seen in the Figure, the residual sidelobe next closest to the large target peak at range bin 13 is quite significant, and can create a false alarm. This residual cannot be made smaller, and therefore, if the dynamic range is

greater than 40 dB, the residual will dominate after suppression, thus creating a false alarm.

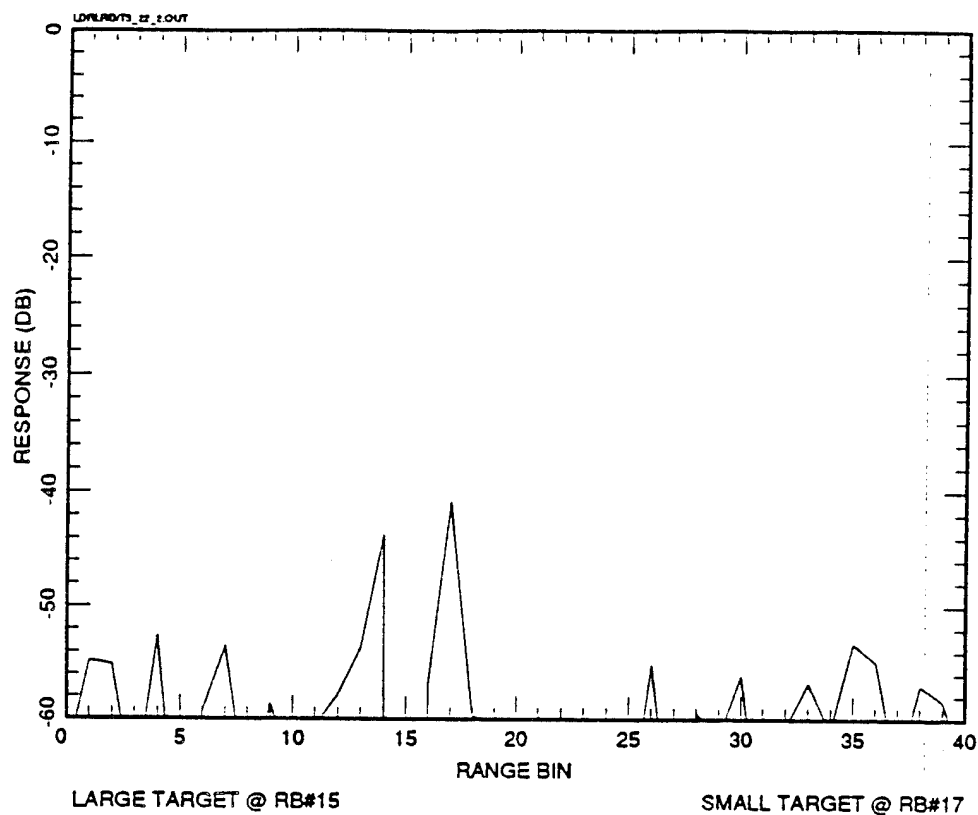


Figure 3.5.2.3-5. Response after range suppression. Two- target case. 2 range bins separation. 40 dB dynamic range.

3.5.2.4 Doppler Cancellation in the Time Domain

There are interesting possibilities for cancellation in the doppler domain. Digitally formed doppler filters exhibit excellent predictable response functions. That is, since coherent radars maintain spectrally clean transmit and reference signals, doppler filter sidelobe control with digital processors are quite feasible. For example, airborne tactical radars utilize 90 dB sidelobe Dolph-Chebyshev Filters to minimize clutter and co-target interference. The disadvantages with such filter response is the mismatch (better known as amplitude weighting) loss and resolution loss since the filter mainlobe broadens in comparison to a uniformly weighted filter. Since detection of low RCS target requires a taxing energy-aperture product, processing losses associated with heavy amplitude weighting may not be acceptable. Given a processing chain with a moderate

amplitude weighted filter bank, a promising technique of cancellation in the doppler domain is described next.

Figure 3.5.2.4-1 shows the functional block diagram of the doppler cancellation in the time domain algorithm. Basically, a three-point quadratic fit scheme is used to estimate the doppler, phase, and magnitude of the large peak. Then this estimated time-domain data of the large target is subtracted from the I/Q data in the range bins where the large target is detected. This resulting data is then passed on down through the processing chain including doppler filtering and pulse-compression. The entire procedure is repeated as many times as desired, with each time taking the largest peak and reducing it further.

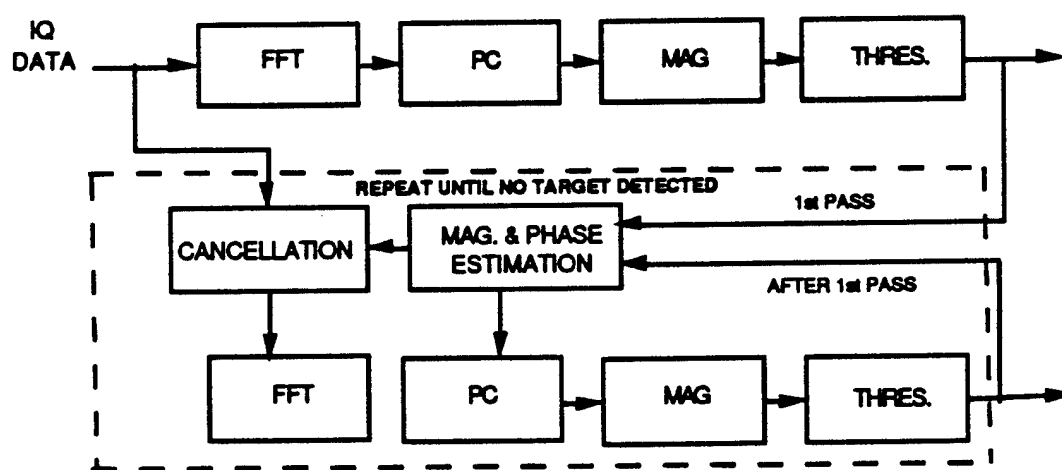


Figure 3.5.2.4-1. Doppler Cancellation in the Time Domain Functional Block Diagram

The performance of this technique is quite good. It has the ability to detect a small target even when the target separation is only one doppler filter apart. This is shown in Figure 3.5.2.4-2 (a) & (b). In (b), the small target definitely pops out clearly while the large target has been reduced by about 50 dB. The performance is also similarly very good when the target separation is 1.5 filters, as shown in Figure 3.5.2.4-3 (a) & (b).

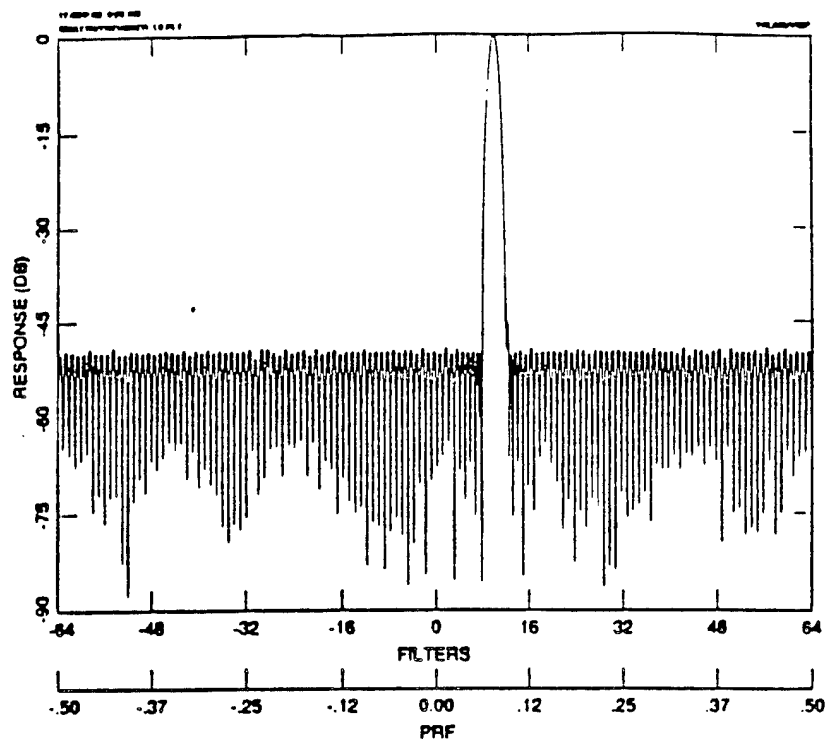


Figure 3.5.2.4-2 (a). Response before doppler cancellation. Two targets.
1 doppler filter separation. 40 dB dynamic range

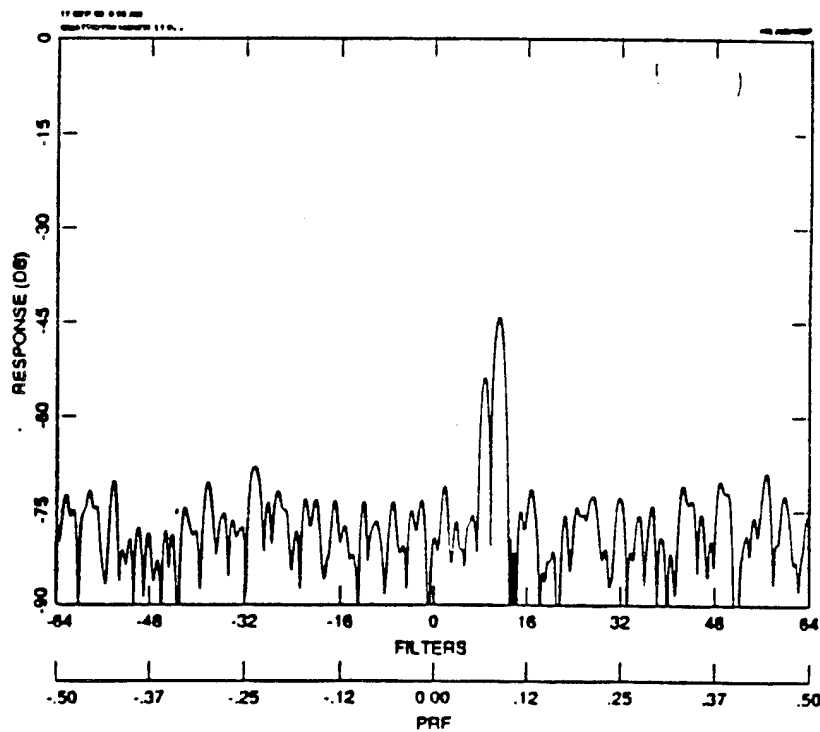


Figure 3.5.2.4-2 (b). Response after doppler cancellation. Two targets.
1 doppler filter separation. 40 dB dynamic range

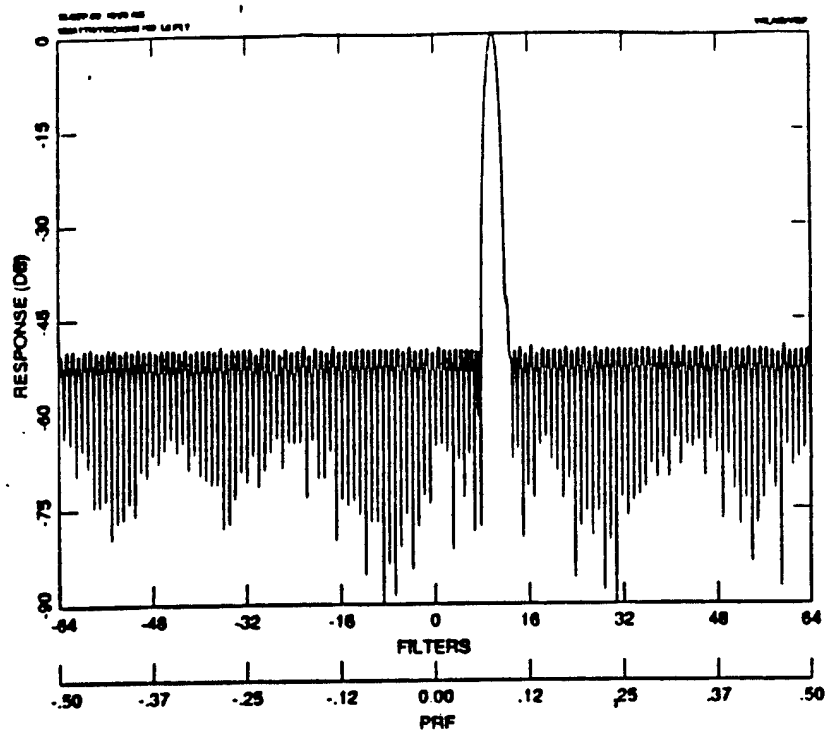


Figure 3.5.2.4-3 (a). Response before doppler cancellation. Two targets.
1.5 doppler filters separation. 40 dB dynamic range

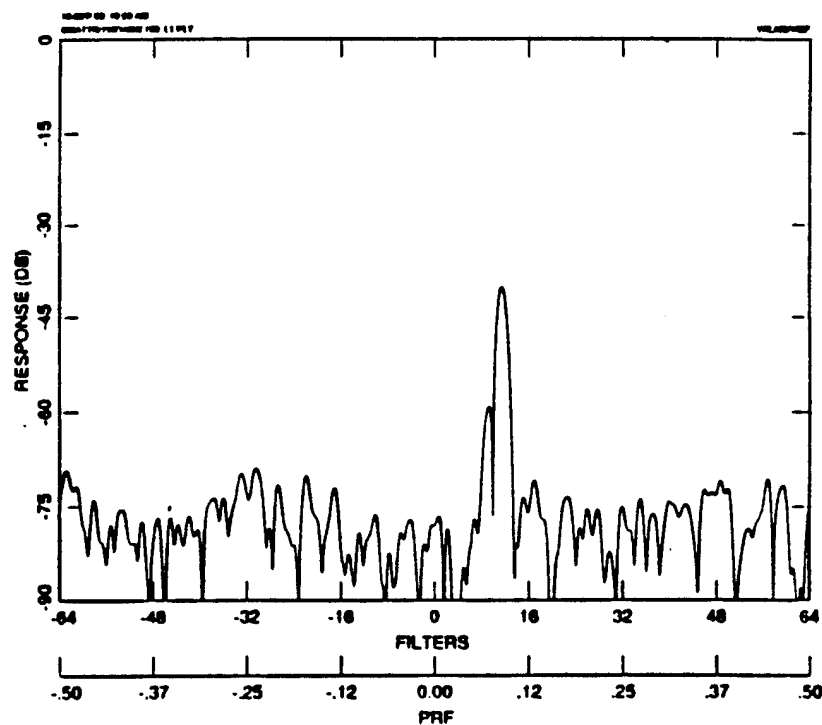


Figure 3.5.2.4-3 (b). Response after doppler cancellation. Two targets.
1.5 doppler filters separation. 40 dB dynamic range

3.5.2.5 Other techniques

We describe two other cancellation techniques that were presented in the proposal. However, the description will be brief since their performance was found to be inadequate. Figure 3.5.2.5-1 shows the functional block diagram for the doppler cancellation in the doppler domain technique. In this technique, the large target signal is detected, and then it is subtracted out from the doppler domain data, which is the output of the FFT block.

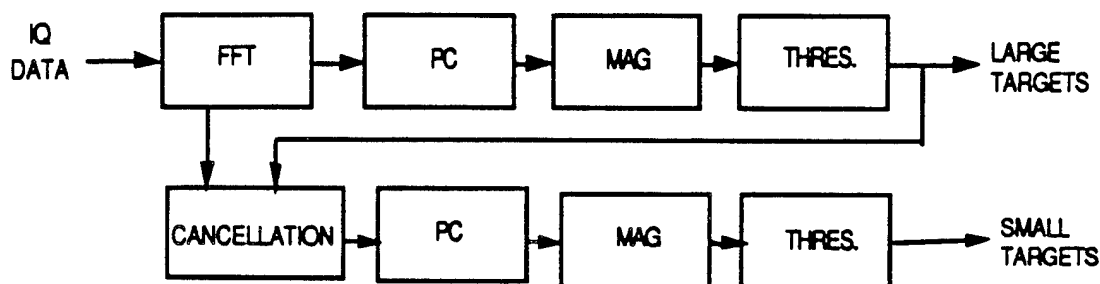


Figure 3.5.2.5-1. Doppler Cancellation in the Doppler Domain Functional Block Diagram

This technique was found to be quite ineffective at removing large-target in the doppler domain. Figure 3.5.2.5-2 is a plot in the doppler domain of a case where the large target is originally at doppler filter 105 and the small target is at filter 108. As the Figure shows, the large target cannot be completely removed; In fact, it still has a very large magnitude. Furthermore, this cancellation scheme shifts the targets to incorrect doppler filters, creating false alarms that are difficult to reject. Because of these characteristics, this technique was not pursued further.

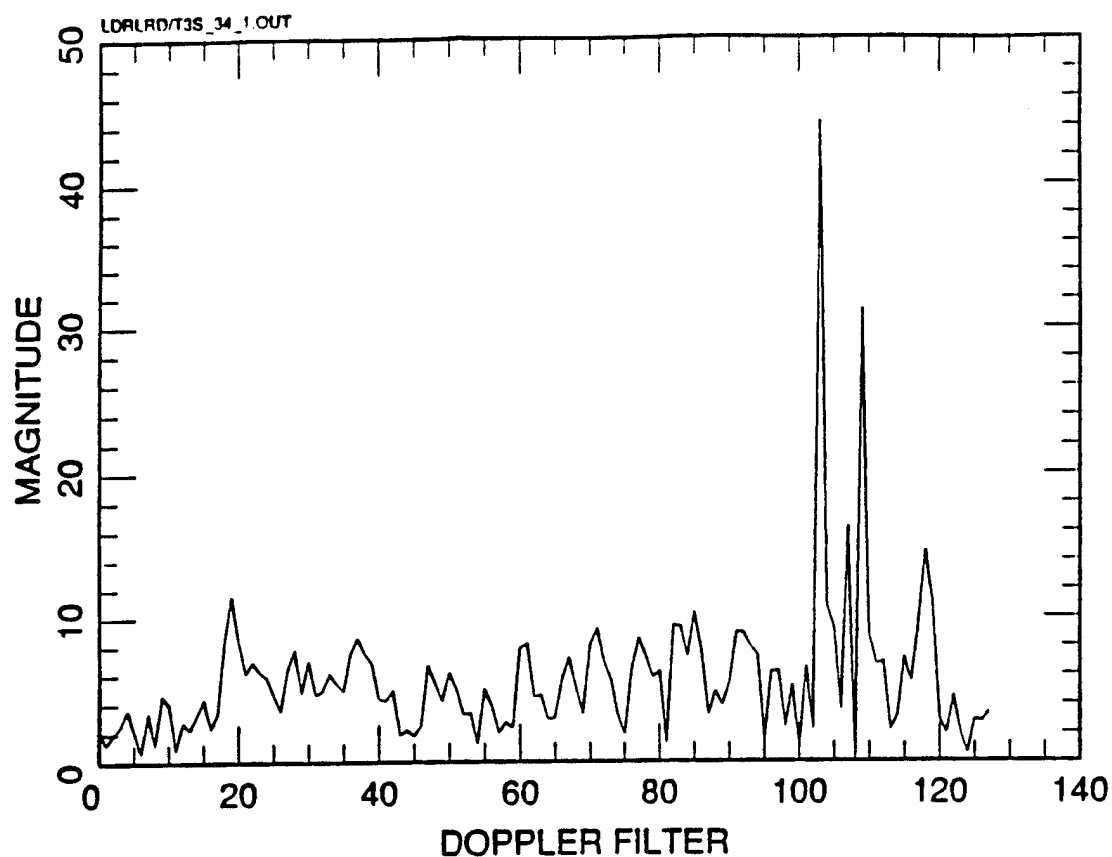


Figure 3.5.2.5-2. Doppler Cancellation in the Doppler Domain. Large Target @ filter #105. Small Target @ filter #108.

Another technique is a doppler domain suppression technique, which concatenates a low-order filter before the doppler filters. The low-order filter places a null in the doppler domain corresponding to each target. The parameters that set the low-order filter nulls can be determined by estimating target doppler and power. A Lattice Filter is an excellent candidate structure for the low-order filter since it is a time and order recursive filter. This means that it has a recursive formulation with time, and also as the order of the filter is increased the adaptively determined reflection coefficients do not have to be recalculated except for the added stage which can be calculated from the existing coefficients. Figure 3.5.2.5-3 shows such a filter, which will be followed by the standard doppler filters, when a strong target is detected. The coefficients are determined adaptively prior to doppler filter formation.

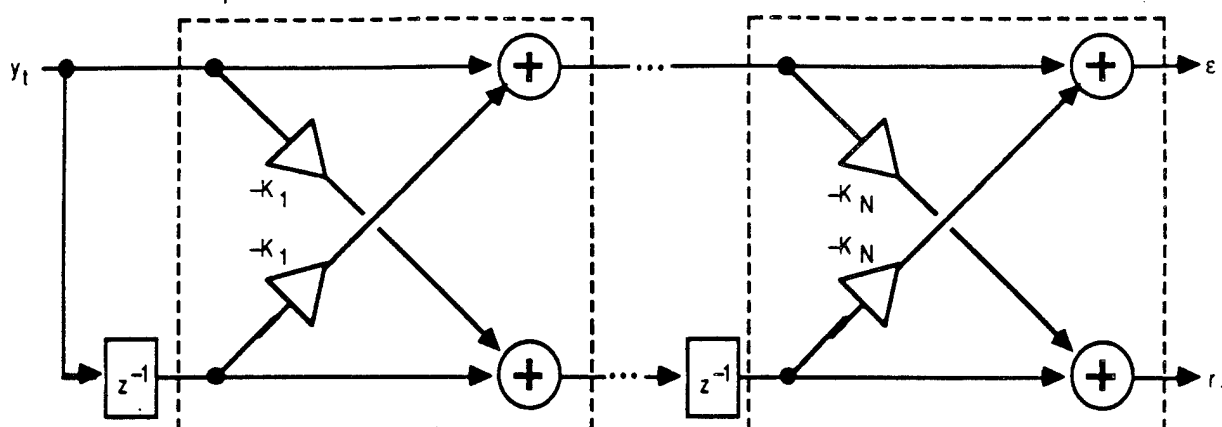


Figure 3.5.2.5-3. Implementation of a Lattice Filter.

Figure 3.5.2.5-4 shows the functional block diagram of the doppler suppression scheme using the Lattice filter. As the Figure shows, the large target information is used to determine filter coefficients that would place nulls in the doppler domain. The entire data is then passed through the FFT doppler filter bank and the usual processing sequence.

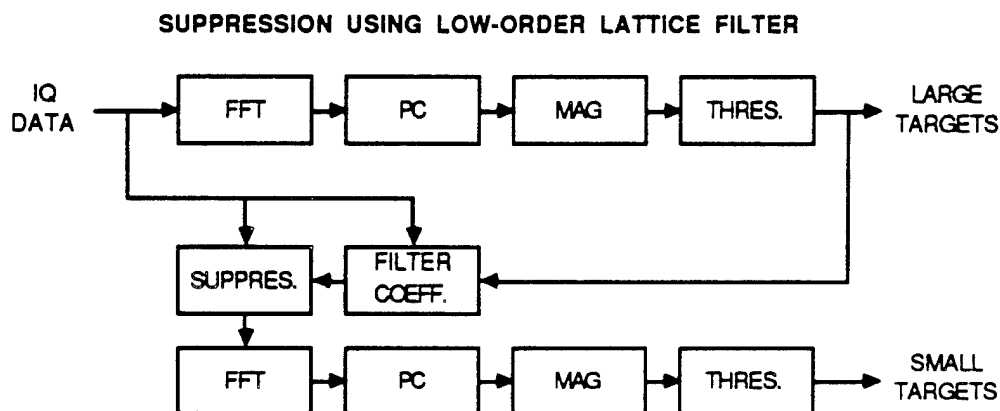


Figure 3.5.2.5-4. Doppler Domain Suppression with Lattice Filter
Functional Block Diagram

The lattice filter technique was also found to be inadequate at removing large-target interference. It is not able to remove the large target and thus there is no way to detect the small target. Hence, the doppler domain suppression with lattice filter technique was not pursued further.

3.5.3 Error Analysis

There are many error factors which must be addressed in the design of the cancellation or suppression mode. In this section, a methodology for incorporating these factors is presented. It is based on the utilization of budgets to establish a structured design approach, which also allows the control of the design.

To begin with, many of the factors can be broken down into contributions which reduce cancellation or suppression ability, increase false alarm (FA) rate or decrease angular, range and doppler accuracy. Hence, it is natural to show the effects by establishing the following budgets:

1. Cancellation/Suppression
2. False alarm
3. Angular, range and doppler estimation error

Besides these budgets, the normal budgets of losses and S/N contributors complete the system specification. From these budgets, probability of detection and estimation performance can be directly evaluated.

The potential error sources in the system are shown in Table 3.5.3-1. Our approach in doing the error sensitivity analysis is composed of three steps:

1. Determine the small target signal-to-interference ratio (SIR) without cancellation in the perfectly errorless system, and without the large target.
2. Introduce a single source of error from the Table into the system.
3. Determine the small target SIR after cancellation.
4. Compute the loss: The difference in SIR between step 3 and step 1 is the loss.

The small target SIR is taken to be the ratio of the small target signal at the peak response to the estimated interference (thermal noise included) in the surrounding range-doppler window. The estimation process is similar to CFAR, where a window is formed around the range-doppler cell of the small target, and the average interference power per cell is estimated. The interference

consists mainly of the large target sidelobes, which although reduced by cancellation, still have residues in the small target range-doppler cell.

TABLE 3.5.3-1. TABLE OF POTENTIAL ERROR SOURCES

Error source	Technique Domain				range of values	Description/Comment
	Angle	Range	Doppler	Joint		
Target Static						
1. Target nonreciprocal scattering	X	X	X	X	30 Hz to 200 Hz	
2. Target extent	X	X		X	30 Hz to 200 Hz	
3. Cross polarization response	X	X	X	X	-15 dB to -40 dB	
Target Dynamic relative to the Radar						
1. Aspect/Azimuth variations	X		X	X	0 to 50 deg/sec	roll rates and maneuvers
2. Polarization response variations	X			X	0 to 50 deg/sec	roll rates and maneuvers
3. Quadratic Error		X	X	X		angular and acceleration
4. Range Walk Error			X	X	0.4 to 2.5 kHz/sec	inbound velocities
Antenna Subsystem						
1. Radome mismatch	X			X		
a. Polarization response						
b. Polarization variations						
c. Frequency response						
2. Antenna static mismatch	X			X	-35 dB to -50 dB	
a. azimuth						
b. elevation						
3. Antenna motion	X		X	X	less than ± 0.5 BW	relative to beamwidth
a. deterministic						
b. random						
Transmit						
1. Code fidelity		X		X	a. 0.1 dB @ 60 Hz. b. 2 % c. ± 5 to 10 degrees ± 1 degree	
a. power supply amplitude modulation						
b. pulse drop						
c. phase errors						
transition random						
fixed random						
random sequences			X			
2. Spectral Purity			X	X	-100 dBc	
Down-Conversion						
1. Receive Code Fidelity		X		X	± 5 to 10 degrees ± 1 degree	
a. phase errors						
transition random						
fixed random						
random sequences			X			
2. Spectral Purity			X	X	-100 dBc	
3. Thermal noise	X	X	X	X	6 to 23 dB SNR	variable model
4. Video Filter Response		X	X	X	1.5 %	sampling BW
5. IQ imbalance	X	X	X	X	0.2 dB and 10 degree	
6. AO quantization	X	X	X	X	10 to 14 bits	
7. Timing Errors			X	X		
a. AO filter and range walk quantization	X	X	X		$\pm 10^{-11}$ sec. $\pm 3 \times 10^{-10}$ sec	
b. Edge effects						
Processing						
Target angle estimation	X			X	a function of SNR	in the estimation model
Range estimation error		X		X		
Doppler estimation			X	X		
Amplitude and Phase	X	X	X	X		cancellation alg.

Table 3.5.3-2 shows the loss associated with the three range domain techniques when there are no errors in the system. The two targets are separated by 4 range bins and there is a 20 dB dynamic range difference between them. The loss shown in this Figure is the difference between small target SIR after cancellation and the small target SIR computed in step 1 above.

TABLE 3.5.3-2. SMALL TARGET LOSS WITH NO ERRORS

Technique	Loss (dB)
Range Response Cancel.	0.099
Zero-Out Blanking	9.07
Range Suppression	1.49

This Table shows that in the errorless system, the range response cancellation technique results in negligible loss while the zero-out blanking technique reduces the small target signal greatly. Hence, zero-out blanking entails a large penalty each time it is used, and is not highly recommended. Range suppression gives good performance with a small amount of loss.

The first error source to be looked at is the effect of the video filter bandwidth. The cancellation loss associated with the three range domain techniques are given in Figure 3.5.3-1. The range response cancellation results in the least amount of loss while blanking gives the most loss. It is seen

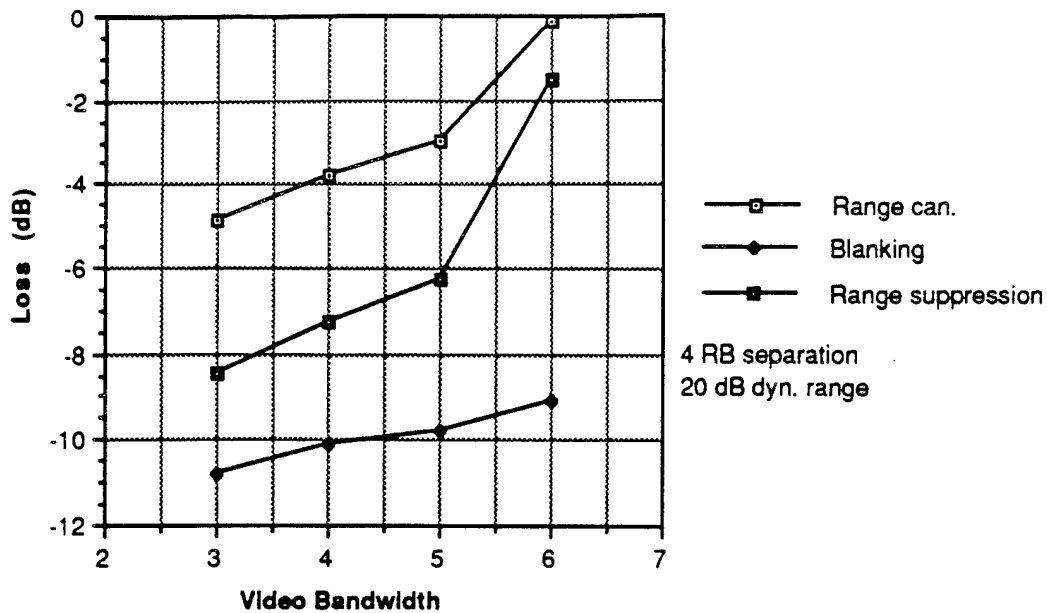


Figure 3.5.3-1. Cancellation loss vs. Video Bandwidth

that small video bandwidth results in large losses for all three techniques, and so the video filter must be designed carefully. In the cancellation simulation, the errorless case corresponds to when the video bandwidth is greater than 6.

Next, Figure 3.5.3-2 shows the effect of A/D quantization bits. In an actual radar processing system, the I/Q data is sampled by the A/D converter into digital data, and naturally this will reduce the accuracy of the data and the cancellation performance.

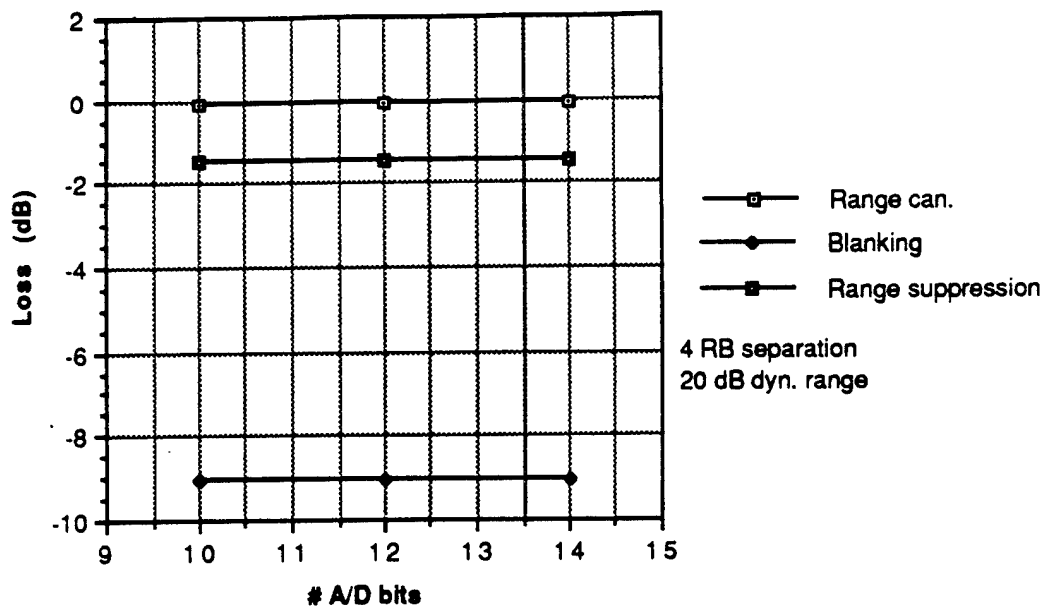


Figure 3.5.3-2. Cancellation loss vs. A/D Quantization bits

As the plot shows, the loss is essentially independent of the number of A/D bits, so the quantization does not have any real effect on the performance. The losses are at the same level as in the case where there are no errors in the system.

The next error to be looked at is I/Q Amplitude Imbalance error. This error affects the I/Q data by increasing the amplitude of the Q component of the data. Figure 3.5.3-3 shows the effect on the cancellation performance.

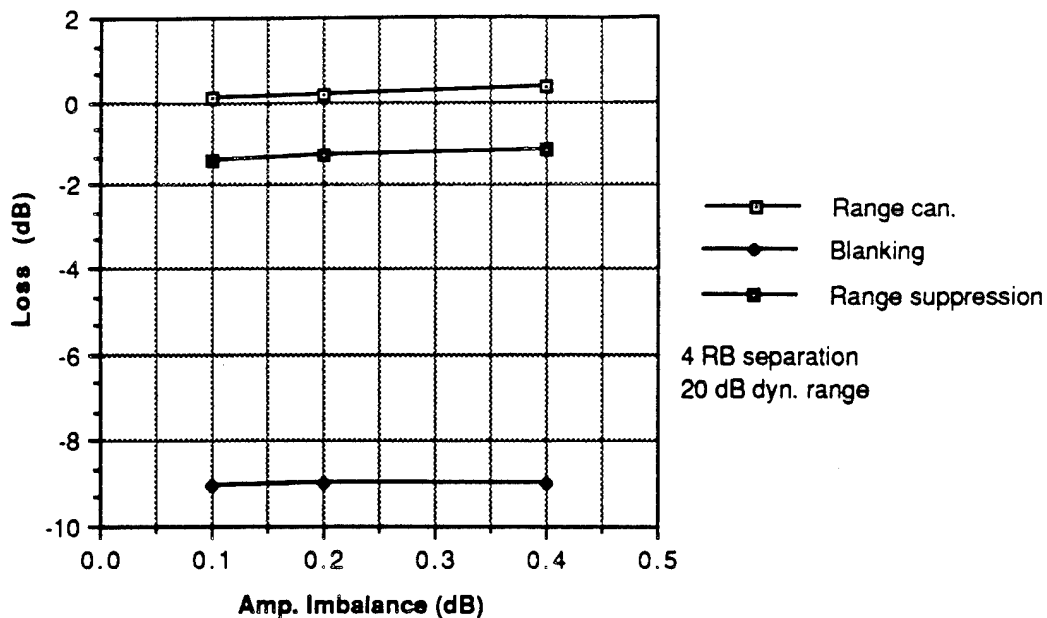


Figure 3.5.3-3. Cancellation loss vs. I/Q Amplitude Imbalance

When amplitude imbalance is in the system, the range response cancellation actually results in signal gain for the small target, as evidenced by the gain of about 0.2 dB. Somehow, the amplitude imbalance has reduced the interference and noise surrounding the small target, which increases the small target SIR. As for range suppression, it has a loss of about -1.5 dB, which is the same level of performance of cancellation as in the ideal case of Table 3.5.3-2.

I/Q Phase Imbalance also affects the Q component of the data, although in a different manner. It changes slightly the phase of the Q component. Figure 3.5.3-4 shows the effect of this error on the cancellation performance.

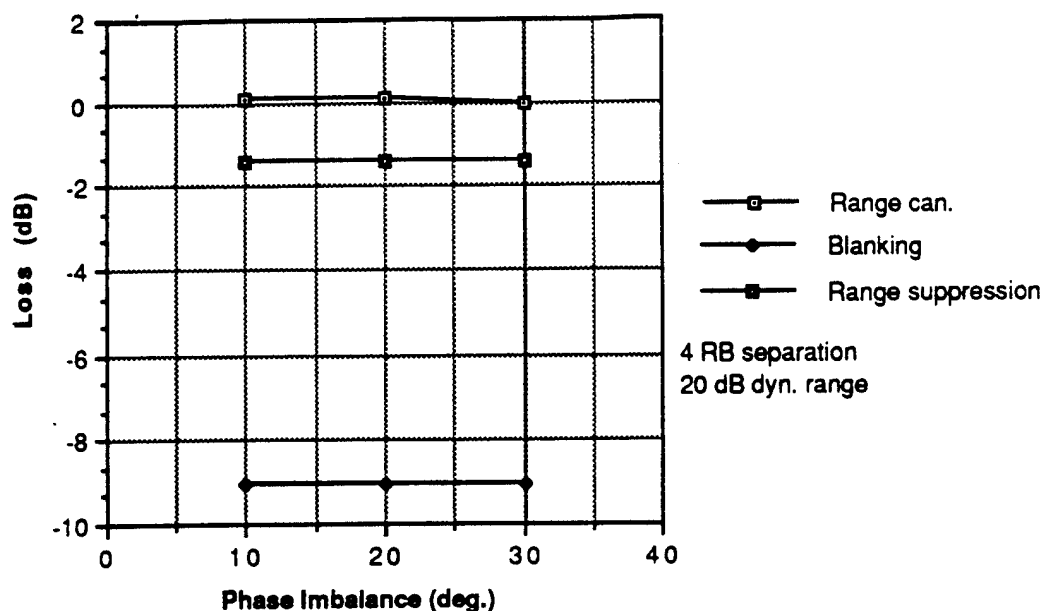


Figure 3.5.3-4. Cancellation loss vs. I/Q Phase Imbalance

I/Q Phase Imbalance has about the same effect upon the performance as the I/Q Amplitude Imbalance error. Range response cancellation has a slight gain over the ideal case while range suppression is about -1.5 dB, which is as good as the ideal case of Table 3.5.3-2.

Power Supply Amplitude Modulation error is examined next. This error is due to the system power supply modulating the target signal with a small 60 Hz sinusoidal ripple. The modulation is given in terms of percent modulation. The cancellation loss performance is given in Figure 3.5.3-5.

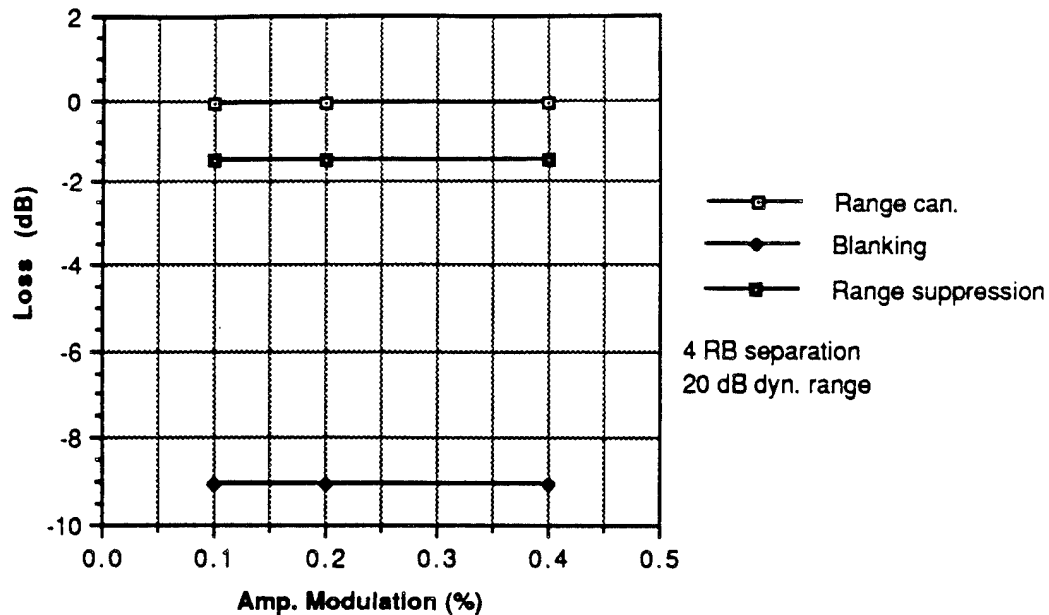


Figure 3.5.3-5. Cancellation loss vs. Power Supply Amplitude Modulation

Power Supply Amplitude Modulation does not seem to affect the system. The losses are the same level as the ideal case.

The next error is timing jitter. This is due to the system clock not being precise at its transitions. Figure 3.5.3-6 shows the effect of this error on cancellation. As is apparent there, the losses are independent of timing jitter. The losses are the same level as the ideal case.

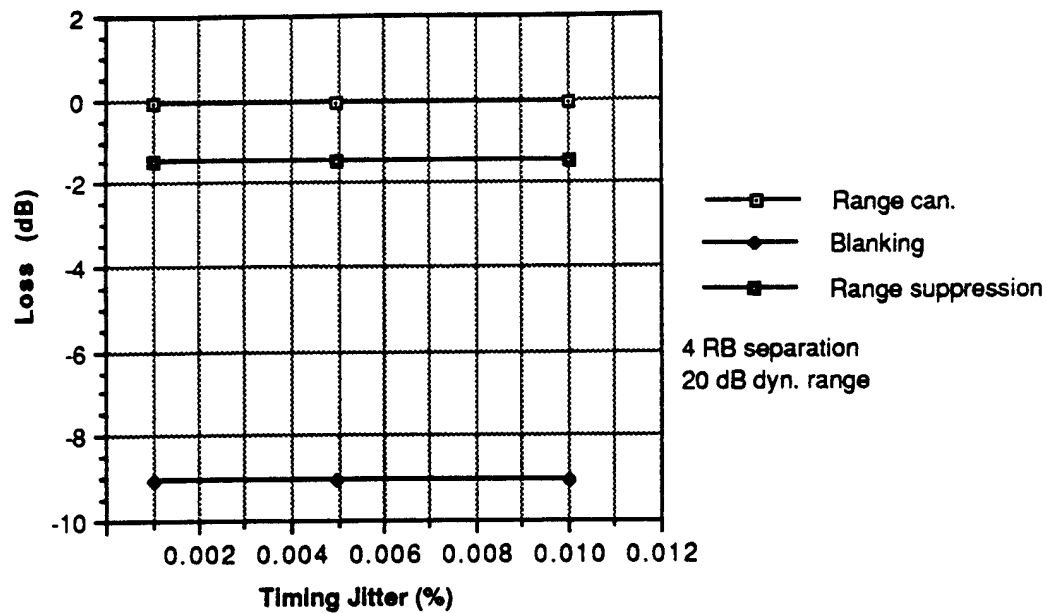


Figure 3.5.3-6. Cancellation loss vs. Timing Jitter

During each frame the radar receives many pulses back from the target. The range to the target is changing continuously during the frame time due to the velocity of the target. Hence, the target will be in a slightly different range bin position for each received pulse. This is called range walk error. Figure 3.5.3-7 shows the result of this error on the cancellation loss.

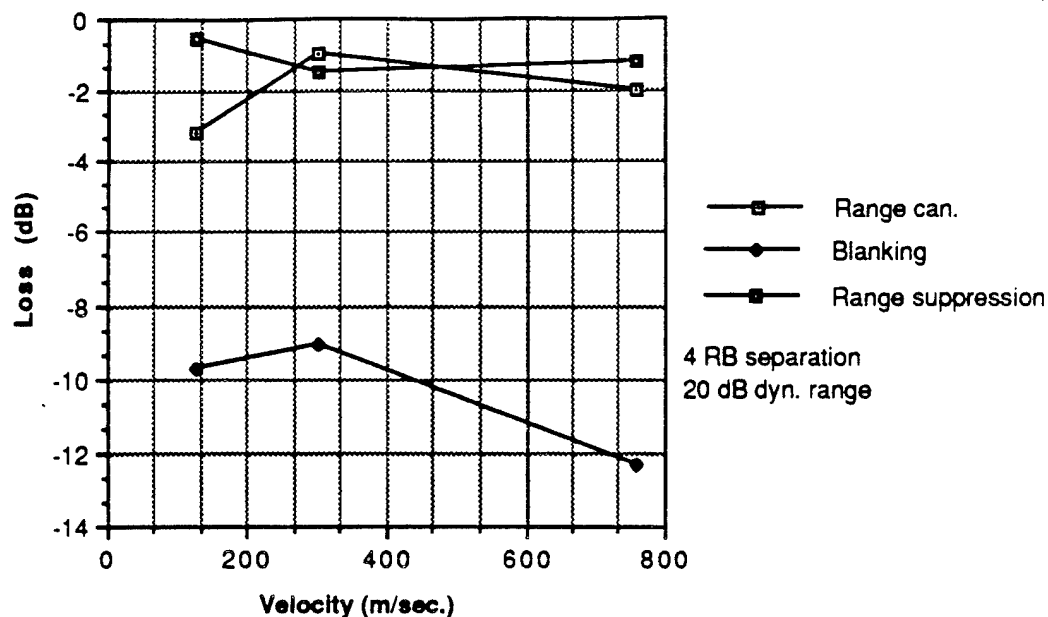


Figure 3.5.3-7. Cancellation loss vs. Range Walk Error

There is no discernible pattern to the loss created by range walk error. For the range response cancellation and zero-out blanking, the velocity of Mach 1 (300 m/sec) seems to create the least loss. Incidentally, it must be noted that in the ideal case of Table 3.5.3-2, range walk was present, at the velocity of 300 m/sec.

The final error to be looked at are the phase transition errors. These are the errors in the phase transition from one Barker bit to the next. Two possible errors sequences of length 13 were looked at and summarized in Table 3.5.3-3.

TABLE 3.5.3-3. LOSS WITH 2 PHASE TRANSITION ERROR SEQUENCES

PHASE ERRORS	SIGNAL LOSS (dB)		
	RANGE RESPONSE CANCELLATION	ZERO-OUT BLANKING	RANGE SUPPRESSION
1°,2°,3°,4°,3°,13°,14°,4°,5°,-5°,5°,0°,-10°	-0.1	-9.07	-1.49
5°,6°,5°,6°,7°,17°,18°,8°,9°,-1°,9°,19°,9°	-0.1	-9.07	-1.49

The losses are exactly the same as in the ideal case of Table 3.5.3-2. Hence, phase errors are not important.

Finally in Table 3.5.3-4 we list all the error sources. They are ranked in terms of the loss of the range response cancellation technique. Several things can be concluded from this table. First, video bandwidth is the most severe source of error. A large video bandwidth of at least 6 is crucial to good cancellation performance. Other error sources are negligible by comparison.

TABLE 3.5.3-4. ERROR SOURCES RANKED WITH LOSS

Error Source /Loss in dB	Range can.	Blanking	Range suppression
Video Bandwidth (Alpha=3.)	-2.78	-8.76	-6.38
Video Bandwidth (Alpha=4.)	-1.71	-8.04	-5.19
Range Walk (125 m/sec)	-1.09	-7.66	1.58
Video Bandwidth (Alpha=5.)	-0.92	-7.71	-4.22
Range Walk (758 m/sec)	0.09	-10.25	0.85
Video Bandwidth (Alpha=6.)	1.96	-7.01	0.57
Quantization (10 bits)	1.96	-7.01	0.57
Quantization (12 bits)	1.96	-7.01	0.57
Quantization (14 bits)	1.96	-7.01	0.57
Timing Jitter (0.001%)	1.96	-7.01	0.57
Timing Jitter (0.005%)	1.96	-7.01	0.57
Timing Jitter (0.01%)	1.96	-7.01	0.57
Range Walk (300 m/sec)	1.96	-7.01	0.57
Phase Errors (a)	1.96	-7.01	0.57
Phase Errors (b)	1.96	-7.01	0.57
Power supply Amp. Mod. (0.1 dB, 60 Hz)	1.96	-7.01	0.57
Power supply Amp. Mod. (0.2 dB, 60 Hz)	1.97	-7.01	0.57
Power supply Amp. Mod. (0.4 dB, 60 Hz)	1.97	-7.01	0.58
I/Q Phase Imbalance (0.1 dB, 30°)	2.01	-6.98	0.67
I/Q Amplitude Imbalance (0.1 dB, 10°)	2.17	-6.98	0.67
I/Q Phase Imbalance (0.1 dB, 10°)	2.17	-6.98	0.67
I/Q Phase Imbalance (0.1 dB, 20°)	2.18	-6.98	0.68
I/Q Amplitude Imbalance (0.2 dB, 10°)	2.24	-6.95	0.75
I/Q Amplitude Imbalance (0.4 dB, 10°)	2.39	-6.9	0.92

(a) = 1°, 2°, 3°, 4°, 3°, 13°, 14°, 4°, 5°,
-5°, 5°, 0°, -10°

(b) = 5°, 6°, 5°, 6°, 7°, 17°, 18°, 8°, 9°,
-1°, 9°, 19°, 9°

Assume 20 dB dyn. range except where
noted.

Small target is 4 RB away.

3.5.4 Processing Requirements

Adaptive processing techniques can have moderate to extreme resource demands depending on the available number of degrees of freedom, N_a . For example, ECM noise cancellation throughput requirements are proportional to N_a^3 . Batch processing demands memory capacity proportional to the number of channels. It is recognized that with judicious application of large target cancellation algorithm, one will have a minimal demand of processing resources.

Three criteria can be used to evaluate the processing resource demands for each candidate technique. Loading or throughput, which is the number of computer arithmetic operations required by each algorithm, is the most important criterion. Second is the VAX CPU time required and third, as a byproduct, the number of VAX Fortran 77 instructions required for executing the algorithms.

Corresponding to each technique, Figure 3.5.4-1 parametrically provides the computational loading formulas and Figure 3.5.4-2 shows an example of throughput loading for a set of waveform parameters. The notation for the formulas is given in Table 3.5.4-1. Finally, in Figure 3.5.4-3, the Fortran lines of code and VAX CPU Secs. required for each algorithm is tabulated.

NO CANCELLATION
$\text{NFFT} \cdot \text{NRB} \cdot (5 \cdot \log_2(\text{NFFT}) + 2 \cdot \text{NPCR} + \text{NTH} + 6)$
CANCELLATION with PC Response
$\begin{aligned} &\text{NFFT} \cdot \text{NRB} \cdot (5 \cdot \log_2(\text{NFFT}) + 2 \cdot \text{NPCR} + \text{NTH} + 6) \\ &+ \text{NFFT} \cdot \text{NRB} \cdot (\text{NTH} + 1) \\ &+ 6 \cdot \text{NTAR} \cdot (\text{NPCR} + 2) \end{aligned}$
BLANKING (Zero Out)
$\begin{aligned} &\text{NFFT} \cdot \text{NRB} \cdot (5 \cdot \log_2(\text{NFFT}) + 2 \cdot \text{NPCR} + \text{NTH} + 6) \\ &+ \text{NFFT} \cdot \text{NRB} \cdot (2 \cdot \text{NPCR} + \text{NTH} + 4) \\ &+ 3 \cdot \text{NTAR} \cdot (\text{NPCR} + 1) \end{aligned}$
RANGE SIDELobe SUPPRESSION
$\begin{aligned} &\text{NFFT} \cdot \text{NRB} \cdot (5 \cdot \log_2(\text{NFFT}) + 2 \cdot \text{NPCR} + \text{NTH} + 6) \\ &+ \text{NFFT} \cdot \text{NRB} \cdot (\text{NTH} + 4) + \text{NV} \cdot \text{NFFT} \cdot (4 \cdot \text{Nt} - 2) \\ &+ \text{NV} \cdot \text{NV} \cdot (2 \cdot \text{Nt} - 1/2) + \text{Nt} \cdot \text{NV} \end{aligned}$
DOPPLER CANCELLATION IN TIME DOMAIN
$\begin{aligned} &\text{NFFT} \cdot \text{NRB} \cdot (5 \cdot \log_2(\text{NFFT}) + 2 \cdot \text{NPCR} + \text{NTH} + 6) \\ &+ \text{NITER} \cdot [\text{NPCR} \cdot \text{NFFT} \cdot (5 \cdot \log_2(\text{NFFT}) \\ &\quad + 2 \cdot \text{NPCR} + \text{NTH} + 6) + 8 \cdot \text{NFFT}] \end{aligned}$

Assume complex operation = 10 real operations
 complex add = 2 real operations
 real operation : real add or real multiply or clear

Figure 3.5.4-1. Signal Processing Loading Computation Formulas

Signal Processing	# of Real Operations per Array Time	Throughput (Mrop)
No Cancellation	540544	103.00
Range Response Cancellation	602382	114.78
Blanking	650494	123.95
Range Sidelobe Suppression	718090	136.83
Doppler Cancel. in the Time Domain	885376	168.71

PRI = 41 ms
 NFFT = 128
 NRB = 41
 NPCR = 13
 NTAR = 1
 NTH = 24
 NK = 15
 Array Time AT = 5.248 ms

Figure 3.5.4-2. An Example of Throughput Calculations

Signal Processing	Lines of FORTRAN Code	CPU Secs.
Range Response Cancellation	145	5.78
Blanking	122	6.42
Range Sidelobe Suppression	172	6.41
Doppler Cancel. in the Time Domain	N/A	N/A

Figure 3.5.4-3. Lines of code and CPU Secs. for the Algorithms

TABLE 3.5.4-1. NOTATION FOR PROCESSOR LOADING COMPUTATIONS

<u>NOTATION</u>	
NFFT	Number of doppler filters
NRB	Number of range bins
NPCR	Pulse Compression ratio
NTH	Number of cells used in threshold estimate
PRI	Pulse repetition interval
NTAR	Number of large targets detected
NDET	Number of (large target) detections (=3NTAR)
NV	The number of sidelobes suppressed
Nt	#of digits in the range suppression code
NITER	Number of iterations desired for the doppler can. in time domain technique
co	complex operation (* & + =10 ro)
ca	complex add (=co/2 other use co/5)
ra	read add
rm	real multiplier (=co/4)

The results of these Figures can be summarized. In the range domain, the range response cancellation technique requires the least processing resources overall while the range suppression requires the most. This only reaffirms the conclusion partially reached in the previous Sections that the range response cancellation technique is the most valuable. It is effective in cancellation, not subjected to as much errors, and also the simplest to implement. Hence, this technique should definitely be the first technique to be used for co-target interference rejection. It must be kept in mind, however, that the range suppression technique is only 20% more resource intensive than range response, as can be seen in Figure 3.5.4-2, while its effectiveness in revealing the small target is almost as good. Zero-out blanking requires only 8% more resources than range response cancellation, but its performance, as seen in the previous Sections is limited.

The doppler cancellation in time domain technique is the most processing intensive. However, it is a very effective technique and should be implemented even with its high cost.

3.5.5 Technique Summary

Table 3.5.5-1 summarizes the effectiveness of the three cancellation algorithms that are effective in rejecting co-target interference. Notice that the zero-out blanking technique has been altogether abandoned since it requires at least 5 range bin target separation to be effective. The two remaining techniques in the range domain show very similar performance except for the throughput requirements, where range suppression requires about 20% more throughput than range response cancellation. Airborne radars are limited in their available processing resources, and this could be the deciding factor in favoring range response cancellation over the range suppression technique. Nevertheless, it is important to have two available techniques in the range domain to expand the available options. In the doppler domain, even though it is processing intensive, we have available a technique that is effective in discriminating targets as close as 1 doppler filter apart.

TABLE 3.5.5-1. EFFECTIVENESS SUMMARY FOR ALGORITHMS

TECHNIQUE	REGION OF EFFECTIVENESS (in separation)	LOSS (dB)	THROUGHPUT (Mrop)
<u>Range domain</u>			
RANGE RESPONSE CANCEL.	@ 2 RB and up	0.099	114.78
RANGE SUPPRESSION	@ 2 RB and up	1.49	136.83
<u>Doppler domain</u>			
DOPPLER CANCEL. IN TIME DOMAIN	@ 1 filter and up	0.60	168.71

3.6 Tracking Implementation

Given that co-target interference reduction can be achieved, the system level effectiveness of the reduction depends on the use of the resulting track data. For example, if a large target and a small target are flying in formation to deliberately conceal the existence of the small target, it would be sufficient to establish the presence of the small target and check from time to time to insure that the formation remained unchanged. In handing off to local fire control assets, the message would be that one (or more) small targets are in close proximity to the designated bright target, and the local assets could then acquire the small target on their own. This would essentially be a surveillance raid assessment strategy. On the other hand, the local assets would need the CTIR techniques to successfully break out and engage the small target(s).

On the other hand, if target (between large and small) separation was sufficiently large, keeping individual tracks of all targets (which would involve repeatedly applying CTIR techniques) could be of tactical value if local fire control assets could benefit from such information. Thus, the system effectiveness of a particular tracking strategy using CTIR techniques depends on the value of the data in the fire control/engagement (or situation assessment) portion of the mission.

In this Section we examine the value of using CTIR techniques and the resulting track data in a comprehensive Multiple Target Tracking (MTT) simulation developed at Hughes. A typical MTT system consists of five basic elements, illustrated in Figure 3.6-1:

- Sensor data processing and measurement formation,
- Data correlation,
- Track maintenance logic (initiation, confirmation, deletion),
- Estimate filtering and prediction, and
- Gating computations.

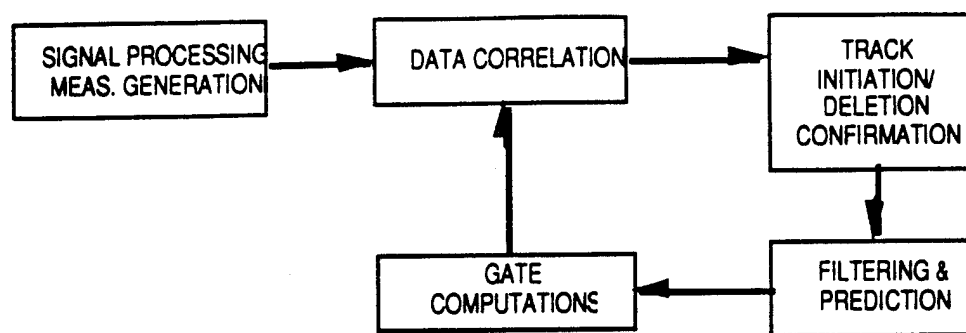


Figure 3.6-1. Elements of a Typical MTT System.

Sensor data processing and measurement formation involves signal processing, including clutter and interference rejection processing, range bin and doppler filter formation, and threshold selection and testing for detection. Measurements typically consist of range, doppler, and angle discriminants. However, when large dynamic ranges exist between closely spaced targets, there are likely to be characteristics of the measurements that differ from those obtained from "standard" targets. These characteristics are called measurement biases and must be understood and taken into account from the start, since they may have a significant impact on tracking system design and performance. The biases are examined in greater details later on in this section.

Data correlation involves assigning new measurement data to existing tracks. This process can be very difficult in closely spaced target situations. If targets are spaced widely enough relative to track and measurement accuracy, unambiguous correlation is easy, and almost any technique will work (sequential Nearest Neighbor, for example). If targets are very closely spaced (relative to track and measurement accuracy), then miscorrelation will occur frequently, but resulting track(s) will be stable. In this case, the targets are too close to be tracked separately, and group or formation tracking is required. Group tracks consist of a group centroid estimate, a group count, and potentially a group extent estimate---the centroid estimate is based on measurements of several targets, and it is the centroid estimate that is used for track filtering and prediction. Group tracking is appropriate when measurements from individual elements of the different targets cannot be reliably differentiated or resolved. Formation tracking differs from group tracking in that although measurements of

individual targets can be resolved, the targets are too closely spaced to allow maintenance of unambiguous tracks. A formation track consists of several target tracks, each propagated by an average formation velocity. Since each element is tracked individually, no estimate of group count or extent is required. Errors in correlation (assigning the wrong measurement to a track) are expected, and occur without degrading tracking performance.

When targets are too closely spaced to be tracked unambiguously, but are too widely spaced to be tracked as a group or formation, the tracking process can become unstable. Errors in correlation can lead to erroneous velocity estimates, which in turn can result in track divergence, track loss, and false tracks. This type of behavior can occur when targets are close enough that the probability of false correlation is significant, but are spaced widely enough that correlation errors can lead to substantial kinematic errors. In this environment, special approaches are required to minimize the probability of false correlation (e.g. Multiple Hypothesis Tracking) and/or minimize the kinematic errors resulting from false correlation (such as Joint Probabilistic Data Association).

Track initiation, confirmation, and deletion are straightforward in unambiguous tracking regimes, but difficult in unstable situations. Track initiation is a tentative decision that certain measurements are from a target not already being tracked. Track confirmation results when this decision is made with more confidence. Deletion results when it is decided that a track is no longer being updated with valid target measurements, either because a target is no longer resolvable (or has disappeared for any other reason), or because the track has diverged and the true target is no longer within the track gates.

Filtering and prediction of estimates of target kinematics are performed by "smoothing" in some sense a sequence of noisy measurements. When detection probability is high, and targets are widely spaced, simple filtering techniques (such as fixed coefficient Alpha-Beta or Alpha-Beta-Gamma filters) are sufficient. When detection probability drops, or targets are more closely spaced, time-varying approaches such as Kalman filters become more desirable to extract as much information as possible from the available data. Although it is possible to use look-up tables for fixed coefficient filters to adapt the filter gains to changes in target behavior, the resulting filters are

complicated, and a simple (low order) Kalman filter is straightforward to design and implement. Unless large numbers of targets are expected or very high data-rates are involved, the processing load due to track kinematic filtering is generally much lower than the loading due to signal processing, since track computations are required relatively infrequently (at intervals on the order of .5 to 5 seconds). The LDR Simulation uses a 9-state Kalman filter.

In order to decide which measurements to use to update each track, a measure of the distance between the predicted track and each observation is computed. A tracking gate is a threshold applied to this distance: if the distance is exceeded, the measurement is not used for updating a track (the measurement is not within the track's gates), while if the distance is less than the threshold (the measurement is within the track's gates), the measurement is considered for use in updating the track (but not necessarily used). Gating is a way of simplifying the correlation process that immediately rules out unlikely correlation possibilities. To form accurate gates, an estimate of target track error is required---the larger the estimated uncertainty, the larger the gates, and conversely. The use of Kalman filters is very desirable from this perspective, since an error variance is explicitly propagated with the track state estimates that takes into account track update rate, measurement accuracy, and anticipated target maneuver capability.

Designing a tracking system involves selecting one or more techniques to perform each of these functions. It is desirable to avoid unnecessary complexity and computational load, but still provide acceptable performance. Target spacing, detection probability, maneuver capabilities, and the effects on measurements resulting from the specific signal processing used in this system must be taken into account, and weighed against available processing resources, number of targets expected, and anticipated antenna loading.

The aforementioned MTT Simulation available at Hughes contains all these elements. Specifically, this Simulation uses Multiple Hypothesis Tracking (MHT) in doing data correlation to existing tracks and to generate track hypotheses. The LDR Program utilizes the information about co-target interference and combine this with the MHT Simulation. The value of doing this is examined in a later section.

3.6.1 Filtering

Of the 5 basic elements of an MTT system described in Section 3.6, only the filtering and prediction element is described in detail. This is because it was necessary to modify the existing MHT Simulation to incorporate a filter that can accommodate a true radar measurement model. Filtering and prediction are the fundamental elements of any tracking system. They are used to estimate present and future target kinematic quantities such as position, velocity, and acceleration. In a tracking simulation when the detection probability is high, and targets are widely spaced, simple filtering techniques (such as fixed coefficient α - β filters) are sufficient. When detection probability drops, or targets are more closely spaced, time-varying approaches such as Kalman filters become more desirable to extract as much information as possible from the available data. This latter case fits more closely with scenarios where the LDR techniques would be applied to.

The choice of a coordinate system is an important element of a tracking system. In most MTT systems, it is important to express tracks in a common coordinate system to facilitate data association and tactical situation assessment. A pseudo-inertial coordinate system such as NED (North, East, Down) is particularly useful for airborne systems, but it is also applicable for surface tracking systems. This coordinate system is shown in Figure 3.6.1-1. The radar system is at the origin.

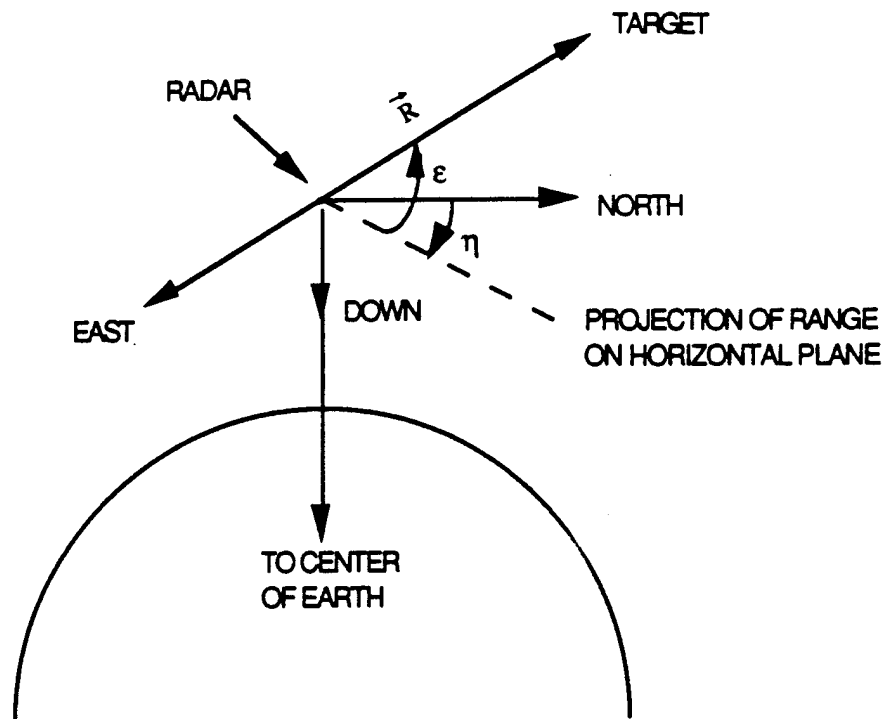


Figure 3.6.1-1. Radar centered inertial (NED) coordinate system

The north, east, and down coordinates are referred to from now on as the x , y , and z coordinates, respectively. The Kalman filter implemented in the LDR Tracking Simulation is a 9-state filter, tracking the position, velocity, and acceleration states for each of the three coordinates. Thus the state vector containing the tracked target dynamics can be written as:

$$\mathbf{x}(k) = \begin{bmatrix} x_1(k) \\ x_2(k) \\ x_3(k) \\ x_4(k) \\ x_5(k) \\ x_6(k) \\ x_7(k) \\ x_8(k) \\ x_9(k) \end{bmatrix} = \begin{bmatrix} x \\ \dot{x} \\ \ddot{x} \\ y \\ \dot{y} \\ \ddot{y} \\ z \\ \dot{z} \\ \ddot{z} \end{bmatrix},$$

where the dot means velocity and double dot means acceleration.

The target dynamic process is assumed to be modeled in the discrete Markov form:

$$\mathbf{x}(k+1) = \Phi \mathbf{x}(k) + \mathbf{q}(k) + \mathbf{f}(k+1|k),$$

where Φ is the transition matrix; $\mathbf{q}(k)$ is the zero-mean, white, Gaussian noise process with known covariance Q ; and $\mathbf{f}(k+1|k)$ is a known deterministic input, such as the relative position change associated with own-ship motion. In the LDR Interaction Simulation $\mathbf{f}(k+1|k)$ is zero because stationary radars are assumed. The discrete-time Markov process can be defined as a process in which the statistical representation of the process in the future (scan $k+1$) is completely determined by the present state (scan k).

The Singer target maneuver model is used. In this model, the acceleration is modeled as a first-order Markov process, which can be written

$$a(k+1) = \rho_m a(k) + \sqrt{1 - \rho_m^2} \sigma_m r(k).$$

The maneuver correlation coefficient ρ_m is defined in terms of the maneuver time constant τ_m

$$\rho_m = e^{-\frac{T}{\tau_m}},$$

and σ_m is the maneuver standard deviation. $r(k)$ is the standard normal random variable while T is the sampling interval.

With the Singer model, and defining β to be $1/\tau_m$, the transition matrix is given by:

$$\Phi_{3 \times 3} = \begin{bmatrix} 1 & T & \frac{1}{\beta^2}(-1 + \beta T + \rho_m) \\ 0 & 1 & \frac{1}{\beta}(1 - \rho_m) \\ 0 & 0 & \rho_m \end{bmatrix}$$

The matrix shown is for the 3-state case. For our 9-state filter, the matrix is duplicated down the main diagonal:

$$\Phi = \begin{bmatrix} \Phi_{3 \times 3} & 0_{3 \times 3} & 0_{3 \times 3} \\ 0_{3 \times 3} & \Phi_{3 \times 3} & 0_{3 \times 3} \\ 0_{3 \times 3} & 0_{3 \times 3} & \Phi_{3 \times 3} \end{bmatrix},$$

where $0_{3 \times 3}$ is the 3 x 3 zero matrix.

The process (or maneuver) excitation covariance matrix is:

$$Q = \begin{bmatrix} Q_{3 \times 3} & 0_{3 \times 3} & 0_{3 \times 3} \\ 0_{3 \times 3} & Q_{3 \times 3} & 0_{3 \times 3} \\ 0_{3 \times 3} & 0_{3 \times 3} & Q_{3 \times 3} \end{bmatrix},$$

where the matrix $Q_{3 \times 3}$ is given in Reference 3, pg. 32.

The radar measurements give the target range (r), range rate (\dot{r}), and angles (η and ϵ). These measured quantities are functions of the state variables in the state vector, corrupted by uncorrelated noise. Thus, the 4-dimensional measurement vector is modeled as

$$y(k) = h(x(k)) + v(k), \quad (\text{Eqn. 3.6.1-1})$$

where

$$h(x(k)) = \begin{bmatrix} r(x(k)) \\ \dot{r}(x(k)) \\ \eta(x(k)) \\ \epsilon(x(k)) \end{bmatrix} = \begin{bmatrix} \sqrt{x^2 + y^2 + z^2} \\ \frac{x\dot{x} + y\dot{y} + z\dot{z}}{\sqrt{x^2 + y^2 + z^2}} \\ \tan^{-1}(y/x) \\ \tan^{-1}(-z/\sqrt{x^2 + y^2}) \end{bmatrix}$$

$v(k)$ is zero mean, white, Gaussian measurement noise with covariance matrix R given by

$$R = \begin{bmatrix} \sigma_r^2 & 0 & 0 & 0 \\ 0 & \sigma_r^2 & 0 & 0 \\ 0 & 0 & \sigma_\eta^2 & 0 \\ 0 & 0 & 0 & \sigma_\epsilon^2 \end{bmatrix}$$

The measurement accuracy of the radar is specified by the terms in the R matrix. For example, range measurement accuracy is given by σ_r .

The generic Kalman filter equations are given by:

$$\hat{\mathbf{x}}(k|k) = \hat{\mathbf{x}}(k|k-1) + K(k) [y(k) - H \hat{\mathbf{x}}(k|k-1)] \quad (\text{Eqn. 3.6.1-2})$$

$$K(k) = P(k|k-1) H^T [H P(k|k-1) H^T + R]^{-1}$$

$$P(k|k) = [I - K(k) H] P(k|k-1)$$

$$\hat{\mathbf{x}}(k+1|k) = \Phi \hat{\mathbf{x}}(k|k)$$

$$P(k+1|k) = \Phi P(k|k) \Phi^T + Q,$$

where $\hat{\mathbf{x}}(k+1|k)$ is the 1-step predicted estimate of the state vector at time k , and $\hat{\mathbf{x}}(k|k)$ is the smoothed estimate of the state vector at time k , K is the gain matrix, H is the measurement matrix, and P is the covariance matrix of the estimation error:

$$P(k) = E\{[\mathbf{x}(k) - \hat{\mathbf{x}}(k)][\mathbf{x}(k) - \hat{\mathbf{x}}(k)]^T\}.$$

Note that in the generic equation 3.6.1-2 above, the measurement matrix H is a linear matrix. However, our measurement model in Eqn. 3.6.1-1 uses a nonlinear \mathbf{h} function. In these cases, it is necessary to linearize the \mathbf{h} function into an H matrix through a Taylor expansion method, which results in what is

called the extended Kalman filter¹³. The H matrix for our filter is a 4 x 9 matrix and is given by:

$$H(\hat{\mathbf{x}}(k|k-1)) = \left. \frac{\partial \mathbf{h}(\mathbf{x})}{\partial \mathbf{x}} \right|_{\mathbf{x} = \hat{\mathbf{x}}(k|k-1)}$$

$$= \begin{bmatrix} \frac{x}{r} & 0 & 0 & \frac{y}{r} & 0 & 0 & \frac{z}{r} & 0 & 0 \\ \frac{[x(y^2+z^2) - x(yy+zz)]}{r^3} & \frac{x}{r} & 0 & \frac{[y(x^2+z^2) - y(xx+zz)]}{r^3} & \frac{y}{r} & 0 & \frac{[z(x^2+y^2) - z(xx+yy)]}{r^3} & \frac{z}{r} & 0 \\ \frac{-y}{x^2+y^2} & 0 & 0 & \frac{x}{x^2+y^2} & 0 & 0 & 0 & 0 & 0 \\ \frac{-xz}{r^2\sqrt{x^2+y^2}} & 0 & 0 & \frac{yz}{r^2\sqrt{x^2+y^2}} & 0 & 0 & \frac{-\sqrt{x^2+y^2}}{r^2} & 0 & 0 \end{bmatrix},$$

$$\text{where } r = \sqrt{x^2 + y^2 + z^2},$$

$x, y, z, \dot{x}, \dot{y}, \dot{z}$ are formed from the predicted state vector $\hat{\mathbf{x}}(k|k-1)$.

Also, the state estimate update equation, Eqn. 3.6.1-2, needs to be modified for the extended Kalman filter. It is given by:

$$\hat{\mathbf{x}}(k|k) = \hat{\mathbf{x}}(k|k-1) + K(k) [y(k) - \mathbf{h}(\hat{\mathbf{x}}(k|k-1))].$$

3.6.2 Masking Region and Measurement Biases

A large target will mask a smaller target from detection if their separation is very small. Depending upon the geometry, the masking region may extend for a significant amount of time. Figure 3.6.2-1 (a), (b), and (c) show the minimum separation required in range, doppler, and angle for small target detection when no LDR cancellation techniques is used. In each plot, the power ratio refers to the dynamic range between large and small target. Using 20 dB dynamic range as a reasonable level, we conclude from Figure 3.6.1-2 (a) that using the Barker 13:1 code, a separation of 10 range bins in range would be necessary to detect the small target. Of course, with even larger dynamic range, 14 range bin separation would be required to detect the small target. For the cases we present, however, a 20 dB dynamic range is in effect

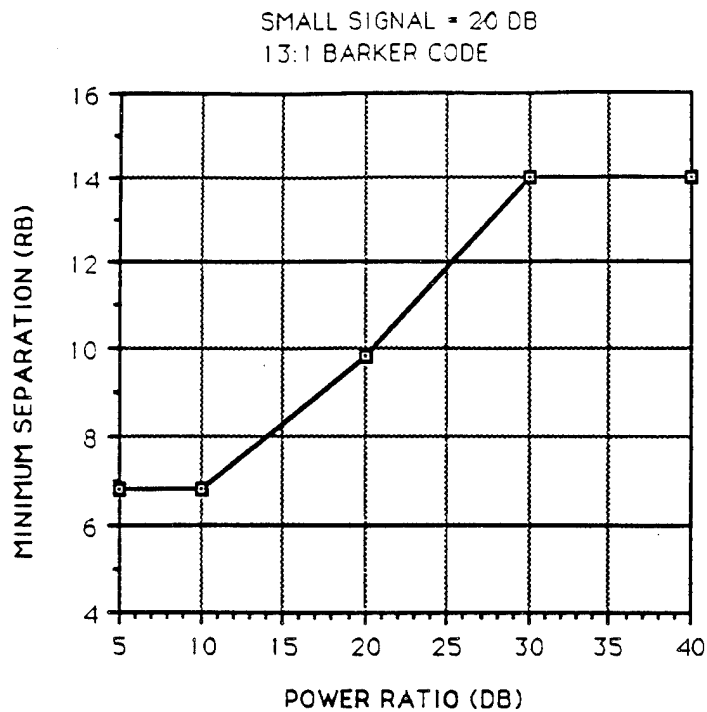


Figure 3.6.2-1 (a). Minimum range separation for small target detection

and so 10 range bins is used. Similarly, in the doppler domain, assuming 75 dB Dolph-Chebyshev filter amplitude weighting, we see that a 2.75 doppler filter separation is necessary, and in angle a 0.8 beamwidth separation is necessary for small target detection.

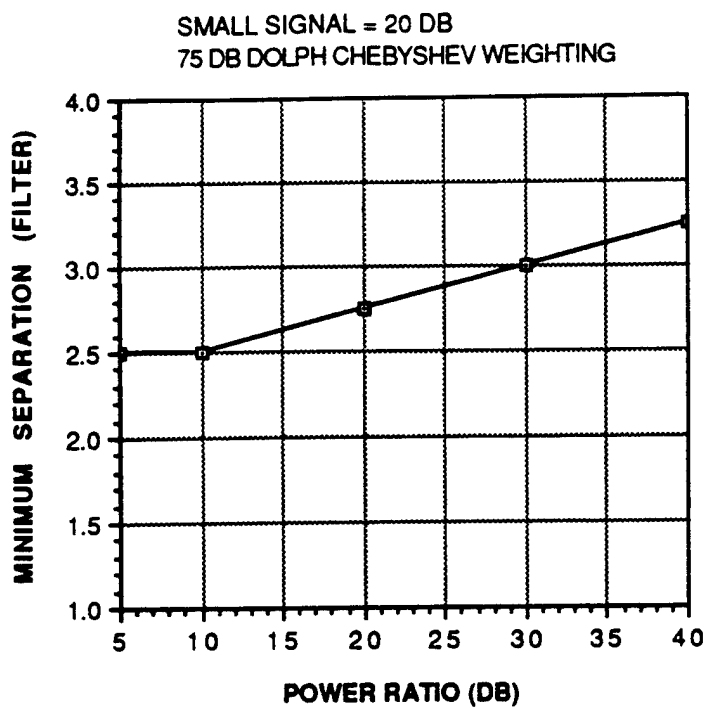


Figure 3.6.2-1 (b). Minimum filter separation for small target detection

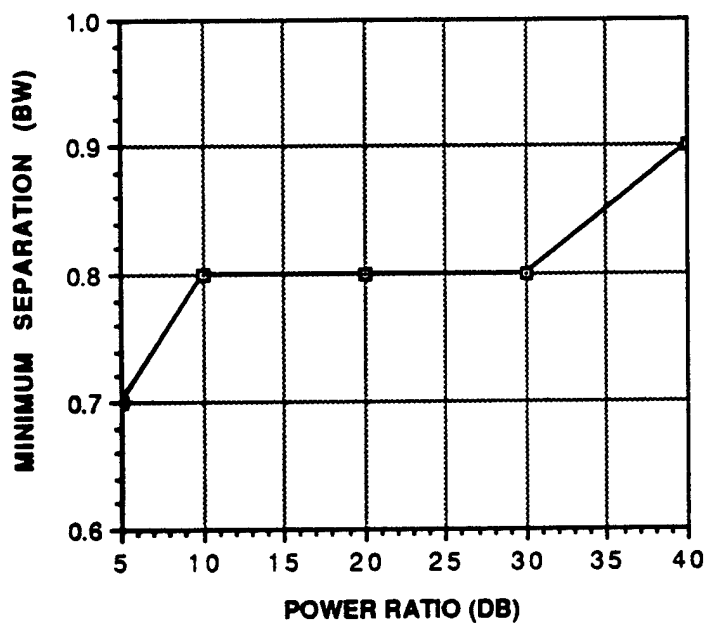


Figure 3.6.2-1 (c). Minimum angular separation for small target detection

Based on these results we can define a masking region as a region where only the large target can be observed. This region is illustrated in Figure 3.6.2-2.

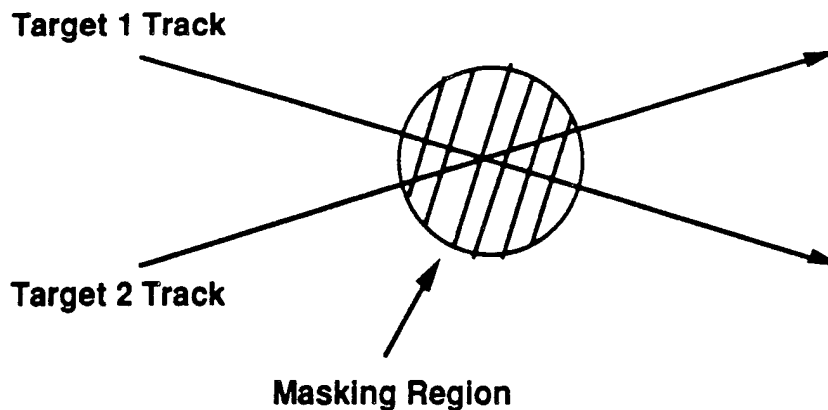


Figure 3.6.2-2. Masking region geometry

The conditions for the two targets to be in the masking region are:

$$\begin{aligned}
 &R_{\text{diff}} < 10 \text{ Range bins} \\
 &\quad \text{and} \\
 &\dot{R}_{\text{diff}} < 3 \text{ Doppler filters} \\
 &\quad \text{and} \\
 &Az_{\text{diff}} < 0.8 \text{ Beamwidth} \\
 &\quad \text{and} \\
 &El_{\text{diff}} < 0.8 \text{ Beamwidth}
 \end{aligned}$$

With or without using LDR techniques to remove large target interference, whenever the two targets are in the masking region, the measurements will be modified by a bias term. The bias is due to interference by each target on one another, and is most severe when the dynamic range is small. Figures 3.6.2-3 (a), (b), and (c) show the large target measurement biases due to small target interference in the range, doppler, and angle domains.

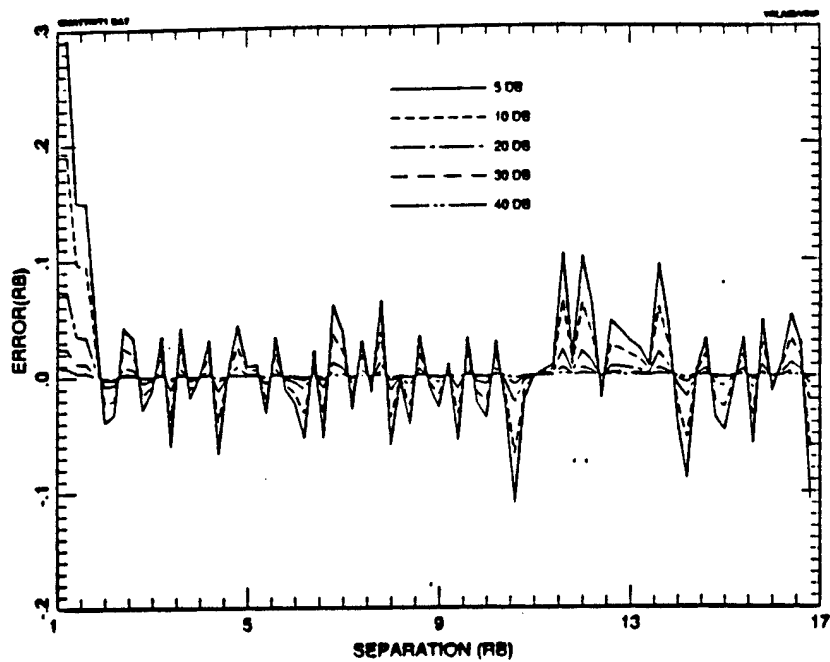


Figure 3.6.2-3 (a). Measurement bias in range

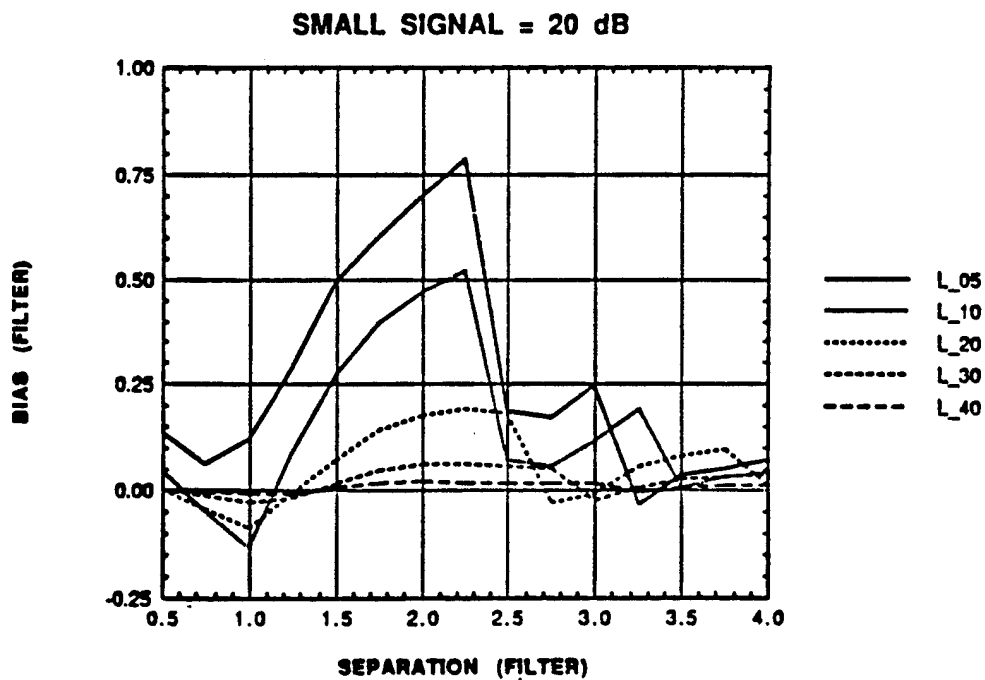


Figure 3.6.2-3 (b). Measurement bias in doppler

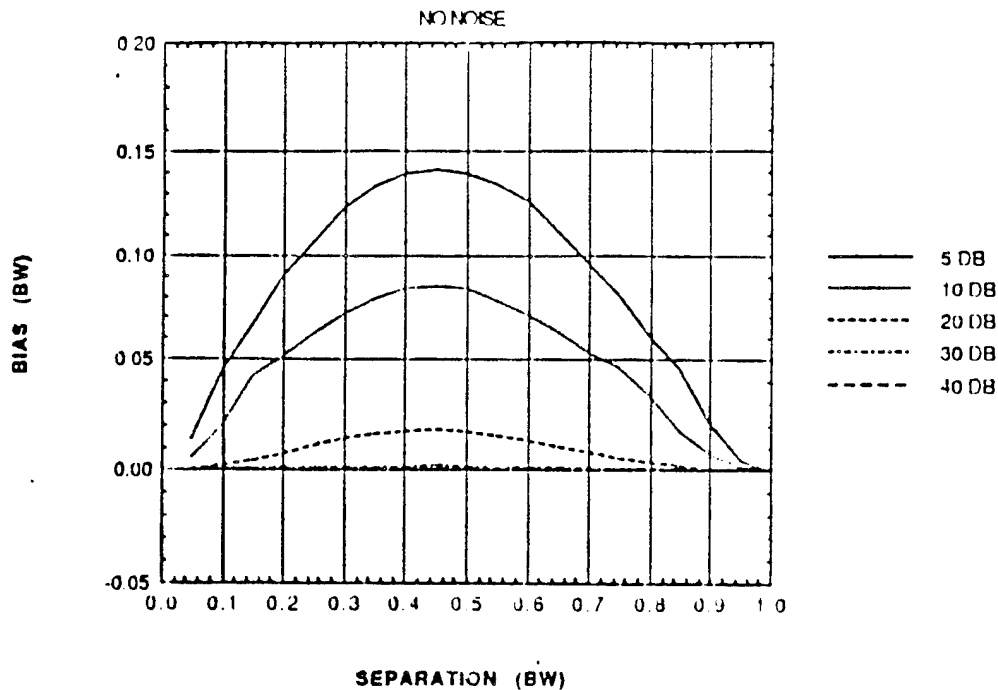


Figure 3.6.2-3 (c). Measurement bias in angle

In all three Figures, the bias is plotted with the dynamic range in dB as the parameter. The bias is worse when the dynamic range is small. Some of the biases can be very substantial, depending upon the separation and dynamic range. In doppler, the bias is as large as 0.8 of a filter when the dynamic range is 5 dB and target separation is 2 filters. In range, the bias is as large as 0.3 of a range bin when the dynamic range is 5 dB and separation of about 1 range bin. The maximum bias for angle is about 0.14 beamwidth.

Now that we have specified the measurement biases, we finally come to the model of target track observations that will be fed into the MHT Simulation to evaluate track effectiveness. There are two scenarios, with and without LDR techniques, and these are summarized in Figure 3.6.2-4.

1. Without LDR Techniques

Case a. Targets in ROM

Measurement is from large target only - with bias

$$\underline{z}_L = \underline{x}_L + \underline{v} + \underline{b}_L$$

Case b. Targets outside ROM

Measurements are from both targets - no biases

$$\underline{z}_L = \underline{x}_L + \underline{v}$$

$$\underline{z}_S = \underline{x}_S + \underline{v}$$

2. With LDR Techniques

Case a. Targets in ROM

Measurements are from both targets - with biases

$$\underline{z}_L = \underline{x}_L + \underline{v} + \underline{b}_L$$

$$\underline{z}_S = \underline{x}_S + \underline{v} + \underline{b}_S \quad (\underline{b}_S = \underline{b}_L \text{ of } \text{SNR}_{\text{diff}} = 0 \text{ dB})$$

Case b. Targets outside ROM

Measurements are from both targets - no biases

$$\underline{z}_L = \underline{x}_L + \underline{v}$$

$$\underline{z}_S = \underline{x}_S + \underline{v}$$

where \underline{v} is gaussian noise with mean 0 and covariance R.

Figure 3.6.2-4. Track measurement model with and without LDR techniques

The covariance matrix R is the same measurement variance matrix R defined in Section 3.6.1 for the Kalman filter.

3.6.3 Results of Tracking

We present color RAMTEK charts that show the target tracks as well as the likelihood probability of the tracks. In all these charts, the X and Y scale are labeled in pixel units, where each pixel is 1/10 nautical miles. The radar is always at the origin (0,0). The velocities of the targets are about Mach 1.

The tracks are color-coded in terms of probability of tracks. Red is the highest probability track while blue and violet are the lowest probability tracks. The yellow crosses in the charts are some of the observations that were not erased from the screen. Faint violet circles are the covariance gates that the MHT algorithm puts around an observation.

In Figure 3.6.3-1, we have the launching of a missile when LDR techniques are not used. In this chart we simulate the launching of a missile from an original target. It can be a bomber launching a cruise missile. The bomber is easily tracked from about (X=460,Y=180) all the way to the end of the run (-25,180). This track is in red. However, at some point in time a missile was launched, as can be seen by the second red track above the bomber track. We cannot detect the origin of this launch since the missile is masked by the bomber. All we see is the sudden appearance of a second red track at (160,220). But by this time many seconds have gone by since the launch of the missile.

In Figure 3.6.3-2, we have the launching of a missile when LDR techniques are used. In this chart we have the same scenario as in the previous Figure except that here LDR techniques are used. The bomber is easily tracked from about (X=460,Y=180) to the middle of the chart (225,180). This track is in red. Then it launches a missile flying upward. Initially the missile is very close to the bomber and thus is masked. However, by using LDR techniques it is possible to obtain observations from the missile within the masking region. Because of this the MHT algorithm is able to hypothesize that there are two low probability tracks close to each other (green and blue). It continues to track the two targets until they separate far enough to be tracked as red tracks. These results suggest that by using LDR techniques it is possible to detect a cruise missile launch.

In Figure 3.6.3-3, we have the case of two parallel targets when LDR techniques are not used. In this chart the two targets are flying closely together in parallel at only 15 m apart. With this separation, the small target is masked by the large target for the length of the run. As a result, the MHT algorithm only hypothesizes one red track. Therefore, the small target escapes detection.

In Figure 3.6.3-4 we have the same scenario here as in Figure 3.6.3-3. Two targets are flying closely together in parallel at only 15 m apart. With this separation the small target is masked by the large target. However, with LDR techniques, the MHT algorithm is able to observe the small target in the masking region. With two closely spaced observations at each update time, the MHT algorithm hypothesizes two or more blue tracks. The extreme closeness of the observations mean that they will fall within each target's covariance gates, thus making it difficult for MHT to hypothesize two definite red tracks.

Figure 3.6.3-5 shows the case of 10° target crossing when LDR techniques are not used. In this chart we have two targets crossing each other at a 10° angle. Initially they start out at about (530,-20) and (530,0) and move to the left of the chart. At first the targets are far enough apart so that we get observations from each target. However, they are also close enough so that their observations fall within each other's covariance gates, making it more difficult to obtain two red tracks. Therefore the tracks are blue or green in color. At about (380,10), the targets cross and are very close together. This is the start of the masking region where we don't observe the small target. As a result, MHT only picks up the large target as a red track. At about (240, 20) the targets again become separated enough for us to have 2 observations. Here MHT creates several hypothesis tracks in blue until about $X=160$ when there are two tracks in light green until the end of the run. This chart shows that without LDR techniques, the small target disappears in the masking region.

In Figure 3.6.3-6 we have the same scenario as in Figure 3.6.3-5 but with LDR techniques used. The difference here is that MHT has 2 observations in the masking region due to LDR. So in the masking region, instead of tracking only a single red track, MHT hypothesizes several blue tracks. With more information, this can suggest that there are two targets flying very closely together.

In Figure 3.6.3-7 we have two targets crossing at 10° but starting from opposite ends of the chart. The targets are easily tracked even when they are very close together. The targets never enter the masking region because their dopplers are so different (head-on approach). Thus LDR techniques are not needed.

These results show that having the extra observation from the small target in the masking region using LDR techniques, the tracking system can hypothesize about the existence of another target. In some cases, as in Figure 3.6.3-2, the existence of the cruise missile is immediately realized. In other cases, while the MHT algorithm is not able to keep clear red tracks of the two targets when LDR techniques are used, it is able to hypothesize weak tracks. This is already a significant improvement over the situation of not receiving this second target observation.

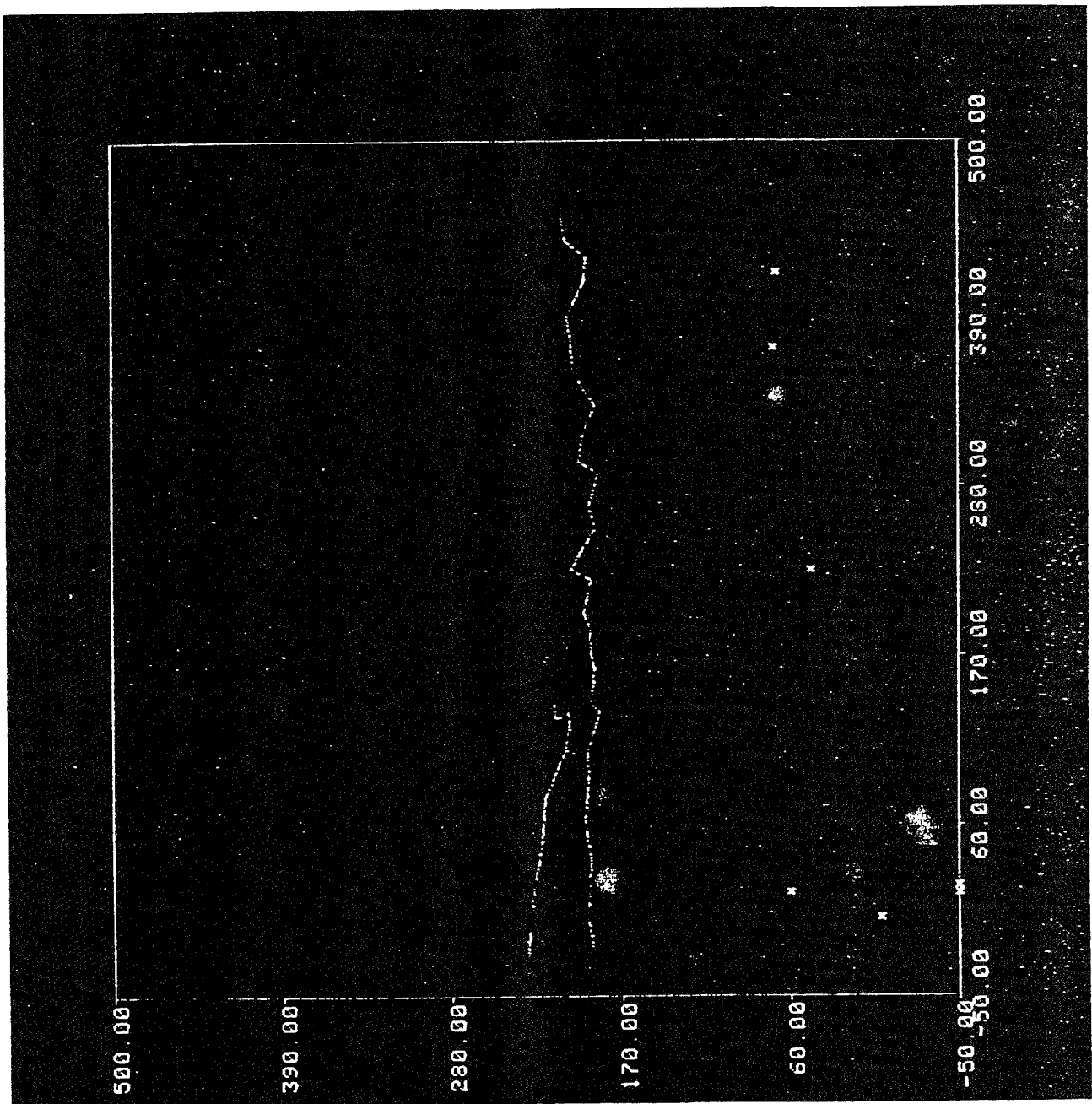


Figure 3.6.3-1. Launching of a missile when LDR techniques are not used

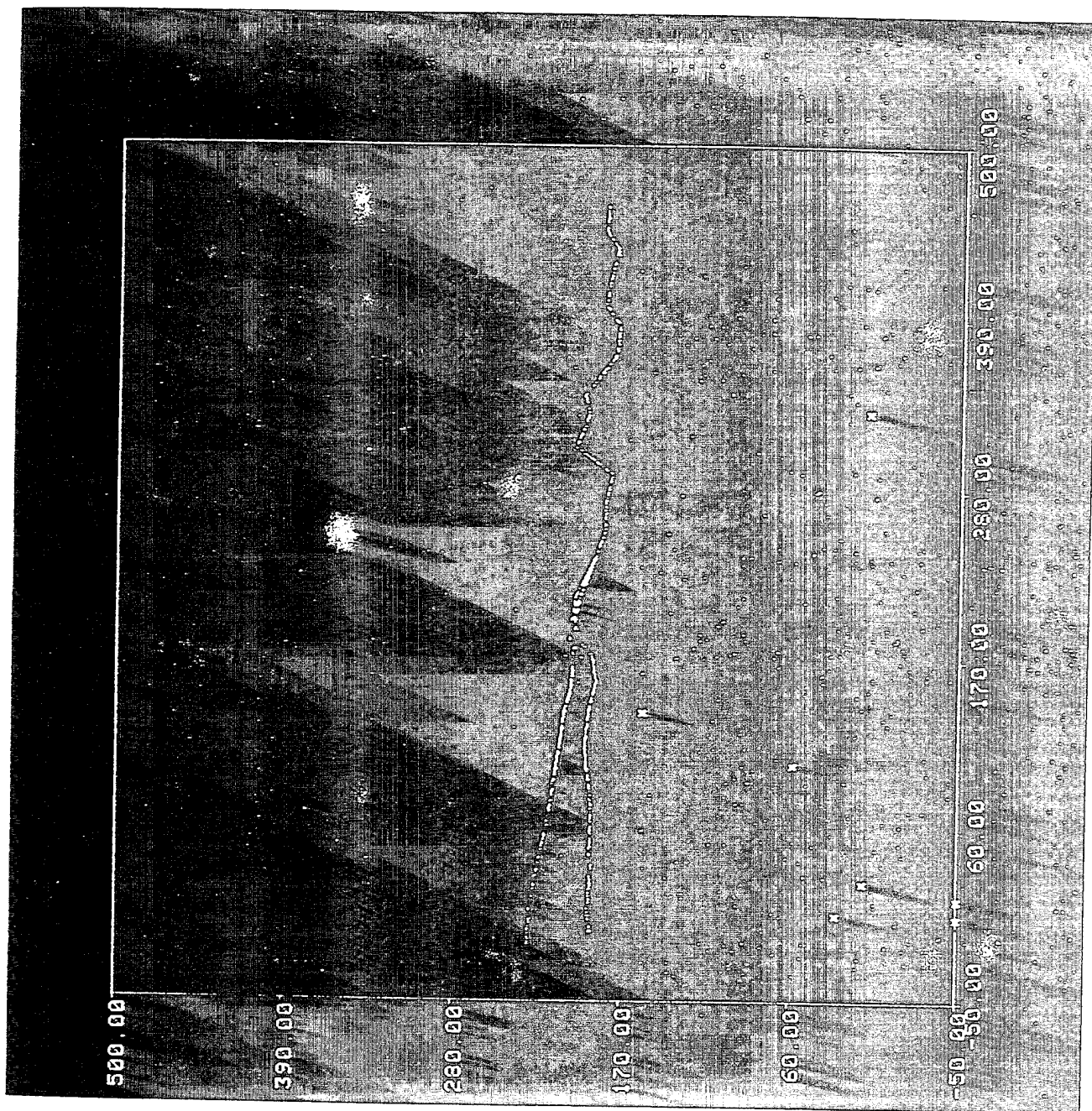


Figure 3.6.3-2. Launching of a missile when LDR techniques are used

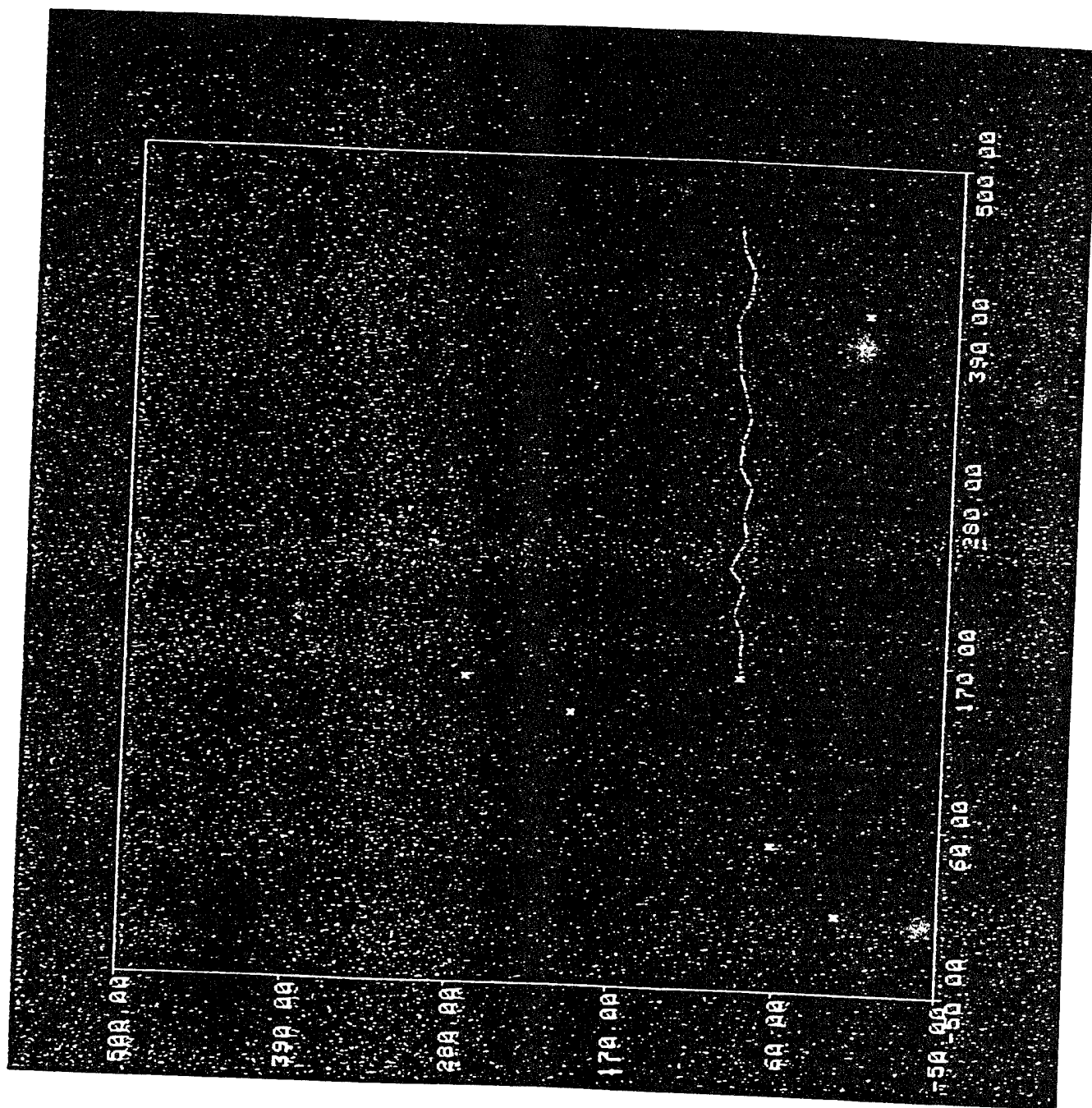


Figure 3.6.3-3. Parallel targets when LDR techniques are not used

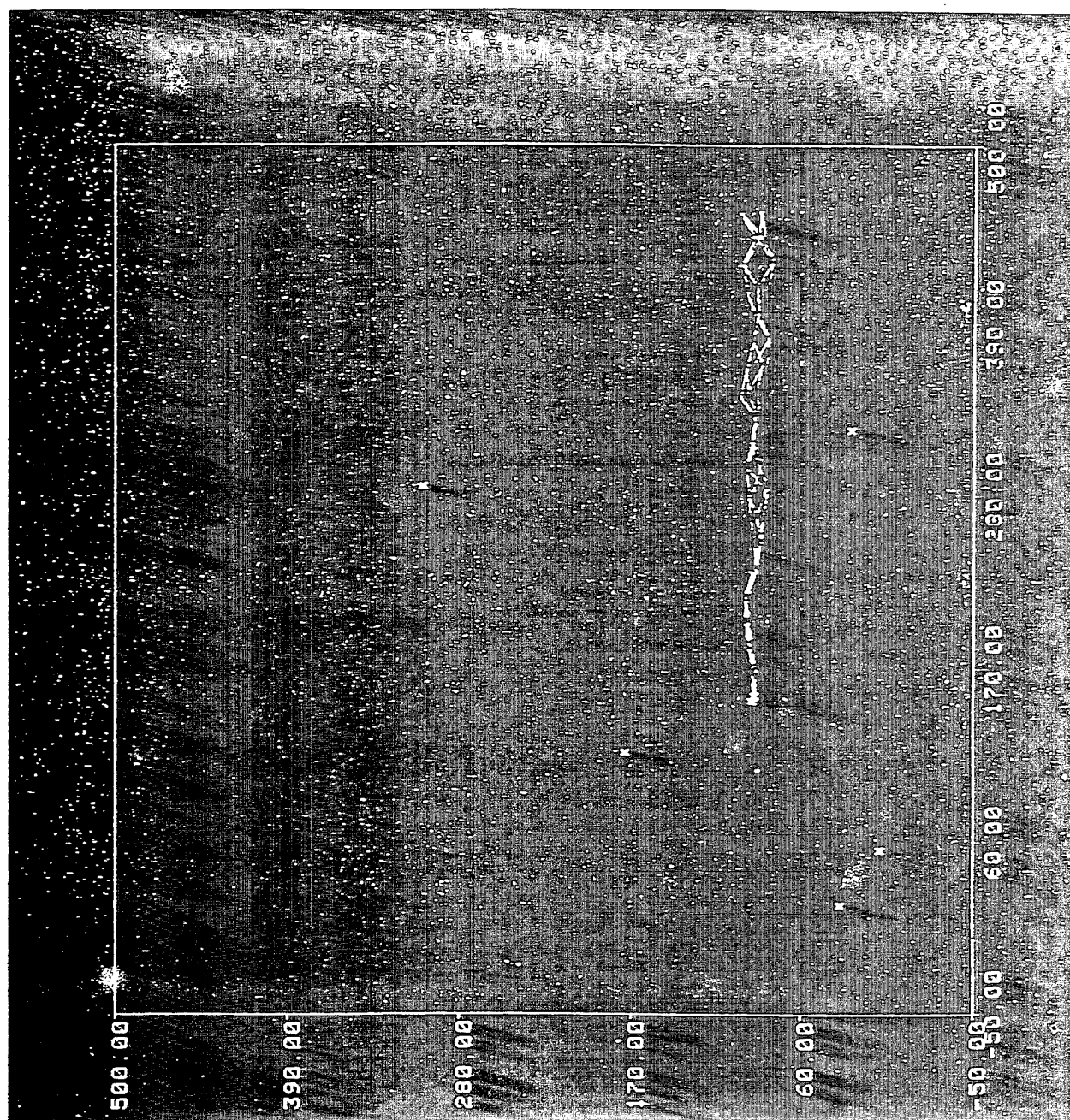


Figure 3.6.3-4. Parallel targets when LDR techniques are used

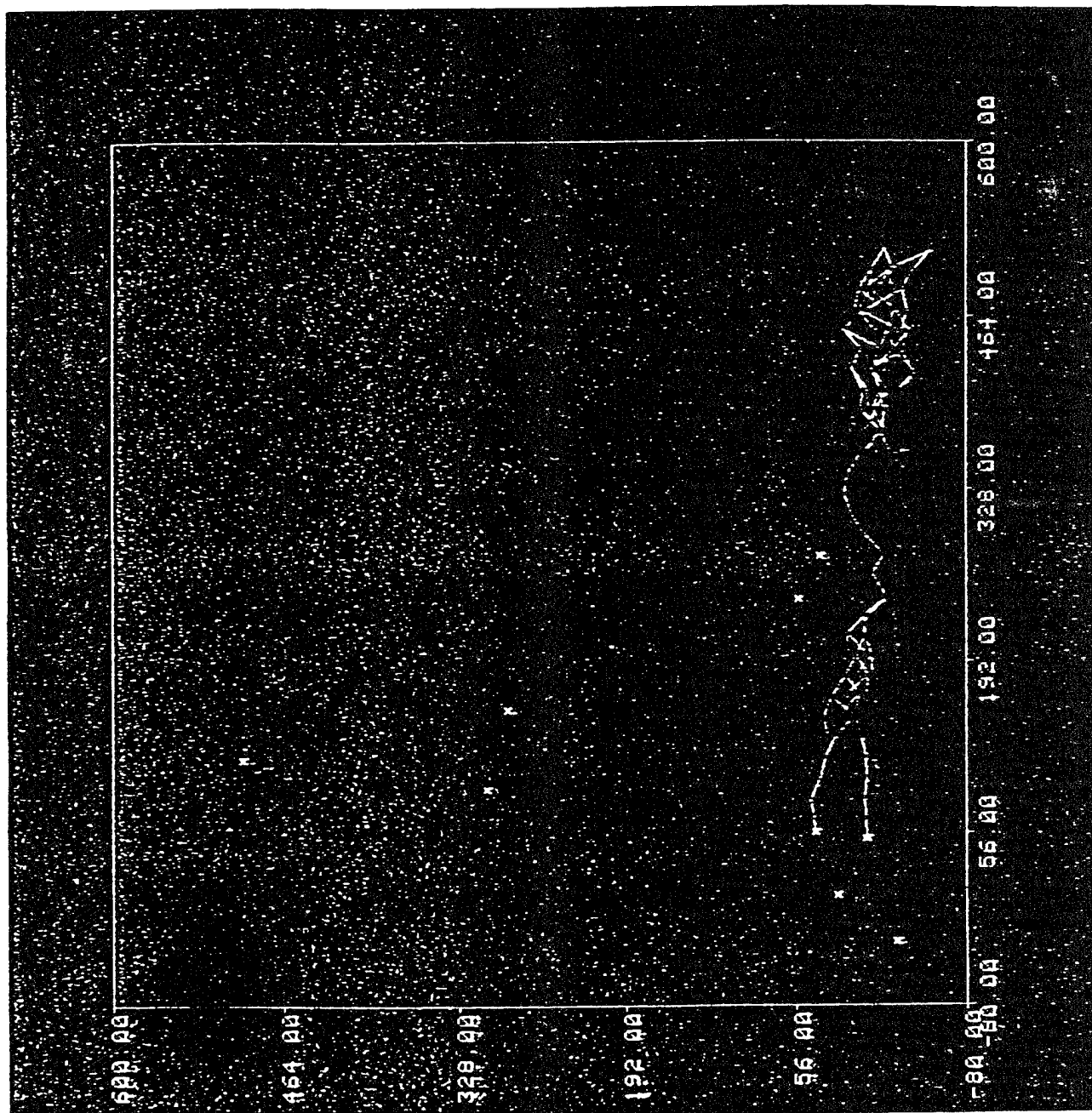


Figure 3.6.3-5. 10° target crossing when LDR techniques are not used

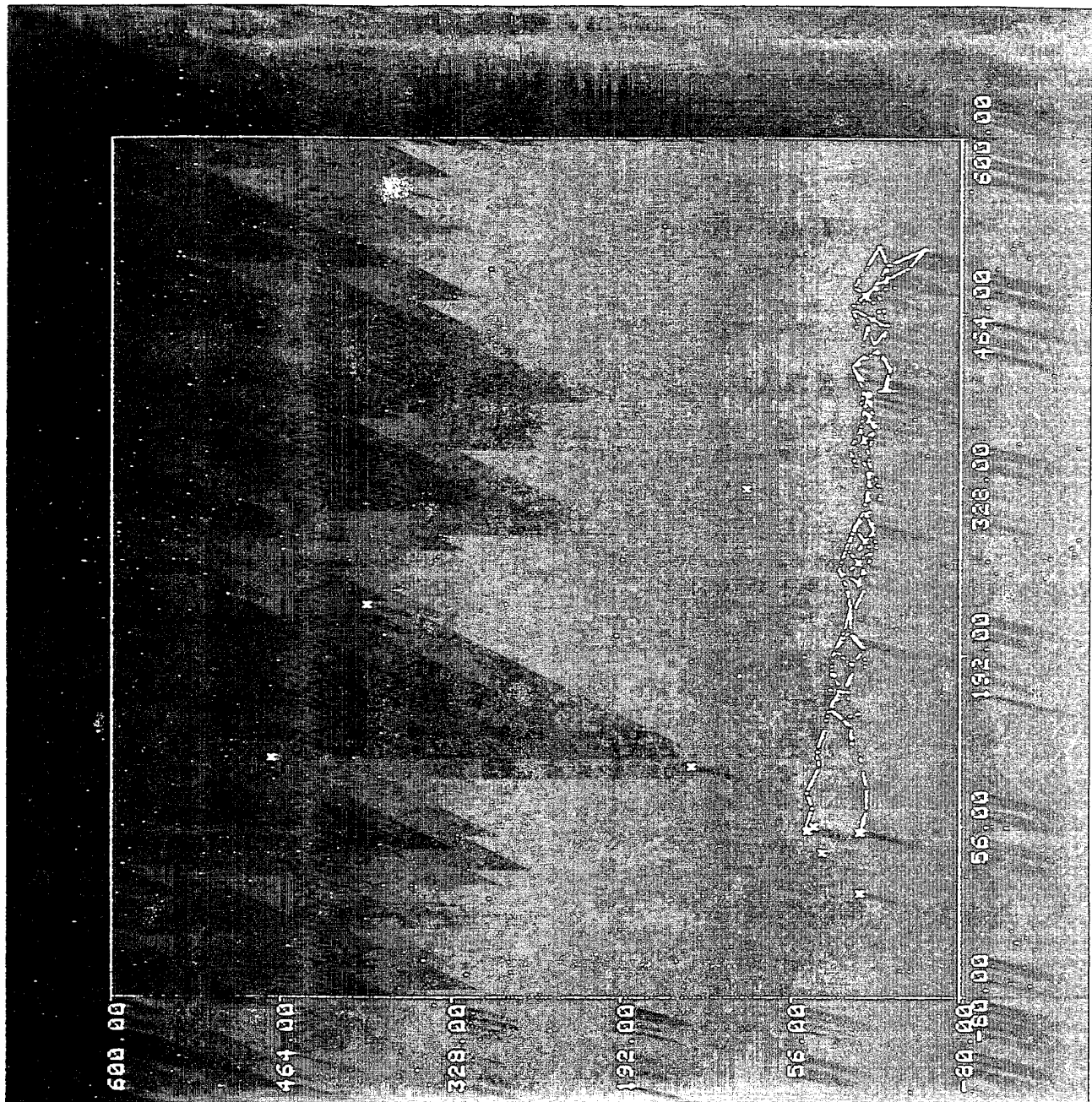


Figure 3.6.3-6. 10° target crossing when LDR techniques are used

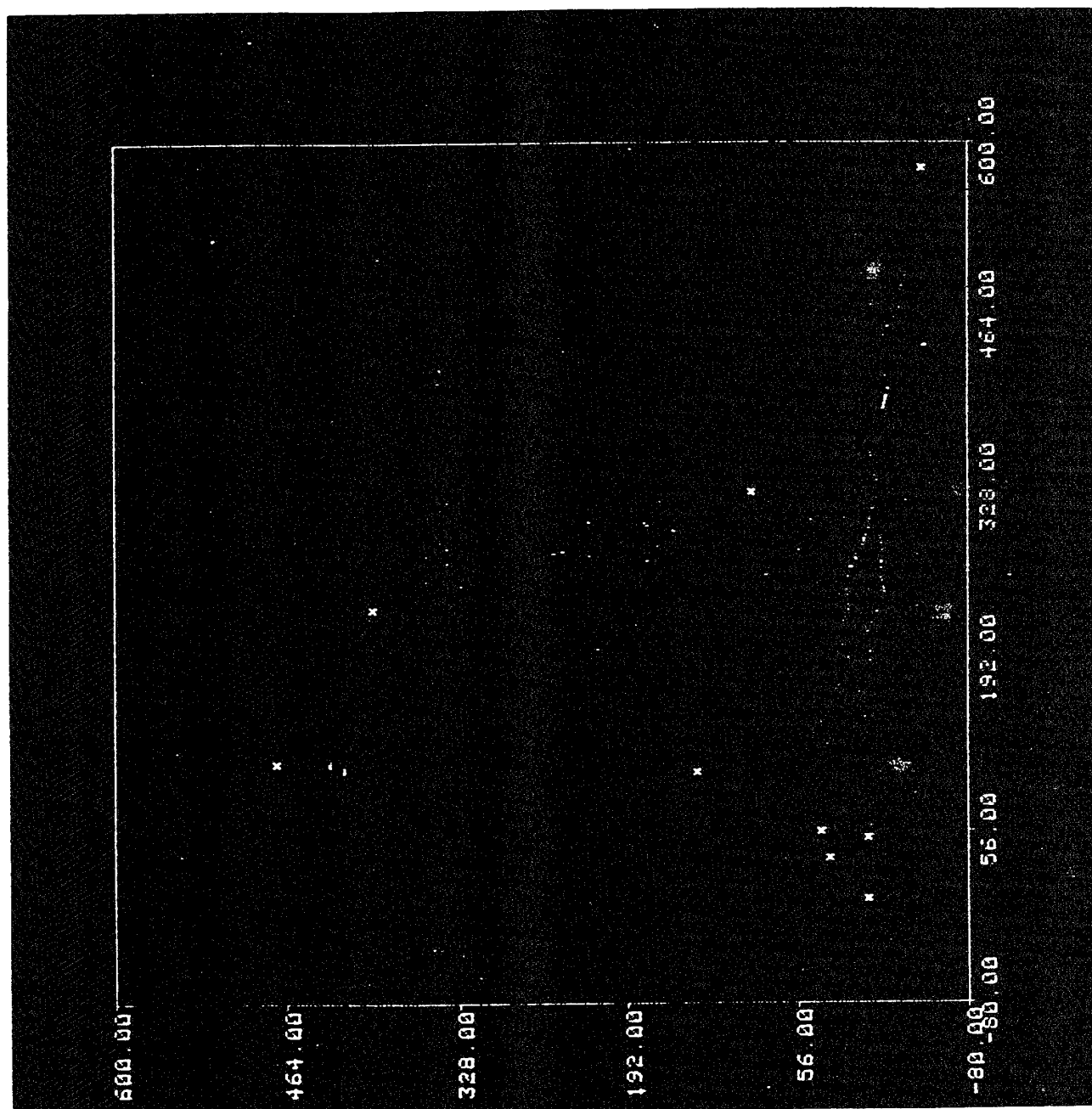


Figure 3.6.3-7. 10° opposing target crossing without LDR techniques

4.0 CONCLUSIONS AND FUTURE WORK

The results of this program indicate potential for greatly improving small target detection and track in the presence of much larger targets. The phenomenology of LDR must be studied using physical systems to determine if the nature and extent of the phenomenology indicated is, in fact, exploitable. A follow-on study which physically models realistic targets, measures radar cross section of the individual targets for comparison with the LDR prediction methods, and examines co-target data collected over a wide range of frequencies, waveforms, and relative position is a logical first step in confirming the results of the LDR study. Adjustments to the assumptions used for the tracking simulation could then be made and the LDR improvement over conventional tracking methods could be determined.

If the LDR results are confirmed by the above approach, a flight test program using full sized targets and operational systems should be conducted to collect and analyze data in the full-scale environment under a variety of conditions.

5.0 FOOTNOTES

1. Knott, E. F., Shaeffer, J. F., and Tuley, M. T., *Radar Cross Section*, Artech House, Norwood, Mass. (1985), p. 114.
2. Ibid.
3. Ibid.
4. Kapogianis, K., and Macfarlane, J. F., Description of a Multiple-Reflector Aircraft Target Model, Hughes Aircraft Co. internal memo., Jan. 26, 1979, Ref. 2312.11/01, p. 2.
5. Crispin, J. W., and Siegel, K. M., *Methods of Radar Cross-Section Analysis*, Academic Press, New York (1968), p. 86.
6. Ruck, G. T., Barrick, D. E., Stuart, W. D., and Krichbaum, C. K., *Radar Cross Section Handbook*, Plenum Press, New York (1970), Vol. 1, p. 62.
7. Ruck, p. 35.
8. Ruck, p. 62.
9. Ruck, p. 287.
10. Crispin, p. 305.
11. Skolnik, M. I., *Introduction to Radar Systems*, McGraw-Hill, New York (1980), p. 50.
12. Skolnik, p. 51.
13. Gelb, A., *Applied Optimal Estimation*, The M.I.T. Press, Cambridge, Mass. (1974), p. 187.

6.0 APPENDIX

RCS Model Limitations

First of all, the LDR interaction model may be optimistic in predicting the strength of the interaction signal. Less energy may be scattered from the missile than predicted. For a stand-alone cylinder, the scattering will be found in a cone around the cylinder in the specular direction. However, the cruise missile cylinder has many components attached to it, and so this result may not be true. Scattering will probably be limited to only certain angles in the specular direction. Also, since the specular point approach was not used, shadowing is not taken into account, and it is possible that for many aspect angles, scattered energy from the cylinder may be blocked by the wings of the missile or other components. Thus, the LDR interaction model may be predicting too much interaction between the two targets.

Secondly, the model relies heavily on the monostatic/bistatic equivalent theorem for scattering from the airplane. As stated in Section 3.1.2.1.6, the bistatic theorem breaks down for large bistatic angles.

***MISSION
OF
ROME LABORATORY***

Mission. The mission of Rome Laboratory is to advance the science and technologies of command, control, communications and intelligence and to transition them into systems to meet customer needs. To achieve this, Rome Lab:

- a. Conducts vigorous research, development and test programs in all applicable technologies;
- b. Transitions technology to current and future systems to improve operational capability, readiness, and supportability;
- c. Provides a full range of technical support to Air Force Materiel Command product centers and other Air Force organizations;
- d. Promotes transfer of technology to the private sector;
- e. Maintains leading edge technological expertise in the areas of surveillance, communications, command and control, intelligence, reliability science, electro-magnetic technology, photonics, signal processing, and computational science.

The thrust areas of technical competence include: Surveillance, Communications, Command and Control, Intelligence, Signal Processing, Computer Science and Technology, Electromagnetic Technology, Photonics and Reliability Sciences.